# Fundamental Mechanistic Studies of Formic Acid Decomposition on Transition Metals

By

Sha Li

A dissertation submitted in partial fulfillment of the requirements for the degree of

Doctor of Philosophy

(Chemical and Biological Engineering)

at the

UNIVERSITY OF WISCONSIN-MADISON

2015

Date of final oral examination: December 07, 2015

The dissertation is approved by the following members of the Final Oral Committee:

Manos Mavrikakis, Professor, Chemical and Biological Engineering

James A. Dumesic, Professor, Chemical and Biological Engineering

Michael David Graham, Professor, Chemical and Biological Engineering

Victor M. Zavala, Assistant Professor, Chemical and Biological Engineering

James Jay Schauer, Professor, Civil and Environmental Engineering

# Abstract

The conflict between increasing world energy demand and the fast depletion of fossil resources, together with the need to decrease our environmental footprint have emphasized the need to develop efficient chemical processes to convert renewable carbon sources to chemicals and fuels. Catalysts have long been used in the chemical industry for efficient chemical transformations which allow the processes to run under mild operating conditions while also keep a high yield and selectivity. Recently, density functional theory (DFT) calculations are increasingly contributing to the understanding of reaction mechanisms on catalytic surfaces, based on which improved catalysts may be designed. In this thesis, DFT calculations were used in combination with experiments and microkinetic modeling to study the catalytic decomposition of formic acid, which is a byproduct generated in biomass reforming and releases hydrogen upon decomposition. In particular, the reaction was studied on four transition metal catalysts ─ gold, palladium, platinum and copper ─ to unravel the reaction mechanism, evaluate their catalytic efficiencies for this chemistry and provide insights into catalyst design.

Using an iterative methodology comprising of DFT calculations, experiments and mean-field microkinetic modeling analysis, the formic acid decomposition reaction is found to proceed via a formate intermediate on both Au and Cu catalysts, and the actives sites are determined to be highly under-coordinated corner sites for Au and the (100) facet for Cu, which is potentially covered by about 0.4 monolayer of formate species during the reaction. The carboxyl intermediate, which is not relevant for the reaction on Au and Cu catalysts, however, is an active intermediate on Pd and Pt catalysts for formic acid decomposition and it is also the source of the poison species CO for the latter two catalysts. As the Pd and Pt catalysts used in experiments are often covered by CO species, the reaction was also investigated at high CO coverage for the two catalysts, and by

comparing with results on the clean surfaces, dramatic CO coverage effect on the reaction energetics and reaction pathways are found.

# Acknowledgements

The completion of this thesis is one important accomplishment to me, but it would not have been possible without help. First and foremost, I'd like to thank my advisor, Prof. Manos Mavrikakis for his support and outstanding scientific guidance throughout the process. His insight has been an invaluable part of the work, and his work ethic, enormous passion for research and immense knowledge in the field of catalysis truly inspire admiration.

I very much appreciate the time and effort spent by Prof. Dumesic, Prof. Graham, Prof. Zavala and Prof. Schauer for serving on my Ph.D. defense committee, and Prof. Kuech, Prof. Murphy and Prof. Reed for their service on my prelim committee. In particular, I want to thank Prof. Dumesic for sharing his insights and knowledge during our collaboration on the majority of the work included in this thesis.

I'm very thankful to my collaborators both in and outside the University of Wisconsin-Madison. Special thanks are due to Suyash, Jey, Ronald, Ana and Srini; they have made outstanding contributions to this thesis. I also thank Prof. Maria Flytzani-Stephanopoulos (Tufts University), Prof. Ye Xu (Louisiana State University) and Ming Yang (Tufts University) for our collaboration on a nice project that leads to a publication in Science. I acknowledge the funding from the Institute of Atom Efficient Chemical Transformation (IACT) and the computational resources provided by the following agencies: ANL, NERSC, PNNL and ORNL.

I would like to thank all the present and past Mavrikakis group members: Jeff and Guowen for helping me learn the density functional theory codes and their technical help during my PhD; Tony and Carrie for putting up with me as officemates; Suyash, Jey, Ahmed and Srini for the close

collaborations at different stages of my PhD; Yunhai, Luke, Lang, Duygu, Sean, Benjamin, Tibor and Fuat for various and sundry reasons.

A special thank goes to all the friends I have made over the past years in Madison. Without their friendship and company, my stay in Madison could not be a pleasant one, and I will never forget the good times we experienced together. Last, but not least, I would like to thank my parents for their never-ending love, support and encouragement.

# Table of Contents

# List of Tables

# List of Figures

# Chapter 1 Introduction

## 1.1 Research motivation

With increasing world energy demand accompanying the population and economic growth and a foreseen depletion of fossil fuels, the need to improve the efficiency in fossil fuels use and identify alternative renewable energy sources is more pressing than ever.[1] Heterogeneous catalysis can contribute significantly to the solution of global energy problem since it is a way to improve the efficiency of chemical conversions by providing alternative pathways for the desired chemical reactions with lower kinetic barriers.[2] Recent development in high-performance computing and electronic structure theory have provide a major thrust to the efforts that implement theoretical methods for developing fundamental atomic-level understanding of the catalytic processes. Among them is the density functional theory (DFT)[3, 4], which has been extensively used in the catalysis community to elucidate the mechanisms of chemical transformations on catalytic surfaces at an atomic level, which can help explain the macroscopic properties of the catalysts.

While first principles DFT calculations are usually performed on idealized single crystal facets with the energetics obtained representing the chemistry under ultra-high vacuum conditions, experiments are often conducted at higher pressures on supported nanoparticle catalysts. There exists a material and pressure gap between the theoretical and experimental studies which can be bridged by a mean-field microkinetic modeling analysis[5-8] that correlates the microscopic structure and composition of the catalysts to the macroscopically observable selectivity and reactivity. Adopting an iterative approach on the surface models used in DFT calculations, results of which serve as the input in the microkinetic model to compare with the experimental results, the reaction mechanism and active sites can be elucidated when the model reproduces the experimental data

with only fine-tuning of the DFT derived parameters and the model predicted surface environment (coverage) is consistent with that being used in the DFT calculations, in which case a 'self-consistent' solution is obtained. The self-consistency in surface coverage from the solution is critical to determine the true active sites for the reaction as the reaction energetics and even the mechanism can change significantly at different surface environments.

While DFT calculations, when combined with reaction kinetics experiments and microkinetic modeling, can capture the essential aspects of the surface chemistry such as the reaction mechanism, reactive intermediates and active sites, and propose ways to enhance the activity and selectivity based on the mechanistic information acquired, design better and cheaper catalysts to improve process efficiency is not trivial and requires much more effort from the entire catalysis community. In the meanwhile, efforts have been made to identify alternative energy sources and processes to mitigate the dependence on fossil fuels, among which biomass upgrading seems to hold a promise for a transition toward a greener and more sustainable energy future.

Though biofuels[9, 10] are among the most promising substitutes for fossil fuels, especially in the transportation sector, first generation biofuels (e.g. corn ethanol and biodiesel) have the disadvantage that they compete with food for their feedstocks. Recently, more interest has been placed on a cheaper and more abundant lignocellulosic material[11, 12], which can be converted to levulinic acid (LA) that is a potential platform molecule for the production of chemicals and liquid fuels using the current infrastructure of chemical industry.[13-17] During the production of LA from lignocellulosic biomass, formic acid (HCOOH) is formed as an equimolar byproduct of LA.[18] Catalytic decomposition of formic acid over heterogeneous catalysts leading to hydrogen production offers an efficient way to purify LA for subsequent upgrading processes and also utilize the byproduct and provide *in situ* hydrogen for the hydrogenation processes in biofuels production.

Adopting this scheme, the external requirement of hydrogen in biomass upgrading is minimized. Hence we are motivated to understand the fundamental chemistry involved in formic acid decomposition on transition metals in order to achieve an efficient hydrogen production process. In addition, formic acid can be used as a fuel in direct formic acid fuel cells (DFAFC)[19-21], the effective production of hydrogen from formic acid can also provide a boost in efficiency of DFAFC.

**1.2 Thesis scope**

Though formic acid decomposition has been extensively studied on transition metals, consensus has not been achieved regarding the reaction mechanism and active sites of the this reaction on different metals, largely due to the different synthetic protocols used for catalyst preparation and the various different reactions conditions and supports adopted in these studies that lead to controversial results. In this thesis, DFT calculations are employed to acquire a fundamental mechanistic understanding of this reaction on several transition metals, and are combined with reaction kinetics experiments, catalyst characterization techniques and microkinetic modeling to determine the active sites and surface environment information which are not captured by solely DFT studies, and to corroborate the reaction mechanism proposed from the DFT analysis.

Chapter 2 provides a brief summary on the background of density functional theory and microkinetic modeling; further details about the methods used in the studies are reported in individual chapters.

Chapter 3 discusses the first principles DFT investigation of formic acid decomposition on several single crystal Au surfaces, which was further combined with reaction kinetics experiments and microkinetic modeling to obtain an unambiguous picture of the reaction mechanism and provide

insights into the nature of active sites for Au catalysts. In Chapter 4, the study on Au catalysts is extended to subnanometer-sized Au clusters with DFT calculations. From comparison of the DFT derived results with the experimental counterpart in a microkinetic model, active sites for the Au catalysts are elucidated.

Chapter 5 and 6 report the DFT investigations of the reaction on Pd and Pt catalysts, particularly focusing on the CO coverage effects on reaction energetics and pathways, as well as the structure sensitivity of the reaction on the two catalysts.

Chapter 7 describes the structure sensitivity study of the reaction on Cu catalysts by investigating several single crystal Cu surfaces with DFT calculations. In Chapter 8, the study on Cu catalysts is extended to determine the active sites for formic acid decomposition by implementing an integrated approach of DFT calculations, experiments and microkinetic modeling.

And finally Chapter 9 provides a summary of the studies included in this thesis and also suggestions for future research.

# Chapter 2 Overview of Methods

## 2.1 Density functional theory (DFT)

Electronic structure calculations forms the foundation of understanding the surface chemical reactivity. The fundamental equation upon which electronic structure theories are based is the time-independent $Schrödinger$ equation (TISE):

$$\hat{H}\Psi(\mathbf{r}) = E\Psi(\mathbf{r}) \tag{2-1}$$

where $\hat{H}$ is the Hamiltonian operator, $\Psi(\mathbf{r})$ is the wave function, and $E$ is the total energy of the system. Solution of this equation yields fundamental information about the system, including probability distributions for all particles in the system and energetic information about particular particle configurations.

For systems of interest in surface science and heterogeneous catalysis, the full TISE is generally simplified by the Born-Oppenheimer approximation which makes use of the fact that electrons move much more quickly than their corresponding nuclei, and allows for decoupling of the electronic and nuclear components of the wave function:

$$\Psi_{total} = \Psi_{electronic} \times \Psi_{nuclear} \tag{2-2}$$

The total wave function is solved in an iterative manner. First, the electronic wave function is solved at fixed nuclear configuration and the overall electronic Hamiltonian is made up of three parts:

$$\hat{H}\Psi_{electronic} = (\hat{T} + \hat{V} + \hat{U})\Psi_{electronic} \tag{2-3}$$

where $\hat{T}$ is kinetic energy of the electrons, $\hat{V}$ is a function of electron's position in space and represents the interaction of electrons with the stationary nuclei, while $\hat{U}$ represents interaction

energy between electrons. The total energy for the fixed configuration of nuclei is then a sum of the kinetic energies of each electron, the interaction energy between electron nuclei, and the sum of all pairwise interactions of the electrons. When the electronic wave function is solved for the fixed nuclear configuration, the total potential energy surface can then be calculated by moving the nuclei around in space, recalculating the electronic potential energy and wave function until the ground state of the overall system is found.

While the Born-Oppenheimer approximation does simplify the problem, solving a many-body $Schrödinger$ equation is extremely difficult. For systems of interest in heterogeneous catalysis, obtaining an analytical solution if not feasible, thus, several approximate numerical schemes have been developed, such as the *Hartree-Fock Self-Consistent Field* (HFSCF) method and the *Configuration Interaction* (CI) method. In the HFSCF approach, the full many-electron wave function is written as the product of one-electron orbitals, and consequently, the $Schrödinger$ equation becomes separable into a set of one-electron equations. While the HFSCF approach is appealing in its simplicity, there are substantial errors in energies calculated from this method due to the lack of explicit electron correlation effects.[22] *Configuration Interaction* (CI) methods corrects this deficiency by making use of unoccupied states to account for correlation effects and allowing for the incorporation of excited electron configurations into the wave function.[23, 24] CI calculations can give a very accurate solution to the TISE but are extremely computationally expensive; the convergence of this method is generally on the order of $N^7$, where N is the number of basis functions. There are other methods with attractive features of providing exact solutions to the TISE, such as *Post-Hartree-Fock* method[25], *Quantum Monte Carlo* techniques[26-29] including *Diffusional Monte Carlo* method and *Variational Monte Carlo* method, but they all involve extremely high computational costs.

The theorems developed in 1960s by Hohenberg and Kohn[30] paved the way for the less computational demanding *Density Functional Theory* (DFT) scheme, which is now widely used in chemical computations. One important theorem proves that the ground-state energy from the $Schrödinger$ equation is a unique functional of the electron density. Thus the $Schrödinger$ equation can be solved by finding a function of only three variables, the electron density, rather than a function of 3N variables, the wave function. The second important theorem states that the electron density that minimizes the energy of the overall functional is the true electron density corresponding to the full solution of the $Schrödinger$ equation, which allows the use of approximate forms of the functional while minimizing the energy associated with it to find the true electron density.

A useful way to write down the energy functional is to split it into a collection of known terms we can write down in a simple analytical form, including the electron kinetic energies, the Coulomb interactions between the electrons and the nuclei, the Coulomb interactions between pairs of electrons, and the Coulomb interactions between pairs of nuclei, and everything else in an exchange correlation (XC) functional which account for all the quantum mechanical effects that are not included in the known terms. And the true electron density can be obtained by solving a set of single-electron equations (Kohn - Sham[31] equations):

$$\left[\frac{\hbar^2}{2m}\nabla^2 + V(\boldsymbol{r}) + V_H(\boldsymbol{r}) + V_{XC}(\boldsymbol{r})\right]\Psi_i(\boldsymbol{r}) = \varepsilon_i\Psi_i(\boldsymbol{r}) \qquad (2\text{-}4)$$

where $\hbar$ is Planck's constant, $m$ is the rest mass of an electron, $\nabla^2$ is the Laplacian, $\varepsilon_i$ is a one-electron eigenvalue and $\Psi_i(\boldsymbol{r})$ is the single-electron wave function. $V$ defines the interaction between an electron and the collection of atomic nuclei, $V_H$ is the Hatree potentials describe the Coulomb repulsion between the electron being considered in one of the Kohn – Sham equations

and the total electron density defined by all electrons, and $V_{XC}$ define the exchange and correlation contributions to the single electron equations.

However, the exact exchange-correlation functional remains unknown and approximations must therefore be used, and the accuracy of the DFT calculations very much depends on the quality of the exchange-correlation energy $E_{XC}$. The LDA (Local Density Approximation) uses an XC functional that depends only on the electron density and takes the XC energy as that for a homogeneous electron gas.[32, 33] The GGA (Generalized Gradient Approximation)[34] incorporates density gradient terms into the XC functional that can give much more accurate values. In this study, the PW91 generalized gradient approximation (GGA-PW91) is used to describe the exchange-correlation potentials, unless otherwise stated. Further details of the DFT methods used will be included in each individual chapter.

**2.2 Microkinetic modeling**

Microkinetic modeling is an important and popular tool to compare the experimentally derived rates with those predicted from DFT calculations, and obtain useful information about the reaction behavior, including the surface coverages under reaction conditions and relative rates of various elementary steps. Microkinetic modeling analysis requires initial guesses for the various parameters like binding energies, activation energies, and frequency factors that can be rigorously calculated from DFT calculations. The implementation of the microkinetic models in this thesis closely follows the procedure described by Dumesic and Gokhale *et al*[7, 8] and further details will be provided in individual chapters where such analysis was performed. Here, we briefly summarize how the macroscopic information about a reaction (such as the reaction rate, selectivity) can be obtained from a microkinetic model using DFT derived parameters that are collected at an atomic-level as input.

Consider an elementary reaction A* + B* → C* + D*, the net reaction rate is calculated in the model as:

$$r = r_{for} - r_{rev} = k_{for}\theta_A\theta_B - k_{rev}\theta_C\theta_D \quad (2\text{-}5)$$

where $r_f$ and $r_r$ denote the rate of the forward and reverse reaction and $\theta_A$, $\theta_B$, $\theta_C$, and $\theta_D$ denote the surface coverages of the species A, B, C and D, respectively. The forward and the reverse rate constants $k_{for}$, $k_{rev}$, and the equilibrium constant $K$ are linked through the relation $K = k_{for}/k_{rev}$ and can be calculated by the following equations:

$$K = \exp\left(-\frac{\Delta G}{k_B T}\right) = \exp\left(\frac{\Delta S}{k_B}\right)\exp\left(-\frac{\Delta H}{k_B T}\right) \quad (2\text{-}6)$$

$$k_{for} = A_o \exp\left(-\frac{Ea}{k_B T}\right) \quad (2\text{-}7)$$

$$Ao = \frac{k_B T}{h} \exp\left(\frac{S^{\ddagger}_{AB} - S_A - S_B}{k_B}\right) \quad (2\text{-}8)$$

where $k_B$ is the Boltzmann constant, $T$ is the reaction temperature, $\Delta G$, $\Delta H$ and $\Delta S$ denote the change in standard-state Gibb's free energy, enthalpy and entropy of the reaction, respectively, Ea is the activation energy of the forward step, $S^{\ddagger}_{AB}, S_A,$ and $S_B$ denote the entropy for the transition state (TS) of the reaction, and species A or B, respectively.

Enthalpy and entropy for each surface intermediate and the TS of each elementary step can be computed from the following relations:

$$t = T[K]/1000 \quad (2\text{-}9)$$

$$H\,[kJ/moI] = At + Bt^2/2 + Ct^3/3 + Dt^4/4 - E/t + F \quad (2\text{-}10)$$

$$S\,[J/mol/K] = A\ln(t) + Bt + Ct^2/2 + Dt^3/3 - E/(2t^2) + G \quad (2\text{-}11)$$

where parameters A – G can be obtained by performing vibrational frequency calculations.

Thus the solely unknown information that is needed to calculate the reaction rate of each elementary step is the surface coverage of intermediates, which can be derived in the model by relating the rates of the elementary steps to each other adopting the fact that rate of change in surface coverage for each intermediate is zero at steady state. After the surface coverage for each intermediate is calculated, reaction rates for individual elementary steps can be obtained and other information regarding the dominant reaction pathway and rate limiting step can be determined by comparing the net rates of various elementary steps occurring in parallel.

# Chapter 3 Formic Acid Decomposition on Au catalysts: DFT, Microkinetic Modeling, and Reaction Kinetics Experiments†

## 3.1 Introduction

The effective utilization of renewable energy carriers produced from biomass based resources is one of the key challenges in the transition towards a sustainable energy future[9, 10]. Formic acid (FA, HCOOH) is a major byproduct in biomass processing[14], and it has attracted significant attention as a potential hydrogen-carrier material[35-40]. As a hydrogen-carrier, FA can be oxidized in direct formic acid fuel cells (DFAFCs)[41]. When generated as an equimolar by-product of levulinic acid [15-17] production from cellulosic biomass, FA can be used for *in-situ* harvesting $H_2$ which can then be utilized for the hydrogenation of levulinic acid to gamma-valerolactone (GVL)[42], thereby eliminating the need of an external hydrogen source in the production of this key biofuel precursor.[13, 18] Also, as the simplest carboxylic acid, FA has for long been considered a paradigmatic molecule in homogeneous and heterogeneous catalysis, and surface science studies, to probe the reactivity on metals[43-52], metal carbides[53-55], and on metal oxides[56-61] specifically for deoxygenation of more complex carboxylic acids, which is a critical step in the selective upgrading of biomass derived platform molecules to fuels. Hence, our motivation for studying the FA decomposition reaction is based on (1) its potential application as a promising liquid hydrogen carrier for *in situ* hydrogen production, and (2) its suitability as a fundamental probe molecule for understanding the reactivity of carboxylic acids on metal catalysts, and using this information to design improved catalysts for effective deoxygenation of these functional groups. FA

† Adapted from "Formic Acid Decomposition on Au Catalysts: DFT, Microkinetic Modeling, and Reaction Kinetics Experiments", S. Singh, S. Li, R. Carrasquillo-Flores, A. C. Alba-Rubio, J. A. Dumesic, M. Mavrikakis, *AIChE Journal* **60**, 1303 (2014). S. Singh contributed to the microkinetic analysis in this study; kinetic experiments were performed by R. Carrasquillo-Flores, and TEM images were provided by A. C. Alba-Rubio.

decomposition can take place via two parallel pathways involving dehydrogenation or dehydration reactions, which are linked by the water gas shift (WGS) [62-64] reaction. In the broader context of FA decomposition on transition metals, steering selectivity towards production of $CO_2$ + $H_2$ (dehydrogenation), rather than CO + $H_2O$ (dehydration) presents an important selectivity challenge in this catalytic chemistry. Even though the dehydration products can be transformed to $CO_2$ and $H_2$ via the WGS reaction, forming the dehydration products may lead to partial poisoning of catalytic sites by CO, thereby limiting the efficiency of the overall catalysis. Accordingly, supported Pt catalysts have frequently been suggested to be the most active catalysts for selective FA dehydrogenation, and for this reason, they find widespread applications as anodes for DFAFCs[19, 65-70]. Yet, there exist major obstacles in using Pt based catalysts as electrode materials and as FA decomposition catalysts, because of the proneness of Pt to CO poisoning[71-73] and its dissolution under operating conditions in fuel cells.

Gold, on the other hand, is not hindered by CO poisoning under most reaction conditions. Ever since Haruta[74] and Hutchings[75] first predicted Au to be an extraordinary catalyst for CO oxidation and ethylene hydrochlorination reactions, there has been an overwhelming interest in exploring the application of supported Au catalysts in both homogeneous and heterogeneous catalysis[76-84]. More recently, Au has been studied as a catalyst for HCOOH decomposition[85]. In particular, Ojeda et al.[86] studied the FA decomposition on supported Au catalysts and showed that the turnover frequencies (TOFs) on well-dispersed Au catalysts were higher than those on Pt catalysts. They proposed that this unprecedented activity on Au catalysts arises from small Au clusters, most likely undetected in transmission electron microscopy (TEM) micrographs. More recently, Gazsi et al.[87] performed vapor phase experiments to study the effect of supports on the selectivity of FA decomposition to the dehydration and dehydrogenation products, and they confirmed the high

activity of Au nanoparticles supported on a wide range of porous and non-porous supports. Although these experimental studies shed light on the possible nature of active sites on Au catalysts, a molecular level understanding of this reaction mechanism is still lacking. In this paper, we develop an integrated approach (**Figure 3-1**) by combining state-of-the-art Density Functional Theory (DFT) with reactivity experiments and microkinetic modeling which can shed additional light into the reaction mechanism and the nature of active sites on Au catalysts[7]. In particular, we choose Au(111), Au(100) and Au(211) model surfaces for our DFT calculations to derive initial guesses for the surface reaction energetics, needed for our microkinetic model. We then develop a comprehensive mean-field microkinetic model including all elementary steps investigated by our DFT calculations. Comparisons between microkinetic modeling reaction rates and reaction orders with the experimental results provide critical insights for the nature of the active site on Au/SiC catalysts for HCOOH decomposition.

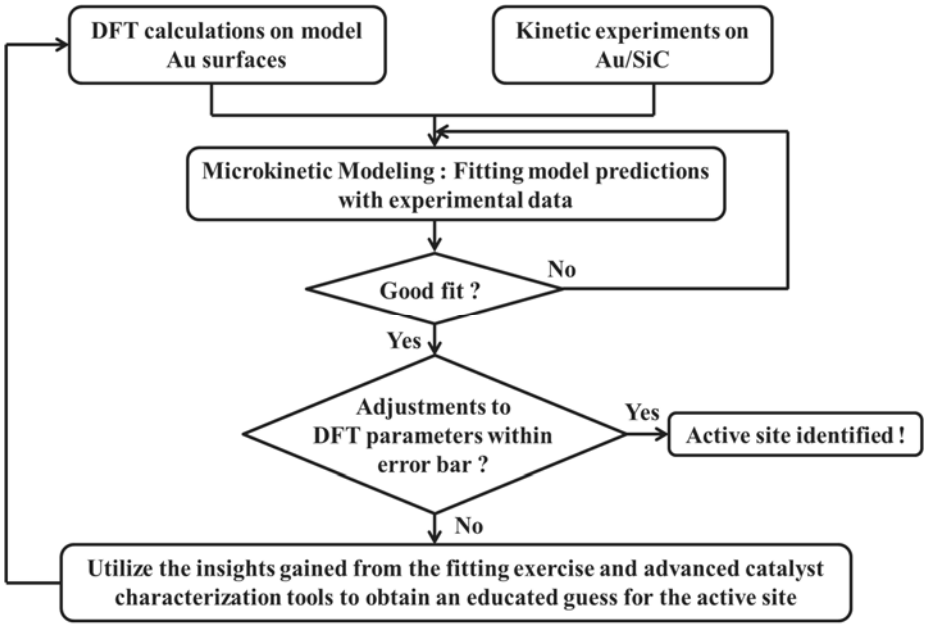


**Figure 3-1** Flow chart for the identification of active sites for FA decomposition on Au/SiC.

## 3.2 Methods

### *Density Functional Theory*

All calculations were performed using the DACAPO total energy code[88, 89]. The Au catalyst was modeled by the (111), (100) and (211) facets of the fcc bulk crystalline structure of Au metal (**Figure 3-2**).

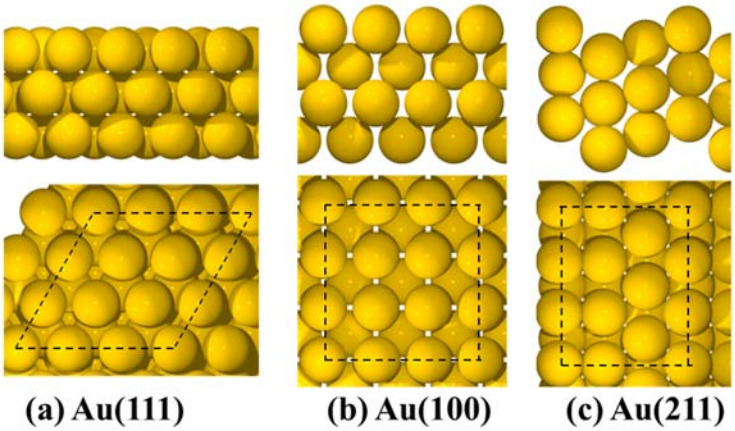


**Figure 3-2** Side and top views of the three model Au surfaces used in this study: (a) Au(111), (b) Au(100), and (c) Au(211).

The Au(111) surface was modeled by a three-layer slab with a p(3×3) unit cell, corresponding to 1/9 monolayer (ML) coverage for a single adsorbate in the unit cell, periodically repeated in a super cell geometry with five equivalent layers of vacuum between any two successive metal slabs. All the Au atoms in this model surface were kept fixed in their bulk truncated positions, as our systematic investigations showed that surface relaxation does not have a significant effect on the energetics for this system. The super cell used to model the Au(100) facet consists of a p(3x3) unit cell with four layers of metal atoms, top two of which were allowed to relax, and five equivalent layers of vacuum spacing separating the periodic slab images. The Au(211) slab was constructed by a 1x3 unit cell and consisted of nine Au layers (having terrace three atoms deep and three atoms

wide). Successive slabs were separated by a vacuum equivalent to 12 such Au(211) layers. Adsorption was allowed on only one of the two exposed surfaces for all three slabs, and the electrostatic potential was adjusted accordingly.[90, 91]

The surface Brillouin zone of (111) slabs was sampled at 18 special Chadi-Cohen[92] k points, while that for the (100) and (211) slabs was sampled by using a 4×4×1 Monkhorst-Pack[93] k-point mesh. Ionic cores were described by ultrasoft Vanderbilt pseudo-potentials[94] and the Kohn-Sham one-electron valence states were expanded in a basis of plane waves below a kinetic energy of 25 Ry. The exchange-correlation energy and potential were described self-consistently using the generalized gradient approximation (GGA-PW91).[95, 96] The electron density was determined by iterative diagonalization of the Kohn-Sham Hamiltonian, Fermi population of the Kohn-Sham states ($k_BT$ = 0.1 eV), and Pulay mixing of the resulting electronic density.[97] The total energies were then extrapolated to $k_BT$ = 0 eV. The calculated equilibrium lattice constant for bulk Au was found to be 4.18 Å, in reasonable agreement with the experimental value (4.08 Å). [98]

The binding energies (BEs) were calculated with respect to the total energy of the clean slabs ($E_{slab}$) and the corresponding adsorbates in the gas phase ($E_{adsorbate,\ gas\text{-}phase}$), i.e., $BE_{adsorbate} = E_{total} - E_{slab} - E_{adsorbate,\ gas\text{-}phase}$. In the discussion of the DFT results, we refer to electronic energy values including the zero point energy (ZPE) corrections unless otherwise noted.

The minimum energy pathways and activation energy barriers for all elementary steps were determined using the climbing image nudged elastic band (CI-NEB) method.[99, 100] The minimum energy path for each elementary step was discretized with at least seven images, in addition to the initial and final states. A vibrational frequency analysis[101] was performed to confirm the true nature of the saddle point by identifying a single imaginary frequency along the reaction coordinate.

The frequencies were calculated using the harmonic oscillator assumption by diagonalization of the mass-weighted Hessian matrix in internal coordinates.[101]

## *Experiments*

### Catalyst Preparation

SiC was chosen as the preferred support for our reaction kinetics experiments because (1) it is an inert support that does not contribute to the overall reaction rated and (2) it results in a clear contrast for Au atoms and clusters in the scanning transmission electron microscopy (STEM) micrographs, due to the large difference in the scattering potentials of the metal and the support. A 1 wt% Au/SiC catalyst was prepared by the deposition-precipitation method. 2.0 g of dry acid-treated silicon carbide was dispersed in 100 mL of a 1 mM chloroauric acid (Sigma-Aldrich) solution at room temperature. The pH of the mix was adjusted to 9 by drop-wise addition of 2.5 M ammonium hydroxide (Sigma-Aldrich). The mixture was aged for 6 h under vigorous stirring at room temperature and was then filtered and washed with deionized water to remove chlorine ions. The sample was dried overnight at 373 K. The dried catalyst was reduced *in situ*, prior to the reaction at a temperature between 623 and 773 K (with a heating rate of 0.5 K $min^{-1}$) under pure hydrogen flow (30 $cm^3$ (STP) $min^{-1}$) for four hours. Catalyst reductions at temperatures above 773 K (and up to 1073 K) were performed in a quartz flow-through cell under the same operating conditions.

### Reactivity measurements

Gas phase HCOOH decomposition studies were conducted in a fixed-bed down-flow reactor containing 500 mg of catalyst mixed with silica chips in a 1/2-inch outer diameter stainless steel tube. The temperature was measured using a K-type thermocouple attached to the outside of the reactor. The temperature of the reactor was adjusted by using a furnace connected to a variable

autotransformer power source controlled with a temperature controller. The total pressure in the reactor was maintained at 1 atm, and the partial pressures of the gases were controlled by adjusting the flow-rates at the reactor inlet. The flow-rates of all gases were fixed using calibrated mass-flow meters. An inlet composition between 0-12% of $H_2$, 0-6% of $CO_2$ and 1-4% of HCOOH was used, with the balance consisting of helium. The gases were used as provided, with a purity of 99.99%. Liquid HCOOH (Sigma-Aldrich) was delivered to the reactor system at room temperature using a syringe pump (Harvard Apparatus) and vaporized at the reactor inlet. The feed and effluent gases were analyzed using gas chromatography (with a TCD). Conversions were maintained below 20% to achieve differential reactor operation. To determine the apparent activation energy barrier, the temperature was varied over a range of 50K, with the concentrations kept at standard conditions. The apparent reaction orders with respect to reactants and products were determined by varying one gas concentration at a time.

**High Resolution Scanning Transmission Electron Microscopy (STEM)**

The particle size distributions were determined from STEM images. STEM characterization was performed using a FEI Titan STEM with CEOS probe aberration corrector operated at 200 kV with spatial resolution of < 0.1 nm. For imaging, a high-angle annular dark-field (HAADF) Z-contrast STEM was used, with HAADF detector angle ranging from 54 to 270 mrad, probe convergence angle of 24.5 mrad, and probe current of ~25 pA. To prepare samples for STEM, the catalyst samples were first suspended in ethanol, ultrasonicated for 5 min, and then deposited onto a ~5 nm thick Si window TEM grids. STEM samples were plasma cleaned for 10 min with 20% $O_2$ + 80% Ar gas immediately before loading into the microscope.

The particle size distributions of the Au/SiC catalysts were calculated from the acquired STEM images. From the particle size distributions, the number average Au particle sizes were determined using the relation $d = {\sum_i d_i}/{n}$ , where $d_i$ is the particle diameter of each Au particle, n is the total number of Au particles counted from the TEM images of a given sample (**Table 3-6**), and the summation is performed over all the particles that were identified in the STEM images.

**Microkinetic Modeling**

A mean-field microkinetic model for FA decomposition was developed on the basis of 17 elementary steps, including some steps that are in common with the water gas shift (WGS) reaction. The initial estimates for the ZPE-corrected binding energies and activation energy barriers were derived from DFT calculations and were later adjusted to reproduce the experimental kinetic dataset collected on the Au/SiC catalysts. Entropies of adsorbed intermediates and pre-exponential factors were determined from the DFT-calculated vibrational frequencies following a procedure described elsewhere.[102] Lateral adsorbate-adsorbate interactions were neglected and all the BEs and activation energy barriers ($E_{AS}$) were assumed to be coverage independent. This assumption is reasonable since we expect surface coverages to be low under our experimental conditions. The maximum surface coverage was restricted to 1 ML and multilayer adsorption was not considered. We assumed that all species occupy exactly one site on the surface, except for the bidentate formate (HCOO), which blocks two surface sites. Given the geometry of the reactor used in our experiments, the reactor was modeled as a plug-flow reactor (PFR). Hence, our reactor model comprised of 5 differential equations for the gaseous flow rate along the reactor length, 8 steady state algebraic equations for the fractional surface coverages of reaction intermediates, and 1 site-

balance equation. Further details of our model formulation can be found in our previous work[7, 102, 103].

### 3.3 Results and discussion

To develop a comprehensive mean field microkinetic model that would enable us to study the structure sensitivity of this reaction on Au surfaces, we have rigorously studied the properties of 5 closed shell species and 8 reaction intermediates, as well as the reaction energetics of 17 elementary steps, on the Au(111), Au(100) and Au(211) facets using first principles DFT calculations. We first present the results from our DFT calculations; followed by the results from our attempts to fit the microkinetic model predicted rates and selectivities to the experimentally measured reaction kinetics data.

#### 3.3.1 Structure and adsorption thermochemistry of reaction intermediates

**Table 3-1** Calculated binding energies (BEs) of adsorbed species and their preferred adsorption sites on Au(111), Au(100) and Au(211). Zero of the energy scale is the slab and the gas phase species at infinite separation from each other.

| **Species** | **Au(111)** | | **Au(100)** | | **Au(211)** | |
|---|---|---|---|---|---|---|
| | **Adsorption** | **BE / eV** | **Adsorption** | **BE / eV** | **Adsorption** | **BE / eV** |
| H* | fcc | -1.90 | bridge | -2.06 | bridge | -2.11 |
| O* | fcc | -2.41 | hollow | -2.69 | bridge | -2.80 |
| OH* | bridge | -1.36 | bridge | -1.96 | bridge | -2.07 |
| $H_2O$* | top | -0.10 | top | -0.14 | Off-top | -0.20 |
| CO* | top | -0.21 | bridge | -0.62 | bridge | -0.67 |
| $CO_2$* | physisorbed | -0.02 | physisorbed | -0.02 | physisorbed | -0.05 |
| HCO* | top | -1.05 | top | -1.26 | top | -1.38 |
| HCOO** | top-top | -1.69 | top-top | -2.02 | top-top | -2.19 |
| COOH* | top | -1.27 | top | -1.48 | top | -1.58 |
| COOHcis* | top | -1.22 | top | -1.48 | top | -1.59 |
| HCOOH* | top | -0.10 | top | -0.16 | top | -0.21 |

The binding energies and preferred adsorption sites of surface species involved in this reaction network on the three Au facets studied are summarized in **Table 3-1**. More detailed information on adsorbed states, including vibrational frequencies of surface intermediates and gas phase species can be found in Supplementary Information (**Table 3S-1 to 3S-4**).

The following description focuses primarily on the most favorable binding configurations for the adsorbates. Schematic representations for these configurations are shown in **Figures 3-3** to **3-6**. In this discussion, and throughout the text, (g) stands for 'gas phase species' and each '*' represents a single surface site occupied by the corresponding adsorbate. Wherever available, the previously reported literature values (as obtained using DFT) for the BEs of surface species and activation energy barriers ($E_A$) of elementary steps are reported in parenthesis next to our DFT derived numbers.

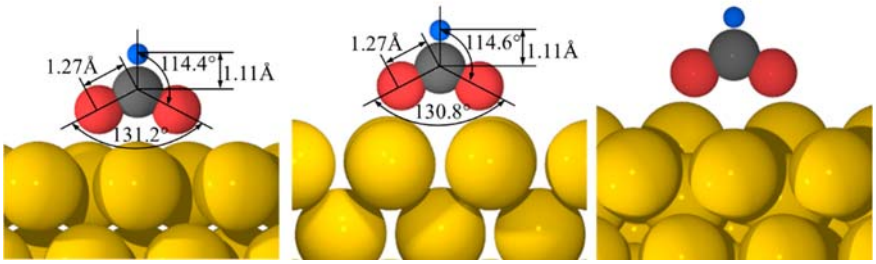


**Figure 3-3** Most stable configurations of Formate (HCOO) intermediate on (a) Au(111), (b) Au(100), and (c) Au(211).

All the closed-shell species involved in this reaction network, with the exception of CO, are found to be weakly bound to all three Au facets studied. They exhibit weak preference for their most stable binding configurations, as evidenced by the near degeneracy of their several adsorption states. Our calculations do not take into account the long-range interactions, such as van der Waals forces,[104, 105] which may contribute an additional stabilization of ~0.1 eV – 0.2 eV per carbon atom.

The absolute magnitude of the binding energies of surface species on the three Au surfaces were observed to decrease in the general order: Au(211) > Au(100) > Au(111), in agreement with the general notion that adsorbates tend to exhibit stronger binding to more open facets. [106]

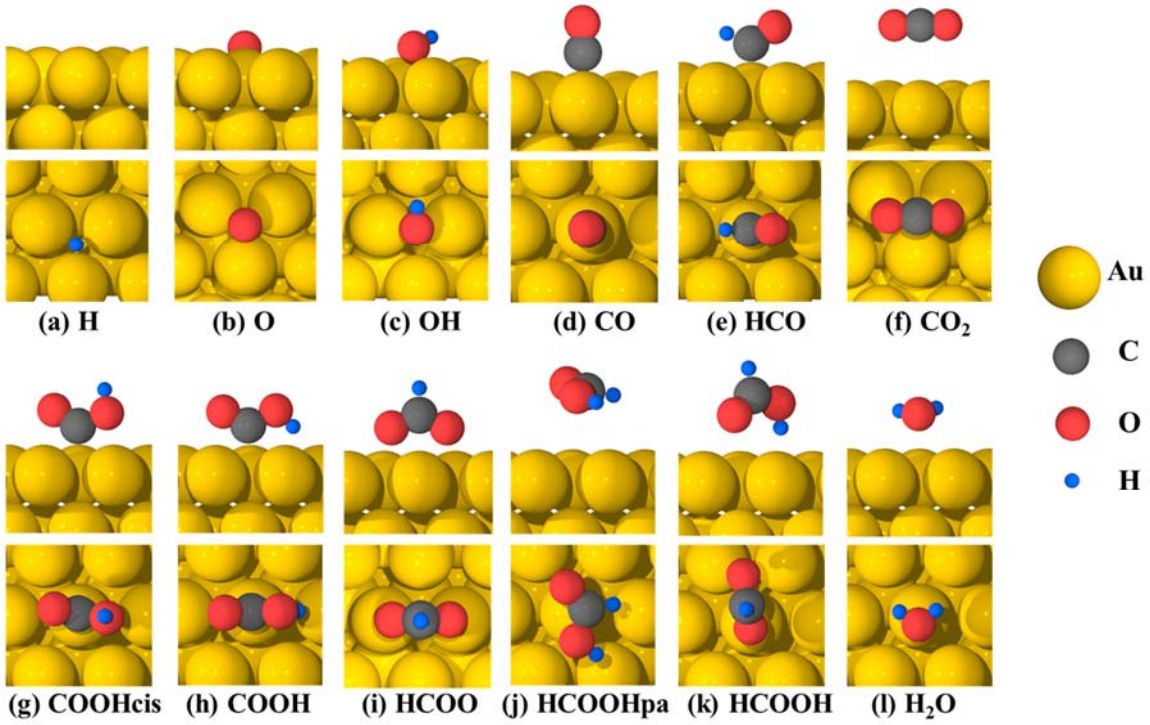


**Figure 3-4** Most stable configurations of FA decomposition intermediates on Au(111) (top panel represents cross-sectional view; bottom panel represents top view).

*Formic Acid* exhibits two distinct stable configurations: one in which all atoms of the HCOOH* molecule lie within a plane perpendicular to the surface (HCOOH*), and another one in which this plane is parallel to the surface (HCOOHpa*). The latter orientation was found to adsorb with practically zero BE on all three surfaces. HCOOH* binds to the three facets via its carbonyl O atom on a top site with the O-H and C-H bonds pointing towards and away from the surface respectively, and has a binding energy of -0.10 eV (-0.15 eV[107]), -0.17 eV (-0.19 eV[108]), and -0.21 eV on Au(111), Au(100), and Au(211) respectively. *Formate* has long been proposed as one of the key reaction intermediates in FA decomposition and has also been frequently cited as a possible

intermediate in WGS[109-111] and methanol synthesis[112-114] reactions. As a result, it has received much scientific attention[61, 86, 115-120], both in the experimental and theoretical literature. Our DFT calculations indicate that HCOO** binds on all three Au facets in a bidentate configuration (**Figure 3-3**) with its O ends on top of two nearest neighbor metal atoms. This structural data is in agreement with the available experimental (NEXAFS and IR)[115] and theoretical evidence. It has a BE of -1.69 eV (-1.82 eV[107]), -2.02 eV (-2.10 eV[108]) and -2.19 eV on Au(111), Au(100) and Au(211) respectively.

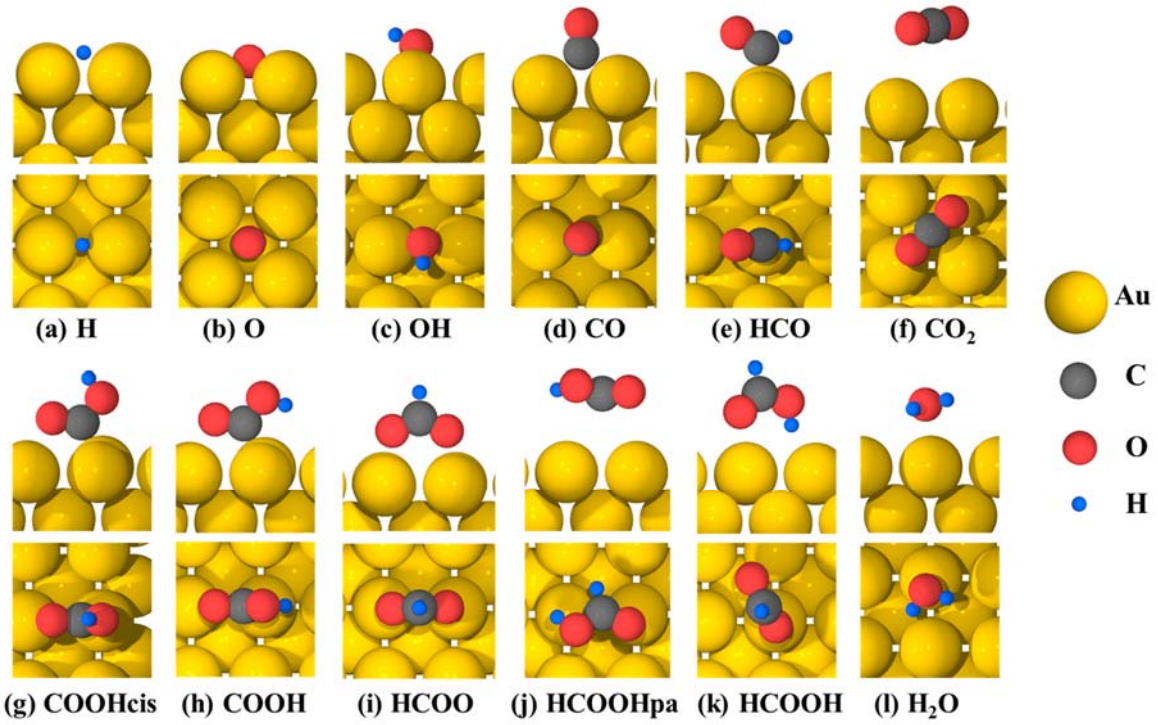


**Figure 3-5** Most stable configurations of FA decomposition intermediates on Au(100) (top panel represents cross sectional view; bottom panel represents top view).

The BEs of *atomic hydrogen* on Au(111), Au(100), and Au(211) are -1.90 eV (-2.03 eV[107], -2.20 eV[121, 122]), -2.06eV (-2.29 eV[108]), -2.11eV (-2.32 eV[123]) respectively. H* binds preferentially on the bridge sites on Au(100) and Au(211), and on the three fold sites on Au(111). The most stable

binding configuration on Au(111) is at the fcc sites, although the hexagonal close packed (hcp) sites are found to be energetically quasidegenerate to the fcc sites.

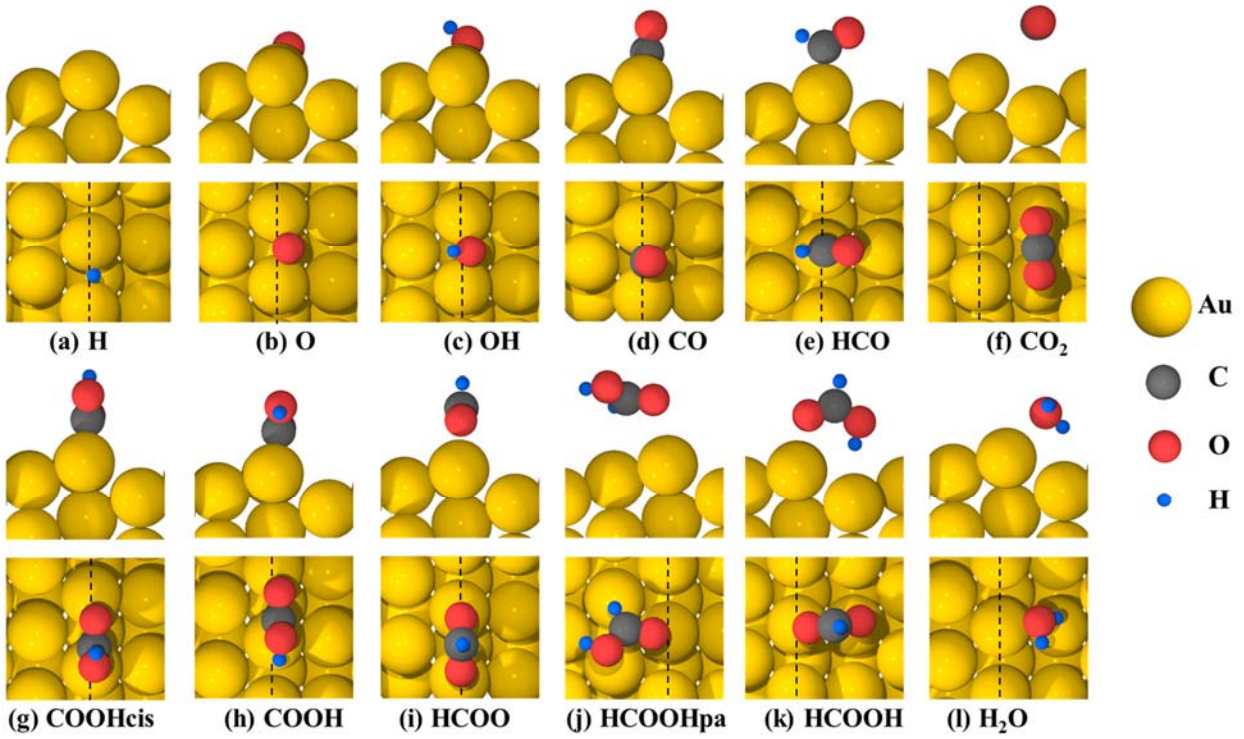


**Figure 3-6** Most stable configurations of FA decomposition intermediates on Au(211) (top panel represents cross-sectional view; bottom panel represents top view; dotted black lines in the top view denote the step edge of Au(211) surface).

*Atomic oxygen* prefers the three fold fcc site on Au(111), the four fold hollow site on Au(100), and the two fold bridge site on the step edge of Au(211), with BEs of -2.41 eV (-2.43 eV[124]), -2.69 eV(-2.85 eV[125]), -2.80 eV(-2.83 eV[126]) respectively. *Hydroxyl* prefers to adsorb in a top-tilted configuration on the bridge sites of all three Au facets with BEs of -1.36 eV (-1.47 eV[124]), -1.96 eV, -2.07 eV on Au(111), Au(100) and Au(211) respectively.

*Carboxyl* exhibits two stable adsorption configurations: (a) one with H pointing downwards towards the surface, the trans isomer (COOH*) and (b) one with H pointing away from the surface, the cis isomer (COOHcis*). COOH* has a BE of -1.27 eV, -1.48 eV (-1.61 eV [108]) and -1.58 eV on Au(111), Au(100) and Au(211) respectively. The *formyl* radical binds preferentially through its C atom to the top sites of all three Au facets, with BEs of -1.05 eV, -1.26 eV and -1.38 eV on Au(111), Au(100), and Au(211) respectively.

**Table 3-2** PW91 reaction energies (ΔE) and activation energy barriers (EA) for the elementary steps considered in the HCOOH decomposition reaction network on Au(111), Au(100) and Au(211) surfaces. All the values are relative to infinite separation in initial/final states.

| # | Reaction | Au(111) | | Au(100) | | Au(211) | |
|---|---|---|---|---|---|---|---|
| | | **ΔE /eV** | **$E_A$ / eV** | **ΔE / eV** | **$E_A$ / eV** | **ΔE / eV** | **$E_A$ / eV** |
| 1 | HCOOH + * ↔ HCOOH* | -0.10 | - | -0.16 | - | -0.21 | - |
| 2 | HCOOH* ↔ HCOOHpa* | 0.24 | 0.55 | 0.29 | 0.59 | 0.26 | 0.63 |
| 3 | HCOOH* + 2* ↔ HCOO** + H* | 0.86 | 1.29 | 0.42 | 0.87 | 0.26 | 0.98 |
| 4 | HCOOHpa* + * ↔ COOH* + H* | 0.80 | 1.22 | 0.44 | 0.83 | 0.37 | 0.87 |
| 5 | HCOOH* + * ↔ HCO* + OH* | 2.32 | 2.16 | 1.57 | 1.91 | 1.38 | 1.74 |
| 6 | HCOO** ↔ $CO_2$* + H* | -0.35 | 0.80 | -0.17 | 0.84 | -0.08 | 0.85 |
| 7 | HCOO** + H* ↔ $H_2$ + $CO_2$* + 2* | -0.84 | 0.99 | -0.34 | 1.11 | -0.15 | 1.30 |
| 8 | COOH* + * ↔ $CO_2$* + H* | -0.54 | 0.54 | -0.48 | 0.68 | -0.46 | 0.74 |
| 9 | COOH* ↔ COOHcis* | 0.05 | 0.45 | 0.00 | 0.52 | -0.01 | 0.44 |
| 10 | COOHcis* + * ↔ CO* + OH* | 1.30 | 1.33 | 0.55 | 0.70 | 0.51 | 1.00 |
| 11 | COOHcis* + H* ↔ CO* + $H_2O$* | -0.33 | 0.55 | -0.36 | 0.68 | -0.30 | 0.87 |
| 12 | HCO* + * ↔ CO* + H* | 0.07 | 0.59 | -0.29 | 0.24 | -0.26 | 0.28 |
| 13 | OH* + H* ↔ $H_2O$* + * | -1.64 | 0.26 | -0.92 | 0.38 | -0.81 | 0.61 |
| 14 | 2H* ↔ $H_2$ + 2* | -0.49 | 0.57 | -0.17 | 0.47 | -0.07 | 0.49 |
| 15 | $CO_2$* ↔ $CO_2$ + * | 0.02 | - | 0.02 | - | 0.05 | - |
| 16 | $H_2O$* ↔ $H_2O$ + * | 0.10 | - | 0.14 | - | 0.20 | - |
| 17 | CO* ↔ CO + * | 0.21 | - | 0.62 | - | 0.67 | -- |

*Carbon monoxide* (CO) binds through the carbon atom, with the C-O bond perpendicular to the surface. It binds preferentially to the top site on Au(111), and the two fold bridge sites on Au(100) and the step-edge of Au(211), with BEs of -0.21 eV (-0.26 eV[107]), -0.62 eV (-0.62 eV[108]) and -0.67 eV (-0.65 eV[127]) respectively. *Water* binds weakly through its oxygen atom to the top site of the three Au facets with the plane containing all the atoms parallel to the surface. It has a BE of -0.10 eV (-0.11 eV[107], -0.15 eV[128], -0.12 eV[122]), -0.14 eV and -0.20 eV (-0.19 eV[123]) on Au(111), Au(100) and Au(211) respectively.

*Carbon dioxide* ($CO_2$) binds weakly on all three Au facets, with binding energies of -0.02 eV ~ -0.05 eV. $CO_2$ retains its gas-phase linear geometry and exhibits very weak site preference with several degenerate binding configurations.

### 3.3.2 Reaction barriers of elementary steps

The calculated activation energy barriers ($E_A$) and reaction energies ($\Delta E$) for all elementary steps studied are reported in **Table 3-2**. All activation energy barriers and reaction energies reported in the following text are relative to the reactant and product states at infinite separation.

#### HCOOH activation

Here we discuss three different pathways of HCOOH activation, namely, the HCOO, the COOH, and the HCO mediated pathways (**Figure 3-7**).

*HCOOH* + 2* → HCOO** + H**

HCOOH* decomposition to HCOO** is found to proceed directly from the most stable, albeit weakly bound perpendicular configuration. The most favorable pathway involves H abstraction from HCOOH* over the top site on Au(111), but bridge site on Au(100) and Au(211) surface.

This step has a ΔE of 0.86 eV (0.89 eV[107]), 0.42 eV, and 0.26 eV, with $E_A$ of 1.29 eV (1.36 eV[107]), 0.87 eV, and 0.98 eV on Au(111), Au(100), and Au(211) respectively.

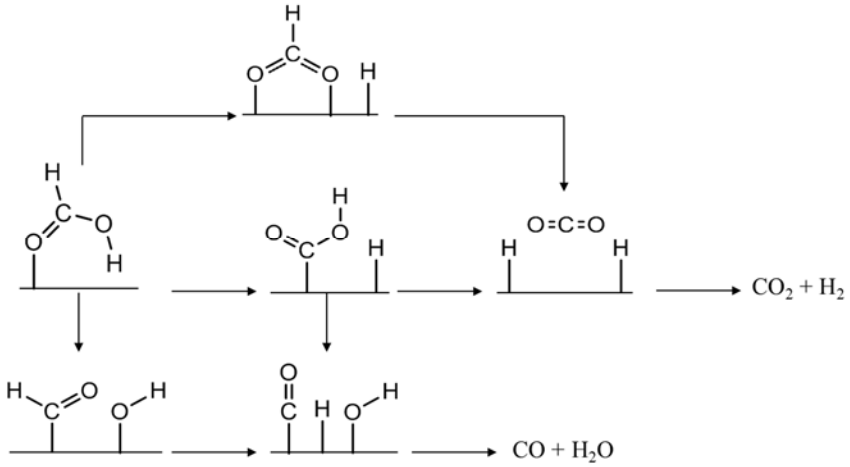


**Figure 3-7** The three HCOOH decomposition pathways considered.

*HCOOH* → HCOOHpa*; HCOOHpa* + * → COOH* + H**

C-H bond scission in HCOOH, yielding adsorbed COOH* and atomic hydrogen, is a two-step process. The first step is the rotation of HCOOH* to yield a metastable HCOOHpa* state. This rotation is quasi structure-insensitive, with a barrier of 0.55 eV to 0.63 eV on the three Au facets. HCOOHpa* is higher in energy than the most stable adsorbed state (HCOOH*), but it brings the carbonic hydrogen in HCOOH* closer to the three Au surfaces, thereby facilitating the C-H bond scission. The specific bond scission in HCOOHpa* to yield COOH* is an endothermic step, with $E_A$ of 1.22 eV, 0.83 eV and 0.87 eV on Au(111), Au(100), and Au(211) respectively.

*HCOOH* + * → HCO* + OH**

The dehydroxylation of HCOOH* to yield HCO* and OH* has a barrier of 2.16 eV, 1.91 eV and 1.74 eV on Au(111), Au(100) and Au(211) respectively, significantly higher than the HCOO** and COOH* formation steps.

**Product Formation**

$HCOO^{**} \rightarrow CO_2^{*} + H^{*}$

H abstraction from HCOO** starts with the rotation of the HCOO** molecule such that the C-H bond becomes parallel to the Au surface, and one Au-O bond is broken just before the C-H bond scission over the top sites of all three Au facets (top site at the step edge for Au(211) facet). The H-C bond length at the transition state is 1.29 Å, 1.37 Å and 1.18 Å on Au(111), Au(100) and Au(211) respectively, as compared to the bond length of 1.11Å in adsorbed HCOO. This step is slightly exothermic on Au(111) ($\Delta E$ = -0.35 eV) and Au(100) ($\Delta E$ = -0.17eV) and near-thermo neutral on Au(211) ($\Delta E$ = -0.08 eV). $E_A$ for this step is relatively invariant to the model surface, with values of 0.80 eV (0.65 eV[129]), 0.84 eV, and 0.85 eV on Au(111), Au(100) and Au(211) respectively.

$COOH^{*} + {*} \rightarrow CO_2^{*} + H^{*}$

Carboxyl decomposition to $CO_2$ is found to proceed directly from the more stable trans configuration (COOH*). The reaction on all three facets starts with rotation of carboxyl within its molecular plane, such that O-H bond-scission takes place over the top site. Atomic hydrogen subsequently diffuses to the closest preferable site, and $CO_2$ settles in its physisorbed state. This step is exothermic, with $\Delta E$ of -0.54 eV (-0.49 eV[122]), -0.48 eV, and -0.46 eV, and has $E_A$ of 0.54 eV (0.58 eV[122]), 0.68 eV, and 0.74 eV on Au(111), Au(100), and Au(211) respectively.

$COOHcis^{*} + {*} \rightarrow CO^{*} + OH^{*}$

Contrary to the previous step, CO formation from carboxyl starts from the cis configuration of carboxyl. For this to take place, the most stable trans configuration of COOH* undergoes activated

rotation (with $E_A$ of 0.45 eV, 0.52 eV, and 0.44 eV on Au(111), Au(100), and Au(211) respectively), to yield the cis configuration (COOHcis*). The dissociation of COOHcis* takes place over the top site on all three Au facets, with $E_A$ of 1.33 eV (1.25 eV[122]), 0.70 eV and 1.00 eV on Au(111), Au(100) and Au(211) respectively.

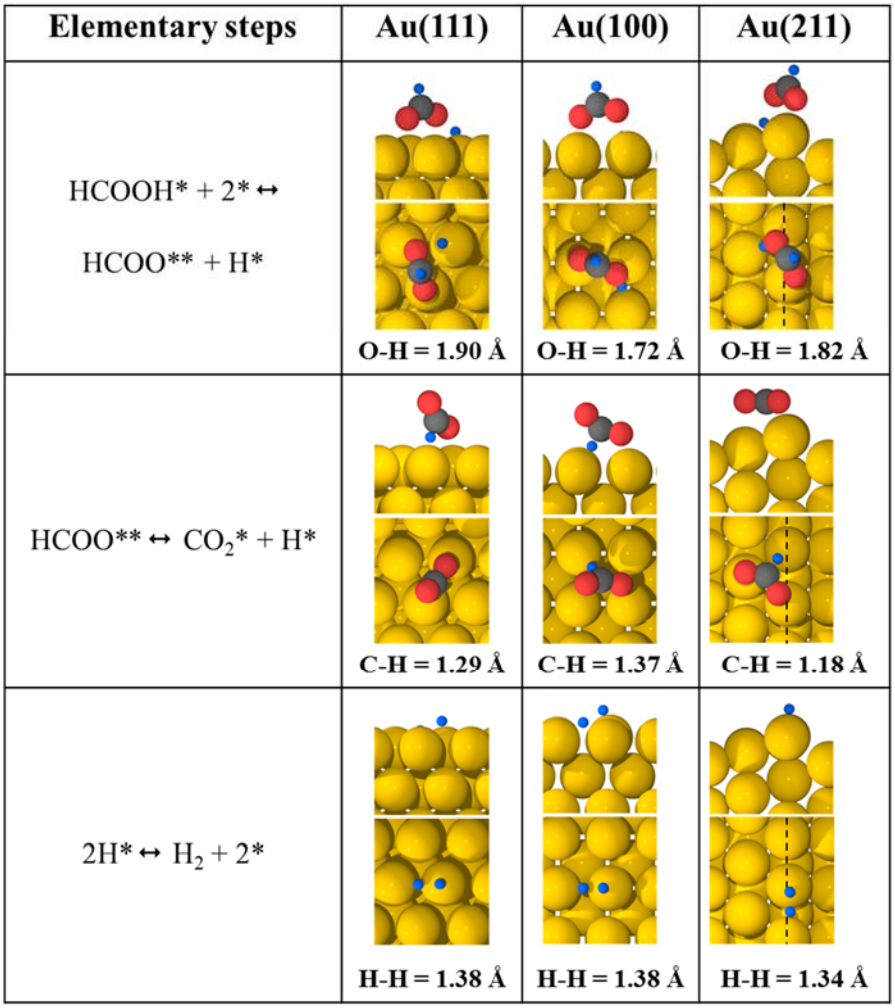


**Figure 3-8** Side and top views of the transition states (TS) for the three kinetically relevant steps (as predicted by our microkinetic modeling results) on Au(111), Au(100), and Au(211) surfaces. The lengths of the bond being broken/formed are reported for each transition state. Dotted black lines in the top views of Au(211) surface indicate the step-edge.

$H^* + H^* \rightarrow H_2 + 2^*$

$H_2$ recombinative formation starts with two H* adsorbed on adjacent bridge sites, and the H-H bond formation takes place over the top site, for all three Au facets. The H-H bond length at the transition state are 1.38 Å, 1.38 Å and 1.34 Å on Au(111), Au(100) and Au(211) respectively, as compared to an $H_2$ gas phase bond length of 0.75 Å.

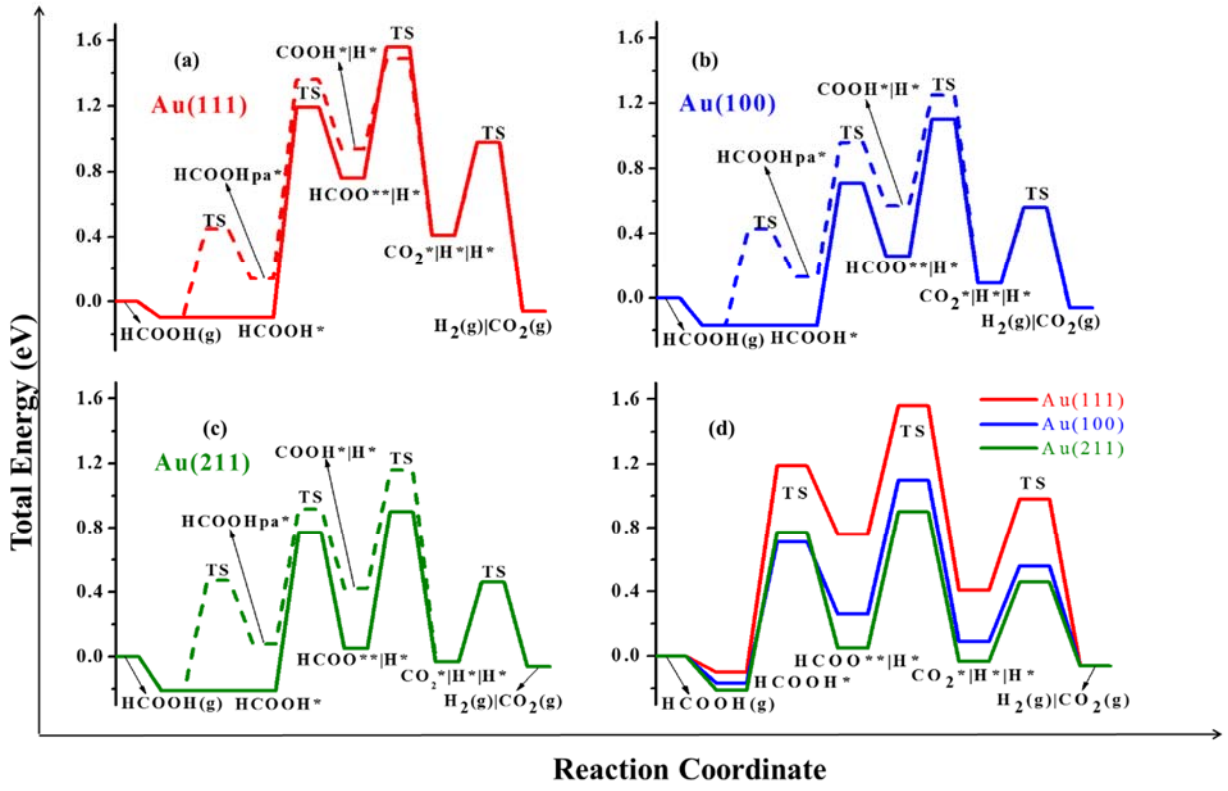


**Figure 3-9** The two-dimensional PESs of FA decomposition reaction via the HCOO (solid lines) and COOH (dashed lines) mediated pathways on Au(111) (red) (a), Au(100) (blue) (b), and Au(211) (green) (c), and a comparison of the most favorable pathways (HCOO mediated) on all three facets **(d)**. Energy zero corresponds to the energy of HCOOH in the gas phase, away from the slab. A '|' between two adsorbates denotes that they are at infinite separation from each other.

### Potential Energy Surfaces

The thermochemistry and activation energy barriers of various elementary steps described in the previous sections can be summarized in the form of two-dimensional potential energy surfaces (PESs) for the three Au facets, as shown in **Figure 3-9**. The PESs shown in **Figure 3-9 (a-c)**

compare the HCOO** and COOH* mediated pathways on the three Au facets respectively (a-c). On the basis of the DFT-derived energetics alone, the HCOO** mediated route appears to be the minimum energy path for FA decomposition on Au(100) and Au(211), whereas both HCOO** and COOH* mediated routes appear to be competitive for the Au(111) facet. **Figure 3-9(d)** compares the HCOO** pathway on all three Au facets, and one can suggest from here that Au(100) and Au(211) are expected to be significantly more active than the Au(111) facet.

**Table 3-3** Reaction rates and selectivities obtained from the kinetics experiments on Au/SiC.

| | **Temperature (K)** | **y(HCOOH)** | **y(He)** | **y($H_2$)** | **y($CO_2$)** | **Experimental Rates (µmol $gcat^{-1}$ $min^{-1}$)** | **Experimental Selectivity ($CO_2$/($CO_2$+CO))** |
|---|---|---|---|---|---|---|---|
| 1 | 373.15 | 0.01 | 0.99 | 0.00 | 0.00 | 9.30 | 1.00 |
| 2 | 373.15 | 0.02 | 0.98 | 0.00 | 0.00 | 15.42 | 1.00 |
| 3 | 373.15 | 0.02 | 0.98 | 0.00 | 0.00 | 18.65 | 1.00 |
| 4 | 373.15 | 0.04 | 0.96 | 0.00 | 0.00 | 33.00 | 1.00 |
| 5 | 343.15 | 0.03 | 0.97 | 0.00 | 0.00 | 5.05 | 1.00 |
| 6 | 353.15 | 0.03 | 0.97 | 0.00 | 0.00 | 8.00 | 1.00 |
| 7 | 363.15 | 0.03 | 0.97 | 0.00 | 0.00 | 15.72 | 1.00 |
| 8 | 368.15 | 0.03 | 0.97 | 0.00 | 0.00 | 21.35 | 1.00 |
| 9 | 373.15 | 0.03 | 0.97 | 0.00 | 0.00 | 24.11 | 1.00 |
| 10 | 378.15 | 0.03 | 0.97 | 0.00 | 0.00 | 32.55 | 1.00 |
| 11 | 383.15 | 0.03 | 0.97 | 0.00 | 0.00 | 41.30 | 1.00 |
| 12 | 373.15 | 0.03 | 0.96 | 0.01 | 0.00 | 23.91 | 1.00 |
| 13 | 373.15 | 0.03 | 0.94 | 0.04 | 0.00 | 24.09 | 1.00 |
| 14 | 373.15 | 0.03 | 0.92 | 0.06 | 0.00 | 24.32 | 1.00 |
| 15 | 373.15 | 0.03 | 0.96 | 0.00 | 0.01 | 23.69 | 1.00 |
| 16 | 373.15 | 0.03 | 0.95 | 0.00 | 0.03 | 23.76 | 1.00 |
| 17 | 373.15 | 0.03 | 0.92 | 0.00 | 0.06 | 23.97 | 1.00 |

*y* denotes mole fraction in the inlet feed. The total flow rate for all the data points is 100 ml/min. Each data point is an average of several experimental runs.

### 3.3.3 Microkinetic modeling

**Table 3-4** Experimental and model predicted reaction orders and apparent activation energy barriers.

| | **Experiment** | **Model** |
|---|---|---|
| HCOOH | 0.95 ± 0.06 | 0.99 |
| $CO_2$ | 0.01 ± 0.003 | 0.00 |
| $H_2$ | 0.01 ± 0.003 | 0.00 |
| $E_A$ | 59.6 ± 1.6 kJ/mol | 60.2 kJ/mol |

A microkinetic model was developed using the results from these DFT calculations as initial guesses for the model parameters. With no adjustments to the DFT derived parameters, the microkinetic model predicts FA decomposition rates that are 11 and 5 orders of magnitude lower on the Au(111) and Au(100)/Au(211) surfaces, respectively, than the measured experimental rates on Au/SiC. The reaction is predicted to take place via the HCOO mediated route, i.e., HCOOH (g) → HCOOH* →HCOO** + H* → $CO_2$* + 2H* → $CO_2$ (g) + $H_2$ (g), on all three facets, with 100% selectivity towards the dehydrogenation products; the rate of CO production is predicted to be negligible. We next carried out studies in which the kinetic parameters were adjusted from the initial values on these three Au facets in attempts to describe the results from reaction kinetic measurements (**Table 3-3**). The adjustable parameters that are modified during this process are the BEs of all surface species and transition state energies of all activated elementary steps. While this procedure gives a total of 26 parameters for our complex reaction network, sensitivity analysis showed that only the BEs of HCOO**, H*, and the transition state energies of the HCOO** formation and direct decomposition steps (steps (3) and (6) in **Table 3-2**) were sensitive parameters. We then made systematic adjustments in these parameters until reasonable agreement between the experimentally measured and model predicted reaction rates was reached, and we subsequently employed a gradient based optimization algorithm in Matlab to obtain optimized

values and confidence intervals for our adjustable parameters. The model predicted reaction orders and apparent activation energy barriers corresponding to the best-fitted solution are reported in **Table 3-4**, and are in close agreement with their experimental counterparts. In addition, the experimentally observed apparent activation energy barrier (59.6 kJ $mol^{-1}$) in the zero-order kinetic regime is in good agreement with past experimental studies on numerous supported Au catalysts[86, 87, 130]. **Figure 3-10** shows the PES for the best fitted solution, compared with the DFT derived PESs for the three Au facets. Here, we only report the energetics of the closed catalytic cycle that is found to carry the entire reaction flux; the energetics of other elementary steps, which do not carry much flux from reactants to products are not included in the figure. We can see from this figure that the adjustments needed in the DFT derived initial guesses to obtain good fits are too large to be attributed to the computational errors in our calculations, which are typically on the order of 0.1 eV – 0.2 eV. With > 0.95 ML of the surface predicted to be vacant under all conditions, we can also rule out any potential stabilization that might result from lateral adsorbate - adsorbate interactions.[131] An additional stabilization of the transition states for the HCOO** formation and decomposition steps by > 0.5 eV is required to obtain good fits with the experimental data, strongly suggesting that (i) the Au(111), Au(100) and Au(211) may not be the most accurate representation of the active sites for this reaction, and (ii) the active site might be an even more under-coordinated environment that would stabilize the transition states to a much greater extent than these three facets. This conclusion is a quantitative confirmation of a previous proposal put forward by Iglesia and coworkers based on their experimental reactivity studies for the same reaction.[86] Importantly, similar suggestions for the reactivity of single metal atoms or very small metal nanoclusters have been made in the literature for other reactions as well[132-135].

***Rate determining step***

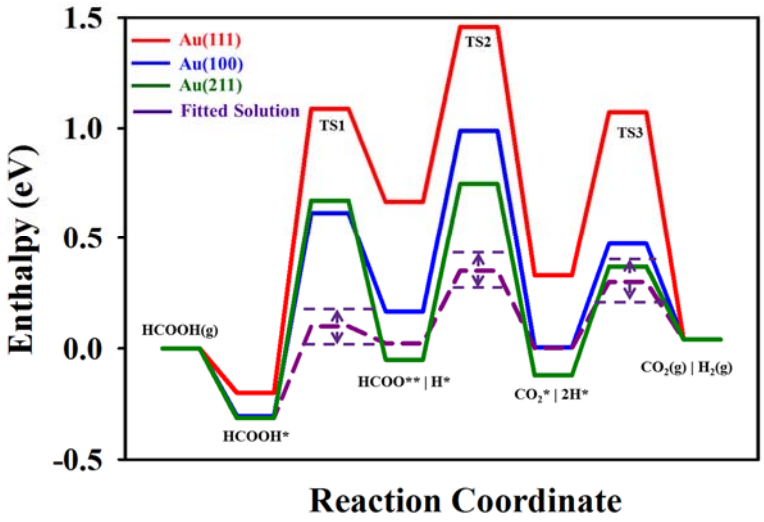


**Figure 3-10** Enthalpy surfaces for FA decomposition via the HCOO** mediated pathway on Au(111), Au(100), and Au(211) facets (red, blue, green, respectively) as obtained directly from DFT calculations, and that corresponding to the best fitted solution (violet) along with the confidence intervals for the transition states. TS denotes the transition state for the respective elementary step. This sequence of elementary steps carries almost the entire flux from reactants to products for all experimental conditions studied.

The individual reaction fluxes of the elementary steps reveal that the overall reaction proceeds entirely through the 'direct HCOO**' route, and no reaction flux is observed through any of the COOH mediated pathways. We further analyzed the reaction mechanism and the rate determining steps in the reaction scheme using Campbell's degree of rate control, [5, 136, 137] which quantifies the kinetic importance of an elementary step in a reaction scheme by computing the relative change in the overall reaction rate upon changing the forward and reverse rate constants for that step, while holding the equilibrium constant for that step as well as the rate constants for all other steps constant. In this formalism, the degree of rate control ($X_{RC}$) of each elementary step can be evaluated using the following relation:

$$X_{RC,i} = \frac{k_i}{r}\left(\frac{\delta r}{\delta k_i}\right)_{K_{i,eq},k_j}$$

where $k_i$ is the rate constant for step $i$, $K_{i,eq}$ is the equilibrium constant for this step and $r$ is the overall reaction rate. For all equilibrated steps (including the adsorption/desorption steps that were assumed to be quasi-equilibrated), $X_{RC,i}$ is 0. **Table 3-5** gives the $X_{RC,i}$ for the kinetically relevant steps in our reaction mechanism. For the 'best-fitted solution', Step 6 exhibits the highest degree of rate control for all reaction conditions and hence is the most rate controlling.

**Table 3-5** Campbell's degree of rate control for kinetically relevant steps.

| Step # | **Elementary Step** | $\mathbf{X_{RC}}$ |
|---|---|---|
| 3 | HCOOH* + 2* ↔ HCOO** + H* | 0.25 |
| 6 | HCOO** ↔ $CO_2$* + H* | 0.64 |
| 14 | 2H* ↔ $H_2$ + 2* | 0.10 |

These numbers are reported for the reaction condition # 9 of Table 3-3

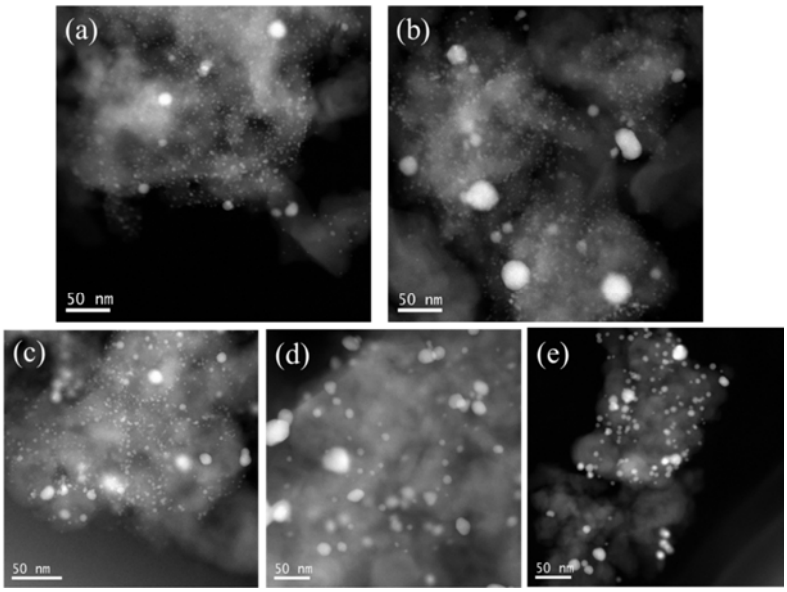


**Figure 3-11** Typical TEM images of Au/SiC catalysts used to determine the Au particle size distributions. The pre-reduction temperatures for these catalysts are (a) 623 K, (b) 673 K, (c) 723 K, (d) 973 K and (e) 1073 K.

**Active Sites**

The results from our microkinetic model suggest that Au(111), Au(100), and Au(211) are, in all likelihood, not the best representation of active sites for this reaction on SiC-supported Au catalysts.

Thus, the major contributors to the overall rates could potentially be the Au atoms with lower (< 7) Au-Au coordination that exhibit even greater stabilization of reaction intermediates and transition states than the more open facets studied here ((100) and (211)). To gain further insights into the nature of the active sites, we synthesized different catalyst samples with a varying degree of Au dispersion by treating the initial catalyst in flowing $H_2$ at different temperatures (623, 673, 723, 973 and 1073 K) for 8 hours, prior to using these materials as catalysts for reaction kinetic studies. Typically, the catalysts that are pre-reduced at low temperatures are more highly dispersed (and less sintered) than the materials that are pre-reduced at high temperatures.

**Table 3-6** Average particle size (as determined by TEM) and experimentally measured reaction rates on the five different Au/SiC catalysts.

| **Catalyst Sample #** | **Pre-Reduction Temperature (K)** | **Number average particle size (d (nm))** | **Experimentally observed reaction rate (μmol $gcat^{-1}$ $min^{-1}$)** |
|---|---|---|---|
| 1 | 623 | 2.55 | 178.58 |
| 2 | 673 | 3.09 | 129.93 |
| 3 | 723 | 3.23 | 97.84 |
| 4 | 973 | 7.53 | 9.02 |
| 5 | 1073 | 10.74 | 2.64 |

*Particle Size distribution*:

**Figure 3-11** shows representative STEM images of the five catalysts that were used to determine the Au particle size distribution (**Figure 3-12**) in these samples. This technique allows for imaging Au nanoparticles as low as 0.3 nm in size. It was observed that reducing the catalysts under a $H_2$ stream at increasingly elevated temperatures resulted in increased averaged Au particle sizes, as reported in **Table 3-6**.

*Kinetic Reaction Rate Measurements*: Reaction kinetic measurements were performed to obtain the FA decomposition rates on five catalysts under same operating conditions (T = 413 K, Total

inlet flow rate = 100 ml/min, Inlet feed composition = 2.5% HCOOH and 97.5% He). A monotonic decrease in the reaction rates with an increase in the pre-reduction temperature (and the average particle size) was observed, as shown in **Table 3-6**.

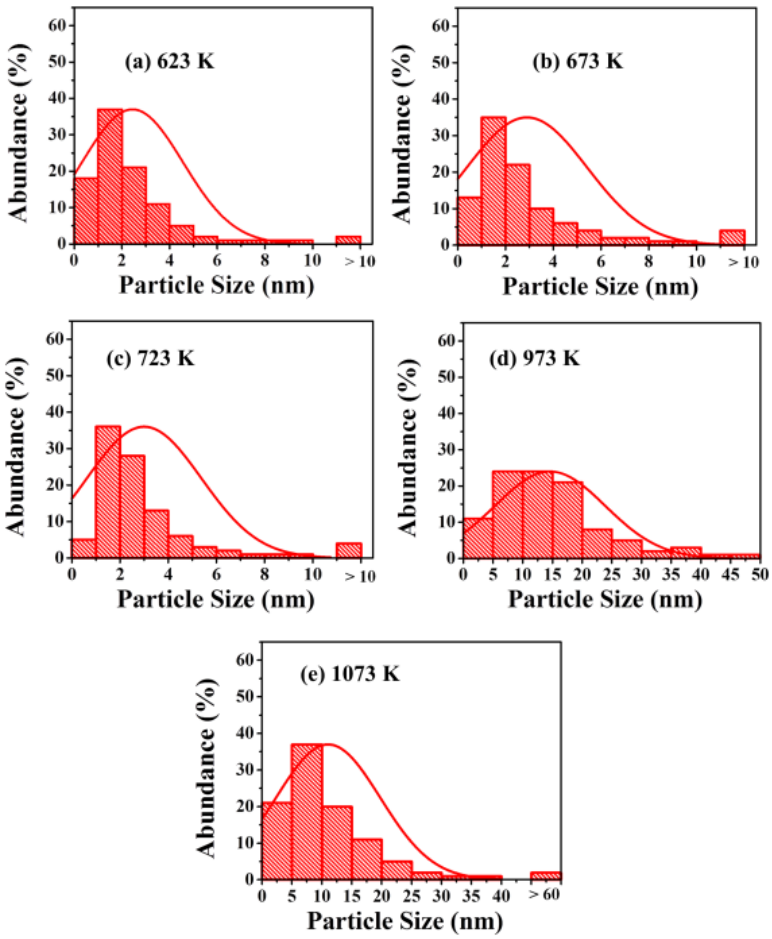


**Figure 3-12** Histograms depicting the Au particle-/cluster-size distributions for the Au/SiC catalysts prereduced at 623–1073 K for 8 h.

Additionally, it is observed that the number (and relative abundance) of subnanometer sized Au clusters decreases sharply upon increasing the calcination temperature. As a result, these reactivity trends provide a first indication that the number of subnanometer sized Au clusters in the catalyst may be correlated with the overall reaction rate. This hypothesis is consistent with the past

experimental studies[85, 86, 130] that have postulated that this remarkable activity on supported Au catalysts arises from subnanometric Au clusters that are undetected in TEM micrographs. To quantify the contributions of different Au atoms in the catalytic particles/clusters to the overall reaction rate, we first classify the different kinds of Au atoms that are present in any given cluster into four categories: (1) Corner (C) atoms: CN = 1 to 4, (2) Perimeter (P) atoms: CN = 5 and 6, (3) Terrace (T) atoms: CN = 7 to 9 and (4) Bulk (B) atoms: CN ≥ 9, where CN refers to the Au-Au coordination number. Surface (S) atoms are defined as the sum total of the C, P, and T atoms.

In their work on the WGS reaction on supported Au catalysts, Ribeiro and co-workers[138-140] employed physical models of Au clusters as truncated cuboctahedra to develop relations for determining the variation of the C, P, and T sites with the number averaged Au particle size. However, these relations hold true only for particles with diameter (d) > ~1.6 nm. Therefore, and given our TEM data, we attempted to develop physical models of Au clusters with d < 1.6 nm to obtain the corresponding relations that provide the dependence of the C, P, and T sites on the average Au particle size. For that purpose, we used the results of past computational studies which employed DFT to identify the most stable configurations of $Au_n$ clusters (with $2 < n < 20$) in the gas-phase,[141-144] along with our physical models. The relative abundance of the C, P and T sites is highly dependent on the choice of the cluster shape for d < 1.6 nm. Since there is no general agreement in the literature on the most stable structures for these small clusters, a computational methodology must be adopted to this end. This approach would involve modeling a SiC support, performing *ab-initio* molecular dynamics (AIMD)[145-147] simulations to determine the most stable configurations of different sized Au clusters on this support under reaction conditions, and finally counting the number of C, P, and T sites in these configurations to develop the structure-site density relations for quantifying the contributions from each of these sites towards the overall

rates. This approach is an ongoing endeavor and will be presented in a future report. However, as a first approximation, we treat these sites together, since the total number/fraction of surface (S) atoms (i.e. C + P + T) is invariant of the actual distribution. In particular, all atoms in clusters of d < 1.6 nm can be assumed to be surface atoms (100% dispersion) without loss of accuracy.

**Table 3-7** Relations used to determine the fraction of different sites from the average particle size obtained from the STEM images.

| Type of Surface Site → / Particle Size ↓ | Terrace (T) | Perimeter (P) | Corner (C) | Surface (S) |
|---|---|---|---|---|
| < 1.6 nm | # | # | # | 1.0 |
| ≥ 1.6 nm[139] | $0.90\ d^{-0.7}$ | $0.46\ d^{-1.8}$ | $0.54\ d^{-2.9}$ | $0.90\ d^{-0.7} + 0.46\ d^{-1.8} + 0.54\ d^{-2.9}$ |

# the actual relations for C, P, and T sites for d < 1.6 nm are currently unavailable. All the relations presented here give the ratio of that particular site to the total Au atoms in the catalyst. For instance, for d > 1.6 nm, (Number of terrace atoms/Total Au atoms) = $0.90\ d^{-0.7}$, and so on.

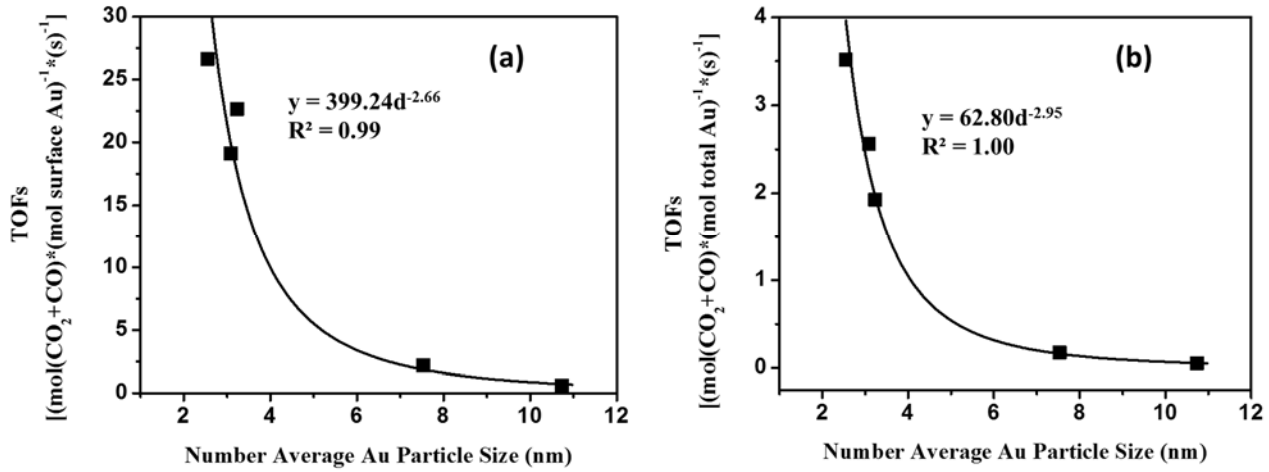


**Figure 3-13** FA decomposition rate normalized by (a) surface Au moles and (b) total Au moles (2% FA inlet feed at 413 K, 1 atm) on Au/SiC catalysts.

The total moles of surface Au in the catalysts can then be calculated by employing the following relation:

$$Total\ moles\ of\ surface\ Au\ = \left(\frac{\sum_n f(d)t(d)}{\sum_n t(d)}\right) * \ Total\ moles\ of\ Au\ in\ the\ catalyst$$

where, *f(d)* is the fraction of surface atoms in the cluster of diameter *d* (**Table 3-7**), *t(d)* is the total number of atoms in that cluster, and the summation is performed over all the Au clusters that were identified from the STEM image of that catalyst, i.e., the full particle size distribution was used for each sample. The TOFs normalized to the surface Au moles and total Au moles are plotted against the average particle size in **Figure 3-13**, and these plots can be used to draw the following key conclusions:

(i) A decreasing trend in the rate per surface site with average Au particle size (**Figure 3-13 (a)**) indicates the heterogeneity of the surface Au sites, i.e., all surface sites do not contribute equally to the overall reaction rate.

(ii) **Figure 3-13(b)** shows that the rate per total mole of Au catalysts varies as $d^{-2.95}$, whereas **Table 3-7** suggests that the fraction of terrace, perimeter, and corner sites vary as $d^{-0.7}$, $d^{-1.8}$, and $d^{-2.9}$ respectively. Thus, the variation in FA decomposition rate per total mole of Au seems to correlate with the 'corner model', i.e., the rate per corner site is independent of the Au particle size, thereby implying that corner sites might be the dominant active sites for this reaction. As mentioned earlier, this conclusion is based on the assumption that the $d^{-2.9}$ dependence of the corner sites will be valid over the entire particle size range, and further studies to confirm this for smaller clusters ($d$ <1.6 nm) will be needed.

### 3.4 Conclusions

Periodic, self-consistent DFT calculations were performed to determine the energetics of 13 adsorbed intermediates for FA decomposition, as well as the activation energy barriers and pre-exponential factors of 13 activated elementary steps on Au(111), Au(100), and Au(211) surfaces,

which were chosen as the representative stable model facets of Au nanoparticles on SiC support. The DFT results suggest that the surface species and transition states are stabilized as the Au-Au coordination of surface atoms decreases, and the reaction rates follow the order: Au(211) ≈ Au(100) > Au(111).

A mean field microkinetic model was employed to describe the experimental rate and selectivity data that were collected under realistic conditions on Au/SiC. Our 'best fitted solution' from the microkinetic model shows a good description of the experimental data ($R^2$ = 0.98), and good agreement between the model predicted apparent activation energy barriers and reaction orders with their experimental counterparts. The reaction is predicted to proceed via the formate mediated route. Importantly, the closed catalytic cycle that adequately describes the FA decomposition mechanism on Au catalysts is found to be comprised of three elementary steps: HCOOH* → HCOO** + H*, HCOO** → $CO_2$* + H* and 2H* → $H_2$(g).

A comparison of the DFT derived binding energies and activation energy barriers with the parameters obtained upon fitting the microkinetic model to the experimental data suggests that Au(111), Au(100) and Au(211) might not provide the most accurate representation of the active site on supported Au catalysts. Further reaction rate experiments and measurements of the Au particle size distribution using STEM corroborated this claim that the coordinatively unsaturated corner sites, with Au-Au coordination of ≤ 4, are most likely the dominant active sites for this reaction. Further DFT studies on Au clusters that possess atoms with Au-Au coordination number ≤ 4 will be needed to identify the exact nature of active site for formic acid decomposition on supported Au nanoparticles. Also, to further enhance the catalytic activity of Au catalysts, different synthesis techniques should be explored that will yield supported Au catalysts with a higher fraction of low coordinated sites.

## 3.5 Supplementary material

**Table 3S-1** Calculated Vibrational Frequencies of Gas Phase species.

| Species | Frequencies [$cm^{-1}$] |
|---|---|
| $H_2$ | 4430 |
| CO | 2205 |
| $CO_2$ | 2469, 1351, 629, 623 |
| $H_2O$ | 3940, 3825, 1575 |
| HCOOH | 3693, 2980, 1725, 1281, 1025, 996, 925, 682, 402 |

**Table 3S-2** Calculated Binding Energies (BE), with (w) and without (w/o) ZPE corrections, and Vibrational Frequencies of Adsorbed Species at their Preferred Adsorption Site on Au(111).

| Species | Adsorption Site | BE / eV | | Frequencies [$cm^{-1}$] |
|---|---|---|---|---|
| | | W/O ZPE | W ZPE | |
| H* | fcc | -2.04 | -1.90 | 879.4, 681.2, 596.5 |
| O* | fcc | -2.46 | -2.41 | 394.2, 250.0, 247.5 |
| OH* | bridge | -1.56 | -1.36 | 3766.3, 576.5, 546.6, 307.3, 165.7, 125.6 |
| $H_2O$* | top | -0.16 | -0.10 | 3884.4, 3773.4, 1551.2, 339.2, 260.4, 244.4, 71.0, 66.4, 59.7 |
| CO* | top | -0.26 | -0.21 | 2138.5, 229.6, 222.1, 214.2, 82.2, 50.4 |
| $CO_2$* | physisorbed | -0.05 | -0.02 | 2458.8, 1349.6, 635.8, 634.3, 144.2, 117.6, 49.2, 35.5, 21.2 |
| HCO* | top | -1.20 | -1.05 | 2903.5, 1814.8, 1138.2, 726.9, 458.5, 263.2, 128.4, 121.0, 97.8 |
| HCOO** | top-top | -1.79 | -1.69 | 2927.4, 1575.7, 1303.6, 1285.0, 968.5, 729.4, 289.4, 263.3, 244.8, 107.4, 91.3, 64.6 |
| COOH* | top | -1.35 | -1.27 | 3446.8, 1824.6, 1200.6, 1104.1, 625.9, 588.6, 447.5, 268.6, 208.7, 126.9, 106.9, 85.7 |
| COOHcis* | top | -1.30 | -1.22 | 3622.3, 1765.6, 1230.1, 1042.2, 627.5, 618.6, 399.0, 267.4, 224.9, 103.0, 96.9, 59.3 |
| HCOOH* | top | -0.16 | -0.10 | 3437.4, 3006.4, 1748.5, 1343.8, 1273.0, 1117.5, 998.4, 663.0, 619.7, 144.3, 100.8, 88.8, 77.9, 59.3, 26.7 |

**Table 3S-3** Calculated Binding Energies (BE), with (w) and without (w/o) ZPE corrections, and Vibrational Frequencies of Adsorbed Species at their Preferred Adsorption Site on Au(100).

| Species | Adsorption Site | BE / eV | | Frequencies [$cm^{-1}$] |
|---|---|---|---|---|
| | | W/O ZPE | W ZPE | |
| H* | bridge | -2.22 | -2.06 | 1126.5, 1055.9, 361.0 |

| | | | | |
|---|---|---|---|---|
| O* | hollow | -2.73 | -2.69 | 250.6, 140.9, 131.8 |
| OH* | bridge | -2.18 | -1.96 | 3789.3, 727.2, 556.4, 317.8, 272.3, 138.5 |
| $H_2O$* | top | -0.20 | -0.14 | 3875.4, 3760.3, 1547.9, 348.3, 334.8, 147.2, 86.9, 63.9, 30.6 |
| CO* | bridge | -0.68 | -0.62 | 1970.6, 293.5, 283.6, 257.1, 224.6, 88.4 |
| $CO_2$* | physisorbed | -0.05 | -0.02 | 2455.7, 1350.7, 627.1, 612.1, 116.5, 96.9, 92.1, 65.5, 51.6 |
| HCO* | top | -1.41 | -1.26 | 2868.4, 1803.2, 1167.5, 731.7, 479.6, 254.3, 130.7, 126.8, 116.8 |
| HCOO** | top-top | -2.13 | -2.02 | 2934.5, 1584.7, 1315.2, 1303.5, 976.1, 725.9, 289.1, 281.6, 257.0, 95.1, 87.8, 49.8 |
| COOH* | top | -1.58 | -1.48 | 3763.8, 1671.2, 1199.4, 1125.6, 665.8, 573.9, 432.3, 248.7, 232.5, 147.3, 93.1, 55.3 |
| COOHcis* | top | -1.57 | -1.48 | 3617.3, 1617.3, 1258.0, 1098.3, 652.1, 645.9, 395.5, 261.6, 233.1, 147.1, 59.9, 57.4 |
| HCOOH* | top | -0.22 | -0.16 | 3273.3, 3014.9, 1732.3, 1342.3, 1284.7, 1131.4, 1000.6, 702.5, 629.3, 170.2, 135.2, 90.4, 88.5, 64.2, 51.4 |

**Table 3S-4** Calculated Binding Energies (BE), with (w) and without (w/o) ZPE corrections, and Vibrational Frequencies of Adsorbed Species at their Preferred Adsorption Site on Au(211).

| **Species** | **Adsorption Site** | **BE / eV** | | **Frequencies [$cm^{-1}$]** |
|---|---|---|---|---|
| | | **W/O ZPE** | **W ZPE** | |
| H* | bridge | -2.27 | -2.11 | 1131.7, 1044.7, 393.4 |
| O* | bridge | -2.86 | -2.80 | 434.9, 398.2, 132.4 |
| OH* | bridge | -2.29 | -2.07 | 3804.9, 730.3, 568.7, 309.3, 262.0, 144.0 |
| $H_2O$* | Off-top | -0.25 | -0.20 | 3864.1, 3711.8, 1547.0, 414.1, 335.1, 144.2, 111.0, 71.3, |
| CO* | bridge | -0.73 | -0.67 | 1967.7, 313.5, 274.5, 250.5, 212.8, 121.2 |
| $CO_2$* | physisorbed | -0.06 | -0.05 | 2454.7, 1349.5, 626.1, 622.1, 111.7, 77.2, 41.6, 35.7, 20.8 |
| HCO* | top | -1.53 | -1.38 | 2876.1, 1808.7, 1176.5, 733.1, 487.3, 220.7, 97.3, 94.5, 82.2 |
| HCOO** | top-top | -2.29 | -2.19 | 2951.7, 1589.5, 1316.7, 1301.1, 971.1, 726.0, 282.8, 277.8, 253.9, 99.4, 93.0, 87.1 |
| COOH* | top | -1.68 | -1.58 | 3764.5, 1637.8, 1209.8, 1134.0, 679.3, 578.1, 436.4, 278.5, 222.0, 157.8, 111.6, 93.1 |
| COOHcis* | top | -1.68 | -1.59 | 3604.6, 1578.9, 1268.5, 1117.7, 664.6, 660.1, 406.8, 282.9, 234.5, 167.6, 114.8, 105.9 |
| HCOOH* | top | -0.28 | -0.21 | 3378.6, 3023.9, 1719.3, 1342.2, 1286.0, 1117.7, 998.9, 702.7, 631.7, 179.4, 158.4, 93.9, 79.6, 58.1, 45.6 |

**Table 3S-5** PW91 reaction energies (ΔE), activation energy barriers ($E_A$) for the elementary steps considered in the HCOOH decomposition reaction network on Au(111). All the values are relative to the infinite separation of species in the initial/final states.

| # | Reaction | Adsorbate Interaction / eV IS / FS | ΔE / eV | | $E_A$ / eV | |
|---|---|---|---|---|---|---|
| | | | W/O ZPE | W ZPE | W/O ZPE | W ZPE |
| 1 | HCOOH + * ↔ HCOOH* | - / - | -0.16 | -0.10 | 0 | - |
| 2 | HCOOH* ↔ HCOOHpa* | - / - | 0.24 | 0.24 | 0.60 | 0.55 |
| 3 | HCOOH* + 2* ↔ HCOO** + H* | - / -0.06 | 1.02 | 0.86 | 1.46 | 1.29 |
| 4 | HCOOHpa* + * ↔ COOH* + H* | - / -0.03 | 0.96 | 0.80 | 1.44 | 1.22 |
| 5 | HCOOH* + * ↔ HCO* + OH* | - / -0.15 | 2.42 | 2.32 | 2.27 | 2.16 |
| 6 | HCOO** ↔ $CO_2$* + H* | - / 0.00 | -0.21 | -0.35 | 0.86 | 0.80 |
| 7 | HCOO** + H* ↔ $H_2$ + $CO_2$* + 2* | -0.06 / 0.00 | -0.71 | -0.84 | 1.08 | 0.99 |
| 8 | COOH* + * ↔ $CO_2$* + H* | - / 0.00 | -0.39 | -0.54 | 0.74 | 0.54 |
| 9 | COOH* ↔ COOHcis* | - / - | 0.05 | 0.05 | 0.50 | 0.45 |
| 10 | COOHcis* + * ↔ CO* + OH* | - / -0.07 | 1.41 | 1.30 | 1.48 | 1.33 |
| 11 | COOHcis* + H* ↔ CO* + $H_2O$* | -0.04 / -0.04 | -0.39 | -0.33 | 0.59 | 0.55 |
| 12 | HCO* + * ↔ CO* + H* | - / 0.04 | 0.23 | 0.07 | 0.77 | 0.59 |
| 13 | OH* + H* ↔ $H_2O$* + * | -0.03 / - | -1.80 | -1.64 | 0.26 | 0.26 |
| 14 | 2H* ↔ $H_2$ + 2* | 0.01 / - | -0.49 | -0.49 | 0.59 | 0.57 |
| 15 | $CO_2$* ↔ $CO_2$ + * | - / - | 0.05 | 0.02 | 0 | - |
| 16 | $H_2O$* ↔ $H_2O$ + * | - / - | 0.16 | 0.10 | 0 | - |
| 17 | CO* ↔ CO + * | - / - | 0.26 | 0.21 | 0 | - |

**Table 3S-6** PW91 reaction energies (ΔE), activation energy barriers ($E_A$) for the elementary steps considered in the HCOOH decomposition reaction network on Au(100). All the values are relative to the infinite separation of species in the initial/final states.

| # | Reaction | Adsorbate Interaction / eV IS / FS | ΔE / eV | | $E_A$ / eV | |
|---|---|---|---|---|---|---|
| | | | W/O ZPE | W ZPE | W/O ZPE | W ZPE |
| 1 | HCOOH + * ↔ HCOOH* | - / - | -0.22 | -0.16 | 0 | - |
| 2 | HCOOH* ↔ HCOOHpa* | - / - | 0.29 | 0.29 | 0.65 | 0.59 |
| 3 | HCOOH* + 2* ↔ HCOO** + H* | - / 0.01 | 0.56 | 0.42 | 1.09 | 0.87 |
| 4 | HCOOHpa* + * ↔ COOH* + H* | - / -0.01 | 0.56 | 0.44 | 1.02 | 0.83 |
| 5 | HCOOH* + * ↔ HCO* + OH* | - / -0.22 | 1.64 | 1.57 | 2.00 | 1.91 |
| 6 | HCOO** ↔ $CO_2$* + H* | - / 0.00 | -0.06 | -0.17 | 1.02 | 0.84 |
| 7 | HCOO** + H* ↔ $H_2$ + $CO_2$* + 2* | 0.01 / - | -0.19 | -0.34 | 1.29 | 1.11 |
| 8 | COOH* + * ↔ $CO_2$* + H* | - / 0.00 | -0.34 | -0.48 | 0.90 | 0.68 |
| 9 | COOH* ↔ COOHcis* | - / - | 0.01 | 0.00 | 0.58 | 0.52 |
| 10 | COOHcis* + * ↔ CO* + OH* | - / -0.04 | 0.62 | 0.55 | 0.78 | 0.70 |
| 11 | COOHcis* + H* ↔ CO* + $H_2O$* | -0.01 / -0.05 | -0.41 | -0.36 | 0.77 | 0.68 |
| 12 | HCO* + * ↔ CO* + H* | - / -0.01 | -0.16 | -0.29 | 0.40 | 0.24 |
| 13 | OH* + H* ↔ $H_2O$* + * | -0.02 / - | -1.03 | -0.92 | 0.45 | 0.38 |
| 14 | 2H* ↔ $H_2$ + 2* | -0.03 / - | -0.13 | -0.17 | 0.53 | 0.47 |
| 15 | $CO_2$* ↔ $CO_2$ + * | - / - | 0.05 | 0.02 | 0 | - |
| 16 | $H_2O$* ↔ $H_2O$ + * | - / - | 0.20 | 0.14 | 0 | - |
| 17 | CO* ↔ CO + * | - / - | 0.68 | 0.62 | 0 | - |

**Table 3S-7** PW91 reaction energies (ΔE), activation energy barriers ($E_A$) for the elementary steps considered in the HCOOH decomposition reaction network on Au(211). All the values are relative to the infinite separation of species in the initial/final states.

| # | Reaction | Adsorbate Interaction/eV IS / FS | ΔE / eV | | $E_A$ / eV | |
|---|---|---|---|---|---|---|
| | | | W/O ZPE | W ZPE | W/O ZPE | W ZPE |
| 1 | HCOOH + * ↔ HCOOH* | - / - | -0.28 | -0.21 | 0 | - |
| 2 | HCOOH* ↔ HCOOHpa* | - / - | 0.31 | 0.26 | 0.68 | 0.63 |
| 3 | HCOOH* + 2* ↔ HCOO** + H* | - / 0.20 | 0.40 | 0.26 | 1.20 | 0.98 |
| 4 | HCOOHpa* + * ↔ COOH* + H* | - / 0.02 | 0.49 | 0.37 | 1.06 | 0.87 |
| 5 | HCOOH* + * ↔ HCO* + OH* | - / -0.03 | 1.47 | 1.38 | 1.85 | 1.74 |
| 6 | HCOO** ↔ $CO_2$* + H* | - / 0.00 | 0.04 | -0.08 | 1.03 | 0.85 |
| 7 | HCOO** + H* ↔ $H_2$ + $CO_2$* + 2* | 0.20 / 0.00 | 0.02 | -0.15 | 1.39 | 1.30 |
| 8 | COOH* + * ↔ $CO_2$* + H* | - / 0.00 | -0.31 | -0.46 | 0.96 | 0.74 |
| 9 | COOH* ↔ COOHcis* | - / - | 0.00 | -0.01 | 0.50 | 0.44 |
| 10 | COOHcis* + * ↔ CO* + OH* | - / 0.15 | 0.58 | 0.51 | 1.10 | 1.00 |
| 11 | COOHcis* + H* ↔ CO* + $H_2O$* | 0.02 / 0.02 | -0.34 | -0.30 | 0.95 | 0.87 |
| 12 | HCO* + * ↔ CO* + H* | - / 0.02 | -0.14 | -0.26 | 0.43 | 0.28 |
| 13 | OH* + H* ↔ $H_2O$* + * | 0.08 / - | -0.92 | -0.81 | 0.69 | 0.61 |
| 14 | 2H* ↔ $H_2$ + 2* | -0.02 / - | -0.02 | -0.07 | 0.55 | 0.49 |
| 15 | $CO_2$* ↔ $CO_2$ + * | - / - | 0.06 | 0.05 | 0 | - |
| 16 | $H_2O$* ↔ $H_2O$ + * | - / - | 0.25 | 0.20 | 0 | - |
| 17 | CO* ↔ CO + * | - / - | 0.73 | 0.67 | 0 | -- |

# Chapter 4 On the Nature of Active Sites for Formic Acid Decomposition on Au Catalysts

## 4.1 Introduction

Using an integrated method of DFT calculations, experiments and microkinetic modeling in Chapter 3, formic acid decomposition mechanism was elucidated to proceed via the formate mediated route, which is comprised of three elementary steps: HCOOH* → HCOO** + H*, HCOO** → $CO_2$* + H*, and 2H* → $H_2$(g). In terms of the active sites, the extended surfaces of gold ─ Au(111), Au(100) and Au(211) with coordination number (CN) of 9, 8, and 7, respectively, for surface atoms ─ were found not to be the active sites on SiC supported Au catalysts for formic acid decomposition. Further experiments conducted on different catalyst samples with a varying degree of Au dispersion together with relations determining the fraction of different types of Au sites as a function of average particle size suggested that coordinatively unsaturated corner sites are most likely to dominate active sites for this reaction. However, the physical models of Au clusters used to develop the relations between site density and particle size are truncated cuboctahedra, which may not represent the most stable structure of Au clusters, especially for subnanometric Au clusters which are postulated to have remarkable activity for this reaction based on the experimental studies. Thus, in the current work, the most stable configurations of subnanometer Au clusters (up to $Au_{25}$ with a size of 0.85 nm) were investigated using *ab initio* molecular dynamic (AIMD) simulations and a full mechanistic study of the formic acid decomposition was performed on several optimized Au clusters identified to be the promising candidates of the active sties. The same integrated method of theory, experiments and microkinetic modeling was adopted in this work to examine the candidate Au clusters and the active site for

formic acid decomposition can be represented by the $Au_{18}$ cluster model, on which the triangular $Au_3$ site with CN=5 is where the reaction takes place.

### 4.2 Computational methods

All calculations in the current work were performed using the Vienna ab initio simulation package (VASP) code[97, 148] based on density functional theory (DFT). The projector augmented wave (PAW)[149, 150] potentials were used for electron−ion interactions, and the generalized gradient approximation (GGA−PW91)[151] was used to describe the exchange-correlation functional. The electron wave function was expanded using plane waves with an energy cutoff of 400 eV. All calculations were performed in a 20×20×20 $Å^3$ cubic cell with 3-dimensional periodic boundary conditions and the Brillouin zones were sampled by the gamma point only.

To obtain the most stable configurations of the Au clusters, DFT calculations were performed in the framework of *ab-initio* molecular dynamics (AIMD)[152]. First, several initial guesses of cluster models were statically optimized to local minima, which subsequently underwent AIMD simulated annealing. In the simulated annealing process, the system was first equilibrated at a high temperature for 2 ps, then quenched to room temperature within 2 ps, and finally, the local minima of the quenching trajectory were statically optimized to yield final structures. From these local minima, the most stable one was chosen as the optimized structure.

During the structure optimization of the adsorbates and activation energy calculations on Au clusters, all Au atoms were fully relaxed without any constraint. Structures were fully relaxed until the Hellmann−Feynman forces acting on the atoms were smaller than 0.05 eV/Å. Binding energy (BE) of the adsorbate was calculated with respect to the pure Au cluster and the corresponding adsorbate (intermediate) in the gas phase. Minimum energy paths and activation energy barriers of the elementary steps were calculated using the climbing image nudged elastic band method (CI-

NEB)[99]. The minimum energy path for each elementary step was discretized by a total of at least nine images, including the initial and final state. Convergence of the NEB calculations was reached when the magnitude of the force on all images was less than 0.1 eV/Å, except for the hydrogen recombination reaction, where a stricter convergence criterion (0.05 eV/Å) was used. The transition states (TS) were confirmed by vibrational frequency calculations yielding a single imaginary frequency along the reaction coordinate.

## 4.3 Results and discussion

### 4.3.1 Optimized $Au_n$ (n=2-25) clusters

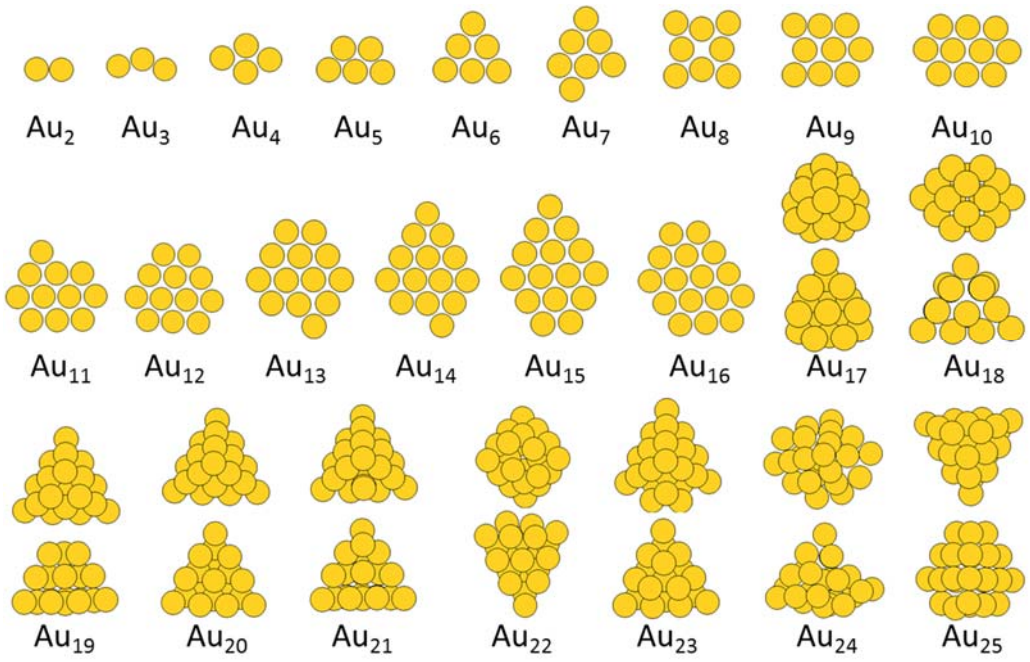


**Figure 4-1** Most stable configurations of $Au_n$ (n=2-25) clusters obtained from AIMD simulations. For $Au_n$ clusters with 3D structures, both the top view and side view are shown.

Since the discovery of the extraordinary catalytic activity of dispersed gold nanoparticles toward CO oxidation by Haruta *et al*[153], considerable efforts have been devoted to understand the secret of the catalytic properties of gold nanoparticles, especially the precise structural information of

small gold clusters in the range of 3-20 gold atoms has been obtained and confirmed with joint theoretic and experimental efforts[154-168]. However, most of these efforts were concentrated on charged Au clusters, anionic Au clusters in particular, because charged species are easily size-selected and the experimental techniques widely used to understand the geometric properties of Au clusters, such as ion mobility spectrometry, photoelectron spectroscopy, and trapped ion electron diffraction, are all restricted to the investigation of charged species.[169] Compared with the charged Au clusters, there is a lack of both experimental and theoretic studies for neutral Au clusters.

In the current work, *ab initio* molecular dynamics simulations were used to obtain the most stable configurations of $Au_n$ (n=25) clusters, which are shown in **Figure 4-1**. It is found that 2-dementional (2D) structures are preferred from $Au_2$ to $Au_{16}$, while $Au_n$ clusters with more than 16 atoms prefer the 3D structures. Most planar structures can be obtained from truncation of a one-layer (111) surface with the exception of $Au_8$, which adopts a highly symmetric ($D_{4h}$ symmetry) star-shaped planar structure and represents a distinct type of site, where two squares are formed by the innermost and outermost four atoms with an angle of 45 degrees between their diagonals. Among the planar structures, $Au_6$ also has a highly symmetric structure ($D_{3h}$ symmetry), but it is an equilateral triangle. $Au_{20}$ is a tetrahedral pyramid with $T_d$ symmetry, which has also been suggested to be the global minimum for anionic $Au_{20}^-$ [166]. Removal of one, two and three corner atoms from $Au_{20}$ tetrahedron leads to a truncated trigonal pyramid $Au_{19}$ with $C_{3v}$ symmetry, $Au_{18}$ with $C_{2v}$ symmetry, and $Au_{17}$ also with $C_{3v}$ symmetry, respectively, while addition of one, two and three atoms on the facet on $Au_{20}$ forms $Au_{21}$, $Au_{22}$ and $Au_{23}$ with reduced symmetries. $Au_{24}$ has an amorphous structure, while $Au_{25}$ can be formed by adding another layer of $Au_6$ triangle under the bottom of $Au_{19}$. Among these 2D and 3D structures, the rhombus ($D_{2h}$) $Au_4$, trapezoid ($C_{2v}$) $Au_5$,

edge-capped triangle ($C_s$) $Au_7$, four-fold edge-capped square $Au_8$, truncated pyramid $Au_{19}$ and pyramid $Au_{20}$ have been confirmed by Fielicke and coworkers[154, 163] using far-infrared multiple-photon dissociation (FIR-MPD) spectroscopy, the only size-selective experimental technique available for structure determination of neutral metal clusters in the gas phase. While the 2D-to-3D transition has been found to appear in the range of n = 12-13 for gold cluster anions $Au_n^-$ [160, 161], it is yet to be determined experimentally for neutral Au clusters.

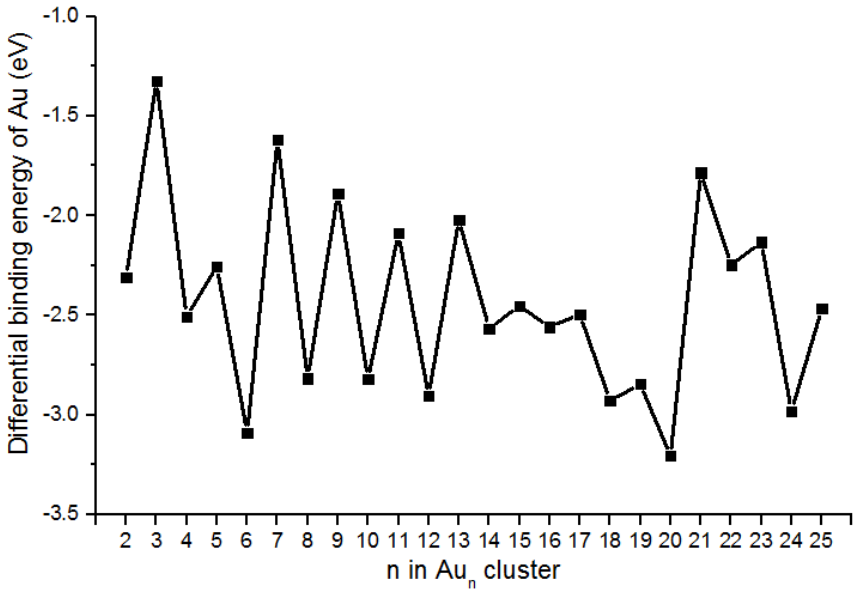


**Figure 4-2** Differential binding energy (dBE) of Au in $Au_n$ (n=2-25) clusters using isolated atomic Au atom as the energy reference. dBE = $E(Au_n) - E(Au_{n-1}) - E(Au)$.

Differential binding energy (dBE) of Au in $Au_n$ clusters is calculated as the BE of adding the last Au atom to the $Au_n$ clusters and is plotted in **Figure 4-2**. A clear odd-even oscillation exhibits in the differential binding energy of Au with even-numbered Au clusters being more stable than neighboring odd-numbered clusters, which can be understood by electron paring effect[170]. Based on the differential BE plot, $Au_6$ and $Au_{20}$ represent two most stable clusters among $Au_n$ clusters with no more than 25 atoms, and if using the energy of bulk Au atom as reference, they are the only two clusters with negative dBE values, -0.06 eV for $Au_6$ and -0.18 eV for $Au_{20}$, indicating

the last Au atom in the two clusters bind even more strongly than bulk Au. Differential BE plot using bulk Au as the energy reference can be find in the supplementary material.

### 4.3.2 BEs of key intermediates of HCOOH decomposition on $Au_n$ (n=4-25) clusters

After the structures of $Au_n$ clusters were optimized, binding energies of the key intermediates in HCOOH decomposition, including HCOOH, formate (HCOO), carboxyl (COOH) and H were calculated on $Au_n$ (n=4-25) clusters to get a first understanding of the interaction between intermediates and gold clusters. The most stable configurations of the four intermediates adsorbed on $Au_n$ clusters can be found in the supplementary material together with their binding energy values. **Figure 4-3** plots the binding energies on $Au_n$ clusters and also compares with the corresponding values on Au(211) surface, as indicated by the black lines in **Figure 4-3**.

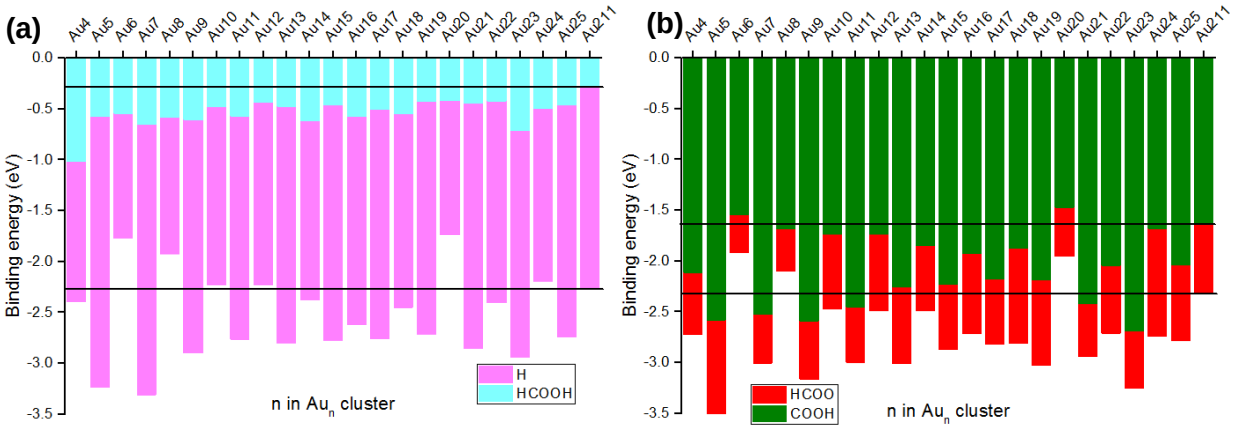


**Figure 4-3** Binding energies of (a) H and HCOOH, (b) HCOO and COOH on $Au_n$ (n=4-25) clusters. Black horizontal lines show the BEs of the intermediates on Au(211) surface.

For HCOOH, it binds mildly more strongly on all $Au_n$ clusters being investigated than on Au(211) surface by 0.15-0.50 eV, except on $Au_4$, a significantly stronger binding energy of -1.02 eV is observed compared with the -0.27 eV on Au(211) surface. In terms of binding energy, the closed-shell HCOOH intermediate is less sensitive to the size of $Au_n$ clusters compared with the other three species, of which the BEs also show an odd-even alternation behavior, similar as the dBE of

Au. Since H, COOH, and HCOO are all species with an odd number of valence electrons, they all bind more strongly on the odd-numbered $Au_n$ clusters than on neighboring even-numbered clusters. For H, on all odd-numbered $Au_n$ clusters, it binds more strongly than on Au(211), while the even-numbered clusters show similar binding energies as Au(211) except for $Au_6$, $Au_8$ and $Au_{20}$ where a 0.3-0.5 eV weaker BE of H is seen and for $Au_{14}$ with a 0.36 eV stronger BE. All $Au_n$ clusters bind HCOO more strongly than Au(211) except for $Au_6$, $Au_8$ and $Au_{20}$, where a weaker BE of HCOO by ca. 0.2-0.4 eV is found. Similarly, COOH also binds more strongly on all $Au_n$ clusters than on Au(211) except for $Au_6$ and $Au_{20}$, on which COOH binds slightly less strongly by ca. 0.1-0.2 eV. Among the $Au_n$ clusters, $Au_6$, $Au_8$ and $Au_{20}$ are found to have a weaker interaction with the intermediates in general, probably due to the relatively high stabilities of these three clusters associated with the nice symmetries found in their structures.

**Table 4-1** Energy difference between formate (HCOO) and carboxyl (COOH) on $Au_n$ (n=4-25) clusters. $dE = E(HCOO/Au_n) - E(COOH/Au_n)$.

| | $Au_4$ | $Au_5$ | $Au_6$ | $Au_7$ | $Au_8$ | $Au_9$ | $Au_{10}$ | $Au_{11}$ | $Au_{12}$ | $Au_{13}$ | $Au_{14}$ | Au(211) |
|---|---|---|---|---|---|---|---|---|---|---|---|---|
| dE(eV) | -0.22 | -0.63 | 0.02 | -0.09 | -0.02 | -0.18 | -0.35 | -0.16 | -0.36 | -0.36 | -0.25 | -0.35 |
| | $Au_{15}$ | $Au_{16}$ | $Au_{17}$ | $Au_{18}$ | $Au_{19}$ | $Au_{20}$ | $Au_{21}$ | $Au_{22}$ | $Au_{23}$ | $Au_{24}$ | $Au_{25}$ | |
| dE(eV) | -0.25 | -0.39 | -0.25 | -0.54 | -0.45 | -0.09 | -0.13 | -0.27 | -0.18 | -0.67 | -0.36 | |

As HCOO and COOH are isomers of each other, their relative stabilities were also compared on the $Au_n$ clusters with energy differences summarized in **Table 4-1**. It can be seen that HCOO is a more stable species than COOH on all $Au_n$ (n=4-25) clusters except for $Au_6$, where HCOO is slightly less stable than COOH by 0.02 eV. Among the $Au_n$ (n=4-25) clusters, compared with COOH, HCOO is stabilized to a higher extent on $Au_5$, $Au_{18}$, $Au_{19}$ and $Au_{24}$ than on Au(211), whereas on the other clusters, stabilization of HCOO (using COOH as the energy reference) is reduced if it is not similar as on Au(211). The energy difference of HCOO and COOH given in

**Table 4-1** is also the reaction energy difference for HCOO and COOH formation from HCOOH: HCOOH → HCOO + H and HCOOH → COOH + H. Hence, the general higher stability of HCOO than COOH on $Au_n$ clusters provides a first indication that HCOO mediated pathway might be more favorable than the COOH mediated pathway for HCOOH decomposition on gold clusters, which will be reexamined by performing rigorous activation energy calculations for the two pathways; results obtained from those calculations will be presented in the following sections.

### 4.3.3 Activation energies for HCOOH dehydrogenation to HCOO on $Au_n$ (n=4-25) clusters

Since HCOOH decomposition is found to proceed through the HCOO mediated path on extended Au surfaces and HCOO formation is energetically more favorable than COOH formation from HCOOH on $Au_n$ clusters, to a first approximation, the reaction mechanism comprised of three elementary steps of the HCOO pathway does not change on $Au_n$ clusters. Then the first step in HCOO pathway, dehydrogenation of HCOOH to HCOO was investigated on $Au_n$ (n=4-25) clusters, and the calculated activation energies serve as a first screen of promising active $Au_n$ clusters for HCOOH decomposition. As Au(211) is less active than the Au catalysts used in experiments by several orders of magnitude, active $Au_n$ clusters should at least have a smaller barrier for HCOO formation than the Au(211) surface, and ideally the active Au site will require an approximate decrease of 0.4-0.5 eV in HCOO formation barrier from the Au(211) value to advance the reaction rate by 5-6 orders of magnitude under reaction temperatures and make it comparable with the experimentally observed rate.

**Table 4-2** summarizes the DFT calculated activation energies for HCOO formation from HCOOH on $Au_n$ clusters and the transition state (TS) configurations are provided in supplementary material. It can be seen that $Au_6$, $Au_8$ and $Au_{20}$ have a higher (albeit not significantly higher) activation energy for HCOO formation than Au(211), which is consistent with the weak interactions found

between these three clusters and the intermediates, leading to a first removal of the three clusters from the candidate pool of active $Au_n$ clusters. $Au_n$ clusters in the range n=9-16 and n=21-23 have a similar activation energy for HCOO formation as Au(211) surface, with differences in Ea being less than 0.2 eV, within the DFT calculation errors. Thus, compared with Au(211) surface, these clusters are expected to exhibit a similar or slightly higher reaction rate, which is far less that the 5 or 6 orders of magnitude increase required to represent the active sites. As a result, $Au_n$ clusters in the range n=9-16 and n=21-23 are also ruled out from candidates of the active gold sites. Among the remaining $Au_n$ clusters, $Au_{18}$ has the lowest activation energy for HCOO formation, implying that $Au_{18}$, in all likelihood, is the most promising active site model. In the following section, the other two steps in the HCOO pathway, and in some cases steps in the COOH pathway will be explored on clusters characterized with low HCOO formation barriers, specifically, $Au_4$, $Au_5$, $Au_7$, $Au_{17}$, $Au_{18}$ and $Au_{19}$.

**Table 4-2** Activation energy (Ea) of HCOOH dehydrogenation to HCOO (HCOOH* + 2* → HCOO** + H*) on $Au_n$ (n=4-25) clusters. Ea on Au(211) is given for comparison.

| | $Au_4$ | $Au_5$ | $Au_6$ | $Au_7$ | $Au_8$ | $Au_9$ | $Au_{10}$ | $Au_{11}$ | $Au_{12}$ | $Au_{13}$ | $Au_{14}$ | Au(211) |
|---|---|---|---|---|---|---|---|---|---|---|---|---|
| Ea(eV) | 0.92 | 0.76 | 1.47 | 0.92 | 1.25 | 1.01 | 1.14 | 1.16 | 1.00 | 1.02 | 1.14 | 1.20 |
| | $Au_{15}$ | $Au_{16}$ | $Au_{17}$ | $Au_{18}$ | $Au_{19}$ | $Au_{20}$ | $Au_{21}$ | $Au_{22}$ | $Au_{23}$ | $Au_{24}$ | $Au_{25}$ | |
| Ea(eV) | 1.14 | 1.09 | 0.84 | 0.67 | 0.85 | 1.35 | 1.14 | 1.17 | 1.20 | 0.86 | 0.93 | |

### 4.3.4 DFT results on a series of promising active site models ($Au_4$, $Au_5$, $Au_7$, $Au_{17}$, $Au_{18}$ and $Au_{19}$)

Detailed reaction pathway studies were performed on the six $Au_n$ clusters identified as promising active site models, $Au_4$, $Au_5$, $Au_7$, and $Au_{17}$─$Au_{19}$. The three elementary steps of the HCOO pathway (reactions 2-4 in **Table 4-3**) were calculated on all six clusters since HCOO pathway is expected to be the preferred pathway, while the COOH pathway was also investigated on four of

the clusters to obtain an unbiased and accurate understanding of the reaction mechanism for HCOOH decomposition. The calculated activation energies and reaction energies on the six gold clusters were summarized in **Table 4-3**.

**Table 4-3** Activation energy (Ea) and reaction energy (ΔE) of key elementary steps in HCOOH decomposition on several $Au_n$ clusters. All values are relative to the best initial/final states and are reported in eV.

| | $Au_4$ | | $Au_5$ | | $Au_7$ | | $Au_{17}$ | | $Au_{18}$ | | $Au_{19}$ | |
|---|---|---|---|---|---|---|---|---|---|---|---|---|
| | Ea | ΔE | Ea | ΔE | Ea | ΔE | Ea | ΔE | Ea | ΔE | Ea | ΔE |
| HCOOH(g) + * → HCOOH* | | -1.02 | | -0.58 | | -0.65 | | -0.50 | | -0.54 | | -0.42 |
| HCOOH* + 2* → HCOO** + H* | 0.92 | -0.50 | 0.76 | -0.16 | 0.92 | -0.08 | 0.84 | -0.12 | 0.67 | -0.18 | 0.85 | 0.15 |
| HCOO** → $CO_2$(g) + H* + * | 1.09 | 0.15 | 1.44 | 0.27 | 0.93 | -0.44 | 1.15 | -0.03 | 1.04 | 0.27 | 1.07 | 0.22 |
| 2H* → $H_2$* + 2* | 0.26 | 0.17 | 0.49 | 0.28 | 0.74 | 0.48 | 0.83 | 0.41 | 0.87 | 0.66 | 0.50 | 0.07 |
| HCOOH* + * → COOH* + H* | -- | -- | 1.06 | 0.13 | 1.15 | 0.27 | -- | -- | 1.22 | 0.33 | 1.36 | 0.59 |
| COOH* → $CO_2$(g) + H* | -- | -- | 0.98 | -0.36 | 1.04 | -0.53 | -- | -- | 1.19 | -0.27 | 1.10 | -0.22 |
| COOH* + * → CO* + OH* | -- | -- | 0.35 | -2.78 | 0.84 | -3.00 | -- | -- | 0.53 | -2.61 | 0.56 | -3.22 |
| OH* + H* → $H_2O$* + * | -- | -- | 1.19 | -0.41 | 0.86 | -0.32 | -- | -- | -- | -- | 0.63 | -0.71 |
| CO* → CO(g) + * | | 1.74 | | 1.27 | | 1.24 | | 1.15 | | 1.11 | | 0.87 |
| $H_2O$* → $H_2O$(g) + * | | -- | | 0.41 | | 0.44 | | -- | | -- | | 0.25 |
| $H_2$* → $H_2$(g) + * | | 0.70 | | 0.29 | | 0.30 | | 0.12 | | 0 | | 0 |

On $Au_4$, an exceptionally strong BE of HCOOH is found, -1.02 eV; along with the adsorption of HCOOH, $Au_4$ undergoes a structural change from the most stable rhombus structure (**Figure 4-1**) to a 'Y-shaped' structure (**Figure 4-4**). Dehydrogenation of HCOOH to HCOO and H on $Au_4$ induces further structural change of $Au_4$ back to the rhombus structure, with the final product HCOO bound to one side of the rhombus and H sitting at a nearby bridge site and the shared Au tom between the two being the one at the end of the longer diagonal. HCOOH dehydrogenation to co-adsorbed HCOO and H is an exothermic reaction with a barrier of 0.92 eV. On $Au_4$, co-adsorbed HCOO and H species exhibit a significantly attractive interaction with an energy of 1.17

eV is required to move the two species to infinite separation. Further dehydrogenation of HCOO involves flipping and rotation of HCOO to first break one O-Au bond and forms a structure of which the C-H bond is pointing towards the cluster and is readily broken in a subsequent close-to-spontaneous step. The overall barrier required for HCOO decomposition is 1.09 eV on $Au_4$. Combination of two co-adsorbed and attractively interacted H atoms (by 0.64 eV) forms a molecularly adsorbed hydrogen, with a quite strong binding energy of -0.70 eV.

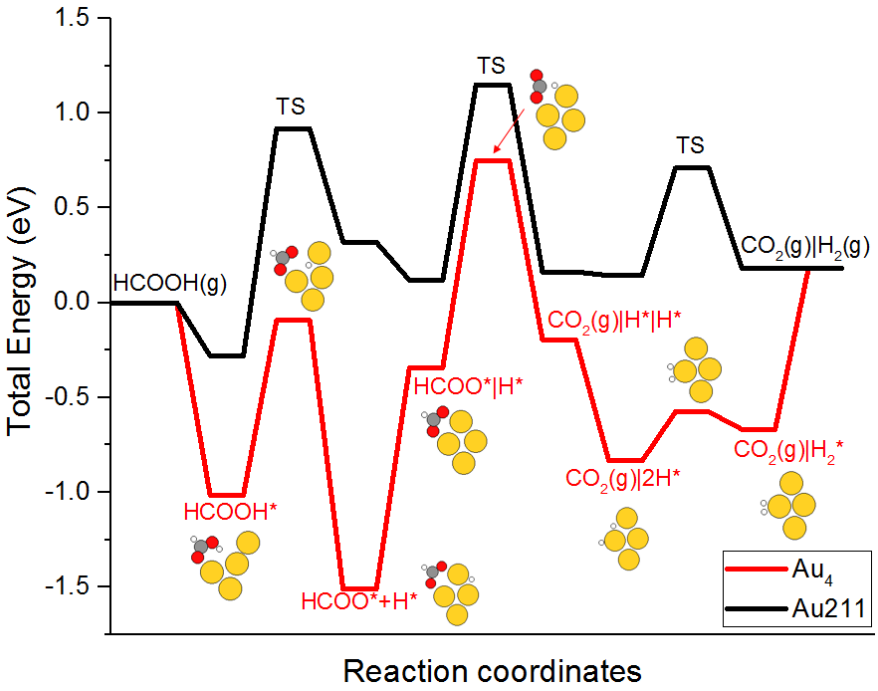


**Figure 4-4** Potential energy surface of HCOOH decomposition through the HCOO path on $Au_4$. PES for Au(211) is shown in black line for comparison. Insets show configurations of the most favorable adsorbed states and transition states on $Au_4$, with Au, C, O and H atoms are represented by yellow, grey, red and white circles. '|' indicates infinite separation, while '+' means the intermediates are co-adsorbed on the surface. The same notation is adopted throughout this chapter.

**Figure 4-4** plots the potential energy surface of the abovementioned HCOO pathway on $Au_4$, and compares with the corresponding PES on Au(211) surface. It can be seen that, the TSs of the three elementary steps in the HCOO pathway are substantially stabilized on $Au_4$ compared with the Au(211) surface, primarily because the adsorbed states are significantly stabilized on $Au_4$. What

seems to be particularly noteworthy is that when HCOO (or H) is co-adsorbed with another H on the $Au_4$ cluster, the co-adsorption state is stabilized by 1.17 eV (or 0.64 eV) compared with the infinite-separation counterpart, forming a deep potential well which implies a partially covered cluster site with HCOO and (or) H species. Furthermore, desorption of molecular hydrogen is a difficult step characterized by the 0.7 eV desorption energy, while its dissociation into atomic hydrogens is fairly easy with a negligible barrier of 0.09 eV, which provides further indication of a H-covered site environment.

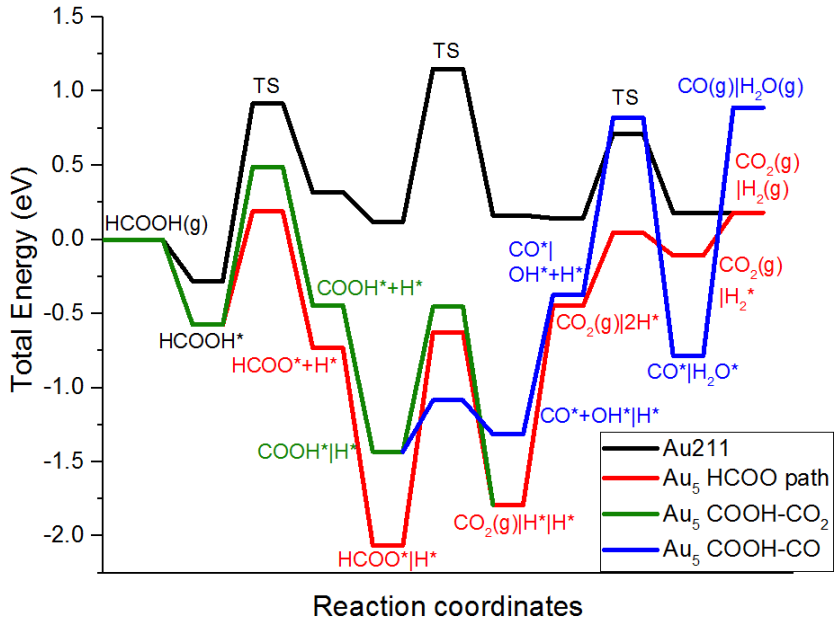


**Figure 4-5** Potential energy surface of HCOOH decomposition through the HCOO path (red line), COOH path leading to $CO_2$ formation (COOH-$CO_2$ path; green line) and COOH path leading to CO formation (COOH-CO path; blue line) on $Au_5$. PES for Au(211) is shown in black line for comparison.

Potential energy surface for HCOOH decomposition through both the HCOO pathway and COOH pathway which can lead to either $CO_2$ (COOH-$CO_2$ path) or CO (COOH-CO path) formation is plotted for $Au_5$ in **Figure 4-5**. It is seen that COOH formation is less favorable than HCOO formation from HCOOH, and COOH decomposition to $CO_2$ also has a higher TS energy than HCOO decomposition on $Au_5$. Hence, the COOH-$CO_2$ path is less preferred compared with the

HCOO path. For the COOH-CO path, COOH decomposition to CO with a barrier of 0.35 eV, is much easier than HCOO decomposition, nevertheless, water formation in the COOH-CO path is associated with a high-lying TS with an energy of more than 0.6 eV higher than the highest TS in the HCOO pathway and may represent the rate limiting step (RLS). Due to the extremely high TS energy in the likely rate limiting step, COOH pathway leading to CO formation should be expected to carry a minor reaction flux compared with the HCOO pathway.

HCOOH adsorbs on the shorter parallel side of the $Au_5$ trapezoid (**Figure 4-6**) with a BE of -0.58 eV and its dehydrogenation has a modest barrier of 0.76 eV, forming HCOO adsorbed on two sites of the longer parallel side and H sitting on the bridge site at the nearby side. On contrary to $Au_4$, on $Au_5$ strong repulsive interaction between co-adsorbed HCOO and H is observed, which leads to a deep potential well for the two adsorbed species at infinite separation. Though subsequent HCOO decomposition has a high barrier of 1.44 eV, the TS lies below the other two TSs in the HCOO pathway due to the low-lying initial state. $H_2$ formation needs to first overcome the repulsion (of 1.34 eV) between two hydrogen atoms and then comes across a barrier of 0.49 eV to form the H-H bond at vertex of the shorter parallel edge. Thus, an overall barrier 1.84 eV is associated with $H_2$ formation on $Au_5$, which may represent the RLS and implies a H-covered site environment.

Compared with Au(211) surface, the PES for HCOOH decomposition through the HCOO path on $Au_5$ (**Figure 4-6**) is significantly shifted towards a lower energy, due to stabilization of intermediates (HCOOH, HCOO and H), especially when they bind to different $Au_5$ clusters. The strong and repulsive interaction between HCOO and H on $Au_5$ allows for fast redistribution of the two species to two different $Au_5$ clusters upon their formation from HCOOH if diffusion barriers are low, which is not a bad assumption under reaction temperatures. The isolated HCOO species

can decompose easily to H with $CO_2$ being released to the gas phase, leaving $Au_5$ clusters each occupied by a H atom, and the repulsive H-H interaction inhibits the transfer of H atoms sitting on different gold clusters to the same cluster, resulting in a very difficult $H_2$ production process, which may take place at the interface between two loosely attached gold clusters, each donating one H to participate in the product formation reaction.

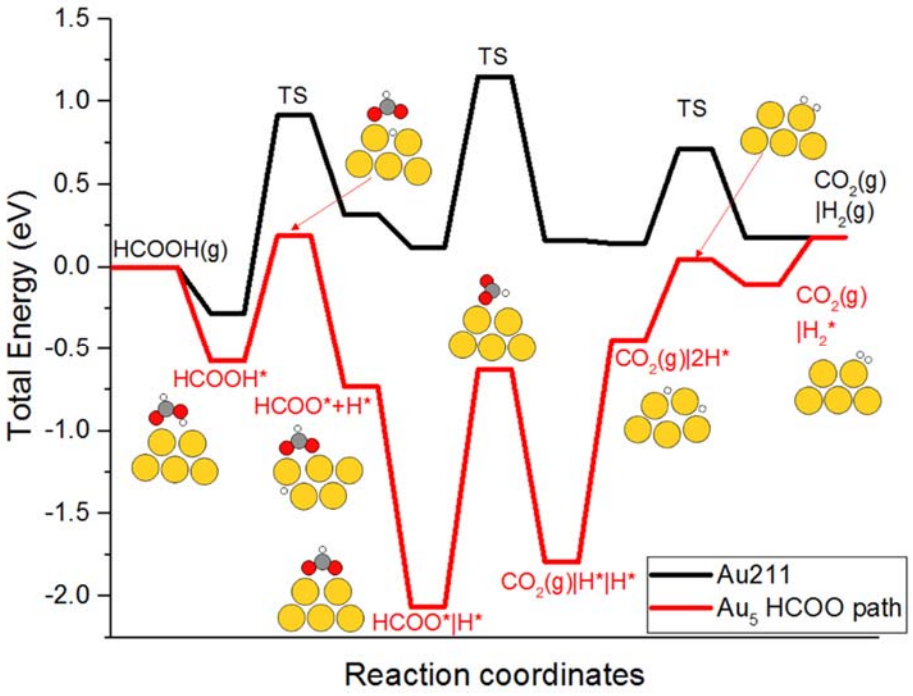


**Figure 4-6** Potential energy surface of HCOOH decomposition through the HCOO path on $Au_5$. PES for Au(211) is shown in black line for comparison.

On $Au_7$, similar trends (see **Figure 4-7**) can be found for the relative contributions of three alternative reaction paths as those shown on $Au_5$: COOH-$CO_2$ path is less favorable than the HCOO path due to the higher dehydrogenation TSs for the former; COOH-CO path should carry a smaller reaction flux than the HCOO path, resulting from the high TS in water formation. So HCOO path is also the most favorable decomposition route for HCOOH on $Au_7$. Most stable favorable configurations of the adsorbed and transition states along the HCOO path are shown in **Figure 4-8**; it can be seen that $Au_7$ undergoes geometric reconstruction upon HCOO adsorption or

co-adsorption of two H species. Though the specific numbers of activation energies and reaction energies on $Au_7$ are different from those on $Au_5$, the general trend stays the same. On $Au_7$, highly repulsive H-HCOO and H-H interactions (**Table 4-4**) are also seen, and the hypothesis made for the reaction processes on $Au_5$ also holds true here with hydrogen recombination being the obstacle to achieve a higher reaction rate.

**Table 4-4** Interaction energy between H and HCOO, H and H in their best co-adsorbed states on several promising $Au_n$ clusters.

| Interaction energy (eV) | $Au_4$ | $Au_5$ | $Au_7$ | $Au_{17}$ | $Au_{18}$ | $Au_{19}$ |
|---|---|---|---|---|---|---|
| H ←→HCOO | -1.17 | 1.33 | 0.81 | 0.18 | -0.23 | 0.69 |
| H←→H | -0.64 | 1.34 | 1.29 | 0.44 | -0.31 | 0.81 |

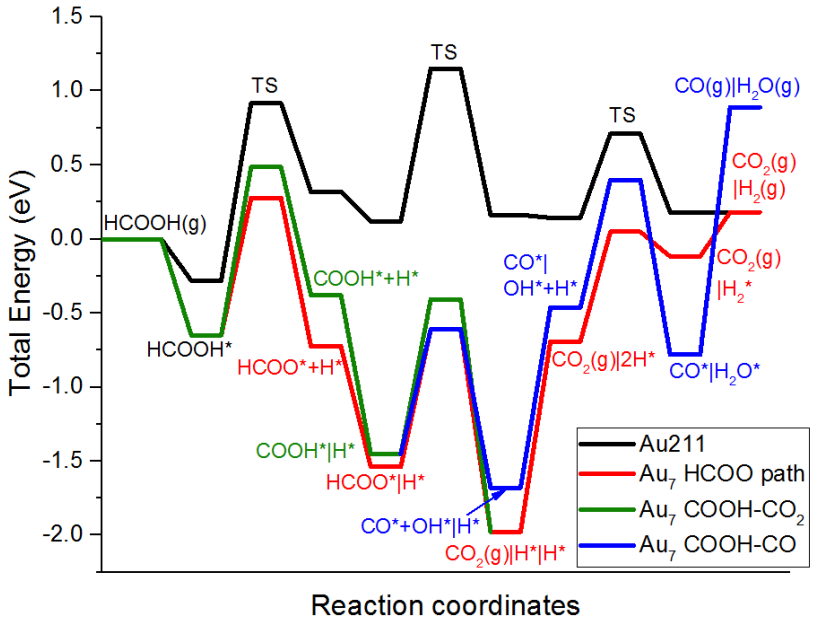


**Figure 4-7** Potential energy surface of HCOOH decomposition through the HCOO path (red line), COOH path leading to $CO_2$ formation (COOH-$CO_2$ path; green line) and COOH path leading to CO formation (COOH-CO path; blue line) on $Au_7$. PES for Au(211) is shown in black line for comparison.

**Table 4-4** summarizes the interaction energy between H and HCOO or H on $Au_4$, $Au_5$, $Au_7$, $Au_{17}$-$Au_{19}$. Due to electron pairing effect, odd-numbered clusters exhibit strong repulsive interaction

between co-adsorbed H and HCOO or H, while even-numbered clusters show strong attractive interaction. The interaction between H and HCOO or H on $Au_{17}$ and $Au_{18}$ has a modest strength of ca. 0.2-0.4 eV (either repulsive or attractive), which is much weaker than on the other four clusters.

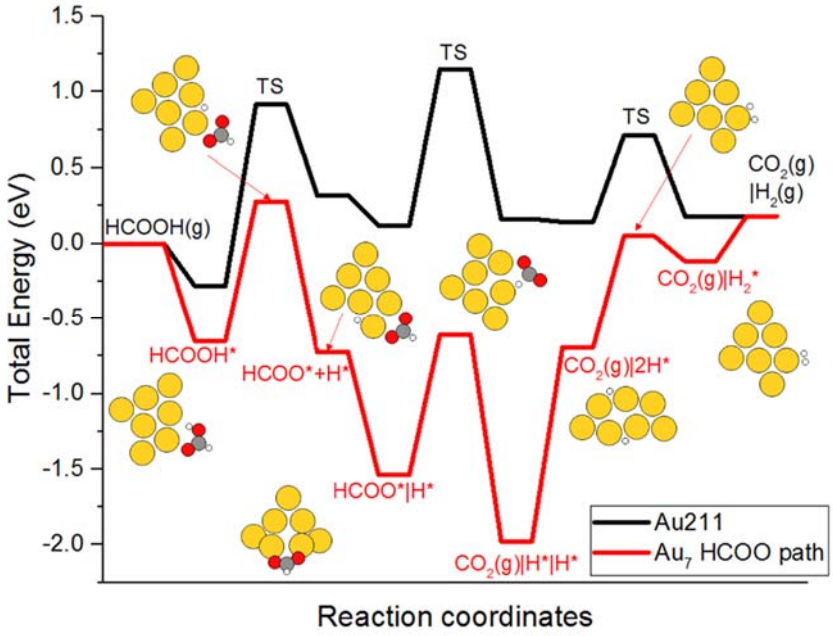


**Figure 4-8** Potential energy surface of HCOOH decomposition through the HCOO path on $Au_7$. PES for Au(211) is shown in black line for comparison.

On $Au_{17}$, only the HCOO pathway was explored (**Figure 4-9**). Though $Au_{17}$ is also an odd-numbered cluster, same as $Au_5$ and $Au_7$, due to the weaker interaction of H with HCOO, TS of the HCOO decomposition is not significantly stabilized as on $Au_5$ and $Au_7$, thus the hypothesis made about the reaction process on $Au_5$ and $Au_7$ based on the easy HCOO decomposition and difficult hydrogen recombination is no longer true for $Au_{17}$. On $Au_{17}$, it is hard to determine the RLS only from DFT based analysis since the three steps have similar TS energies. But due to the strong binding of the intermediates and the consequent stabilization of the TSs on $Au_{17}$, it is still a more active model for HCOOH decomposition than Au(211). On $Au_{17}$, all three reactions in the HCOO pathway take place on a triangular $Au_3$ site with coordinate number (CN) of 5 for every Au atom

on this particular site. This site preference is seen also in $Au_{18}$ and $Au_{19}$, and will be further discussed in the following sections.

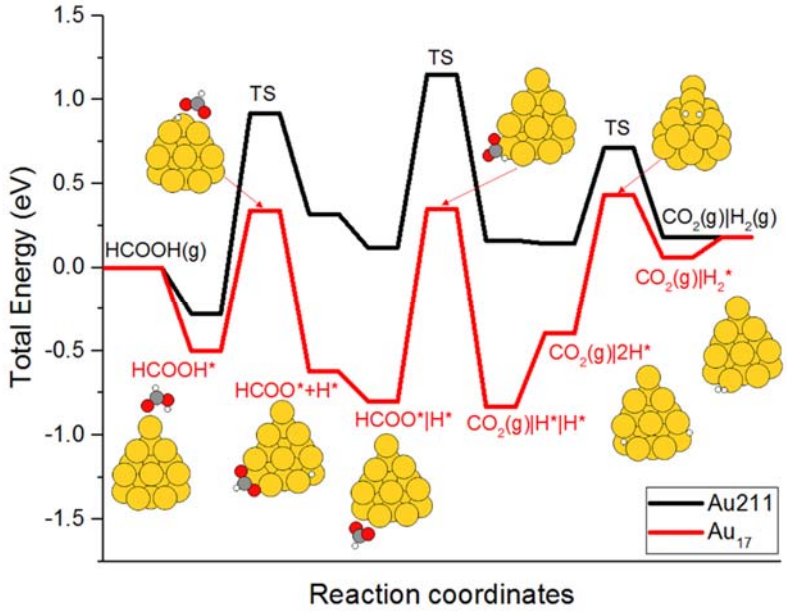


**Figure 4-9** Potential energy surface of HCOOH decomposition through the HCOO path on $Au_{17}$. PES for Au(211) is shown in black line for comparison.

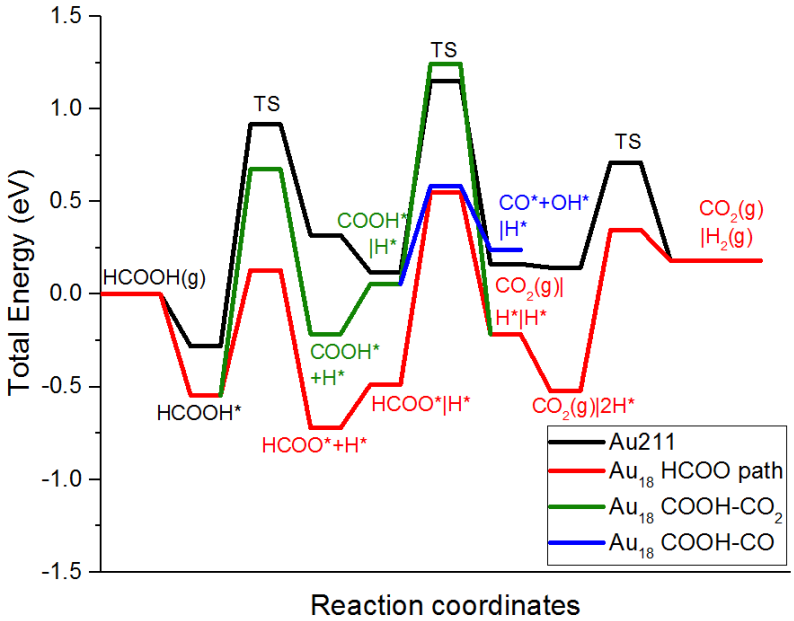


**Figure 4-10** Potential energy surface of HCOOH decomposition through the HCOO path (red line), COOH path leading to $CO_2$ formation (COOH-$CO_2$ path; green line) and COOH path leading to CO formation (COOH-CO path; blue line) on $Au_{18}$. PES for Au(211) is shown in black line for comparison.

On $Au_{18}$, COOH formation from HCOOH has a barrier of more than 0.5 eV higher than the barrier for HCOO formation. Subsequent dehydrogenation of COOH also has a slightly higher (ca. 0.15 eV) than HCOO dehydrogenation, combining this with the fact that COOH is less stale than HCOO by 0.54 eV on $Au_{18}$, the TS for COOH dehydrogenation lies much higher (by ca. 0.7 eV) above that for HCOO decomposition (see **Figure 4-10**) on the same PES diagram. Thus, COOH-$CO_2$ is an unfavorable decomposition path on $Au_{18}$. Though with a small barrier of 0.53 eV, COOH decomposition to CO provides an alternative reaction path for COOH, its formation from HCOOH is very difficult at the first place. As a result, HCOOH preferentially decomposes through the HCOO intermediate.

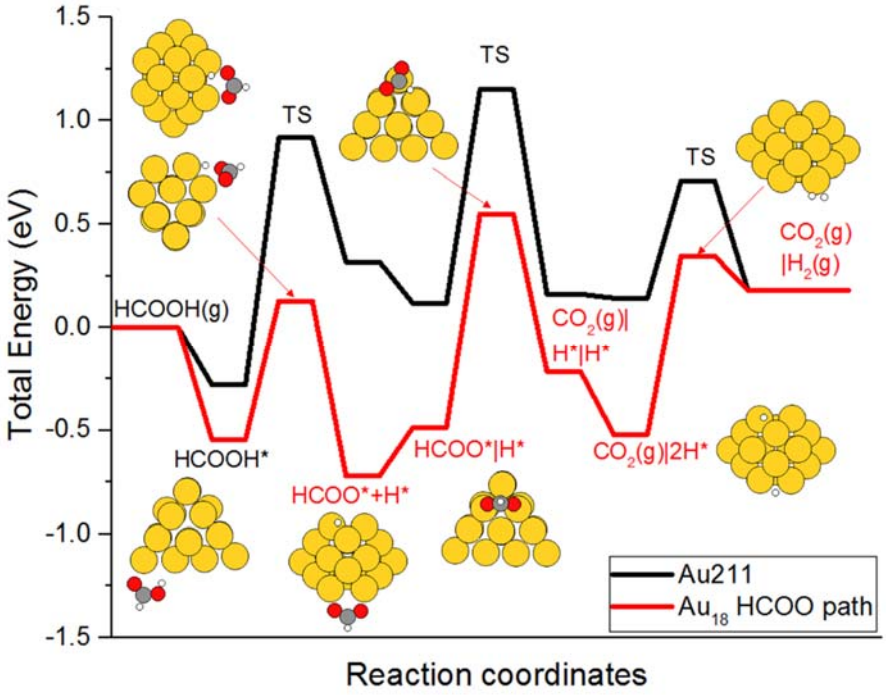


**Figure 4-11** Potential energy surface of HCOOH decomposition through the HCOO path on $Au_{18}$. PES for Au(211) is shown in black line for comparison.

On $Au_{18}$, since it is an even-numbered gold cluster, there is modest attractive interaction between co-adsorbed HCOO and H, and co-adsorbed H atoms. And similar as all the other clusters that have been discussed, $Au_{18}$ is a more active model than Au(211) for HCOOH decomposition due

to the low-lying PES compared with Au(211). $Au_{18}$ exposes two $Au_3$ sites with CN of 5, which are also the preferred sites for adsorption and reaction on $Au_{18}$ (see **Figure 4-11**).

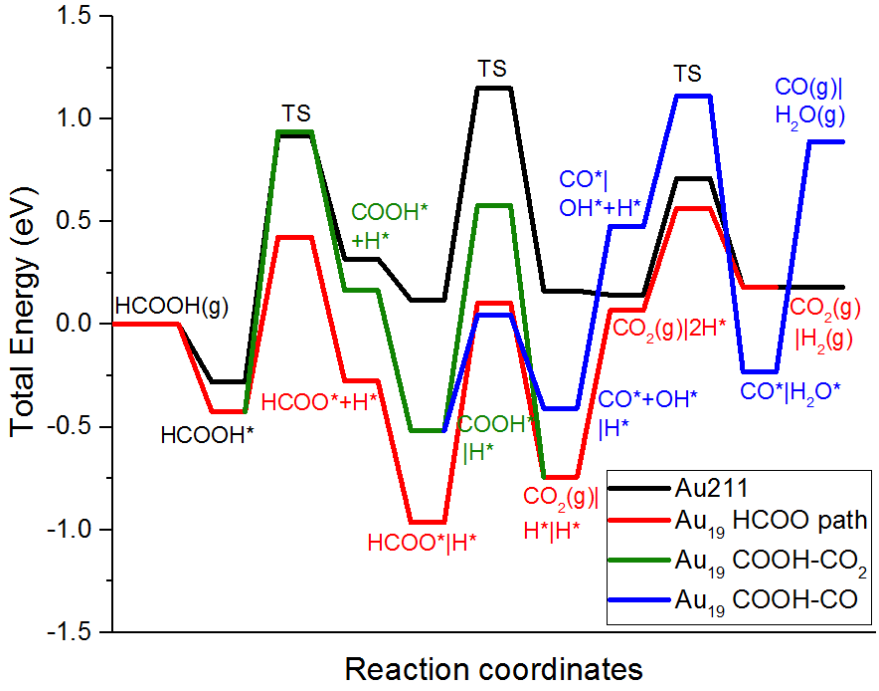


**Figure 4-12** Potential energy surface of HCOOH decomposition through the HCOO path (red line), COOH path leading to $CO_2$ formation (COOH-$CO_2$ path; green line) and COOH path leading to CO formation (COOH-CO path; blue line) on $Au_{19}$. PES for Au(211) is shown in black line for comparison.

On $Au_{19}$, similar as on $Au_{18}$, due to the difficulty in COOH formation from HCOOH (**Figure 4-12**), which has a barrier of 0.51 eV higher than the alternative decomposition of HCOOH to HCOO, HCOO pathway is the preferred decomposition path for HCOOH. $Au_{19}$ is more active than Au(211) for HCOOH decomposition, and the active site on $Au_{19}$ is the triangular $Au_3$ site (see **Figure 4-13**) with CN of 5, similar as on $Au_{17}$ and $Au_{18}$.

From the above discussions, all six gold clusters ($Au_4$, $Au_5$, $Au_7$, $Au_{17}$-$Au_{19}$) on which the complete catalytic cycle of HCOOH decomposition is examined are more active than Au(211) for the reaction, which proceeds preferentially through the HCOO-mediated pathway, same as on

extended surfaces of Au (Au(111), Au(100) and Au(211)). But to determine which of the clusters represent the active site of Au catalysts used in experiments for HCOOH decomposition, a microkinetic analysis is needed to compare the DFT results with the experimental results, which will be presented in the next section.

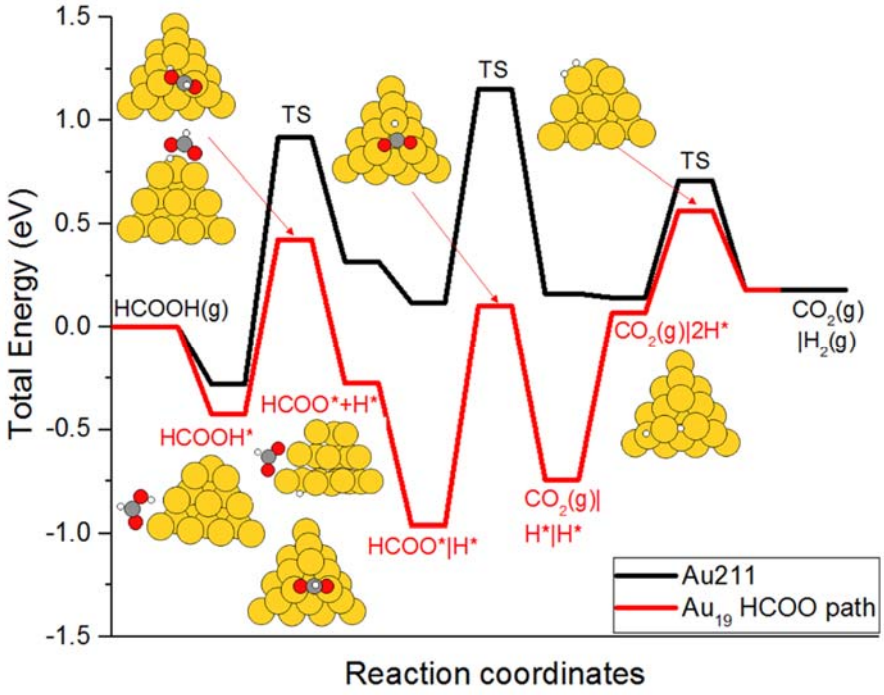


**Figure 4-13** Potential energy surface of HCOOH decomposition through the HCOO path on $Au_{19}$. PES for Au(211) is shown in black line for comparison.

### 4.3.5 Microkinetic modeling results

The experimental data to be fitted in the model is the same set as that given in Chapter 3. DFT results on each of the six clusters just discussed serve as the input to the microkinetic model. By making adjustments to the DFT obtained results, we could get a good fit with the experimental results (with mean absolute errors less than 15%). Adjustments needed on the six clusters are summarized in **Table 4-5** together with the surface coverage predicted from the model after adopting these adjustments.

In general, destabilization in H binding is needed in all clusters except for $Au_{18}$ to obtain a good fit with the experimental results, especially on $Au_5$ and $Au_7$, where H has to be destabilized by 0.62 eV and 0.81 eV (representing the largest adjustment needed on the two clusters), which confirms our earlier hypothesis that a H-covered surface is expected for $Au_5$ and $Au_7$, with H recombination being the rate limiting step. On $Au_4$, H has to be destabilized by 0.41 eV, while the TS of HCOO decomposition is stabilized by 0.51 eV, which is the largest adjustment needed on $Au_4$. On $Au_{17}$ ─ $Au_{19}$, a stabilization of ca. 0.1-0.4 eV is required for the TSs of the three elementary steps to obtain a good fit and the adjustments required are much smaller than those needed the three smaller clusters $Au_4$, $Au_5$ and $Au_7$, which are less likely to be the active site for HCOOH decomposition as a result. On all clusters, the surface is expected to be covered by up to 0.58 ML of HCOO except for $Au_4$, which is covered by 0.04-0.40 ML of HCOOH resulting from the particularly strong binding of HCOOH (BE is -1.02 eV). H is predicted to occupy less than 0.01 ML of the surface sites on all clusters.

**Table 4-5** Adjustments needed in DFT derived BE (ΔBE) of the intermediates and transition state energy (ΔETS) of the elementary steps on $Au_4$, $Au_5$, $Au_7$ and $Au_{17}$-$Au_{19}$ corresponding to the best fit and the model predicted surface coverage.

| Adjustments (eV) | $Au_4$ | $Au_5$ | $Au_7$ | $Au_{17}$ | $Au_{18}$ | $Au_{19}$ |
|---|---|---|---|---|---|---|
| ΔBE(HCOOH) | 0.10 | | 0.57 | | | |
| ΔBE(HCOO) | -0.15 | | -0.02 | -0.09 | -0.10 | -0.10 |
| ΔBE(H) | 0.41 | 0.62 | 0.81 | 0.22 | | 0.32 |
| ΔETS(HCOOH→HCOO+H) | | -0.15 | -0.28 | -0.36 | -0.16 | -0.33 |
| ΔETS(HCOO→$CO_2$+H) | -0.51 | -0.32 | | -0.41 | -0.29 | -0.21 |
| ΔETS(H+H→$H_2$) | | -0.21 | | -0.21 | -0.05 | -0.43 |
| Surface coverage (ML) | | | | | | |
| θ(H) | 0.00 | <0.01 | <0.01 | <0.01 | 0.00 | <0.01 |
| θ(HCOO) | 0.00 | 0.10-0.58 | 0.11-0.50 | 0.06-0.34 | 0-0.1 | 0.1-0.5 |
| θ(HCOOH) | 0.04-0.40 | 0.00 | 0.00 | 0.00 | 0.00 | 0.00 |

Among the six Au clusters, $Au_{18}$ seems to be the most promising cluster model for the active sites of HCOOH decomposition, seen from the smallest adjustment required to obtain a good fit. On $Au_{18}$, the largest adjustment needed is for the TS of HCOO decomposition, which is stabilized by 0.29 eV, while all the other adjustments made are smaller than 0.2 eV and can be attributed to the errors in our DFT calculations. While the 0.29 eV stabilization on the TS of HCOO decomposition outreaches the error bar in DFT calculations, van der Waals' interactions is overlooked the current calculations. We further calculated the BE of HCOO on $Au_{18}$ by including van der Waals' interactions, and found a stronger binding by 0.22 eV, which will bring a stabilization of about the same amount to the TS of HCOO decomposition. Thus, by taking into account the van der Waals' interactions, TS of HCOO decomposition only requires a stabilization of 0.07 eV, which can now be attributed to the DFT errors. Same arguments might be made also on $Au_{17}$ and $Au_{19}$ for the TSs since the adjustment needed for these two clusters are close to those on $Au_{18}$, but on these two clusters H binding should be weakened by 0.2-0.3 eV, whereas van der Waals' interactions will contribute to a stronger binding of H (by 0.17 eV on $Au_{18}$, and similar values are expected on $Au_{17}$ and $Au_{19}$), which leads to an even larger adjustment required for the H binding.

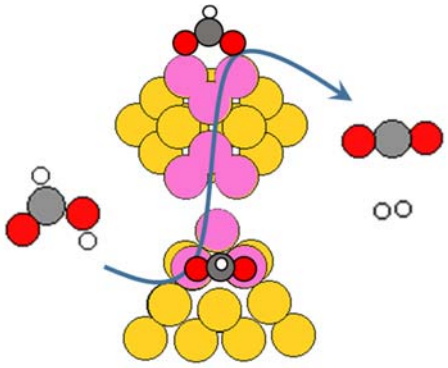

**Figure 4-14** Schematic illustration of the HCOOH decomposition process on $Au_{18}$. Au, C, O and H atoms are represented by the yellow, grey, red and white circles. The triangular $Au_3$ site on $Au_{18}$ is indicated by the pink circles.

Thus, based on the microkinetic modeling results, $Au_{18}$ is found to be the active site for HCOOH decomposition as a good fit to the experimental results can be obtained by adjusting the DFT

derived results by small amounts, which can be attributed to errors in our DFT calculations. On $Au_{18}$, HCOOH decomposes through the HCOO intermediate at the triangular $Au_3$ site where CN=5 is found for the Au atoms (**Figure 4-14**). $Au_{17}$ and $Au_{19}$, though have the similar $Au_3$ site, are not accurate representations of the active site based on the fitting results from the microkinetic model.

### 4.4 Conclusions

*Ab initio* molecular dynamics simulations were performed for sub-nanometer gold clusters (up to $Au_{25}$ with a size of 0.85 nm) to determine their most stable structures, on which the formic acid decomposition reaction was systematically studied using DFT calculations and compared with the experimental results in a microkinetic modeling analysis to identify the active site for this reaction.

The DFT results suggest that planar structures are preferred for small-sized gold particles and the 2D-to-3D transition takes place at $Au_{17}$. An odd-even oscillation feature is seen for the differential binding energy of Au in $Au_n$ clusters and also the binding energies of intermediates which are not closed-shell species, such as H and HCOO, as a result of the electron pairing effect. Odd-numbered Au clusters binds these two intermediates more strongly than their neighboring even-numbered Au clusters. As a result, strongly repulsive interactions between H and HCOO (or H) are observed on odd-numbered Au clusters while the interactions are attractive on even-numbered clusters. All the clusters being investigated show a stronger binding for the intermediates than Au(211), except a few, $Au_6$, $Au_8$ and $Au_{20}$, due to the high stabilities resulted from the nice symmetries seen in their structures. This is a first indication that sub-nanometer gold clusters might be more active than Au(211) and hence the active site for HCOOH decomposition.

HCOOH dehydrogenation, as the first step in formic acid decomposition, was studied on $Au_4$-$Au_{25}$. Based on the comparison of the activation energies of this step with that on Au(211) surface, a

subset of the clusters were screened out for further studies, namely $Au_4$, $Au_5$, $Au_7$ and $Au_{17}$-$Au_{19}$. A comprehensive investigation of the elementary reactions on these six clusters was then conducted, including not only the HCOO mediated route suggested as the preferred pathway by previous studies, but also the COOH mediated route. It turned out that on all six clusters, HCOO pathway is much more favorable than the COOH pathway.

A mean-field microkinetic model was used to fit the DFT derived BEs of the intermediates and activation energies of the elementary steps on the six gold clusters to obtain the same reaction rate as that measured in experiments. The fitting results suggest that among the six gold clusters, $Au_{18}$ is the most accurate representation of the active site for HCOOH decomposition, since only small adjustments within the DFT calculation errors are required for the DFT derived parameter values on $Au_{18}$ in order to obtain a good fit with the experimental data. On $Au_{18}$, the reaction proceeds via the HCOO intermediate on a triangular $Au_3$ site with a coordination number of 5 for the Au atoms. Although the same $Au_3$ site also presents at $Au_{17}$ and $Au_{19}$, the large adjustments needed in fitting the experimental rates imply they are not active site models for the reaction. Hence, we show an atom-by-atom size-sensitivity of the catalytic properties of sub-nanometer gold particles for HCOOH decomposition.

## 4.5 Supplementary material

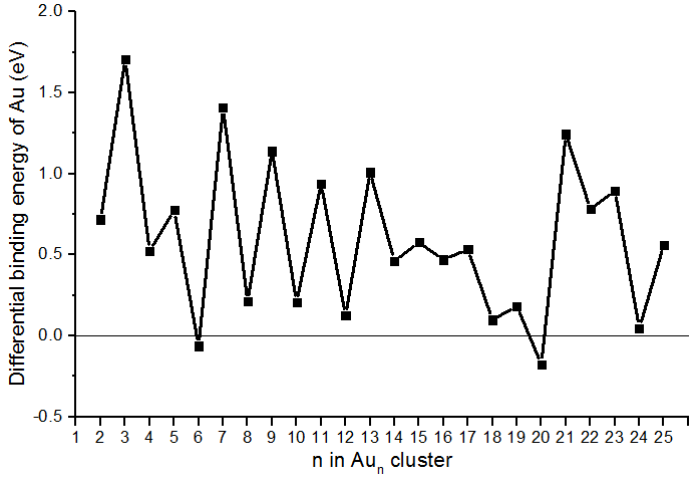


**Figure 4S-1** Differential binding energy (dBE) of Au in $Au_n$ (n=2-25) clusters using Au atom in the bulk as the energy reference. dBE = $E(Au_n) - E(Au_{n-1}) - E(Au_{bulk})$.

**Table 4S-1** Binding energies of H, COOH, HCOO and HCOOH on $Au_n$ (n=2-25) clusters.

| | BE(H) | BE(COOH) | BE(HCOO) | BE(HCOOH) |
|---|---|---|---|---|
| $Au_4$ | -2.39 | -2.11 | -2.72 | -1.02 |
| $Au_5$ | -3.23 | -2.58 | -3.61 | -0.58 |
| $Au_6$ | -1.77 | -1.55 | -1.92 | -0.54 |
| $Au_7$ | -3.31 | -2.52 | -3.00 | -0.65 |
| $Au_8$ | -1.93 | -1.68 | -2.10 | -0.58 |
| $Au_9$ | -2.90 | -2.59 | -3.16 | -0.60 |
| $Au_{10}$ | -2.23 | -1.73 | -2.47 | -0.47 |
| $Au_{11}$ | -2.76 | -2.45 | -3.00 | -0.57 |
| $Au_{12}$ | -2.23 | -1.73 | -2.49 | -0.43 |
| $Au_{13}$ | -2.80 | -2.26 | -3.01 | -0.47 |
| $Au_{14}$ | -2.38 | -1.85 | -2.49 | -0.62 |
| $Au_{15}$ | -2.77 | -2.22 | -2.87 | -0.46 |
| $Au_{16}$ | -2.62 | -1.93 | -2.71 | -0.57 |
| $Au_{17}$ | -2.76 | -2.18 | -2.82 | -0.50 |
| $Au_{18}$ | -2.45 | -1.87 | -2.81 | -0.54 |
| $Au_{19}$ | -2.71 | -2.19 | -3.03 | -0.42 |
| $Au_{20}$ | -1.74 | -1.47 | -1.95 | -0.42 |
| $Au_{21}$ | -2.85 | -2.42 | -2.94 | -0.44 |
| $Au_{22}$ | -2.41 | -2.04 | -2.71 | -0.42 |
| $Au_{23}$ | -2.94 | -2.68 | -3.25 | -0.71 |
| $Au_{24}$ | -2.19 | -1.68 | -2.74 | -0.49 |
| $Au_{25}$ | -2.74 | -2.04 | -2.78 | -0.46 |

| | | | | |
|---|---|---|---|---|
| Au(211) | -2.26 | -1.63 | -2.31 | -0.27 |

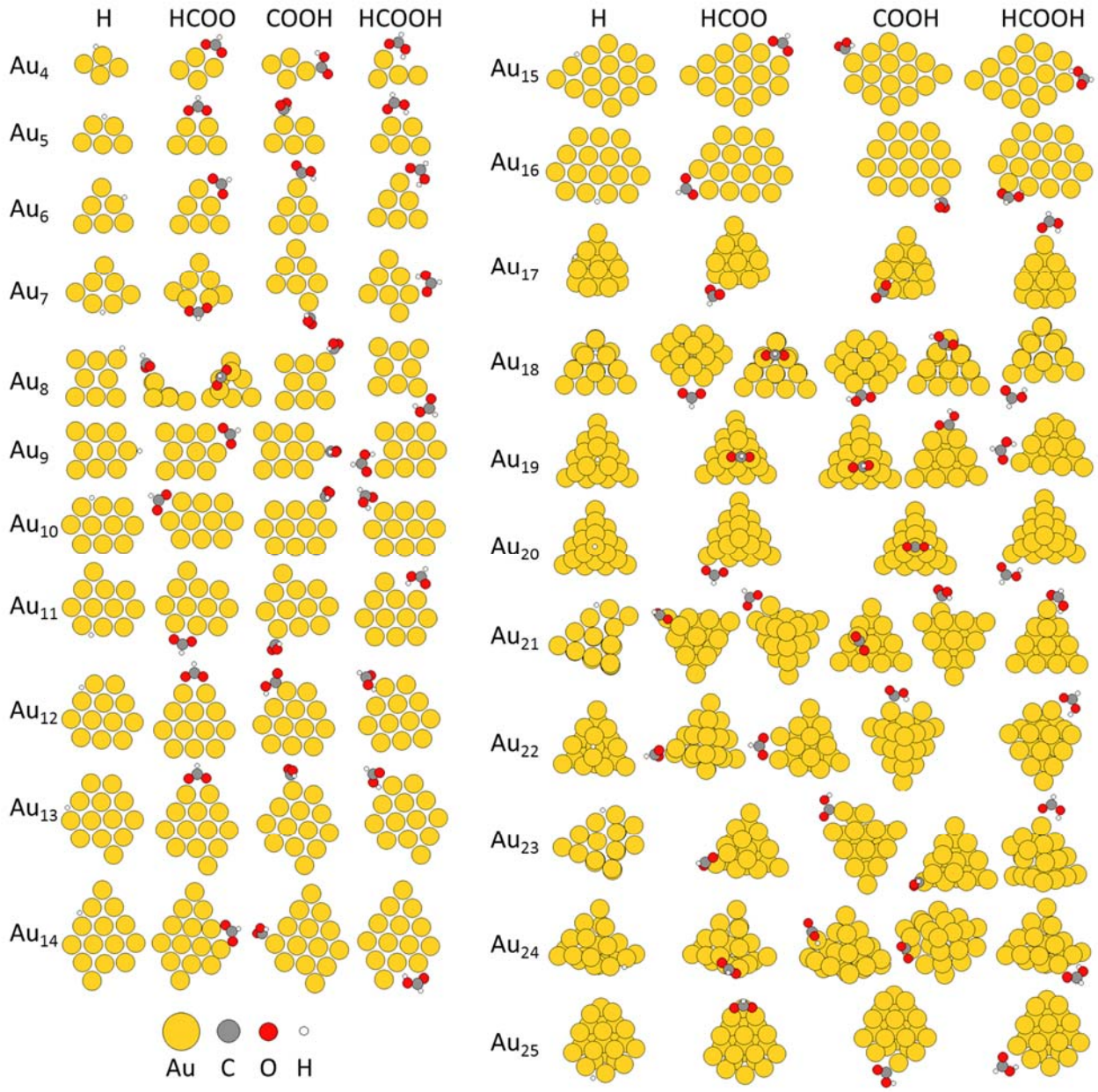


**Figure 4S-2** Most stable configurations of H, HCOO, COOH and HCOOH on $Au_n$ (n=4-25) clusters.

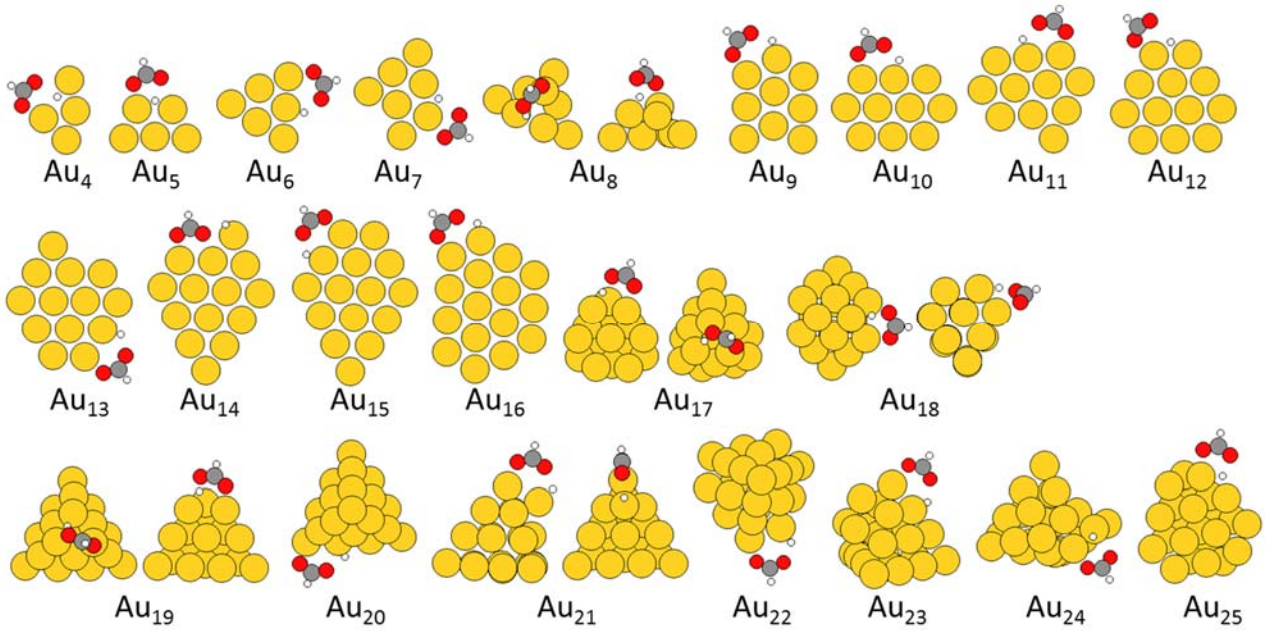


**Figure 4S-3** Transition state configurations found in the minimum energy path for HCOOH dehydrogenation to HCOO on $Au_n$ (n=4-25) clusters.

# Chapter 5 Formic Acid Decomposition on Pd Catalysts†

## 5.1 Introduction

Formic acid (HCOOH) is an equimolar byproduct during the conversion of 5-hydroxy-methyl furfural (HMF) to levulinic acid and catalytic decomposition of HCOOH into hydrogen is an attractive method of utilizing this byproduct and also providing in-situ hydrogen for further hydrogenation processes in biomass upgrading.[15, 17] In addition, as an energy source, HCOOH has been used in direct formic acid fuel cells (DFAFC).[66, 171, 172] Obtaining a fundamental mechanistic understanding of HCOOH decomposition on transition metal surfaces would also shed light on the electro-oxidation of HCOOH.

Palladium is one the most active transition metals for gas-phase HCOOH decomposition and it is also widely employed as the anode material in DFAFC.[173-175] Despite the large amount of experimental[49, 176-181] and theoretical[176, 182-186] studies of this reaction on Pd catalysts, there is still a lack of consensus about the reaction mechanism, including the most favorable reaction pathway, active surface intermediates and their coverages on the surface, as well as the active site. Though the formate[187 188](HCOO) intermediate has been identified on oxygen-dosed Pd(100) and clean Pd(111) surface, decomposition through the carboxyl (COOH) intermediate is still possible because the selectivity to $H_2$ and $CO_2$ is not 100% in all experimental studies and there is some amount of CO produced, indicating the contributions from the COOH pathway since as we will show in this study that COOH is the only source possible source for CO production. CO once formed, becomes a poison species to Pd catalysts. In this study, DFT calculations were performed on both (100) and (111) facets of Pd by examining a complete reaction network comprising of 29

†, Calculations on clean Pd(111) and Pd(100) were performed by J. Scaranto; calculations on CO-covered Pd(100) were performed by S. Rangarajan.

elementary steps and 13 surface intermediates to evaluate the structure sensitivity of the reaction and determine the most favorable decomposition path among this large reaction network. As CO is a poisoning species to Pd catalysts, CO coverage effects on the reaction energetics and reaction pathway were also studied by repeating the calculations on 5/9 ML of CO covered Pd(111) and Pd(100) surfaces.

### 5.2 Computational methods

All DFT calculations were performed with DACAPO code. Pd(111) surface was modeled by a 3-atomic layers slab using a (3 × 3) unit cell, while Pd(100) surface was modeled with by a 4-atomic layers slab with a (3 × 3) unit cell, corresponding to a surface coverage of 1/9 ML for each adsorbate. All three layers in the (111) slab were fixed during the calculations, while the two layers of the (100) slab were allowed to relax during the calculations. Surface Brillouin zone of the (111) slab was sampled at 6 special Chadi-Cohen k-points, while that for the (100) slab was sampled using a 4×4×1 Monkhorst-Pack k-point mesh. Other computational details are the same as those used for the studies on Au catalysts, and can be found in Chapter 3.

### 5.3 Results and discussion

We studied formic acid decomposition on the (111) and (100) facets of Pd catalysts. Dependence of the reaction pathways and energetics on the surface structure was explored by comparing the results obtained on the two facets. Since the Pd catalysts used in experiments are found to be covered by CO, CO coverage effects on the BE of key intermediates (COOH, HCOO, CO and H) were investigated and the reaction was also studied CO covered Pd catalysts, using 5/9ML of CO covered Pd(111) and Pd(100) as the model surfaces. Effect of spectator CO molecules on the

reaction pathways and energetics was discussed from comparison of the clean surfaces with the CO-covered surfaces.

### 5.3.1 Results on clean Pd(111) surface

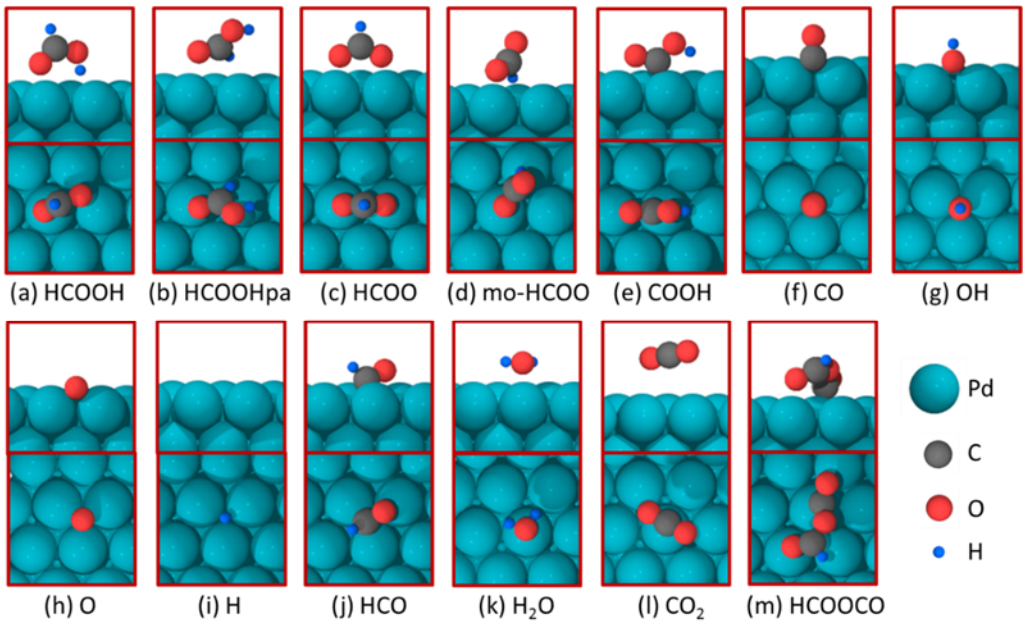


**Figure 5-1** Side and top views of the most stable configurations of intermediates on Pd(111). Palladium, carbon, hydrogen and oxygen atoms are indicated in dark green, dark grey, blue and red, respectively.

For the clean Pd(111) surface, a reaction network comprised of 29 elementary steps and 13 intermediates was proposed for investigation. The most stable configurations of the adsorbates on clean Pd(111) surface were shown in **Figure 5-1**, with their corresponding binding energies (BE) given in **Table 5-1**.

On Pd(111), formic acid (HCOOH, by default denotes the most stable perpendicular formic acid) prefers a trans-perpendicular configuration, which binds through its carbonyl O atom on the top site while the O-H bond is pointing down towards a bridge site on the surface and the C-H bond is pointing upward. The molecular plane of HCOOH is perpendicular to the surface with a BE of -

0.41 eV. A less stable configuration of formic acid is the cis-parallel one, where the molecular plane is almost parallel to the surface, and it binds through the HCO fragment with a very weak binding energy of -0.03 eV.

**Table 5-1** Calculated PW91 binding energies (BE) at their preferred adsorption site on Pd(111) and Pd(100).

| **Species** | **Pd(111)** | | **Pd(100)** | |
|---|---|---|---|---|
| | **adsorption site** | **BE / eV** | **adsorption site** | **BE / eV** |
| HCOOH* | top-bridge | -0.41 | top-hollow | -0.50 |
| HCOOHpa* | top-bridge | -0.03 | top-top | -0.19 |
| HCOO* | top-top | -2.34 | top-top | -2.54 |
| mo-HCOO* | top-top | -1.59 | top-top | -1.76 |
| COOH* | top-top | -2.22 | bridge-bridge | -2.50 |
| CO* | fcc | -1.99 | bridge | -2.03 |
| OH* | fcc | -2.16 | hollow | -2.54 |
| O* | fcc | -3.73 | hollow | -3.88 |
| H* | fcc | -2.83 | hollow | -2.78 |
| HCO* | bridge | -2.25 | bridge-bridge | -2.63 |
| $H_2O$* | top | -0.31 | top | -0.23 |
| $CO_2$* | physisorbed | -0.05 | physisorbed | -0.07 |
| HCOOCO* | top-bridge-top | -2.47 | -- | -- |

Formate (HCOO, by default indicates the bidentate formate) prefers a bidentate structure with both O atoms bound to surface on two top sites and the C-H bond is pointing upward; BE of HCOO is -2.34 eV. A less stable configuration of formate binds the surface through one O atom and the CH group on two top sites, and the C-H bond is pointing towards the surface; mo-HCOO will be used to represent this configuration. With a BE of -1.59 eV, mo-HCOO is much less stable than bidentate formate, by 0.75 eV. Being an isomer of formate, carboxyl (COOH) binds to the top-top site of the surface through its C and O atom, with O-H bond pointing downward; BE of COOH is -2.22 eV.

Carbon monoxide (CO), hydroxyl (OH), oxygen (O) and hydrogen (H) all bind strongly to the fcc site, while formyl (HCO) prefers the bridge site and $H_2O$ binds weakly on the top site with a BE of -0.31 eV. $CO_2$ is physisorbed on the surface with the same linear geometry in the gas phase; BE of $CO_2$ is -0.05 eV. HCOOCO binds through its carbonyl C atom and the O atom from the HCO end to two top sites; it has a BE of -2.47 eV.

**Table 5-2** PW91 reaction energies (ΔE) and activation energy barriers (Ea) for the elementary steps considered in the HCOOH decomposition reaction network on Pd(111) and Pd(100) . All the values are relative to the infinite separation initial/final state.

| # | Reaction | Pd(111) | | Pd(100) | |
|---|---|---|---|---|---|
| | | **$E_a$ / eV** | **ΔE / eV** | **$E_a$ / eV** | **ΔE / eV** |
| 1 | HCOOH + * ↔ HCOOH* | | -0.41 | | -0.50 |
| 2 | HCOOH* + * ↔ HCOO* + H* | 0.60 | -0.08 | 0.63 | -0.14 |
| 3 | HCOOH* ↔ HCOOHpa* | 0.71 | 0.38 | 0.84 | 0.31 |
| 4 | HCOOHpa* + * ↔ COOH* + H* | 0.34 | -0.60 | 0.11 | -0.67 |
| 5 | HCOOHpa* + * ↔ HCO* + OH* | 0.93 | 0.62 | 0.76 | 0.04 |
| 6 | HCOO* ↔ mo-HCOO* | 0.93 | 0.76 | 0.81 | 0.78 |
| 7 | mo-HCOO* + * ↔ $CO_2$* + H* | 0.00 | -1.21 | 0.00 | -1.00 |
| 8 | HCOO* + O* ↔ $CO_2$* + OH* | 1.44 | -0.66 | -- | -- |
| 9 | HCOO* + OH* ↔ $CO_2$* + $H_2O$* | 1.24 | -1.00 | -- | -- |
| 10 | HCOO* + H* ↔ $H_2$ + $CO_2$* + * | 1.66 | 0.64 | 1.59 | 0.78 |
| 11 | HCOO* + CO* ↔ HCOOCO* + * | 1.61 | 1.51 | -- | -- |
| 12 | HCOOCO* + * ↔ HCO* + $CO_2$* | 0.08 | -0.72 | -- | -- |
| 13 | HCOO* + * ↔ HCO* + O* | 1.95 | 1.30 | -- | 0.97 |
| 14 | COOH* + * ↔ $CO_2$* + H* | 0.70 | -0.31 | 0.89 | 0.00 |
| 15 | COOH* + * ↔ CO* + OH* | 0.80 | -0.02 | 0.66 | -0.15 |
| 16[a] | COOH* + O* ↔ $CO_2$* + OH* | -0.08 | -0.53 | 0.32 | -0.48 |
| 17[a] | COOH* + OH* ↔ $CO_2$* + $H_2O$* | -0.12 | -0.86 | -0.43 | -0.14 |
| 18 | COOH* + H* ↔ CO* + $H_2O$* | 1.40 | -0.56 | 1.27 | -0.29 |
| 19 | COOH* + CO* ↔ HCO* + $CO_2$* | 1.54 | 0.93 | -- | 0.86 |
| 20 | HCOO* + COOH* ↔ HCOOHpa* + $CO_2$* | 0.44 | -0.23 | 0.49 | 0.14 |
| 21 | HCO* + * ↔ CO* + H* | 0.14 | -1.24 | 0.24 | -0.86 |
| 22 | CO* + O* ↔ $CO_2$* + * | 1.42 | -0.51 | 0.71 | -0.34 |

| | | | | | |
|---|---|---|---|---|---|
| 23 | OH* + * ↔ O* + H* | 1.42 | 0.21 | 1.11 | 0.48 |
| 24[a] | 2OH* ↔ $H_2O$* + O* | -0.15 | -0.34 | 0.16 | 0.34 |
| 25 | OH* + H* ↔ $H_2O$* + * | 0.59 | -0.55 | 0.65 | -0.14 |
| 26 | 2H* ↔ $H_2$ + 2* | 1.09 | 1.09 | 1.00 | 1.00 |
| 27 | $CO_2$* ↔ $CO_2$ + * | | 0.05 | | 0.07 |
| 28 | $H_2O$* ↔ $H_2O$ + * | | 0.31 | | 0.23 |
| 29 | CO* ↔ CO + * | | 1.99 | | 2.03 |
| a, these reactions have negative Ea or Ea values that are less positive than the ΔEs, this is because the initial sate used is the adsorbates at infinite separation state, and when they are coadsorbed on the surface, an attractive interaction is observed. | | | | | |

Activation energies and reaction energies of the 29 elementary steps explored on Pd(111) are summarized in **Table 5-2**. HCOOH can decompose via three routes ─ HCOO route, COOH route and HCO route ─ through reactions 2-5 in **Table 5-2**. HCOOH decomposition to HCOO starts from the most stable configuration of formic acid, and it is a slightly exothermic reaction (ΔE = -0.08 eV) with a barrier of 0.60 eV. HCOOH decomposition to COOH is a two-step reaction, during which HCOOH first goes through a transformation step and forms HCOOHpa, and then breaks the C-H bond. The first step is endothermic by 0.38 eV with a barrier of 0.71 eV, while the second step is exothermic by 0.60 eV with a barrier of 0.34 eV. So the overall barrier for COOH formation from HCOOH is 0.72 eV, which is 0.12 eV higher than HCOO formation from HCOOH. HCOOH decomposition to HCO is also a two-step reaction which requires the same transformation step in COOH formation and an additional C-O bond breaking step. The C-O bond breaking step in HCOOHpa is an endothermic reaction with an activation energy of 0.93 eV. So the overall activation energy for HCO formation from HCOOH is 1.31 eV, which is 0.71 eV and 0.59 eV higher than the barrier required for HCOO and COOH formation from HCOOH, respectively. Due to the huge activation energy required for HCO formation, HCOOH is not likely to go through the HCO route.

Further decomposition of HCOO and COOH can proceed directly by breaking the C-H, O-H or C-O bond, or by reacting with other adsorbates on the surface, such as CO, OH, O and H. For HCOO, since the C-H bond is pointing upward, breaking the C-H bond requires HCOO first transforms to mo-HOO, which has a configuration that the C-H bond is readily broken. Transformation of HCOO has a barrier of 0.93 eV, while the bond breaking step in moHCOO is spontaneous. C-O bond breaking in HCOO forms HCO and O, it is a highly endothermic reaction ($\Delta E$=1.30 eV) with and activation energy of 1.95 eV, which is 1.02 eV higher than the barrier required for C-H bond breaking in HCOO. Thus for the direct decomposition of HCOO, it will preferentially go through the dehydrogenation route and form $CO_2$ and H. The reactions of HCOO with other adsorbates (reactions 8-12 in **Table 5-2**) all have a much higher activation energy than the direct decomposition of HCOO to $CO_2$. OH-assisted HCOO decomposition has the lowest activation energy among these reactions, 1.24 eV, which is still 0.31 eV higher than the direct decomposition to $CO_2$, leading to a lower reaction rate by 3-4 orders of magnitude under a reaction temperature of 100 °C. So HCOO prefers to decompose directly to form $CO_2$ and H, rather than react with other adsorbates, such as O, OH, O and CO.

Direct decomposition of COOH forms $CO_2$ and H or CO and OH. $CO_2$ and H formation from COOH has an activation energy of 0.70 eV, which is 0.10 eV lower than the activation energy for CO and OH formation. H- and CO-assisted COOH decomposition are energetically more difficult than the direct decomposition of COOH, while O- and OH-assisted COOH decomposition are spontaneous on Pd(111). The reaction of COOH and HCOO is also an easy step with a barrier of 0.44 eV, forming HCOOHpa and $CO_2$.

In the current reaction network, HCO can be formed from several reactions: C-O bond breaking in HCOOH, C-O bond breaking in HCOO, CO-assisted HCOO decomposition, and CO-assisted

COOH decomposition. But due to the huge reaction barriers, all these reactions are far less favorable than their alternatives, thus HCO is less likely to be formed during HCOOH decomposition, which will proceed through either the COOH pathway or the HCOO pathway. In **Figure 5-2**, the potential energy surface for the COOH and HCOO pathways comprised of only direct decomposition steps is drawn.

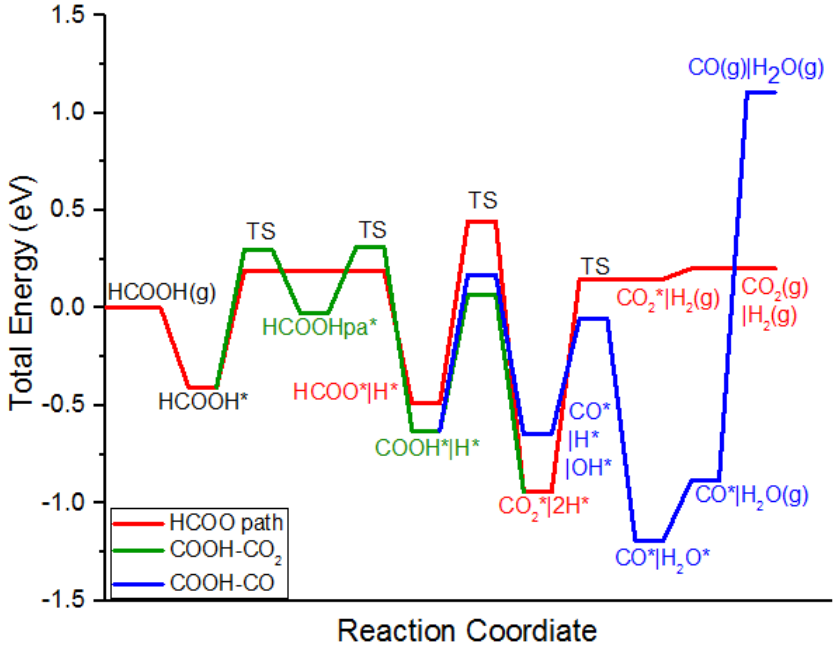


**Figure 5-2** Potential energy surface of HCOOH decomposition on Pd(111). Red line is the HCOO pathway, green line is the COOH pathway leading to $CO_2$ formation (COOH-$CO_2$ pathway) and blue line is the COOH pathway leading to CO formation (COOH-CO pathway).

It can be seen from **Figure 5-2** that COOH formation is slightly more difficult than HCOO formation, while COOH decomposition is more favorable than HCOO decomposition. The highest TS in HCOO pathway is 0.13 eV higher in energy than the highest TS in COOH pathway, leading to slightly higher contribution of the COOH pathway to the overall reaction based on the DFT results only. And the formed COOH preferentially decomposes to $CO_2$ rather than CO.

### 5.3.2 Results on clean Pd(100) surface

The most stable configurations of the intermediates on clean Pd(100) surface are shown in **Figure 5-3** with the corresponding BEs summarized in **Table 5-1**. On clean Pd(100) surface, HCOOH, HCOOHpa, HCOO and mo-HCOO have similar adsorption configurations as those on clean Pd(111) surface, but binding of these species on the open facet is generally 0.1-0.2 eV stronger than that on the closed facet. COOH and HCO bind through their C and O atoms on the bridge-bridge site, with BEs of -2.50 eV and -2.63 eV, respectively. CO prefers the bridge site with a BE of -2.03 eV, while OH, O and H bind preferentially to the hollow site. $H_2O$ prefers the top site with a BE of -0.23 eV, which is 0.08 eV weaker than its binding on the closed facet. Similar as on Pd(111), $CO_2$ is also physisorbed on Pd(100) with a BE of -0.07 eV.

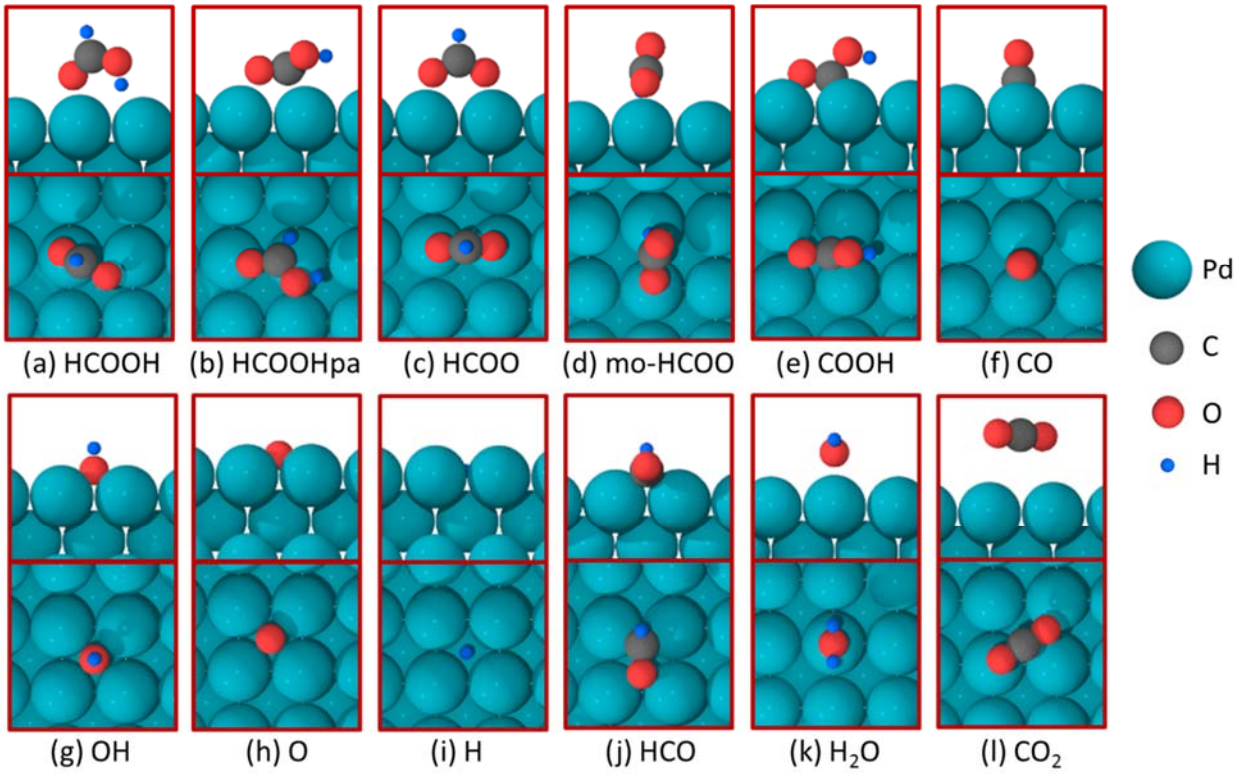


**Figure 5-3** Side and top views of the most stable configurations of intermediates on Pd(100). Palladium, carbon, hydrogen and oxygen atoms are indicated in dark green, dark grey, blue and red, respectively.

Comparing the BEs of the intermediates on the two facets, we can find that except for H and $H_2O$, all the other species bind more strongly on the open (100) facet than on the closed (111) facet of Pd(111), with OH and HCO being two species that are most sensitive to the surface structure with 0.38 eV of stabilization on the open facet.

HCOOH decomposition to HCOO on Pd(100) surface has a barrier of 0.63 eV, similar to the barrier 0.60 eV on Pd(111) surface. HCOOH decomposition to COOH and HCO also require a first transformation step of HCOOH which has an activation energy of 0.84 eV and a reaction energy of 0.31eV, before breaking the C-H or C-O bond with an activation energy of 0.11 eV and 0.76 eV, respectively. Thus HCOOHpa will preferentially decompose to COOH rather than HCO since a barrier of 0.65 eV higher is required for HCO formation. The overall reaction barrier of COOH is 0.84 eV, which is 0.21 eV higher than the barrier for HCOO formation from HCOOH.

HCOO decomposition to $CO_2$ proceeds through a first transformation of HCOO to moHCOO with an activation energy of 0.81 eV, followed by a spontaneous H-C bond breaking step in moHCOO, which forms $CO_2$ and H. The activation energy for HCOO transformation on Pd(100) is 0.12 eV lower than that on Pd(111). Due to the high activation energies, other decomposition paths for HCOO explored on Pd(111) were not investigated on Pd(100), except for H-assisted HCOO decomposition, which has a barrier of 1.59 eV on Pd(100), much more difficult than the direct decomposition of HCOO to $CO_2$.

COOH decomposition to $CO_2$ has a barrier of 0.89 eV, which is less favorable than its decomposition to CO with a barrier of 0.66 eV on Pd(100). The barrier of the former reaction is 0.19 eV higher than that on Pd(111), while that for the latter reaction is 0.14 eV lower than the barrier on Pd(111) surface. OH and O could facilitate COOH decomposition with barriers of 0 and 0.32 eV, respectively. H-assisted COOH decomposition, similar as the H-assisted HCOO

decomposition, is also a very difficult reaction with a barrier of 1.27 eV on Pd(100). The reaction of COOH and HCOO which forms HCOOH and $CO_2$ requires a similar barrier as on Pd(111), 0.49 eV.

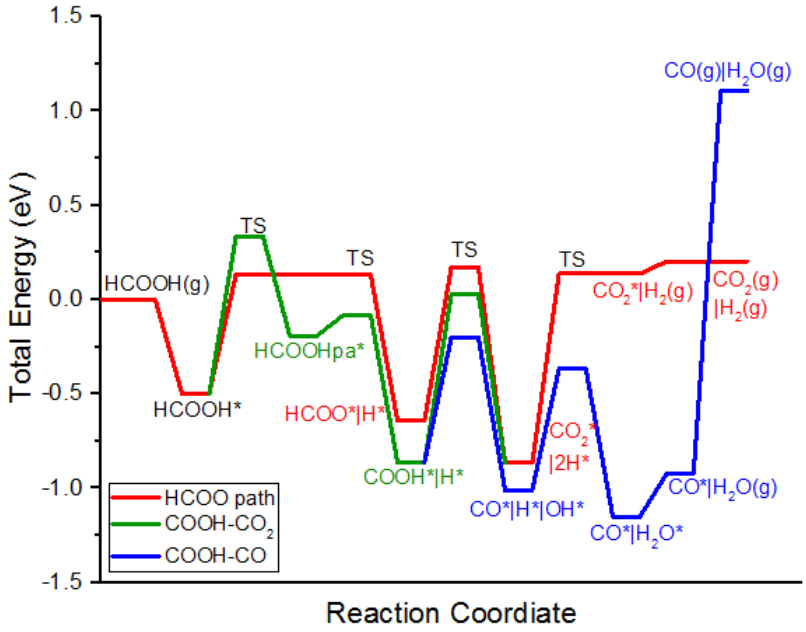


**Figure 5-4** Potential energy surface of HCOOH decomposition on Pd(100). Red line is the HCOO pathway, green line is the COOH pathway leading to $CO_2$ formation (COOH-$CO_2$ pathway) and blue line is the COOH pathway leading to CO formation (COOH-CO pathway).

**Figure 5-4** plots the PES of HCOOH decomposition on Pd(100) through the COOH and HCOO intermediates. It is seen that COOH formation is more difficult than HCOO decomposition, due to the higher barrier needed for the formation of the precursor of COOH formation HCOOHpa, than the O-H bond breaking step of HCOOH which forms HCOO. COOH decomposition, however, is more favorable than HCOO decomposition. And COOH decomposition to $CO_2$ is more favorable than its decomposition to CO on Pd(100) surface, on contrary to that on Pd(111) surface. The highest TS in the COOH pathway is the transformation of HCOOH to HCOOHpa, which is about 0.17 eV higher in energy than the highest TS in the HCOO pathway, HCOO dehydrogenation.

Thus, based on DFT analysis only, on Pd(100) surface contribution of the HCOO pathway to the overall reaction should be higher than the COOH pathway, which is on contrary to that on Pd(111). **Figure 5-5** compares the COOH and HCOO pathway of HCOOH decomposition on the two facets of Pd. It is seen that except for the transformation of HCOOHpa, which has a TS that is 0.06 eV higher on Pd(100) than on Pd(111), TSs of all other steps are stabilized on Pd(100) compared with their corresponding states on Pd(111). Thus Pd(100) should be more active than Pd(111) for HCOOH decomposition.

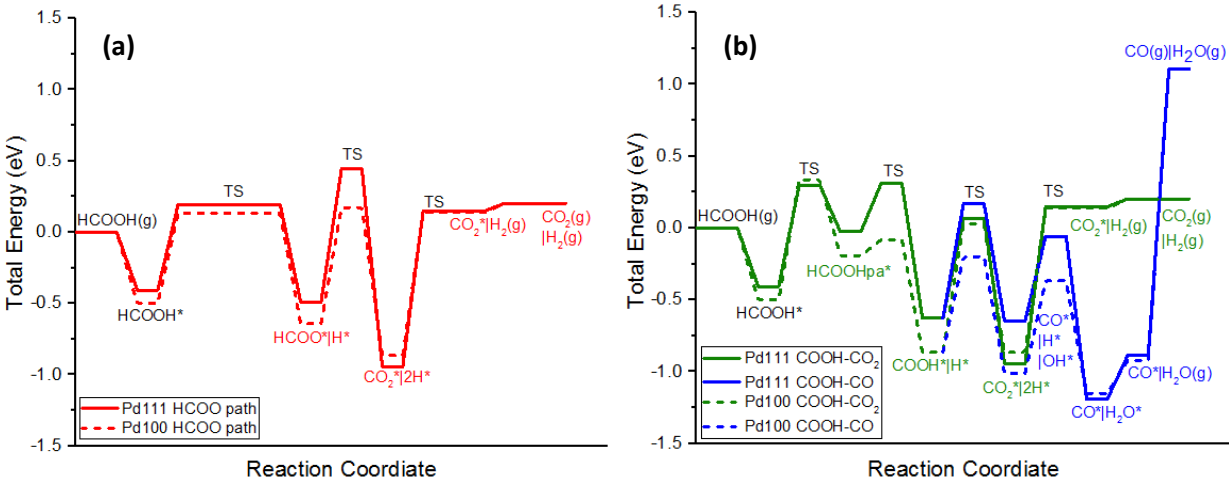


**Figure 5-5** Comparison of the PESs for (a) the HCOO pathway, and (b) the COOH pathway of HCOOH decomposition on Pd(100) and Pd(111). Solid lines are for Pd(111) while dashed lines are for Pd(100). Red color indicates the HCOO pathway, green color indicates the COOH leading to $CO_2$ formation, blue line indicates the COOH pathway leading to CO formation.

### 5.3.3 CO coverage effects on the BEs of key intermediates HCOO, COOH, CO and H

As the Pd catalysts used in the experiments are found to be covered by CO, the CO coverage effects (up to 2/3 ML of CO) on the BE of the key intermediates HCOO, COOH, CO and H were investigated on Pd(111) and Pd(100), and the results are shown in **Figure 5-6** and **Table 5-3**. CO coverage used its binding energy calculations is the total coverage of CO on the surface, including the spectator CO molecules and the one being treated as the adsorbate; BE of CO is calculated in

a differential manner. Pd(100) binds the intermediates more strongly than Pd(111) at all coverages, except for H at CO coverage of 1/9, 5/9 and 2/3 ML, where Pd(111) binds H more strongly than Pd(100) by 0.03 eV, 0.09 eV and 0.06 eV, respectively. For the other intermediates, HCOO, COOH and CO, Pd(100) binds them more strongly than Pd(111) by 0-0.25 eV, 0.10-0.40 eV and 0-0.45 eV, respectively, at CO coverages being explored.

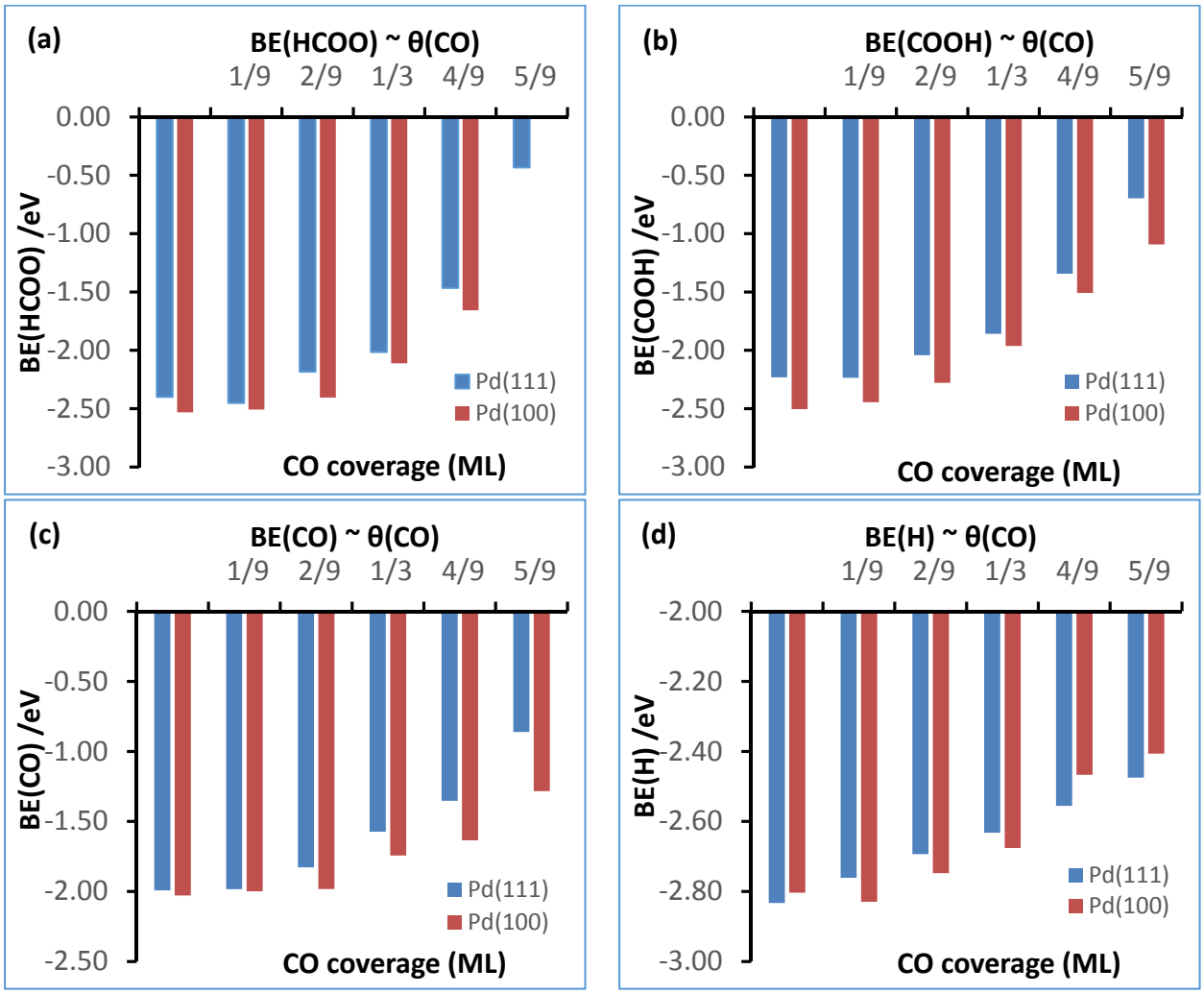


**Figure 5-6** Binding energy (BE) of (a) HCOO, (b) COOH, (c) CO and (d) H as a function of surface coverage of CO. Blue bars indicate BEs on Pd(111) while red bars indicate BEs on Pd(100).

Up to CO coverage of 1/3 ML, there is little variance (less than 0.25 eV) in the binding energies of the three species on both facets, further increase of the CO coverage leads to more dramatic

change in BEs of the intermediates. When CO coverage is increased from 1/3 to 4/9 ML, BE of HCOO decreases by 0.16 eV on Pd(111) and 0.29 eV on Pd(100), which further decreases significantly by 0.55 eV and 0.45 eV on Pd(111) and Pd(100), respectively, when CO coverage is increased to 2/3 ML. For COOH, when CO coverage is increased from 1/3 to 4/9 ML, there is a decrease in its BE of 0.18 eV and 0.32 eV on Pd(111) and Pd(100), respectively, and another significant decrease of 0.53 eV and 0.45 eV on Pd(111) and Pd(100) when CO coverage is increased to 5/9 ML, followed by a further decrease of 0.64 eV and 0.42 eV on Pd(111) and Pd(100), respectively, as CO coverage is increased by another 1/9 ML. For CO, its BE decreases by 0.48 eV and 0.35 eV on Pd(111) and Pd(100), respectively, when CO coverage is increased from 1/3 to 5/9 ML, followed by another 0.49 eV and 0.35 eV on Pd(111) and Pd(100) as CO coverage is increased to 2/3 ML. For H, the change in its BE as a function of CO coverage is more gradual compared with other species, with a total decrease in its BE of 0.36 eV and 0.39 eV on Pd(111) and Pd(100) as CO coverage is increased from 0 to 2/3 ML.

**Table 5-3** Binding energies (BEs) of HCOO, COOH, CO and H on Pd111) and Pd(100) at CO coverage of 1/9~2/3 ML with an increment of 1/9ML.

| CO coverage (ML) | BE(HCOO) | | BE(COOH) | | BE(CO) | | BE(H) | |
|---|---|---|---|---|---|---|---|---|
| | Pd(111) | Pd(100) | Pd(111) | Pd(100) | Pd(111) | Pd(100) | Pd(111) | Pd(100) |
| 1/9 | -2.40 | -2.53 | -2.23 | -2.50 | -1.99 | -2.03 | -2.83 | -2.80 |
| 2/9 | -2.45 | -2.51 | -2.23 | -2.44 | -1.98 | -2.00 | -2.76 | -2.83 |
| 1/3 | -2.18 | -2.40 | -2.04 | -2.28 | -1.83 | -1.98 | -2.69 | -2.75 |
| 4/9 | -2.02 | -2.11 | -1.86 | -1.96 | -1.57 | -1.74 | -2.63 | -2.68 |
| 5/9 | -1.47 | -1.66 | -1.34 | -1.51 | -1.35 | -1.63 | -2.56 | -2.47 |
| 2/3 | -0.43 | | -0.70 | -1.09 | -0.86 | -1.28 | -2.47 | -2.41 |

As we see, there is a dramatic change in the BEs of COOH, HCOO and CO during CO coverage of 4/9-2/3 ML, so in the following sections, we will investigate the CO coverage effects on the HCOOH decomposition chemistry by studying the reaction at CO coverage of 5/9 ML.

### 5.3.4 Results on 5/9 ML of CO covered Pd(111) surface

**Figure 5-7** shows the most stable configurations of the intermediates on 5/9 ML of CO covered Pd(111) surface with their corresponding binding energies being summarized in **Table 5-4**.

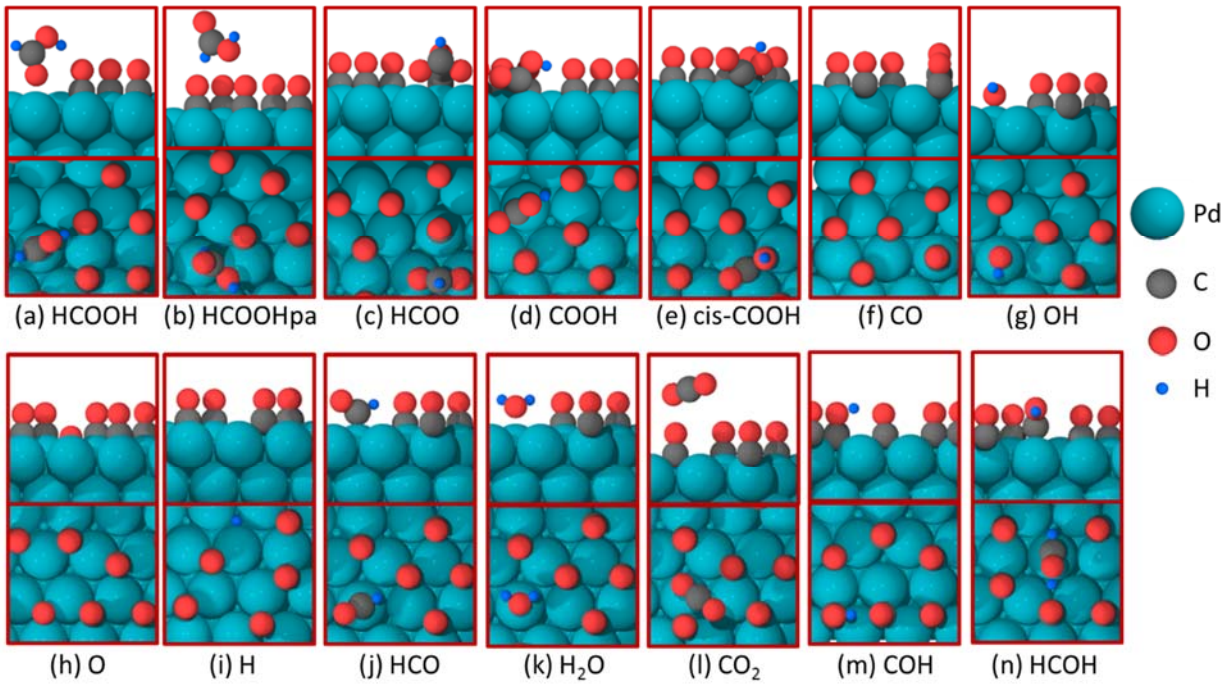


**Figure 5-7** Side and top views of the most stable configurations of intermediates on 5/9 ML of CO covered Pd(111). Palladium, carbon, hydrogen and oxygen atoms are indicated in dark green, dark grey, blue and red, respectively.

On 5/9 ML of CO covered Pd(111) surface, formic acid (HCOOH) prefers a trans-perpendicular configuration where the O-H bond is pointing towards a nearby preadsorbed CO, forming a weak hydrogen bonding with a O-H bond length of 2.0 Å. BE of HCOOH is -0.30 eV, which is more stable than another configuration of formic acid serves as the precursor of COOH formation, HCOOHpa, by 0.45 eV. Formate still prefers the bidentate structure on the top-top site of the surface with a BE of -1.47 eV. Carboxyl (COOH, by default indicates then trans carboxyl) prefers a trans configuration which binds through its C and carbonyl O atom on the top and bridge site, respectively, with a BE of -1.34 eV. There is also hydrogen bonding between the hydroxyl group

in COOH and the nearby CO with a O-H bond length of 1.8 Å. Another less stable configuration of carboxyl being explored is the one with a cis structure (cisCOOH), which has a BE of -1.05 eV and binds on the bridge and top site through its C and hydroxyl O atom.

**Table 5-4** Calculated PW91 binding energies (BE) at their preferred adsorption site on 5/9 ML of CO covered Pd(111) and Pd(100).

| Species | 5/9 ML of CO covered Pd(111) | | 5/9 ML of CO covered Pd(100) | |
|---|---|---|---|---|
| | adsorption site | BE / eV | adsorption site | BE / eV |
| HCOOH* | top | -0.30 | bridge | -0.20 |
| HCOOHpa* | top | 0.15 | bridge-top | 0.13 |
| HCOO* | top-top | -1.47 | bridge-top | -1.66 |
| COOH* | top-bridge | -1.34 | top-top | -1.51 |
| cisCOOH* | bridge-top | -1.05 | top-top | -1.51 |
| CO* | fcc/top | -0.86 | bridge | -1.28 |
| OH* | top | -1.58 | bridge | -1.96 |
| O* | fcc | -2.79 | hollow | -2.86 |
| H* | fcc | -2.56 | hollow | -2.47 |
| HCO* | top | -1.53 | bridge-bridge | -1.71 |
| $H_2O$* | top | -0.31 | top | -0.18 |
| $CO_2$* | physisorbed | -0.08 | physisorbed | -0.10 |
| COH* | hcp | -3.44 | hollow | -3.73 |
| HCOH* | top | -2.40 | bridge | -2.62 |

At low coverage, the three-fold sites on Pd(111) is the most favorable site for CO, while at CO coverage of 5/9 ML, top site is the secondary preferred site where there is 1/9 ML of CO. Hydroxyl (OH), formyl (HCO), hydroxymethylene (HCOH) all prefer the top site, while oxygen, hydrogen and hydroxymethylidyne (COH) prefer the three-fold site on CO covered Pd(111) surface. COH and HCOH are two new intermediates being explored on CO covered Pd(111) surface, and there is also hydrogen bonding seen in COH and HCOH with preadsorbed CO in their vicinity with a O-H bond length of 1.7 Å and 1.6 Å, respectively.

While CO coverage effects on binding energies of HCOO, COOH, CO and H have been discussed in the previous section, OH and HCO are destabilized by 0.6-0.7 eV and O is destabilized by about 1 eV with the presence of 5/9 ML of CO on Pd(111). A less dramatic destabilization effect, however, is seen on the closed-shell species HCOOH, $H_2O$ and $CO_2$, by only less than 0.2 eV.

On 5/9 ML of CO covered Pd(111) surface, steps related to HCO formation were not investigated since relatively high barriers are found to be required for these reactions on clean Pd(111). The reactions of HCOO and COOH with other adsorbates were also not explored on a crowded Pd(111) surface with CO coverage of 5/9 ML, however, at high CO coverage, reactions of the intermediates with preadsorbed CO species, which are H transfer reactions from the intermediates to CO (reactions 15-20 in **Table 5-5**), could occur and were also calculated. In total, 26 elementary steps were investigated on 5/9 ML of CO covered Pd(111) surface, and their reaction energies and activation energies are summarized in **Table 5-5**.

On 5/9 ML CO covered Pd(111) surface, HCOOH decomposition to HCOO is an endothermic reaction with a reaction energy 0.96 eV and an activation energy of 1.39 eV. HCOOH decomposition to COOH on CO covered Pd(111) also takes two steps with a barrier of 0.46 eV for the transformation step and a barrier of 1.11 eV for the C-H bond breaking step. The overall reaction barrier for COOH formation is 1.56 eV, which is 0.17 eV higher than the barrier for HCOO formation. Compared with the clean Pd(111) surface, at CO coverage of 5/9 ML, transformation of HCOOH has a barrier of 0.25 eV lower, while the bond breaking steps (either O-H bond breaking forming HCOO or C-H bond breaking forming COOH) of HCOOH has a barrier of 0.7-0.8 eV higher.

At CO coverage of 5/9 ML, HCOO decomposition to $CO_2$ on Pd(111) has a barrier of 1.67 eV, which is 0.53 eV higher than the barrier for COOH decomposition to $CO_2$. COOH decomposition

**Table 5-5** PW91 reaction energies (ΔE) and activation energy barriers (Ea) for the elementary steps considered in the HCOOH decomposition reaction network on 5/9 ML of CO covered Pd(111) and Pd(100) surface . All the values are relative to the infinite separation initial/final state.

| # | Reaction | 5/9 ML of CO covered Pd(111) | | 5/9 ML of CO covered Pd(100) | |
|---|---|---|---|---|---|
| | | $E_a$ / eV | ΔE / eV | $E_a$ / eV | ΔE / eV |
| 1 | HCOOH + * ↔ HCOOH* | | -0.30 | | -0.20 |
| 2 | HCOOH* + * ↔ HCOO* + H* | 1.39 | 0.96 | 1.07 | 0.76 |
| 3 | HCOOH* ↔ HCOOHpa* | 0.46 | 0.45 | 0.74 | 0.32 |
| 4[a] | HCOOHpa* + * ↔ COOH* + H* | 1.11 | 0.37 | 1.25 | 0.65 |
| 5 | HCOO* + * ↔ $CO_2$* + H* | 1.67 | -1.08 | 0.96 | -0.83 |
| 6 | COOH* + * ↔ $CO_2$* + H* | 1.14 | -0.94 | 0.71 | -0.71 |
| 7 | COOH* ↔ cisCOOH* | 0.40 | 0.30 | 0.30 | 0.00 |
| 8 | cisCOOH* + * ↔ CO* + OH* | 0.56 | 0.52 | 1.07 | 0.18 |
| 9 | HCO* + * ↔ CO* + H* | 0.49 | -0.56 | 0.09 | -0.72 |
| 10 | CO* + O* ↔ $CO_2$* + * | 0.49 | -2.60 | 0.44 | -2.13 |
| 11 | OH* + * ↔ O* + H* | 1.90 | 0.84 | 1.55 | 1.24 |
| 12[b] | 2OH* ↔ $H_2O$* + O* | -0.46 | -0.57 | 0.19 | 0.25 |
| 13 | OH* + H* ↔ $H_2O$* + * | 0.31 | 0.00 | 0.58 | -0.99 |
| 14 | 2H* ↔ $H_2$ + 2* | 0.97 | 0.55 | 0.69 | 0.37 |
| 15[c,d] | HCOOH* + CO* ↔ COH* + HCOO* | 1.46 | 1.37 | 0.47 | 0.47 |
| 16[c] | HCOO* + CO* ↔ COH* + $CO_2$* | 0.74 | -0.67 | -- | -0.38 |
| 17[c] | COOH* + CO* ↔ COH* + $CO_2$* | 0.60 | -0.53 | 0.79 | -0.26 |
| 18[c] | HCO* + CO* ↔ COH* + CO* | 0.91 | -0.15 | 0.91 | -0.27 |
| 19[c] | OH* + CO* ↔ HCO* + O* | 1.53 | 1.25 | -- | -- |
| 20[c] | OH* + CO* ↔ COH* + O* | 2.84 | 1.40 | -- | -- |
| 21 | COH* + * ↔ CO* + H* | 1.36 | -0.41 | 1.09 | -0.45 |
| 22 | COH* + H* ↔ HCOH* + * | 1.06 | 0.16 | 0.80 | 0.14 |
| 23 | HCOH* + * ↔ HCO* + H* | 0.79 | -0.01 | 1.02 | 0.12 |
| 24 | $CO_2$* ↔ $CO_2$ + * | | 0.08 | | 0.10 |
| 25 | $H_2O$* ↔ $H_2O$ + * | | 0.31 | | 0.18 |
| 26 | CO* ↔ CO + * | | 0.86 | | 1.28 |

a, this reaction on CO covered Pd(100) starts with HCOOH instead of HCOOHpa.
b, Ea of this reaction is are less positive than the ΔE, this is because the initial sate used is the adsorbates at infinite separation state, and when they are coadsorbed on the surface, an attractive interaction is observed.
c, CO* in red color indicates the preadsorbed CO molecule.
d, this reaction starts with HCOOHpa instead of HCOOH on CO covered Pd(100).

to CO first goes through a transformation step to cisCOOH, then breaks the C-O bond forming CO and OH. Transformation of COOH is endothermic by 0.30 eV with an activation energy of 0.40 eV, while the C-O bond breaking step of COOH has a barrier of 0.56 eV. The overall barrier required for COOH decomposition to CO is 0.86 eV, which is much lower than the barrier required for COOH decomposition to $CO_2$. Thus, COOH preferentially decomposes to CO on 5/9 ML of CO covered Pd(111) surface, which is on contrary to the clean Pd(111) surface. Compared with the clean Pd(111) surface, at CO coverage of 5/9 ML, CO formation from COOH requires a similar barrier, while the barrier for $CO_2$ formation from HCOO and COOH is 0.74 eV and 0.44 eV higher, respectively.

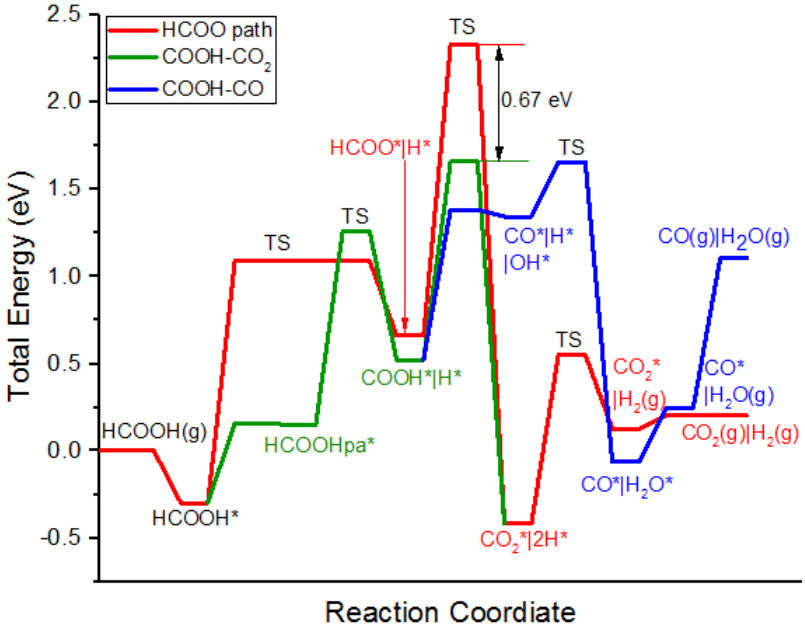


**Figure 5-8** Potential energy surface of HCOOH decomposition on 5/9 ML of CO covered Pd(111). Red line is the HCOO pathway, green line is the COOH pathway leading to $CO_2$ formation (COOH-$CO_2$ pathway) and blue line is the COOH pathway leading to CO formation (COOH-CO pathway).

**Figure 5-8** plots the HCOO and COOH pathway of HCOOH decomposition we just discussed on the same PES diagram. From the plot, we can see that COOH formation is more difficult than HCOO formation, while COOH decomposition is much easier than HCOO decomposition, the TS

of COOH decomposition to $CO_2$ is lower in energy than the TS of HCOO decomposition by 0.67 eV. Based on the DFT analysis, the COOH pathway seems to be more favorable than the HCOO pathway for HCOOH decomposition on 5/9 ML of CO covered Pd(111), however, formation of COOH needs to go through a metastable state HCOOHpa, which easily desorbs from the surface, thus the relative favorability of the COOH and HCOO pathway will depend on the competition between HCOOHpa desorption with its decomposition. COOH preferentially decomposes to CO on CO covered Pd(111) surface.

Comparing HCOOH decomposition on clean Pd(111) surface and on 5/9 ML of CO covered Pd(111) surface (**Figure 5-9**), one can find that all TSs and adsorption state related to the HCOO and COOH pathway are all destabilized at high CO coverage, leading to a lower reactivity of HCOOH decomposition at high CO coverage.

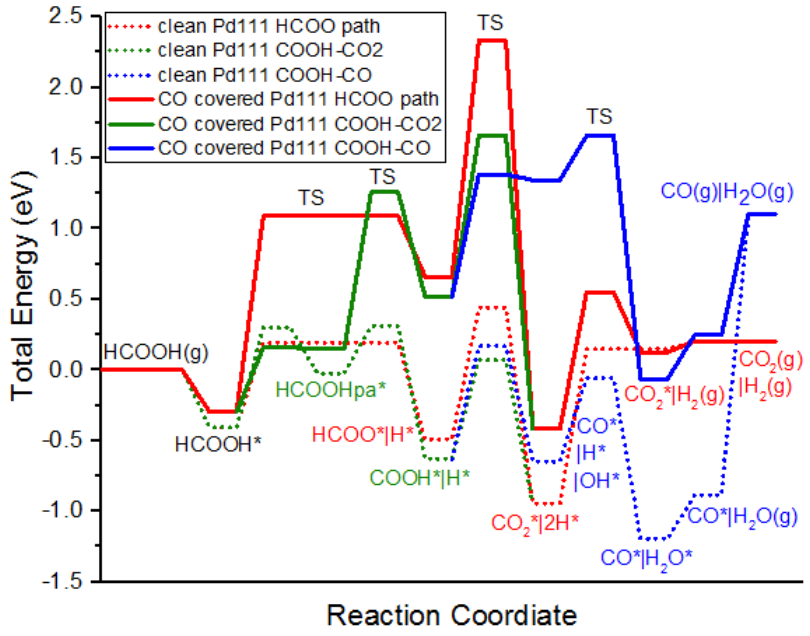


**Figure 5-9** Comparison of the HCOO pathway, COOH-$CO_2$ pathway and COOH-CO pathway of HCOOH decomposition on clean Pd(111) surface with 5/9 ML of CO covered Pd(111) surface. Red line is the HCOO pathway, green line is the COOH pathway leading to $CO_2$ formation, blue line is the COOH pathway leading to CO formation. Solid line indicates the CO covered Pd(111) surface, while dotted line indicates the clean Pd(111) surface.

Besides the direct decomposition through the HCOO and COOH intermediates, HCOOH can also decompose through the H transfer reactions to preadsorbed CO species on 5/9 ML of CO covered Pd(111) surface. The precursor CO species work as a H reservoir, which stores the H atoms being transferred in the form of COH that can decompose and form CO and H again. Transfer of the hydroxyl H in HCOOH to a precursor CO forming HCOO and COH is an endothermic reaction with a barrier of 1.46 eV, which is only 0.07 eV higher than the barrier for the direct decomposition to HCOO. Transfer of the H in HCOO to a precursor CO requires a barrier of 0.74 eV, which is 0.93 eV lower than the barrier required for the direct decomposition to $CO_2$, while the H transfer from COOH to CO has a barrier that is 0.54 eV lower than the direct decomposition of COOH. Although the CO-assisted decomposition of the intermediates are generally more favorable than their direct decomposition reactions, subsequent decomposition of COH is quite difficult. The direct decomposition of COH has a barrier of 1.36 eV, while a barrier of 1.06 eV is required for its direct transformation to HCO or its transformation to HCO through the HCOH intermediate, further decomposition of HCO is relatively easy with a barrier of 0.49 eV.

By plotting the CO-assisted decomposition routes with the direct decomposition routes on the same PES diagram (**Figure 5-10**), it is found the most favorable reaction route includes direct decomposition of HCOOH to either COOH or HCOO followed by the CO-assisted decomposition of either COOH or HCOO, which forms a COH species that can decompose through a first transformation to HCO followed by a dehydrogenation step: HCOOH → COOH/HCOO + H → $CO_2$ + COH + H →$CO_2$ + HCO + H → $CO_2$ + 2H. The COOH pathway is energetically more favorable than the HCOO pathway, of which the highest TS is 0.15 eV higher in energy than the highest TS in the COOH pathway. But as discussed earlier, the relative contributions of the two

pathways will depend on the competition between HCOOHpa desorption and HCOOHpa decomposition to COOH.

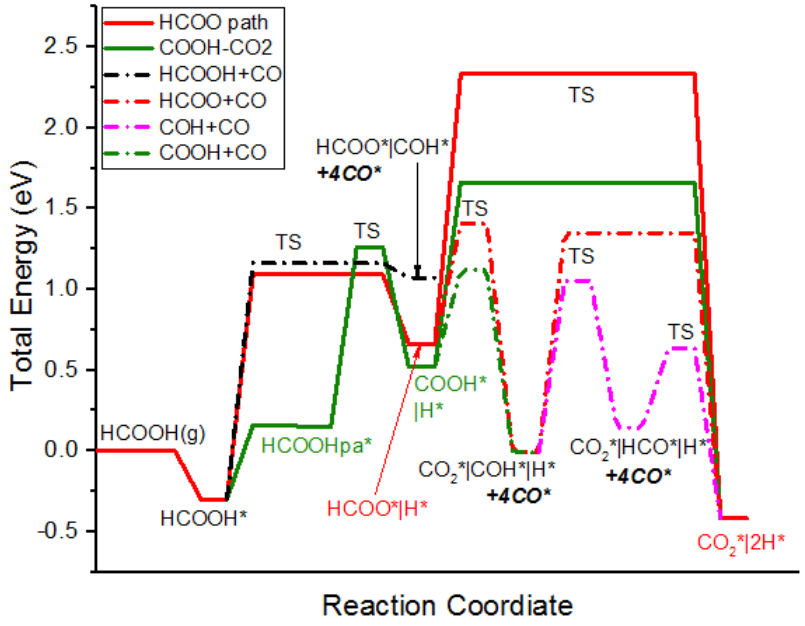


**Figure 5-10** Potential energy surface of HCOOH decomposition through HCOO and COOH pathway including CO assisted decomposition routes on 5/9 ML of CO covered Pd(111) surface. Solid red line is the HCOO pathway, solid green line is the COOH pathway leading to $CO_2$ formation, and dash dotted lines indicate various CO assisted decomposition routes. Whenever a COH/HCO is formed, the CO coverage on Pd(111) becomes 4/9 ML, as indicated by '***+4CO***'.

### 5.3.5 Results on 5/9 ML of CO covered Pd(100) surface

On 5/9 ML of CO covered Pd(100) surface, formic acid prefers the trans-perpendicular configuration which binds the surface through it O atom to the bridge site and the O-H bond is pointing towards a nearby CO forming a weak hydrogen bonding with a bond length of 1.9 Å between the hydroxyl H in HCOOH and O in the nearby CO; BE of HCOOH is -0.20 eV. The precursor for COOH formation adopts a cis-perpendicular configuration which binds the surface through the two O atoms on the top site and the second nearest bridge site; for the ease of comparison with other surfaces, this configuration is still denoted as HCOOHpa, which has a positive BE value on CO covered Pd(100). Unlike other surfaces, formate binds to the top site and

a second nearest bridge site through the two O atoms on CO covered Pd(100), with a BE of -1.66 eV. Both COOH and cisCOOH prefer to adsorb on the top-top site their C and carbonyl O atom; the two configurations of carboxyl have the same BE -1.51 eV. CO, OH and HCOH all prefer the bridge site, while O, H and COH prefer the four-fold hollow site, and HCO prefers to bind to a bridge site and a second nearest bridge site through its C and O atom. The hydrogen bonding exists between both COH and HCOH with CO species in vicinity; bond length between H in COH/HCOH and O in CO is 1.9 Å.

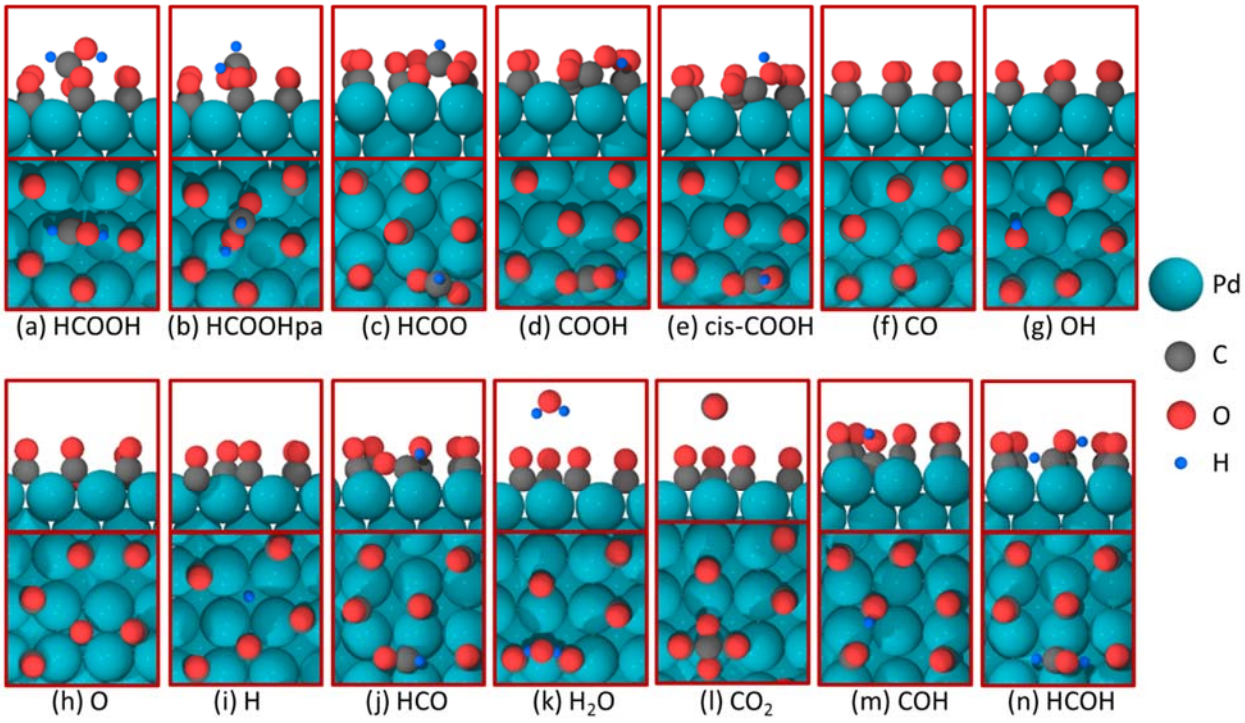


**Figure 5-11** Side and top views of the most stable configurations of intermediates on 5/9 ML of CO covered Pd(100). Palladium, carbon, hydrogen and oxygen atoms are indicated in dark green, dark grey, blue and red, respectively.

While CO coverage effects on the BEs of HCOO, COOH, CO and H on Pd(100) surface have been discussed, OH is destabilized by around 0.6 eV and O and HCO are destabilized by 0.9-1.0 eV with the presence of 5/9 ML of CO on Pd(100). The closed-shell species HCOOH, $H_2O$ and $CO_2$ are less affected by the 5/9 ML of CO coverage, at which a destabilization of 0-0.3 eV is seen.

At CO coverage of 5/9 ML, Pd(100) binds the intermediates more strongly than Pd(111) except for H and $H_2O$, of which a stronger BE is observed on Pd(111) by 0.09 eV and 0.12 eV, respectively. For the other species, at CO coverage of 5/9 ML, there is a stabilization of 0.4-0.5 eV for cisCOOH, CO and OH on Pd(100) than on Pd(111), while the stabilization effect for the rest of the intermediates is less dramatic, ca. 0-0.3 eV.

On 5/9 ML of CO covered Pd(100) surface, HCOOH decomposition to HCOO has a barrier of 1.07 eV, while HCOOH decomposition to COOH can proceed directly without going through the transformation step to HCOOHpa, the barrier required for COOH formation is 1.25 eV. The barriers for HCOO and COOH formation on CO covered Pd(100) surface are ca. 0.3 eV lower compared with the corresponding barriers on CO covered Pd(111) surface, and about 0.4-0.5 eV higher compared with the barriers on the clean Pd(100) surface.

At CO coverage of 5/9 ML, on Pd(100), HCOO decomposition has a barrier of 0.96 eV, which is higher than the barrier required for COOH decomposition to $CO_2$, 0.71 eV. The corresponding barriers on Pd(111) at the same CO coverage are about 0.7 eV and 0.4 eV higher for HCOO and COOH dehydrogenation, respectively. COOH decomposition to CO proceeds through a first transformation to cisCOOH with a barrier of 0.30 eV, followed by the C-O bond breaking in cisCOOH with a barrier of 1.07 eV, which is more difficult than the O-H bond breaking in COOH forming $CO_2$. Unlike COOH decomposition to $CO_2$, cisCOOH decomposition to CO has a barrier of more than 0.5 eV higher on Pd(100) than on Pd(111) at CO coverage of 5/9 ML. Compared with the clean Pd(100) surface, the barrier for HCOO decomposition and COOH decomposition to CO are about 0.1 and 0.4 eV higher on 5/9 ML of CO covered Pd(100) surface, while COOH decomposition to $CO_2$ has a barrier of about 0.2 eV lower on CO covered Pd(100) surface.

The potential energy surface for HCOOH decomposition on 5/9 ML of CO covered Pd(100) surface including only direct decomposition routes through COOH and HCOO is shown in **Figure 5-12**. It can be seen that COOH formation from HCOOH is more difficult than HCOO formation, while COOH dehydrogenation is easier than HCOO dehydrogenation, which has the highest TS in HCOO pathway with an energy of 0.36 eV higher than the highest TS in the COOH pathway. Thus, COOH pathway is energetically more favorable than the HCOO pathway for HCOOH decomposition on CO covered Pd(100) surface.

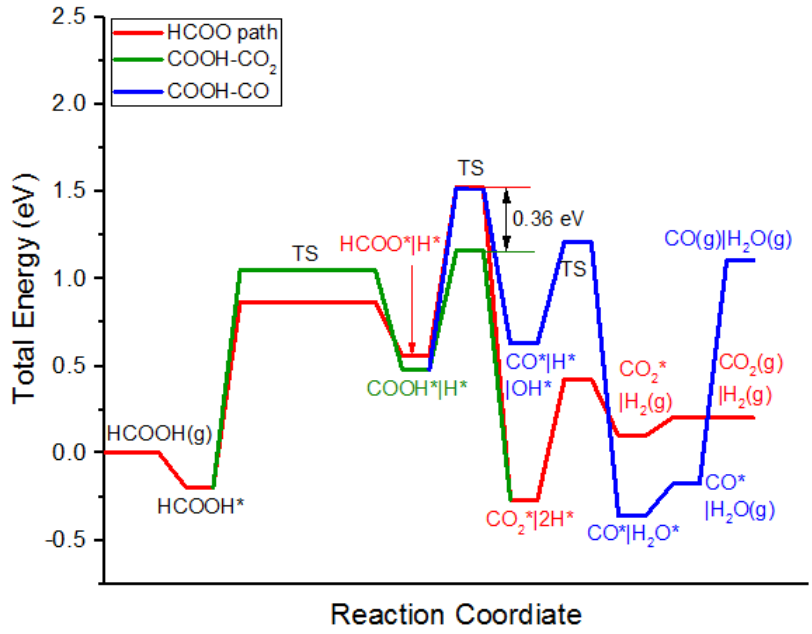


**Figure 5-12** Potential energy surface of HCOOH decomposition on 5/9 ML of CO covered Pd(100). Red line is the HCOO pathway, green line is the COOH pathway leading to $CO_2$ formation (COOH-$CO_2$ pathway) and blue line is the COOH pathway leading to CO formation (COOH-CO pathway).

Comparing HCOOH decomposition on clean Pd(100) surface with that on 5/9 ML of CO covered Pd(100) surface (**Figure 5-13**), it is found that all TSs and adsorption states related to the HCOO and COOH pathway are all destabilized with presence of 5/9 ML of CO on the surface, leading to a lower reactivity of HCOOH decomposition on Pd(100) at high CO coverage.

Comparing with HCOOH decomposition on 5/9 ML of CO covered Pd(111) surface, on 5/9 ML of CO covered Pd(100) surface, it is found that all TSs in the COOH and HCOO pathways are stabilized except for the TS of COOH decomposition to CO, which is destabilized on Pd(100) compared with Pd(111) at CO coverage of 5/9 ML. Thus, at CO coverage of 5/9 ML, Pd(100) is more active than Pd(111) for HCOOH decomposition, and Pd(100) also has a higher selectivity to $CO_2$ compared with Pd(111).

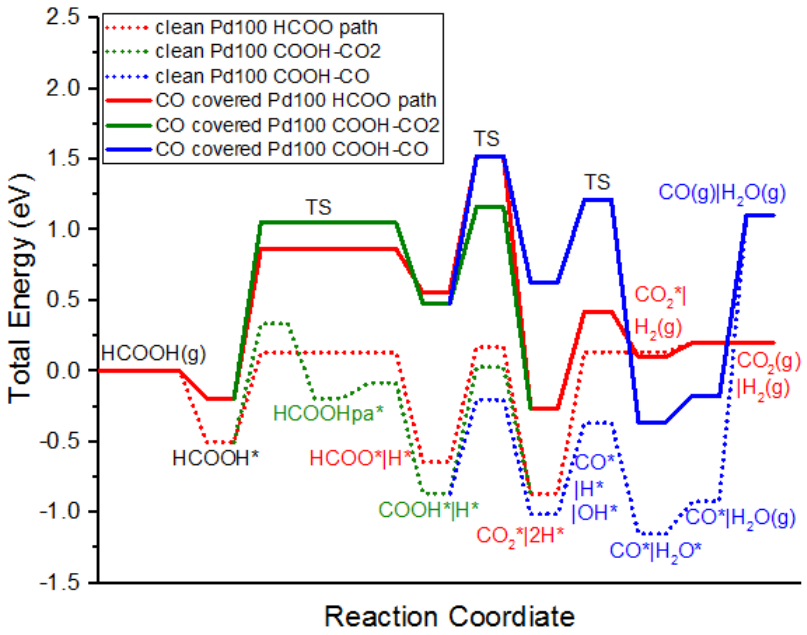


**Figure 5-13** Comparison of the HCOO pathway, COOH-$CO_2$ pathway and COOH-CO pathway of HCOOH decomposition on clean Pd(100) surface with 5/9 ML of CO covered Pd(100) surface. Red line is the HCOO pathway, green line is the COOH pathway leading to $CO_2$ formation, blue line is the COOH pathway leading to CO formation. Solid line indicates the CO covered Pd(100) surface, while dotted line indicates the clean Pd(100) surface.

Besides the direct decomposition routes through the COOH and HCOO intermediates that are discussed above, HCOOH can also decompose through H transfer reactions to preadsorbed CO species. H transfer from HCOOH to CO is a two-step reaction, during which HCOOH first transforms to HCOOHpa with a reaction energy 0.32 eV and an activation energy of 0.74 eV, followed by the H transfer from HCOOHpa to a nearby CO with a barrier of 0.47 eV. Thus the

overall barrier for H transfer from HCOOH to CO forming HCOO and COH is 0.79 eV, which is 0.28 eV lower than the barrier of direct decomposition of HCOOH to HCOO. COOH decomposition through the H transfer to CO requires a barrier of 0.79 eV, which is only 0.08 eV higher than the barrier of direct decomposition to COOH. COH formed from the H transfer reactions prefer to decompose directly with a barrier of 1.09 eV, rather than decompose through its transformation to HCO and further decomposition of HCO or hydrogenation to HCOH followed by dehydrogenation steps through HCO.

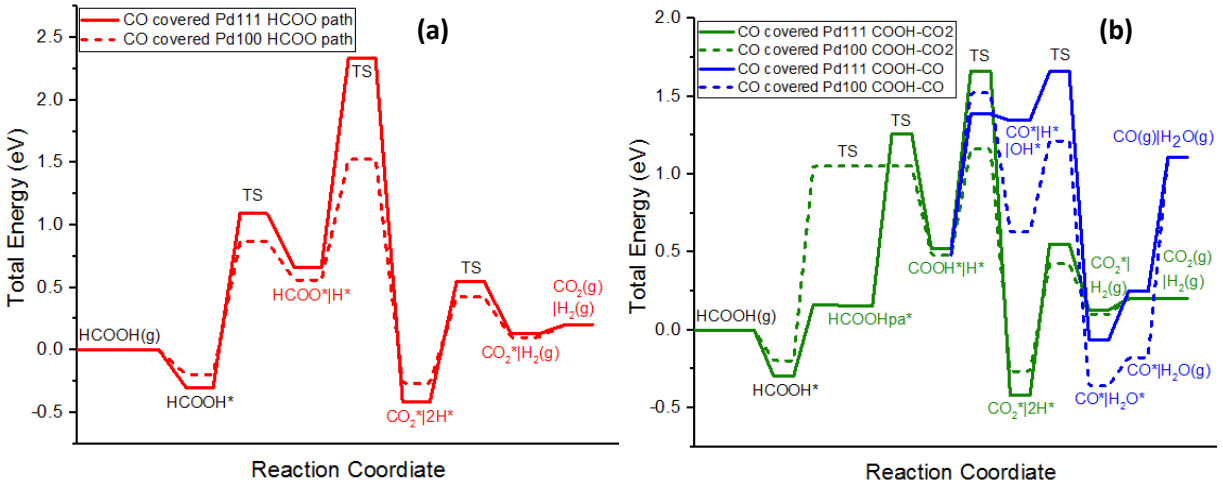


**Figure 5-14** Comparison of the PESs for (a) the HCOO pathway, and (b) the COOH pathway of HCOOH decomposition on 5/9 ML of CO covered Pd(100) and Pd(111). Solid lines are for CO covered Pd(111) while dashed lines are for CO covered Pd(100). Red color indicates the HCOO pathway, green color indicates the COOH pathway leading to $CO_2$ formation, blue line indicates the COOH pathway leading to CO formation.

**Figure 5-15** compares the direct decomposition routes with the CO-assisted decomposition routes on 5/9 ML of CO covered Pd(100) surface. It can be found that the most favorable decomposition path does not include the CO assisted decomposition steps. CO assisted COOH decomposition is less favorable than direct decomposition to $CO_2$ (dash dotted green line in **Figure 5-15**). While CO-assisted HCOOH decomposition is more favorable than its direct decomposition to HCOO,

further dehydrogenation of the COH formed generating the CO assumed in the previous step has a very high TS, thus the overall reaction of CO assisted HCOOH decomposition to HCOO is less favorable than the direct decomposition of HCOOH to HCOO. As a result, CO-assisted decomposition steps are not relevant for HCOOH decomposition on 5/9 ML of CO covered Pd(100) surface, on contrary to that on CO covered Pd(111) surface.

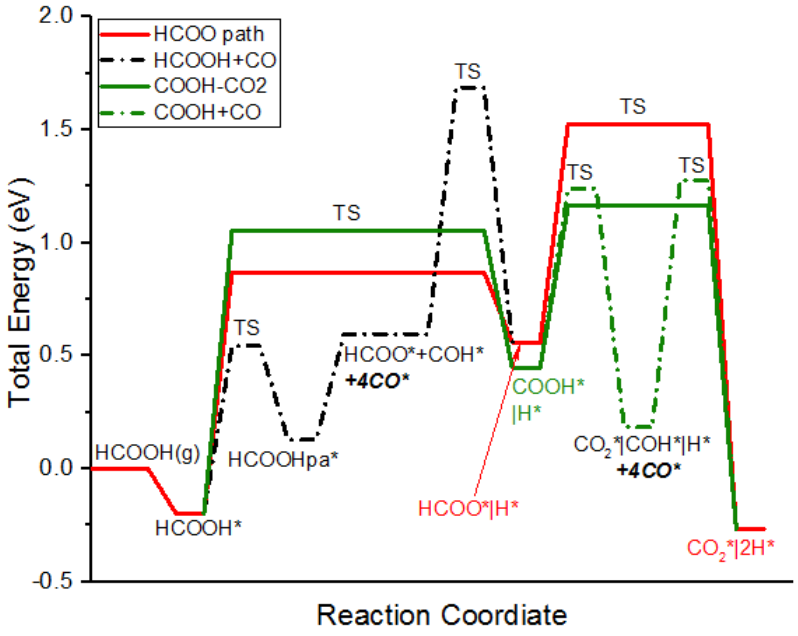


**Figure 5-15** Potential energy surface of HCOOH decomposition through HCOO and COOH pathway including CO-assisted decomposition routes on 5/9 ML of CO covered Pd(100) surface. Solid red line is the HCOO pathway, solid green line is the COOH pathway leading to $CO_2$ formation, and dash dotted lines indicate various CO assisted decomposition routes. Whenever a COH/HCO is formed, the CO coverage on Pd(111) becomes 4/9 ML, as indicated by ***'+4CO'***.

### 5.4 Conclusions

Using DFT calculations, formic acid decomposition was investigated on both (111) and (100) facets of Pd to explore the structure sensitivity of this reaction, and the reaction was also studied on the two facets at CO coverage of 5/9 ML to explore the CO coverage effects on the reaction energetics as well as the reaction pathways.

On clean surfaces, HCOOH decomposition through the HCO intermediate is far less favorable than its decomposition through either COOH or HCOO intermediate. On both clean Pd(111) and Pd(100) surfaces, COOH formation is more difficult than HCOO formation, while COOH decomposition is more favorable than HCOO decomposition. On clean Pd(111), COOH preferentially decomposes to $CO_2$, while CO formation is more favorable than $CO_2$ formation from COOH on clean Pd(100).

Binding of the key intermediates in HCOOH decomposition, HCOO, COOH and CO are significantly weakened when the Pd surface is exposed to a CO coverage of more than 4/9 ML. At CO coverage of 5/9 ML of CO, all TSs in HCOOH decomposition are also destabilized on both (111) and (100) facets of Pd, leading to a lower reactivity for HCOOH decomposition at high CO coverage. At CO coverage of 5/9 ML, COOH formation is also more difficult than HCOO formation, while COOH decomposition is more favorable than HCOO decomposition. But compared with the results on clean surfaces, the relative favorability of COOH decomposition to $CO_2$ and CO is reversed at CO coverage of 5/9 ML for both facets of Pd.

On 5/9 ML of CO covered Pd(100) surface, COOH can form from the most stable HCOOH directly, while on all the other surfaces being explored, a transformation step is required for HCOOH to its isomer HCOOHpa, which desorbs easily from the surface, especially on CO covered Pd(111) surface, where adsorbed HCOOHpa is a metastable state. Thus, on all surfaces except for the CO covered Pd(100) surface, contribution of the COOH pathway to the overall reaction depends on the relative easiness of HCOOHpa decomposition compared with HCOOHpa desorption, while on 5/9 ML of CO covered Pd(100), COOH pathway is more favorable than the HCOO pathway.

On 5/9 ML of CO covered Pd(111) surface, CO-assisted COOH and HCOO decomposition are more favorable than their direct decomposition, while the CO-assisted decomposition steps are not relevant on 5/9 ML of CO covered Pd(100) surface.

These findings are based on the DFT analysis only, for a more accurate analysis, these DFT results should be compared with the experimental results in a microkinetic model to obtain a true understanding of the reaction mechanism.

# Chapter 6 Fundamental Mechanistic Studies of Formic Acid Decomposition on Pt Catalysts: Structure Sensitivity and CO Coverage Effects†

## 6.1 Introduction

Similar as Pd catalysts, Pt is also among the most active transition metals for gas-phase HCOOH decomposition and a commonly used anode material for direct formic acid fuel cells (DFAFC).[21, 171, 173-175] However, experimental[43, 50, 86, 189-192] and theoretical studies[182, 184, 185, 193-195] exist in literature lead to controversial conclusions about the reaction mechanism on Pt catalysts, including the reactive intermediates. Experimental studies on Pt only observed the HCOO intermediate[196-198], whereas theoretical studies have proposed that CO can be possibly formed from the COOH intermediate, which implies the contribution of the COOH pathway to the overall reaction since CO production has been found in experimental studies, though its selectivity is low. So the relative favorabilities of the HCOO and COOH pathway and their relative contributions to the overall reaction are still not resolved. CO poisoning has been a well-known problem for Pt catalysts. But how CO is formed in the HCOOH decomposition reaction and affects the reaction energetics are not clear.

Here we report a detailed study of gas-phase HCOOH decomposition on (111) and (100) facets of Pt catalysts using plane wave density functional theory (DFT-PW91), aiming to evaluate the structure sensitivity of this reaction and provide some insights into the reaction mechanism and the active sites. CO poisoning effects were also investigated by comparing the results on clean surfaces of Pt with that obtained from the CO-covered Pt surfaces at a coverage of 4/9 ML.

†, Calculations on clean Pt(100) were performed by J. Scaranto.

## 6.2 Computational methods

All DFT calculations were performed with DACAPO code. Pt(111) surface was modeled by a 3-atomic layers slab using a (3 × 3) unit cell, while Pt(100) surface was modeled with by a 4-atomic layers slab with a (3 × 3) unit cell, corresponding to a surface coverage of 1/9 ML for each adsorbate. Surface Brillouin zone of the (111) slab was sampled at 6 special Chadi-Cohen k-points, while that for the (100) slab was sampled using a 4×4×1 Monkhorst-Pack k-point mesh. Other computational details are the same as those used for the studies on Au and Pd catalysts, and can be found in previous chapters.

## 6.3 Results and discussion

We studied formic acid decomposition on the (111) and (100) facets of Pt catalysts. Dependence of the reaction pathways and energetics on the surface structure was explored by comparing the results obtained on the two facets. Since the Pt catalysts used in experiments are expected to be covered by CO, CO coverage effects on the binding of key intermediates (COOH, HCOO, CO) were investigated and the reaction was also studied on CO-covered Pt catalysts, using 4/9ML of CO covered Pt(111) and Pt(100) as the model surfaces. Effect of spectator CO on the reaction pathways and energetics was discussed from comparison of the clean surfaces with the CO-covered surfaces.

### 6.3.1 Results on clean Pt(111) and Pt(100) surface

Scaranto[199] did mechanistic studies of HCOOH decomposition on Pt(111) surface using a reaction network comprised of 21 elementary steps and 10 surface intermediates. Key conclusions from her work include: (1) HCOO formation from HCOOH is more favorable than COOH formation, which requires a transformation step of HCOOH from a perpendicular trans-configuration to a

parallel cis-configuration, and HCO formation is far less favorable than either HCOO or COOH formation from HCOOH; (2) HCOO decomposition requires a much higher activation energy barrier than COOH decomposition so that $CO_2$ is generated primarily through the COOH intermediate; (3) CO is possibly produced from the COOH intermediate, but its formation is less favorable than $CO_2$ production from COOH; (4) co-absorbed O and OH species could facilitate COOH decomposition. The potential energy surface (PES) of HCOOH decomposition on Pt(111) surface is shown in **Figure 6-1**, from which the abovementioned conclusions can be deduced.

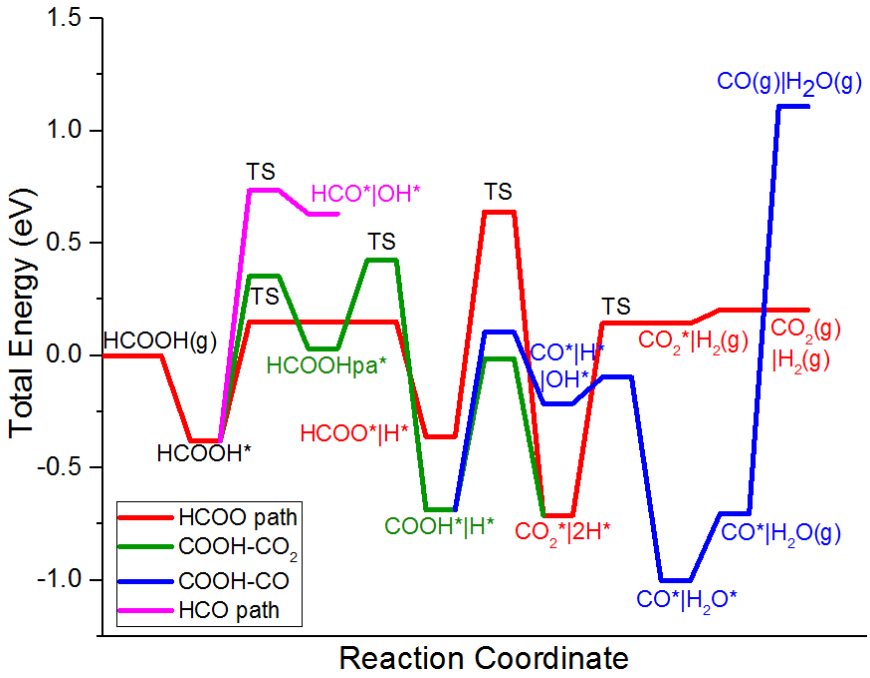


**Figure 6-1** Potential energy surface of HCOOH decomposition on Pt(111). Red line is the HCOO pathway, green line is the COOH pathway leading to $CO_2$ formation, blue line is the COOH pathway leading to CO formation, purple line is the HCO pathway while orange line shows the HCO formation from HCOO. PES is reproduced using data reported in Ref [199].

A reduced reaction network was used for studies on Pt(100), where non-relevant reactions found on Pt(111) were removed from the reaction network, such as CO and H assisted decomposition of COOH, H/O/OH assisted HCOO decomposition, and HCO formation from HCOO/HCOOH. **Table 6-1** and **6-2** summarize the binding energy values of the intermediates and reaction energies

and activation energies of elementary reactions on Pt(100), results reported in Scaranto's work were also provided for comparison.

**Table 6-1** Calculated PW91 binding energies (BE) at their preferred adsorption site on Pt(111) and Pt(100).

| Species | Pt(111)[a] | | Pt(100) | |
|---|---|---|---|---|
| | **adsorption site** | **BE / eV** | **adsorption site** | **BE / eV** |
| HCOOH* | top-bridge | -0.38 | top-bridge | -0.52 |
| HCOO* | top-top | -2.33 | top-top | -2.58 |
| mo-HCOO* | top | -1.63 | top-top | -1.85 |
| COOH* | top | -2.40 | top-top | -2.74 |
| CO* | fcc | -1.81 | bridge | -2.18 |
| OH* | bridge | -2.03 | bridge | -2.71 |
| O* | fcc | -3.74 | bridge | -3.89 |
| H* | top | -2.71 | bridge | -2.91 |
| HCO* | top | -2.35 | top | -2.52 |
| $H_2O$* | top | -0.30 | top | -0.35 |
| $CO_2$* | physisorbed | -0.06 | physisorbed | -0.07 |
| a, BE values are cited from Ref [199]. | | | | |

It is found that Pt(100) binds the intermediates more strongly than the Pt(111) surface by 0.1-0.7 eV, which is expected since Pt(100) is a more open facet than Pt(111). Hydroxyl (OH) is the species has the most dramatic stabilization on Pt(100) compared with Pt(111), with a BE increase of 0.68 eV. The most stable adsorption configurations of the intermediates on Pt(100) are shown in **Figure 6-2**. Carbon monoxide (CO), hydroxyl, oxygen atom and hydrogen atom all prefer the bridge site on Pt(100). Monodentate formate (mo-HCOO) binds through one of its oxygen atoms and the hydrogen atom on two top sites of Pt(100), with C-H bond pointing down towards the surface. Carboxyl (COOH) also binds to two top sites of the surface through its O atom and C atom. Similar as on Pt(111), bidendate formate (HCOO) still prefers to bind to two adjacent top sites through its two O atoms on Pt(100). The cis-parallel configuration of formic acid (HCOOHpa) is also given in **Figure 6-2**; the DFT calculated BE of HCOOHpa is a slightly positive number

(0.03 eV on Pt(100)), indicating HCOOHpa is very likely to desorb from the surface, especially when a high barrier is required for the subsequent decomposition reactions. The trans-perpendicular configuration of formic acid (HCOOH, by default, indicates the most stable perpendicular configuration) is more stable than its parallel counterpart by 0.56 eV on Pt(100).

**Table 6-2** PW91 reaction energies (ΔE) and activation energy barriers (Ea) for the elementary steps considered in the HCOOH decomposition reaction network on Pt(111) and Pt(100) . All the values are relative to the best initial/final state.

| # | Reaction | Pt(111)[a] | | Pt(100) | |
|---|---|---|---|---|---|
| | | $E_a$ / eV | ΔE / eV | $E_a$ / eV | ΔE / eV |
| 1 | HCOOH + * ↔ HCOOH* | | -0.38 | | -0.52 |
| 2 | HCOOH* + * ↔ HCOO* + H* | 0.53 | 0.03 | 0.70 | -0.06 |
| 3 | HCOOH* ↔ HCOOHpa* | 0.73 | 0.41 | 0.89 | 0.56 |
| 4 | HCOOHpa* + * ↔ COOH* + H* | 0.39 | -0.71 | 0.09 | -1.03 |
| 5 | HCOOHpa* + * ↔ HCO* + OH* | 0.70 | 0.29 | -- | -- |
| 6 | HCOO* ↔ mo-HCOO* | 1.00 | 0.71 | 1.08 | 0.73 |
| 7 | mo-HCOO* + * ↔ $CO_2$* + H* | 0.00 | -1.04 | 0.00 | -1.05 |
| 8 | HCOO* + O* ↔ $CO_2$* + OH* | 2.02 | -0.65 | -- | -- |
| 9 | HCOO* + OH* ↔ $CO_2$* + $H_2O$* | 1.13 | -1.06 | -- | -- |
| 10 | HCOO* + H* ↔ $H_2$ + $CO_2$* + * | 1.42 | 0.46 | 2.04 | 0.88 |
| 11 | HCOO* + CO* ↔ HCOOCO* + * | 1.23 | 1.16 | -- | -- |
| 12 | HCOOCO* + * ↔ HCO* + $CO_2$* | 0.25 | -0.69 | -- | -- |
| 13 | HCOO* + * ↔ HCO* + O* | 1.82 | 1.16 | -- | -- |
| 14 | COOH* + * ↔ $CO_2$* + H* | 0.67 | -0.01 | 0.91 | 0.11 |
| 15 | COOH* + * ↔ CO* + OH* | 0.79 | 0.40 | 0.57 | 0.34 |
| 16 | COOH* + O* ↔ $CO_2$* + OH* | 0.22 | -0.23 | 0.00 | -0.30 |
| 17 | COOH* + OH* ↔ $CO_2$* + $H_2O$* | 0.14 | -0.77 | 0.10 | -0.18 |
| 18 | COOH* + H* ↔ CO* + $H_2O$* | 0.78 | -0.39 | -- | -- |
| 19 | COOH* + CO* ↔ HCO* + $CO_2$* | 1.10 | 0.45 | -- | -- |
| 20 | HCOO* + COOH* ↔ HCOOHpa* + $CO_2$* | 0.70 | 0.52 | 0.46 | 0.39 |
| 21 | HCO* + * ↔ CO* + H* | 0.23 | -0.74 | 0.09 | -1.31 |
| 22 | CO* + O* ↔ $CO_2$* + * | 0.83 | -0.78 | 0.50 | -0.13 |
| 23 | O* + H* ↔ OH* + * | 0.79 | -0.20 | 0.47 | -0.53 |
| 24 | 2OH* ↔ $H_2O$* + O* | 0.04 | -0.17 | 0.42 | 0.38 |
| 25 | OH* + H* ↔ $H_2O$* + * | 0.19 | -0.71 | 0.76 | -0.11 |
| 26 | 2H* ↔ $H_2$ + 2* | 0.85 | 0.85 | 1.25 | 1.25 |
| 27 | $CO_2$* ↔ $CO_2$ + * | | 0.06 | | 0.07 |
| 28 | $H_2O$* ↔ $H_2O$ + * | | 0.30 | | 0.35 |

| | | | | | |
|---|---|---|---|---|---|
| 29 | CO* ↔ CO + * | | 1.81 | | 2.18 |
| a, Ea and ΔE values are cited from Ref [199]. | | | | | |

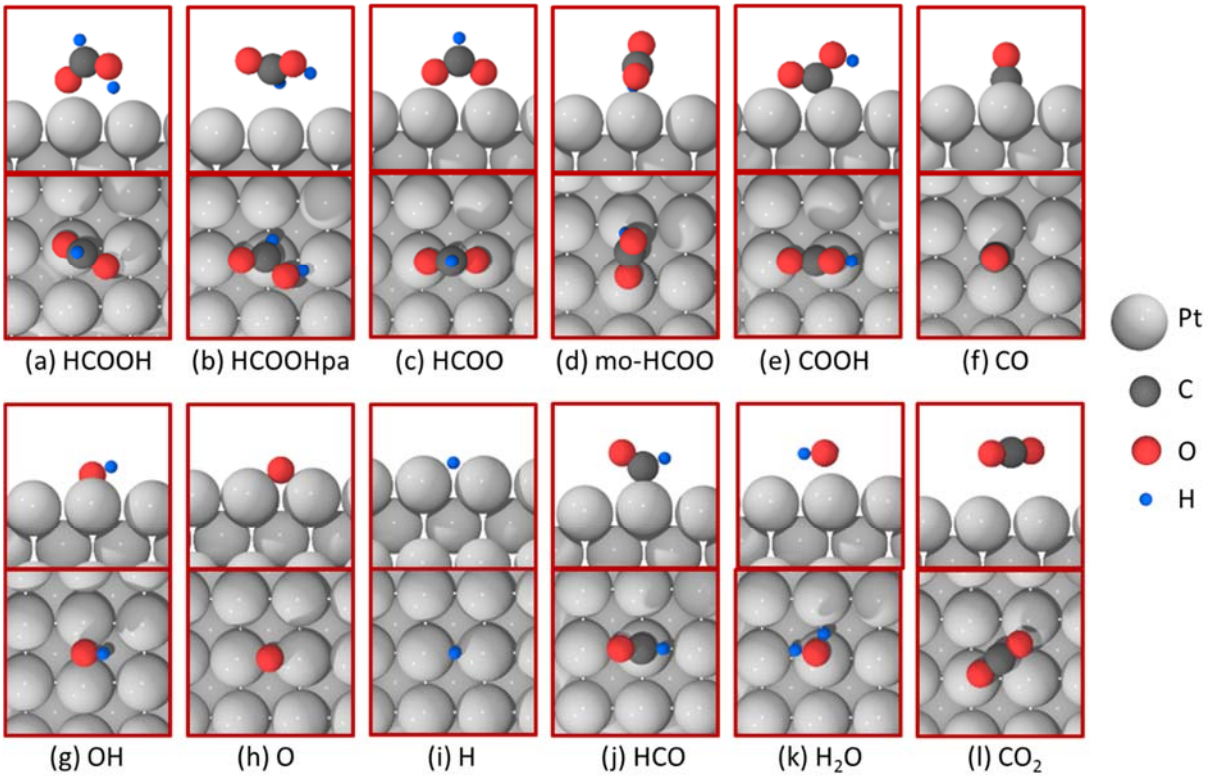


**Figure 6-2** Side and top views of the most stable configurations of intermediates on Pt(100). Platinum, carbon, hydrogen and oxygen atoms are indicated in silver, dark grey, blue and red, respectively.

On Pt(100), HCOO formation from HCOOH is an exothermic (-0.06 eV) reaction with an activation barrier of 0.70 eV, which is slightly smaller than the barrier of transformation of HCOOH to its cis-parallel configuration (HCOOHpa) 0.89 eV. The subsequent decomposition of HCOOHpa to COOH, however, is fairly easy on Pt(100) with a negligible barrier of 0.09 eV. Similar as on Pt(111), HCOO decomposition is also a two-step reaction going through its isomer mo-HCOO, though the second step (decomposition of mo-HCOO) is a spontaneous reaction. Transformation of formate from the bidentate to the monodentate structure requires a barrier of 1.08 eV. COOH preferentially decomposes to CO rather than $CO_2$ on Pt(100), with a barrier of

0.57 eV for the former and 0.91 eV for the latter. O- or OH-assisted COOH decomposition is even easier on Pt(100) with the former reaction being spontaneous and the latter has a negligible barrier of 0.10 eV, while H-assisted HCOO decomposition is very difficult on Pt(100) with a large activation energy of 2.04 eV.

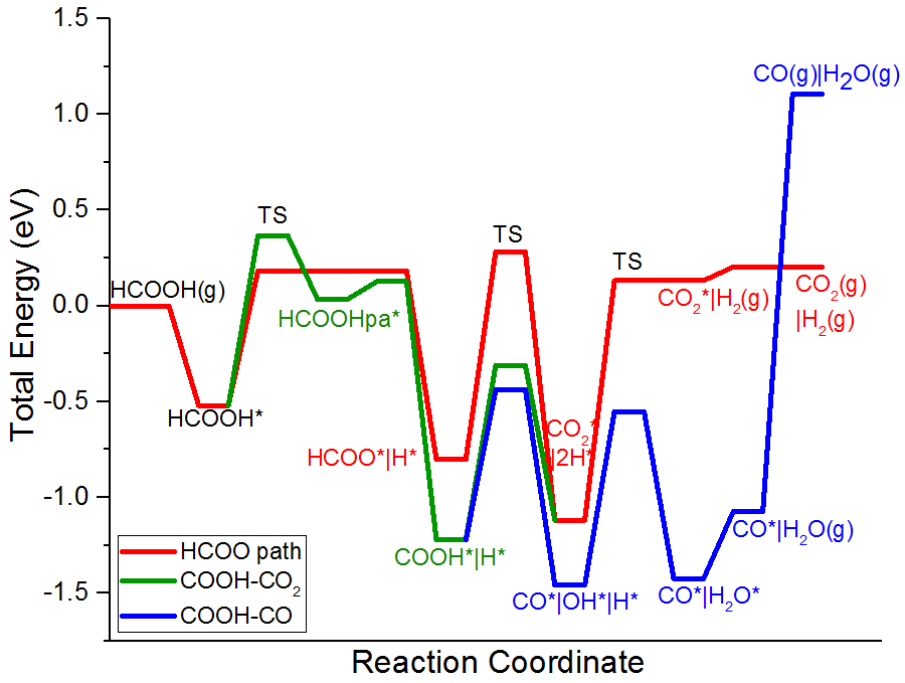


**Figure 6-3** Potential energy surface of HCOOH decomposition on Pt(100). Red line is the HCOO pathway, green line is the COOH pathway leading to $CO_2$ formation, blue line is the COOH pathway leading to CO formation.

Most bond-breaking steps on Pt(100) have a larger activation energy barrier than those on Pt(111), presumably due to the more endothermic nature of these reactions on Pt(100), except for the decomposition of HCOOHpa to COOH and COOH decomposition to CO, which are more exothermic on Pt(100) facet and consequently require a smaller barrier. **Figure 6-3** shows the PES of HCOOH decomposition on Pt(100). It can be found that on Pt(100) surface, COOH formation is more difficult (by 0.19 eV) than HCOO formation due to higher barrier of formic acid transformation during COOH formation, however, COOH decomposition is much easier (by more

than 0.5 eV) than HCOO decomposition, primarily because COOH is more stable than HCOO by 0.42 eV on Pt(100); this trend is similar as on Pt(111) surface. COOH is also the main source for $CO_2$ production on Pt(100). On contrary to the closed facet, COOH preferentially decomposes to CO on Pt(100) rather than $CO_2$.

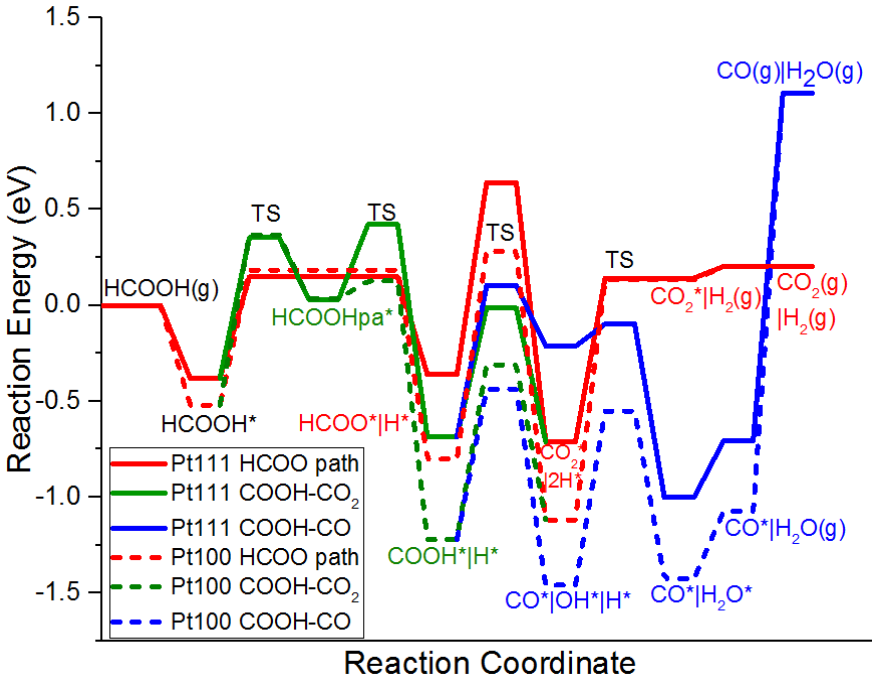


**Figure 6-4** Comparison of the PESs of HCOOH decomposition on Pt(100) and Pt(111). Solid lines are for Pt(111) while dashed lines are for Pt(100). Red color indicates the HCOO pathway, green color indicates the COOH pathway leading to $CO_2$ formation, and blue line indicates the COOH pathway leading to CO formation.

**Figure 6-4** compares the PESs on the two facets Pt(100) and Pt(111). It is clear that although most decomposition steps have a higher activation energy on Pt(100) than on Pt(111), due the stabilization of intermediates on Pt(100), the transition states (TS) are also stabilized on Pt(100), especially for the TS of the second dehydrogenation step. Another noteworthy point is that HCOOHpa decomposition has a negligible barrier (0.09 eV) on Pt(100), while the corresponding barrier on Pt(111) is a modest value 0.39eV, as we mentioned earlier that HCOOHpa desorbs easily from the surface, there is a higher potential for HCOOHpa to leave the surface of Pt(111)

than Pt(100). And since HCOOHpa is the precursor for COOH formation, which provides the main source for $CO_2$ production, Pt(100) should be more active than Pt(111) for HCOOH decomposition. But, Pt(100) is more prone to CO poisoning than Pt(111) first because Pt(100) binds CO more strongly than Pt(111) by 0.37 eV, and also because CO formation is a favorable decomposition path for COOH.

### 6.3.2 CO coverage effects on the BEs of key intermediates HCOO, COOH and CO

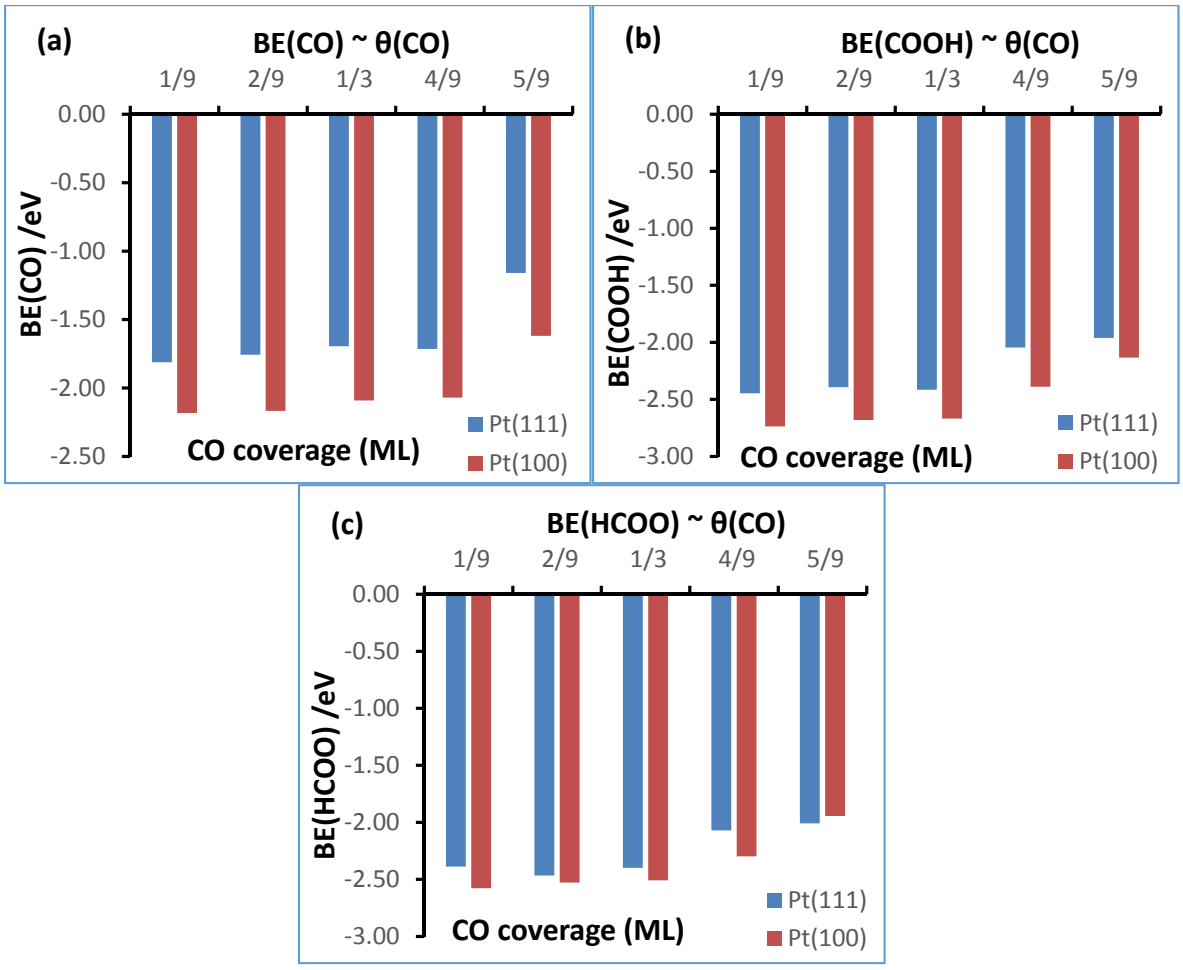


**Figure 6-5** Binding energy (BE) of (a) CO, (b) COOH and (c) HCOO as a function of surface coverage of CO. Blue bars indicate BEs on Pt(111) while red bars indicate BEs on Pt(100).

Since the Pt catalysts used in HCOOH decomposition experiments are expected to be covered by CO, we also investigated the CO coverage effects on the binding energies of the key intermediates HCOO, COOH and also CO itself on Pt(111) and Pt(100). BEs of the three intermediates were calculated on the two surfaces with different CO coverages (up to 5/9 monolayer (ML)) and results are shown in **Figure 6-5** and **Table 6-3**. CO coverage used in its binding energy calculations is the total coverage of CO on the surface, including the spectator CO molecules and the one being treated as the adsorbate; BE of CO is calculated in a differential manner. Clearly, Pt(100) binds the three intermediates more strongly than the Pt(111) surface, except for HCOO at CO coverage of 5/9 ML, where Pt(111) binds HCOO slightly more strongly than Pt(100) by 0.07 eV. At CO coverage lower than 5/9 ML, Pt(100) binds HCOO more strongly than Pt(111) by 0.05-0.25 eV. Among the three intermediates, the largest BE difference between the two facets is seen on CO, of which the BE is increased by 0.35-0.50 eV going from Pt(111) to Pt(100), indicating that binding of CO is very sensitive to the surface structure. In terms of BE, COOH has the intermediate structure sensitivity among the three species, with BE difference between the two facets ranges from 0.15 eV to 0.35 eV.

**Table 6-3** Binding energies (BEs) of CO, COOH and HCOO on Pt(111) and Pt(100) at CO coverage of 1/9~5/9 ML with an increment of 1/9ML.

| CO coverage (ML) | BE(CO) | | BE(COOH) | | BE(HCOO) | |
|---|---|---|---|---|---|---|
| | Pt(111) | Pt(100) | Pt(111) | Pt(100) | Pt(111) | Pt(100) |
| 1/9 | -1.81 | -2.18 | -2.45 | -2.74 | -2.39 | -2.58 |
| 2/9 | -1.76 | -2.17 | -2.39 | -2.68 | -2.47 | -2.53 |
| 3/9 | -1.70 | -2.09 | -2.42 | -2.67 | -2.40 | -2.51 |
| 4/9 | -1.71 | -2.07 | -2.05 | -2.39 | -2.07 | -2.30 |
| 5/9 | -1.16 | -1.62 | -1.96 | -2.13 | -2.01 | -1.94 |

Up to CO coverage of 1/3 ML, there is little variance (ca. 0.1 eV) in the binding energies of the three species on both facets. For CO, its binding energy does not change much with increasing CO

coverage until 4/9 ML, with another increase of 1/9 ML in CO coverage, its binding energy decreases by 0.55 eV and 0.45 eV on Pt(111) and Pt(100), respectively. For COOH, when CO coverage is increased from 1/3 ML to 4/9 ML, there is a decrease of 0.37 eV in its BE on Pt(111) and 0.28 eV on Pt(100); further increase of the CO coverage to 5/9 ML leads to a further decrease in the BE of COOH by 0.09 eV and 0.26 eV on Pt(111) and Pt(100), respectively. On Pt(111), BE of HCOO decreases from -2.40 eV to -2.07 eV when surface CO coverage is increased from 1/3 ML to 4.9 ML, and further increase in CO coverage to 5/9 ML does not affect the BE of HCOO much; there is a total decrease of 0.38 eV in BE of HCOO when Pt(111) surface is exposed to 5/9 ML of CO. On Pt(100), BE of HCOO decreases by 0.21 eV when CO coverage is increased from 1/3 ML to 4/9 ML, and further increase of CO coverage to 5/9 ML result in another decrease of 0.36 eV in BE of HCOO. The total decrease in BE of HCOO on Pt(100) when 5/9 ML of CO is introduced into the system is 0.64 eV, much higher than the corresponding value on Pt(111). Thus the CO coverage effect on the BE of HCOO is more dramatic on Pt(100) than on Pt(111), especially when CO coverage is high.

Since there is a noticeable change in the binding energies of the key intermediates in formic acid decomposition, namely, CO, COOH and HCOO, when CO coverage is around 4/9~5/9 ML, further calculations were conducted on 4/9 ML of CO-covered Pt(111) and Pt(100) surfaces for HCOOH decomposition to investigate the CO coverage effects on the reaction pathways and the reaction energetics. Results will be discussed in the following sections.

### 6.3.3 Results on 4/9 ML of CO covered Pt(111)

The most stable configurations of the intermediates on 4/9 ML of CO covered Pt(111) are shown in **Figure 6-6** and their BEs are summarized in **Table 6-4**. The most stable configuration of formic acid is still the trans-perpendicular configuration, similar as on the clean surfaces, with a BE of -

0.22 eV. The precursor for COOH formation is a cis-perpendicular configuration of formic acid (**Figure 6-6 (b)**), unlike all the other configurations of formic acid have been discussed where the molecule binds through its O atom with the C-H bond pointing away from the surface, the C-H bond the cis-perpendicular formic acid is pointing down towards the surface, but for the ease of comparison with other surfaces, the same denotation HCOOHpa is used for this cis-perpendicular formic acid. There is weak hydrogen bonding between the hydroxyl H in HCOOHpa and a nearby CO with a O-H bond length of 1.9 Å; even with the hydrogen bonding, BE of HCOOHpa is still calculated to be a positive value 0.30 eV, indicating easy desorption of HCOOHpa from the surface.

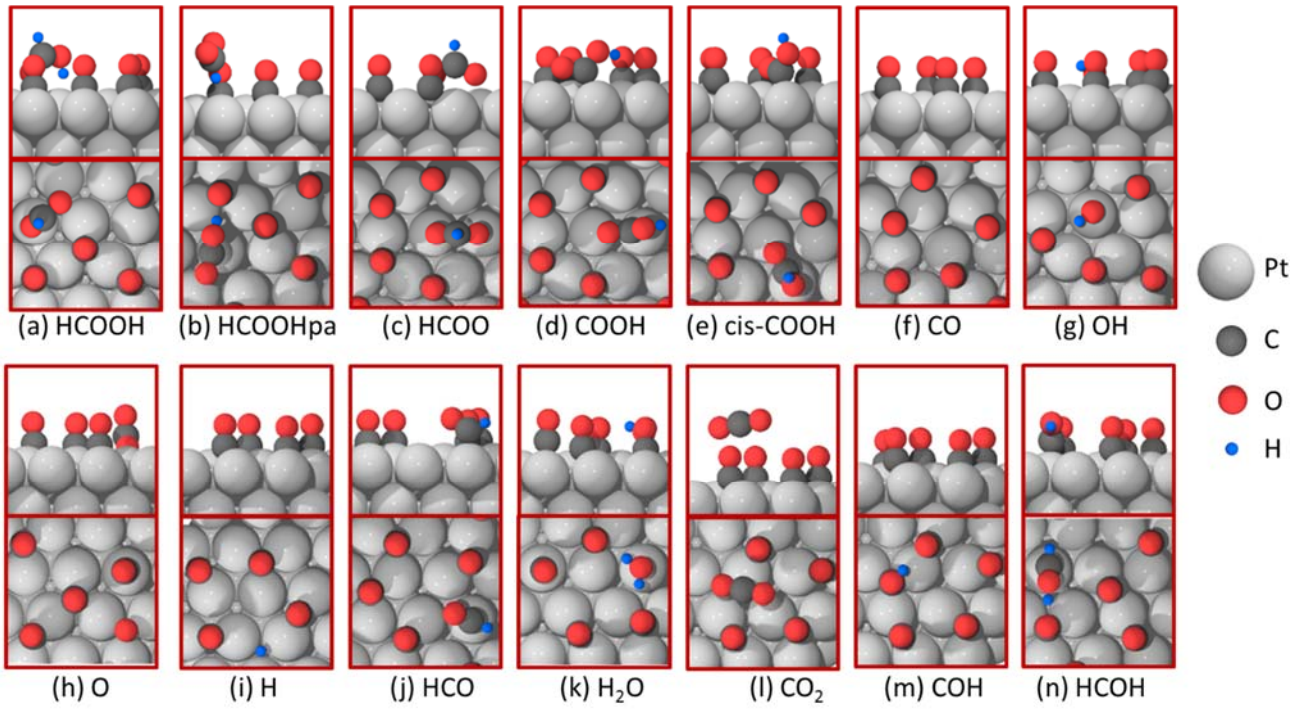


**Figure 6-6** Side and top views of the most stable configurations of intermediates on 4/9 ML of CO covered Pt(111). Platinum, carbon, hydrogen and oxygen atoms are indicated in silver, dark grey, blue and red, respectively.

Formate (HCOO) still prefers the bindentate configuration where two O atoms bind to two adjacent top sites; it has a BE of -2.07 eV. On CO covered Pt(111) surface, two configurations of carboxyl were explored: trans carboxyl (COOH, by default, indicates the trans carboxyl) and cis

carboxyl (cisCOOH). They both bind through the C and O atom to two adjacent top sites, the only difference is that O-H bond in trans carboxyl is pointing down towards the surface while in cis carboxyl the O-H bond is pointing away from the surface. Trans carboxyl is slightly more stable than cis carboxyl with a BE of -2.05 eV for the former and -1.97 eV for the latter. Carbon monoxide, oxygen atom and hydrogen atom all prefer the three-fold fcc site, with BEs of -1.16 eV, -3.20 eV and -2.59 eV, respectively. Hydroxyl (OH), formyl (HCO) and water all prefer the top site, with BEs of -1.92 eV, -2.00 eV and -0.36 eV, respectively. Carbon dioxide is physisorbed on the surface with a BE of -0.08 eV.

**Table 6-4** Calculated PW91 binding energies (BE) of intermediates at their preferred adsorption site on 4/9 ML of CO covered Pt(111) and Pt(100).

| **Species** | **4/9 ML of CO covered Pt(111)** | | **4/9 ML of CO covered Pt(100)** | |
|---|---|---|---|---|
| | **adsorption site** | **BE / eV** | **adsorption site** | **BE / eV** |
| HCOOH* | top-bridge | -0.22 | top-hollow | -0.43 |
| HCOOHpa* | top | 0.30 | top | -0.16 |
| HCOO* | top-top | -2.07 | top-top | -2.30 |
| COOH* | top-top | -2.05 | top-top | -2.39 |
| cisCOOH* | top-top | -1.97 | top-top | -2.35 |
| CO* | fcc/hcp | -1.16 | bridge | -1.62 |
| OH* | top | -1.92 | bridge | -2.43 |
| O* | fcc | -3.20 | bridge | -3.38 |
| H* | fcc | -2.59 | bridge | -2.77 |
| HCO* | top | -2.00 | top-top | -2.33 |
| $H_2O$* | top | -0.36 | hollow | -0.23 |
| $CO_2$* | physisorbed | -0.08 | physisorbed | -0.13 |
| COH* | fcc | -4.17 | bridge | -4.43 |
| HCOH* | top | -3.08 | bridge | -3.53 |

Two additional intermediates were explored on CO covered Pt(111) surface: hydroxymethylidyne (COH) and hydroxymethylene (HCOH). COH binds through its C atom to the 3-fold fcc site with C-O bond being perpendicular to the surface and an angel of 112 degree for C-O-H. COH has a

BE of -4.17 eV and it is more stable than its isomer HCO by 0.41 eV. HCOH prefers the top site with C-H bond pointing upward and O-H bond pointing downward. There is a clear hydrogen bonding between the hydroxyl H in HCOH and a nearby CO, with the H-O bond length being 1.5 Å; BE of HCOH is -3.08 eV.

**Table 6-5** PW91 reaction energies(ΔE) and activation energy barriers (Ea) for the elementary steps considered in the HCOOH decomposition reaction network on 4/9 ML of CO covered Pt(111) and Pt(100) . All the values are relative to the infinite separation initial/final state.

| # | Reaction | 4/9 ML of CO covered Pt(111) | | 4/9 ML of CO covered Pt(100) | |
|---|---|---|---|---|---|
| | | $E_a$ / eV | ΔE / eV | $E_a$ / eV | ΔE / eV |
| 1 | HCOOH + * ↔ HCOOH* | | -0.22 | | -0.43 |
| 2 | HCOOH* + * ↔ HCOO* + H* | 0.85 | 0.24 | 0.73 | 0.04 |
| 3 | HCOOH* ↔ HCOOHpa* | 0.62 | 0.52 | 0.34 | 0.26 |
| 4[a] | HCOOHpa* + * ↔ COOH* + H* | 0.50 | -0.51 | 0.43 | -0.54 |
| 5 | HCOO* + * ↔ $CO_2$* + H* | 1.26 | -0.51 | 1.25 | -0.52 |
| 6 | COOH* + * ↔ $CO_2$* + H* | 1.04 | -0.27 | 1.20 | -0.17 |
| 7 | COOH* ↔ cisCOOH* | 0.49 | 0.08 | 0.45 | 0.04 |
| 8 | cisCOOH* + * ↔ CO* + OH* | 0.71 | 0.57 | 0.84 | 0.22 |
| 9 | COOH* + O* ↔ $CO_2$* + OH* | 0.64 | -1.00 | 0.59 | -1.05 |
| 10 | COOH* + OH* ↔ $CO_2$* + $H_2O$* | 0.34 | -1.36 | 0.28 | -0.43 |
| 11 | HCOO* + COOH* ↔ HCOOHpa* + $CO_2$* | 0.89 | -0.52 | 1.08 | -0.21 |
| 12 | HCO* + * ↔ CO* + H* | 0.63 | -0.42 | 0.65 | -0.73 |
| 13 | CO* + O* ↔ $CO_2$* + * | 0.52 | -1.89 | 0.28 | -1.30 |
| 14 | O* + H* ↔ OH* + * | 0.71 | -0.73 | 0.40 | -0.88 |
| 15 | 2OH* ↔ $H_2O$* + O* | -0.17 | -0.36 | 0.48 | 0.62 |
| 16 | OH* + H* ↔ $H_2O$* + * | 0.30 | -1.09 | 0.68 | -0.26 |
| 17 | 2H* ↔ $H_2$ + 2* | 1.02 | 0.61 | 1.04 | 0.98 |
| 18 | HCOOH* + 2CO* ↔ 2COH* + $CO_2$* | 2.31 | -0.26 | -- | -- |
| 19 | HCOOH* + CO* ↔ COH* + HCOO* | 1.03 | 0.25 | -- | -- |
| 20 | HCOO* + CO* ↔ COH* + $CO_2$* | 2.04 | -0.50 | 2.44 | -0.13 |
| 21 | COOH* + CO* ↔ COH* + $CO_2$* | 0.94 | -0.27 | 1.26 | 0.22 |
| 22 | HCO* + CO* ↔ COH* + CO* | 0.96 | -0.41 | 1.02 | -0.35 |
| 23 | OH* + CO* ↔ HCO* + O* | 1.63 | 1.15 | 2.61 | 1.61 |
| 24 | OH* + CO* ↔ COH* + O* | 1.36 | 0.74 | 1.60 | 1.27 |
| 25 | COH* + * ↔ CO* + H* | 1.41 | -0.01 | 1.17 | -0.39 |
| 26 | COH* + H* ↔ HCOH* + * | 1.10 | 0.25 | 1.16 | 0.25 |
| 27 | HCOH* + * ↔ HCO* + H* | 0.68 | 0.16 | 0.73 | 0.10 |

| | | | | | |
|---|---|---|---|---|---|
| 28 | HCOH* + 2* ↔ CO* + 2H* | 1.23 | -0.26 | -- | -- |
| 29 | $CO_2$* ↔ $CO_2$ + * | | 0.08 | | 0.13 |
| 30 | $H_2O$* ↔ $H_2O$ + * | | 0.36 | | 0.23 |
| 31 | CO* ↔ CO + * | | 1.16 | | 1.62 |
| CO* in red color indicates the preadsorbed CO molecule.<br>a, this reaction forms cisCOOH on 4/9ML of CO covered Pt(100). | | | | | |

CO coverage effects on the BEs of COOH, HCOO and CO have been discussed in the previous section. Destabilization of other intermediates at high CO coverage is also found by comparing the BEs on clean Pt(111) and 4/9 ML of CO covered Pt(111). It is found that O is destabilized by 0.54 eV and HCO is destabilized by 0.35 eV with the presence of 4/9 ML of CO on Pt(111) surface, while for the rest of the species the stabilization is around 0.10 eV.

At CO coverage of 4/9 ML, the reaction network we proposed for HCOOH decomposition is comprised of 31 elementary steps. The first 17 steps were also investigated on the clean surfaces, while the rest are H transfer reactions between adsorbates and preadsorbed molecules and reactions related to the new intermediates COH and HCOH, which are unique reactions only occur on CO covered surfaces.

On 4/9 ML of CO covered Pt(111) surface, HCOOH needs to come across a barrier of 0.85 eV to decompose to HCOO, which directly decomposes to $CO_2$ and H without going through its monodentate isomer; the barrier of the second dehydrogenation step is 1.26 eV. Hydrogen recombination is endothermic by 0.61 eV with a barrier of 1.02 eV; unlike the clean Pt(111) surface, the reverse reaction ($H_2$ decomposition) is no longer spontaneous on CO covered Pt(111) surface. For the three steps in HCOO pathway, the activation energy is increased by 0.15-0.35 eV with the presence of 4/9 ML of CO on the Pt(111) surface.

COOH formation from HCOOH is a three-step reaction on CO covered Pt(111) surface. The most stable trans-perpendicular configuration of HCOOH (**Figure 6-6 (a)**) first transforms to a tilted cis configuration (HCOOHt, inset in **Figure 6-7 (a)**) with a barrier of 0.63 eV, then further transforms to HCOOHpa (**Figure 6-6 (b)**) with a barrier of 0.43 eV; the last C-H bond breaking step from HCOOHpa requires another barrier of 0.50 eV to form COOH and H. The first two transformation step is combined as reaction 3 in **Table 6-5**, which reports the Ea calculated from the higher TS among the two and the overall reaction energy. Decomposition of COOH to $CO_2$ and H is exothermic by -0.27 eV with an activation energy of 1.04 eV. Comparing with the energetics on clean Pt(111), we found that similar barriers are required for COOH formation on CO covered Pt(111), while COOH decomposition to $CO_2$ at high CO coverage needs to come across a barrier of 0.37 eV higher.

COOH decomposition to CO is a two-step reaction at CO coverage of 4/9 ML on Pt(111). The most stable trans carboxyl first transforms to its isomer cisCOOH with a barrier of 0.49 eV, which then breaks the C-O bond with a barrier of 0.71 eV. The high CO coverage does not affect the activation energy barrier for COOH decomposition and a similar barrier of 0.79 eV is found on the clean Pt(111) surface, except that the reaction goes through an additional transformation step at high CO coverage.

**Figure 6-7 (a)** plots the abovementioned three pathways on the same PES diagram. It is clear that on 4/9 ML of CO covered Pt(111) surface, COOH formation is slightly more difficult than HCOO formation, as the highest TS in COOH formation is 0.17 eV higher than the TS for HCOO formation, while HCOO decomposition has a TS that is 0.46 eV higher than the TS for COOH decomposition to $CO_2$. And COOH preferentially decomposes to CO rather than $CO_2$, which is on contrary to the case on clean Pt(111). Although the COOH pathway is energetically more favorable

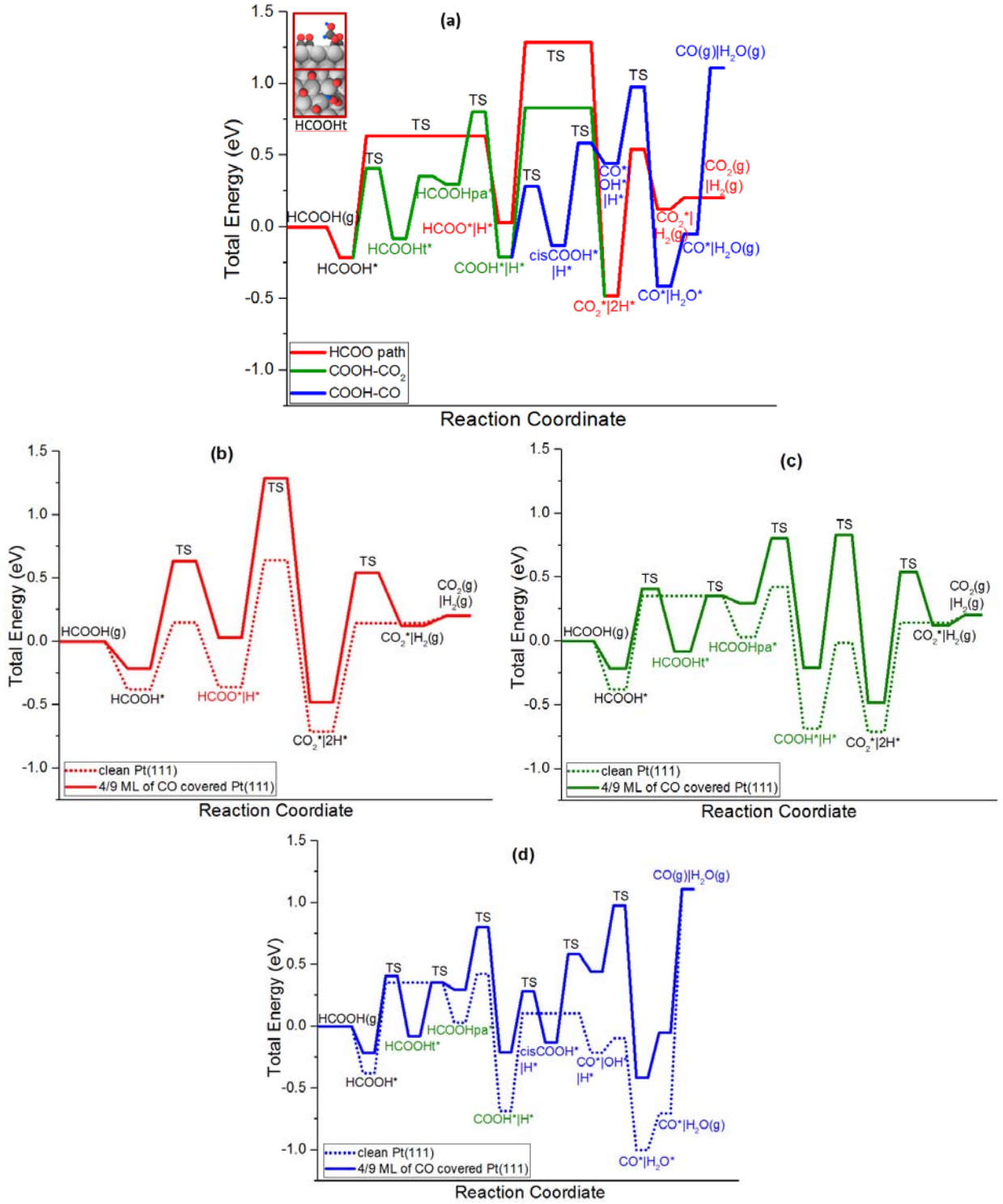


**Figure 6-7** (a) Potential energy surface of HCOOH decomposition on 4/9 ML of CO covered Pt(111), and comparison of (b) the HCOO pathway, (c) COOH-$CO_2$ pathway and (d) COOH-CO pathway on clean Pt(111) with CO covered Pt(111). Red line is the HCOO pathway, green line is the COOH pathway leading to $CO_2$ formation, blue line is the COOH pathway leading to CO

formation. Solid line indicates the CO covered Pt(111) surface, while dotted line indicates the clean Pt(111) surface.

than HCOO pathway, which has a very high TS for HCOO decomposition, COOH formation needs to go through a metastable state HCOOHpa which desorbs from the surface very easily; if desorption of HCOOHpa happens, subsequent COOH formation and decomposition will not take place, and reaction has to proceed through the HCOO pathway. The relative favorability of the HCOO and COOH pathways will depend on the competition between desorption and decomposition of HCOOHpa under reaction environments. **Figure 6-7 (b), (c)** and **(d)** compare the three pathways on clean Pt(111) and 4/9 ML of CO covered Pt(111) surface. It can be seen that although the difference in absolute activation energy barriers on the two surfaces is not big (at most 0.37 eV), due to the destabilization of the intermediates with CO presence, the TSs in all three pathways are significantly destabilized on CO covered Pt(111), leading to a lower reactivity for HCOOH decomposition at high CO coverage.

Besides the three pathways we just discussed, formic acid decomposition could also proceed through H transfer reactions (reactions 18-24 in **Table 6-5**) to preadsorbed CO molecules, forming COH or HCO, which can either decompose directly or through the HCOH intermediate. However, the H transfer reactions are found to be very difficult, e.g. transfer of the two hydrogens in HCOOH simultaneously to two nearby CO molecules forming two COH species requires a barrier of 2.31 eV, while transfer of one hydrogen in HCOOH to one nearby CO forming HCOO and COH requires a lower barrier of 1.03 eV, which is still 0.18 eV higher than the barrier for the direct decomposition of HCOO. Similar for HCOO, COOH and HCO, the H transfer reactions of which are also more difficult that their direct decomposition by 0.3-0.8 eV. Furthermore, decomposition of COH formed from the H transfer reactions, either the direct decomposition or decomposition

through the HCOH intermediate are also very difficult, with barriers more than 1 eV. Thus the hydrogen transfer reactions on 4/9 ML of CO covered Pt(111) surface are not relevant for HCOOH decomposition.

### 6.3.4 Results on 4/9 ML of CO covered Pt(100)

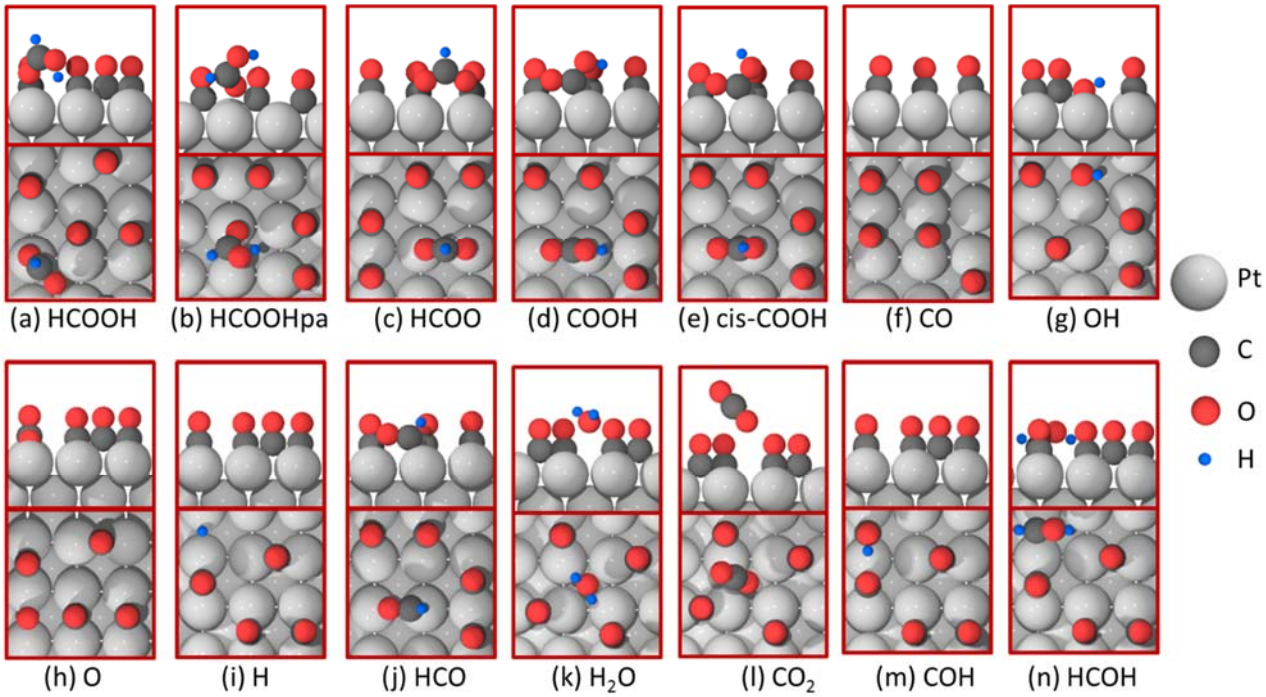


**Figure 6-8** Side and top views of the most stable configurations of intermediates on 4/9 ML of CO covered Pt(100). Platinum, carbon, hydrogen and oxygen atoms are indicated in silver, dark grey, blue and red, respectively.

The most stable configurations of the intermediates on 4/9 ML of CO covered Pt(100) surface are summarized in **Figure 6-8**. For formic acid, the trans-perpendicular configuration is the most stable configuration with a BE of -0.43 eV, which is 0.27 eV more stable than the trans-parallel configuration HCOOHpa. Formate (HCOO) binds through the two oxygen atoms to the top-top site on the surface, with a BE of -2.30 eV. Carboxyl (COOH), cis carboxyl (cisCOOH) and formyl (HCO) all bind through their C and O atoms to the top-top site on the surface, with BEs of -2.39

eV, -2.35 eV and -2.33 eV, respectively. $H_2O$ prefers the hollow site with a weak BE of -0.23. $CO_2$ is also physisorbed on the surface with a BE of -0.13 eV. For all the other intermediates (CO, OH, O, H, COH and HCOH), bridge site is the most favorable adsorption site.

CO coverage effects on the BE of COOH, HCOO and CO on the (100) facet of Pt have been discussed in section 6.3.2. Destabilization of other intermediates at high CO coverage is also found on Pt(100), epically for OH and O, which are destabilized by 0.28 eV and 0.51 eV with the presence of 4/9 ML of CO. For the other species, the destabilization at high CO coverage is generally between 0.1 and 0.2 eV.

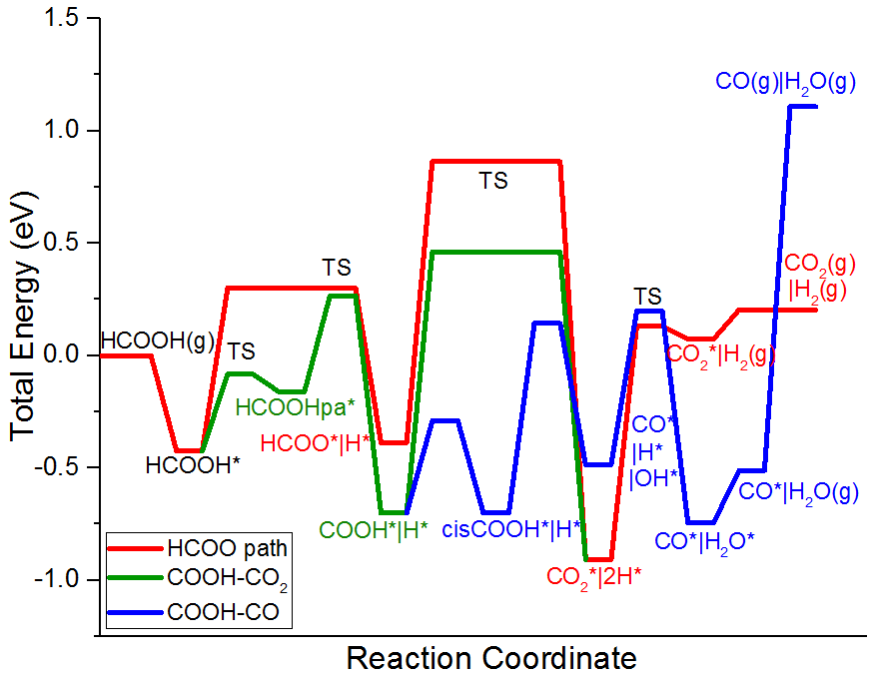


**Figure 6-9** Potential energy surface of HCOOH decomposition on 4/9 ML of CO covered Pt(100). Red line is the HCOO pathway, green line is the COOH pathway leading to $CO_2$ formation, blue line is the COOH pathway leading to CO formation.

At CO coverage of 4/9 ML, compared with Pt(111), Pt(100) binds the intermediates more strongly by ca. 0.2-0.5 eV. Similar as on clean surfaces, OH is also the species most sensitive to surface

structure at CO coverage of 4/9 ML, where it is stabilized by 0.51 eV on Pt(100) compared with Pt(111).

On 4/9 ML of CO covered Pt(100) surface, HCOOH need to come across a barrier of 0.73 eV to break the O-H bond and form HCOO, which further goes through another dehydrogenation step with a barrier of 1.25 eV to form $CO_2$. The two hydrogen atoms formed from the two dehydrogenation steps recombine to a $H_2$ molecule with a barrier of 1.04 eV. Small differences in activation energies of the three steps are found between the clean Pt(100) surface and 4/9 ML of CO covered Pt(100) surface, around 0-0.2 eV.

For the COOH pathway on 4/9 ML of CO covered Pt(100) surface, HCOOH needs to go through a transformation step first with a barrier of 0.34 eV, and then breaks the C-H bond forming COOH with a barrier of 0.43 eV. Further decomposition of COOH to $CO_2$ is an exothermic reaction with a barrier of 1.20 eV. At CO coverage of 4/9 ML, the transformation step of formic acid has a barrier of 0.55 eV lower than that on clean Pt(100), while the C-H bond breaking in HCOOH and O-H bond breaking in COOH have a barrier of 0.34 eV and 0.29 eV higher than that on clean Pt(100).

On CO covered Pt(100) surface, COOH decomposition to CO proceeds through a transformation step to cisCOOH with a barrier of 0.45 eV, followed by the C-O bond breaking step with a barrier of 0.84 eV, which is 0.27 eV higher than the barrier on clean Pt(100) surface.

**Figure 6-9** plots the three pathways we just discussed on the same PES diagram. It can be seen than on 4/9 ML of CO covered Pt(100) surface, the COOH pathway is more favorable than the HCOO pathway, TSs of which are much higher in energy than those in the COOH pathway. CO covered Pt(100) is the only surface on which the COOH formation is easier than HCOO formation from HCOOH, among the four surfaces we have discussed. And unlike the other three surfaces,

the precursor for COOH formation, HCOOHpa, on CO covered Pt(100) surface is a stable intermediate with a BE of -0.16 eV. Further decomposition of COOH preferentially forms CO rather than $CO_2$.

For the H transfer reactions of COOH, HCOO, HCO and OH, the barriers are much higher than the direct decomposition these intermediates by 0.3-1.2 eV, and further decomposition of the product formed from the H transfer reactions, COH, is also very difficult with barriers of more than 1 eV. Thus the hydrogen transfer reactions are not relevant for HCOOH decomposition on 4/9 ML of CO covered Pt(100) surface.

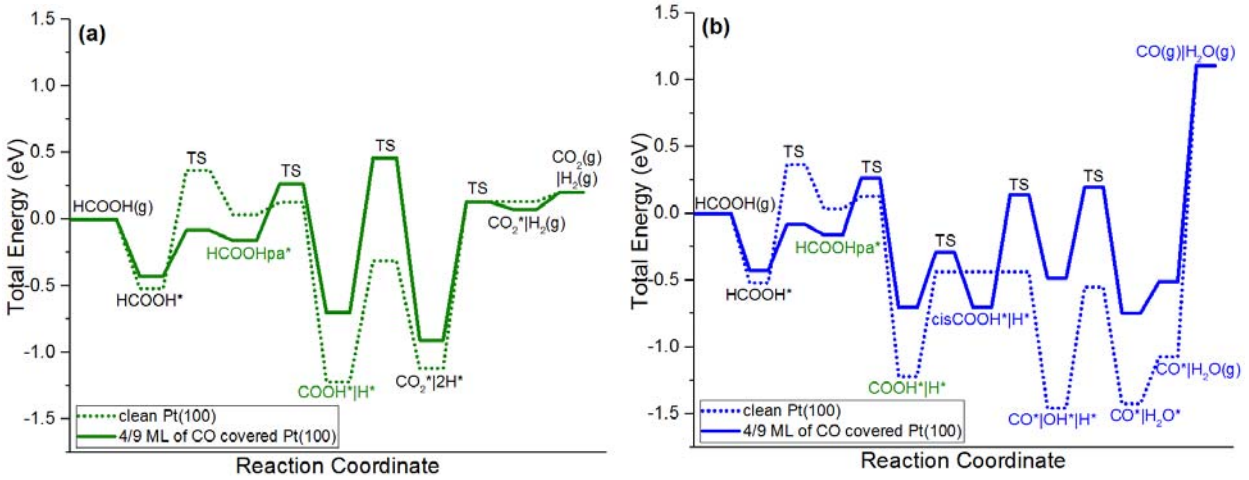


**Figure 6-10** Comparison of (a) the COOH-$CO_2$ pathway and (b) the COOH-CO pathway on clean Pt(100) and 4/9 ML of CO covered Pt(100) surface. Solid line indicates the CO covered Pt(100) surface, while dotted line indicates the clean Pt(100) surface.

Since COOH pathway is more favorable than the HCOO pathway on 4/9 ML of CO covered Pt(100) surface, **Figure 6-10** compares the COOH pathway on the CO covered Pt(100) surface with that on the clean Pt(100) surface. It can be seen that transformation of formic acid is slightly easier on CO covered Pt(100) surface than on the clean Pt(100) surface, while HCOOH decomposition to COOH and COOH decomposition to $CO_2$ or CO has much higher TS energies on CO covered

Pt(100) surface than on clean Pt(100), leading to more difficult decomposition of COOH at high CO coverage.

At CO coverage of 4/9 ML, although the differences in absolute activation energies of the three pathways between Pt(111) and Pt(100) are very small, less than 0.3 eV, due to the stabilization of the intermediates on the more open facet by ca. 0.2-0.5 eV, the TSs are significantly stabilized on CO covered Pt(100) surface (**Figure 6-11**), leading to much higher reactivity for HCOOH decomposition on Pt(100) than Pt(111) at high CO coverage.

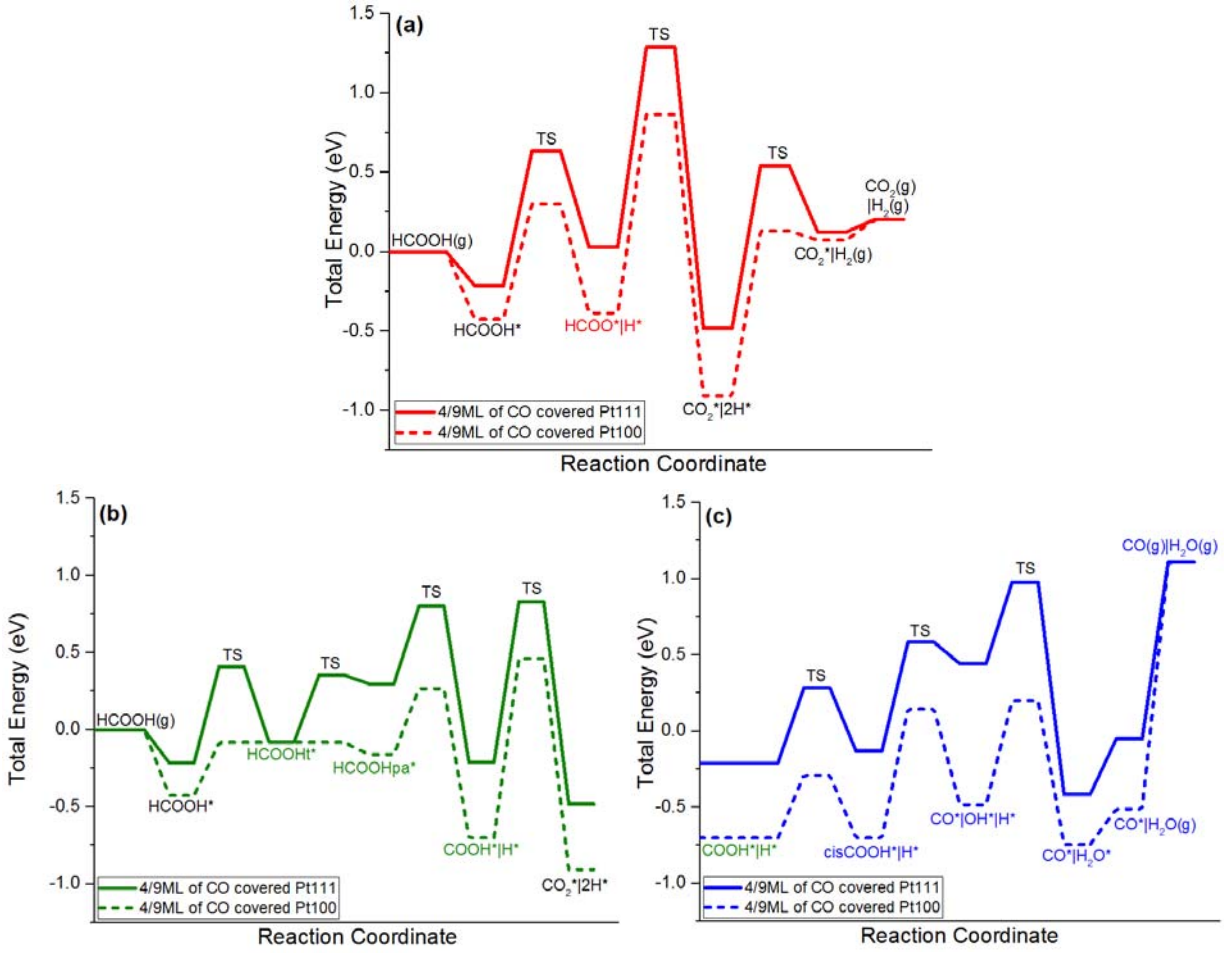


**Figure 6-11** Comparison of (a) the HCOO pathway, (b) COOH-$CO_2$ pathway, and (c) COOH-CO pathway on Pt(111) and Pt(100) at CO coverage of 4/9 ML. Solid line indicates the CO covered Pt(111) surface, while dashed line indicates the CO covered Pt(100) surface.

## 6. 4 Conclusions

Using DFT calculations, the structure sensitivity of formic acid decomposition on Pt catalysts was investigated by comparing results on (111) and (100) facets of Pt, and the CO coverage effects were explored by comparing results on clean and 4/9 ML of CO covered Pt(111) and Pt(100). It is found that Pt(100) binds the intermediates more strongly by 0.1-0.5 eV than Pt(111), both on the clean surface and at CO coverage of 4/9 ML. And Pt(100) also has a high activity for formic acid decomposition than Pt(111), both for the clean surface and 4/9 ML of CO covered surface.

Three reaction pathways were explored: HCOO pathway, COOH pathway leading to $CO_2$ formation, and COOH pathway leading to CO formation. It is found that on all surfaces being examined, COOH formation is more difficult than HCOO formation except for the CO covered Pt(100) surface where the reverse trend is true, while COOH decomposition is much easier than HCOO decomposition. And except on clean Pt(111), COOH preferentially decomposes to CO. The precursor for COOH formation, HCOOHpa, is a metastable intermediate which desorbs easily on all surfaces being examined except for CO covered Pt(100). So the contribution of the COOH pathway to the overall reaction and also the selectivity to $CO_2$ and $H_2$ will depend on the easiness of decomposition of HCOOHpa compared with its desorption under reaction conditions. CO covered Pt(100) surface has the highest possibility for the COOH pathway to contribute to the overall reaction, since HCOOHpa binds more strongly on CO covered Pt(100) than on the other surfaces. Since COOH decomposition leads to CO formation on CO covered Pt(100), the selectivity to CO is also higher than on the other surface being examined.

At high CO coverage, hydrogen transfer reaction between the adsorbates and the preadsorbed CO molecules were also explored, and it is found that these reactions are not relevant for HCOOH decomposition due to the high activation energy barriers.

At high CO coverage, all intermediates are destabilized by 0.1-0.7 eV. All transition states except for transformation of formic acid are also destabilized significantly, partly due to the destabilization of intermediates, leading to a lower reactivity for formic acid decomposition at high CO coverage on Pt catalysts.

# Chapter 7 On the Structure Sensitivity of Formic Acid Decomposition on Cu Catalysts†

## 7.1 Introduction

Decomposition of formic acid (HCOOH) is an important process since HCOOH is a by-product produced in large quantities in the formation of levulinic acid from hydroxyl-methyl-furfural (HMF) during the production of fuels from biomass resources [9]. The *in-situ* catalytic dehydrogenation of HCOOH may provide hydrogen, which is necessary to hydrogenate levulinic acid to gamma-valerolactone (GVL) [14]. GVL is a valuable platform molecule with potential for producing both renewable fuels and chemicals. Also, HCOOH may be used directly as a fuel in direct formic acid fuel cells [19, 20, 65, 68] or as a hydrogen carrier [35, 36, 38] with a closed carbon cycle for other hydrogenation reactions.

The vapor-phase decomposition of HCOOH has been widely used to test the catalytic properties of various metals [43-45, 47], metal oxides [56, 57, 59] and alloys since the 1960s as HCOOH is one of the simplest organic molecules and carboxylic acids. HCOOH can decompose on metal surfaces through dehydrogenation or dehydration processes: the dehydrogenation leads to carbon dioxide ($CO_2$) and hydrogen ($H_2$) formation, while dehydration leads to production of water ($H_2O$) and carbon monoxide (CO), which is a poisoning species for noble metal catalysts such as Pt and Pd. Dehydrogenation products have been reported as the only products for HCOOH decomposition on Cu catalysts [200]. Spectroscopic studies of this reaction on Cu catalysts show the presence of a stable formate (HCOO) intermediate [201] on the catalyst surface that results from dissociation of the acidic hydrogen from HCOOH. Formate has also been proposed as a surface intermediate in several key catalytic reactions, including the water-gas shift (WGS) reaction [64, 103] and methanol synthesis [202].

†, Calculations on Cu(100) were performed by J. Scaranto.

Despite the large amount of experimental work concerning HCOOH decomposition on Cu catalysts, there is still an ongoing debate on the reaction mechanism and its structure sensitivity. Iglesia and Boudart [200] measured similar activation energies (94.5-100 kJ/mol) for HCOOH decomposition on Cu catalysts with various supports. These were also similar to those measured on different preferentially oriented and polycrystalline Cu catalysts by other researchers [203-205]. Based on these findings together with the observed insensitivity of the turnover rates to the particle size and to the nature of the catalyst support, they argued that HCOOH decomposition on Cu was structure insensitive. In contrast, Nakamura and coworkers [206] claimed that HCOOH decomposition on Cu catalysts was structure sensitive with dramatically different activation energies for dehydrogenation of HCOO on Cu(111) and Cu(110), although formate formation from $CO_2$ was structure insensitive when comparing these two Cu surfaces . Hu and Boyd [207] also found a strong dependence of the adsorption energy of HCOO on the surface structure of Cu; the adsorption energy of HCOO decreases in the order Cu(110) > Cu(100) > Cu(111). Bowker and other researchers [208, 209] reported that HCOOH deprotonates to HCOO on the clean Cu(110) and Cu(100) surfaces, but not on the clean Cu(111) surface where the presence of atomic oxygen is critical for formate to be formed.

A first-principles investigation of vapor-phase HCOOH decomposition on different Cu facets can help elucidate the reaction mechanism as well as to enable a better understanding of the behavior of Cu catalysts in terms of activity and structure sensitivity. In contrast to the abundant experimental studies, there is a lack of systematic theoretical studies for HCOOH decomposition on Cu surfaces. However, several elementary steps involved in the process are common to methanol synthesis and WGS reactions and have been investigated theoretically. In terms of shared reaction intermediates, prior work combining DFT, experimental kinetic studies, and microkinetic

modeling showed that HCOO formed on the surface of Cu [64] and Pt [103] catalysts during the WGS reaction but that intermediate is only a spectator species, whereas the reaction proceeds via a carboxyl (COOH)-mediated pathway. COOH is also a possible intermediate in the course of the HCOOH decomposition reaction through dissociation of the carbonic hydrogen from HCOOH. In a previous study of $CO/CO_2$ hydrogenation to methanol on Cu, Grabow and Mavrikakis [102] found that HCOOH is a relevant reactive intermediate and it prefers to decompose through the HCOO-mediated route on Cu(111). In this work, density functional theory (DFT) calculations were performed on two additional Cu model surfaces (Cu(100) and Cu(211)), exploring both COOH- and HCOO-mediated pathways and comparing with the previous results on Cu(111) to elucidate the reaction mechanism and its structure sensitivity of these Cu surfaces.

**7.2 Computational methods**

Periodic, self-consistent density functional theory calculations were performed with PW91-GGA [95, 151] exchange correlation functional using the DACAPO [88, 89] total energy code. Results on Cu(111) surface are taken from a previous work [102]. The methods used are restated here for clarity. The Cu(111) surface was modeled by a three-layer slab using a (3 × 3) unit cell, repeated in a super cell geometry with five equivalent layers of vacuum (~10.6 Å) between two successive metal slabs. Since the surface relaxation effects have been shown to be negligible for similar systems [210, 211], Cu atoms on Cu(111) surface were fixed in their bulk truncated positions during the calculation. The Cu(100) surface was modeled by a four-layer slab using a (3 × 3) unit cell with 11.0 Å of vacuum spacing separating the periodic slabs and the optimization was carried out by relaxing the top two layers. The Cu(211) slab was constructed using a (1 × 3) unit cell and consisted of nine Cu layers (having a terrace three atoms deep and three atoms wide). Successive slabs were separated by a vacuum equivalent to 12 Cu layers (~ 12.1 Å) and the top four layers of the slab

were allowed to relax during the calculation. The surface Brillouin zone was sampled at 54 Chadi-Cohen [92] k-points for Cu(111) and using a (4 × 4 × 1) Monkhorst-Pack grid [93] for Cu(100) and Cu(211) surfaces. Ultrasoft Vanderbilt pseudopotentials [94] were utilized to describe core electron interactions, and the Kohn-Sham one-electron valence states were expanded on the basis of plane waves with kinetic energy below 25 Ry. The electron density was determined by iterative diagonalization of the Kohn–Sham Hamiltonian, Fermi population of the Kohn–Sham states ($k_BT$ = 0.1 eV), and the Pulay mixing of the resulting electronic density. [97] All total energies were extrapolated to $k_BT$ = 0 eV. Adsorption was permitted on only one of the two exposed surfaces, and the electrostatic potential [91] was adjusted accordingly. Structures were fully relaxed until the Hellmann−Feynman forces acting on the atoms were smaller than 0.05 eV/Å. We calculated a lattice constant of 3.66 Å for bulk Cu, in good agreement with the experimental value 3.61 Å [212].

Binding energy (BE) of a surface intermediate was calculated with respect to the clean slab and the corresponding adsorbate (intermediate) in the gas phase. All the BE values, activation energies and heats of reactions in this work were reported with zero point energy (ZPE) corrections that were calculated by assuming a quantum harmonic oscillator possessing the calculated vibrational frequencies. The vibrational frequencies were calculated by numerical differentiation of forces using a second-order finite difference approach with a step-size of 0.015 Å. [101] Binding energies, activation energies and reaction energies without ZPE corrections can be found in the Supplementary Material. All activation energy barriers and reaction energies reported were relative to the reactant and product states at infinite separation. Minimum energy paths and activation energy barriers for all elementary steps were calculated using the climbing image nudged elastic band method (CI-NEB) [99]. The minimum energy path for each elementary step was discretized by a total of seven images, including the initial and final state. Convergence of the NEB

calculations was reached when the magnitude of the force on all images was less than 0.1 eV/Å, except for the hydrogen recombination reaction, where a stricter convergence criterion (0.05 eV/Å) was used. The transition states (TS) were confirmed by vibrational frequency calculations yielding a single imaginary frequency along the reaction coordinate.

### 7.3 Results and discussion

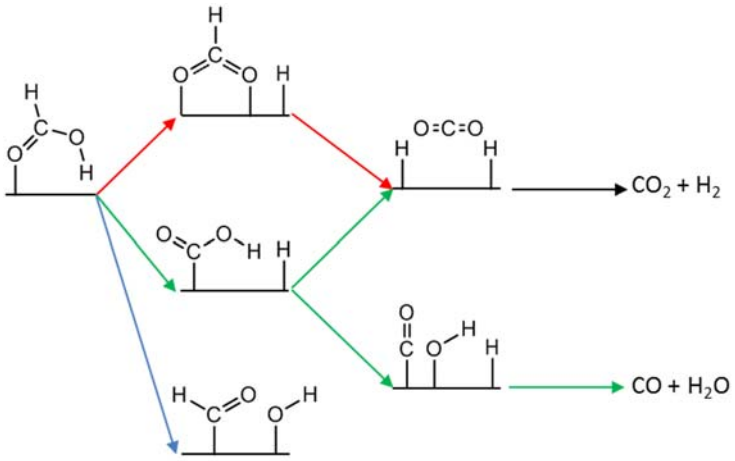


**Scheme 7-1**. Reaction pathways of HCOOH decomposition on Cu catalysts. Red arrows represent the HCOO pathway; green arrows represent the COOH pathway; blue arrow represents the HCO pathway. The shared elementary step (recombinative desorption of $H_2$) for HCOO and COOH pathways is indicated by the black arrow.

In a previous publication [213], a comprehensive reaction network consisting of seventeen elementary steps was proposed for HCOOH decomposition on Au catalysts. Three pathways were explored: HCOO pathway, COOH pathway and HCO (formyl) pathway; see **Scheme 7-1**. The HCO intermediate is obtained from dehydroxylation of HCOOH, which is found to have a significantly higher activation energy compared with the formation of the other two intermediates HCOO and COOH on low-index Au surfaces. The same conclusion can also be reached for Cu(111), based on the results from our previous work [102] on methanol synthesis. For this reason, this HCO pathway was neglected in the present study, and a reduced reaction network with five intermediates (**Table**

**7-1**) and seven key elementary steps (**Table 7-2**) was explored on Cu(100) and Cu(211) surfaces. For the Cu(111) surface, BE values of intermediates, activation energies and reaction energies of elementary steps have been reported in the previous methanol synthesis work [102] and were corrected using the ZPE in this study ─ summarized in **Tables 7-1** and **7-2** together with the newly calculated results on Cu(100) and Cu(211).

### 7.3.1 Structure and adsorption energetics of reaction intermediates

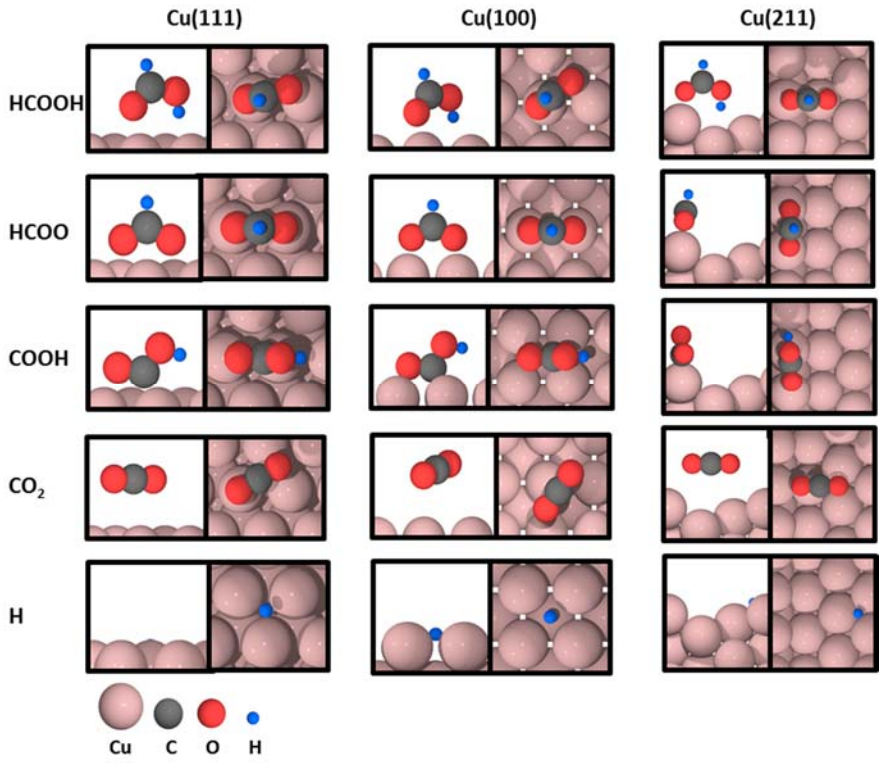


**Figure 7-1** Most stable adsorption configurations of all reaction intermediates on clean Cu(111) 101, Cu(100) and Cu(211) facets. For each intermediate, both cross-section (left) and atop (right) views are shown. Cu, C, O and H atoms are represented by pink, grey, red and blue spheres.

The most stable adsorption configurations of the five intermediates studied on the three Cu facets are shown in **Figure 7-1**. Atomic hydrogen preferentially binds at the three fold fcc site of Cu(111) with a binding energy of -2.26 eV. Similar binding energy of H (-2.27 eV) is found on Cu(100) at

its most favorable fourfold hollow site. The threefold fcc site, closest to the step edge, is the preferred adsorption site for H on Cu(211); the binding strength is slightly stronger than that on Cu(111) and Cu(100) at -2.38 eV. Carbon dioxide exhibits no site preference on all three Cu surfaces and retains its gas-phase linear geometry with weak binding energies (weaker than -0.1 eV), suggesting only physisorption on Cu.

**Table 7-1** ZPE-corrected binding energies (BEs) on clean Cu(111), Cu(100) and Cu(211) facets

| | Cu(111)[a] | | Cu(100) | | Cu(211) | |
|---|---|---|---|---|---|---|
| Species | Adsorption Site | BE / eV | Adsorption Site | BE / eV | Adsorption Site | BE / eV |
| H | Fcc | -2.26 | Hollow | -2.27 | Fcc, terrace | -2.38 |
| $CO_2$ | Physisorbed | -0.06 | Physisorbed | -0.05 | Physisorbed | -0.09 |
| HCOO | Top-Top | -2.57 | Top-Top | -2.95 | Top-Top, edge | -3.17 |
| COOH | Top-Top | -1.44 | Bridge-Bridge | -1.74 | Top-Top, edge | -1.90 |
| HCOOH | Top | -0.16 | Top | -0.32 | Top, edge | -0.47 |

a: BEs on Cu(111) are taken from ref. [102], but were corrected with ZPEs here.

Carboxyl binds to two Cu atoms on the Cu(111) surface through its C and O atoms with the C-O bond almost parallel to the surface and O-H bond pointing towards the surface; the BE is calculated to be -1.44 eV. A similar adsorption configuration is found on the Cu(211) surface at the step edge. On Cu(100), however, COOH binds to two opposite bridge sites in a square encompassing a hollow site. COOH binds more strongly on Cu(100) and Cu(211) than on Cu(111) by 0.30 eV and 0.46 eV, respectively. On all three surfaces, formate binds in a bidentate configuration with both of its O atoms bound to adjacent top sites; step-edge top sites are preferred for HCOO on Cu(211). The calculated BEs of HCOO are -2.57 eV, -2.95 eV, and -3.17 eV on Cu(111), Cu(100), and Cu(211), respectively. The most stable configuration for formic acid binds to the top site on all three surfaces through its O atom with the C-H bond pointing away from the surface, and the O-H bond pointing towards the surface. On Cu(211), HCOOH binds to the top site on the step edge and the O-H bond is pointing towards the step foot atoms on the terrace. The binding strength of

HCOOH increases in the order Cu(111) < Cu(100) < Cu(211), with BE values of -0.16 eV, -0.32 eV, and -0.47 eV on the three Cu surfaces respectively.

With the exception of $CO_2$, which is physisorbed on all three surfaces, all intermediates prefer to bind to sites on the step edge of Cu(211). The magnitudes of the BEs of reaction intermediates on the three Cu surfaces are observed to decrease in the order Cu(211) > Cu(100) > Cu(111), in agreement with the general notion that adsorbates tend to exhibit stronger binding to more open facets.

**Table 7-2** ZPE-corrected reaction energies (ΔE) and activation energies ($E_a$) on clean Cu(111), Cu(100) and Cu(211) facets.

| # | Reaction | Cu(111)[a] | | Cu(100) | | Cu(211) | |
|---|---|---|---|---|---|---|---|
| | | ΔE / eV | $E_a$ / eV | ΔE / eV | $E_a$ / eV | ΔE / eV | $E_a$ / eV |
| 1 | HCOOH(g) + * ↔ HCOOH* | -0.16 | - | -0.32 | - | -0.47 | - |
| 2 | HCOOH* + 2* ↔ HCOO** + H* | -0.33 | 0.48 | -0.57 | 0.42 | -0.74 | 0.41 |
| 3 | HCOOH* + 2* ↔ COOH** + H* | 0.49 | 1.13 | 0.35 | 0.94 | 0.22 | 1.06 |
| 4 | HCOO** ↔ $CO_2$* + H* | 0.15 | 0.95 | 0.52 | 1.21 | 0.60 | 1.47 |
| 5 | COOH** ↔ $CO_2$* + H* | -0.68 | 0.98 | -0.39 | 1.12 | -0.36 | 1.08 |
| 6 | 2H* ↔ $H_2$(g) + 2* | 0.23 | 0.74 | 0.25 | 0.72 | 0.47 | 0.97 |
| 7 | $CO_2$* ↔ $CO_2$(g) + * | 0.06 | - | 0.05 | - | 0.09 | - |

a: Reaction energies and activation energies on Cu(111) are taken from ref. [102], but were corrected with ZPEs here.

### 7.3.2 Elementary steps: reaction energies and activation energies

In this section, we will describe the characteristics of the minimum energy path identified for each of the elementary steps considered in this study. The configurations of the transition states in each minimum energy path are shown in **Figure 7-2,** and the respective reaction energies and activation energies are summarized in **Table 7-2**. HCO formation from dehydroxylation of HCOOH on Cu(111) has a reaction energy of 1.10 eV [102] and an activation energy of 1.52 eV [102], which is more

than three times higher than the activation energy of HCOO formation from HCOOH and 0.39 eV higher than COOH formation from HCOOH on Cu(111). Thus HCOOH is not likely to decompose through the HCO intermediate. Furthermore, decomposition of HCO would lead to CO production while there is experimental evidence [200] that $CO_2$ and $H_2$ are the only products of HCOOH decomposition on Cu catalysts. Therefore, HCO pathway may not contribute to the overall reaction and was not studied on Cu(100) and Cu(211).

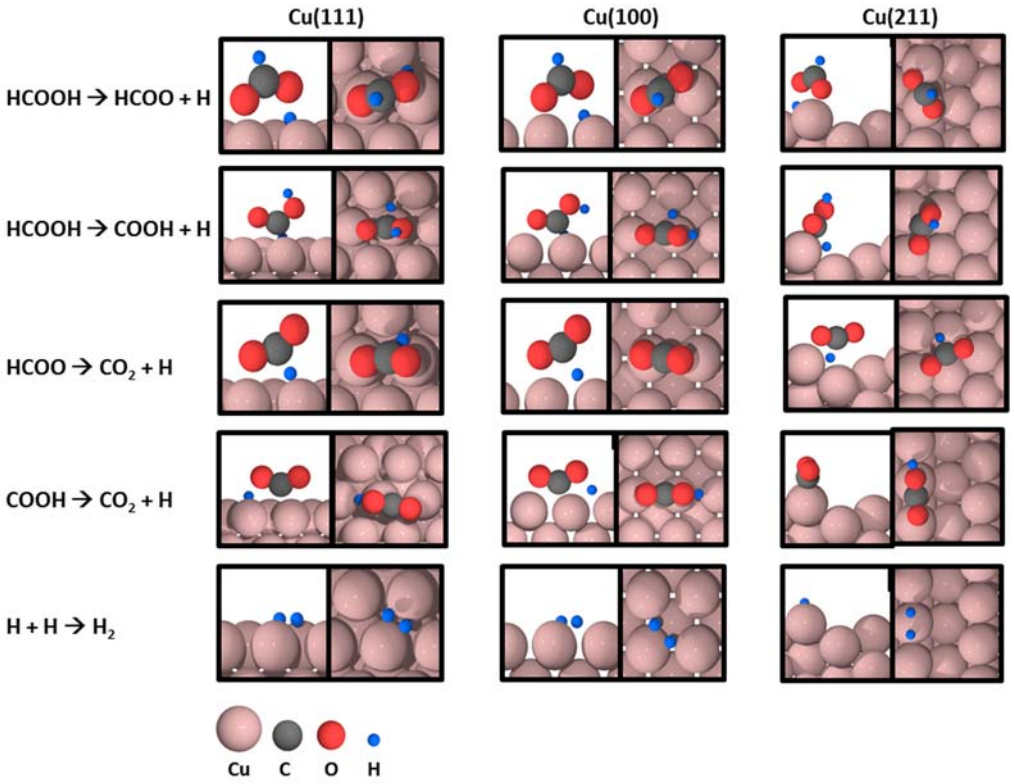


**Figure 7-2** Cross-section (left) and atop (right) views of the transition state configurations for the elementary steps on Cu(111), Cu(100) and Cu(211) surfaces. Cu, C, O and H atoms site are represented by pink, grey, red and blue spheres.

$$HCOOH^* + 2^* \rightarrow HCOO^{**} + H^*$$

HCOOH decomposition to HCOO proceeds from the most stable configuration of HCOOH with O-H bond-breaking taking place over a bridge site on Cu(111) and Cu(100), and an off-top site on the step edge of the Cu(211) surface. This reaction is exothermic on all three Cu surfaces with reaction energies -0.33 eV, -0.57 eV and -0.74 eV, increasing in magnitude in the order Cu(111) < Cu(100) < Cu(211), due to the much stronger binding of reaction product HCOO on the more open facets. Similar activation energies in the range of 0.41 eV to 0.48 eV, however, are found on all three Cu surfaces, indicating a rather weak structure-sensitivity of the O-H activation in HCOOH on the three Cu surfaces, further evidenced by the similar configurations of the transition states on the three surfaces.

$$HCOOH^* + 2^* \rightarrow COOH^{**} + H^*$$

C-H bond-breaking in HCOOH, yielding adsorbed COOH and atomic hydrogen, involves rotation of the molecule such that the C-H bond is pointing towards the surface. At the transition state, C-H bond scission occurs over a top site where the product COOH readily adsorbs through its C atom after the reaction and the produced H atom adsorbs on the nearest fcc or bridge sites on Cu(111) and Cu(100), respectively. On the Cu(211) surface, the C-H bond is broken over the top site on the step edge; after the reaction, COOH adsorbs on the adjacent top sites of the step edge while H adsorbs on the hollow site at the step. In contrast to the HCOOH decomposition to HCOO, COOH formation from HCOOH is an endothermic reaction on all three surfaces, presumably because of the higher energy of adsorbed COOH than adsorbed HCOO. The activation energy of this reaction step varies slightly across the three surfaces, being 1.13 eV, 0.94 eV and 1.06 eV on Cu(111), Cu(100) and Cu(211), respectively. As COOH formation has a much higher (more than 0.5 eV higher) activation energy than HCOO formation from HCOOH, Cu will preferentially break the O-H bond in HCOOH to form HCOO on all three surfaces.

*HCOO** → $CO_2$* + H**

Similarly to the C-H scission in HCOOH, C-H bond scission in HCOO also involves a rotation of the molecule such that the C-H bond moves closer towards the surface. One Cu-O bond is already broken at the transition state, with the C-H bond-breaking taking place over a bridge site on Cu(111) and Cu(100), and the bridge site on the step of Cu(211). This reaction is endothermic on all three surfaces with reaction energies being 0.15 eV, 0.52 eV and 0.60 eV on Cu(111), Cu(100) and Cu(211), respectively. Both reaction energy (all, endothermic) and activation energy increase in the order Cu(111) < Cu(100) < Cu(211), indicating that this is a structure sensitive reaction on Cu surfaces. There is an increase of ~0.26 eV in the activation energy of HCOO decomposition each time we go from Cu(111) (0.95eV) to Cu(100) (1.21 eV) and to Cu(211) (1.47 eV), presumably because of the stronger binding of HCOO, the reactant, on the more open facets. The structure-sensitive character found for this reaction step is in agreement with Nakamura's findings that HCOO dehydrogenation has notably different activation energies on Cu(111) and Cu(110) [206]. On Cu(111), the activation energy of HCOO decomposition measured by Nakamura is 108 kJ/mol [206] (~1.12 eV), comparable to our calculated value 0.95 eV. The activation energy of this step is much higher than that of the HCOO formation, indicating HCOO decomposition is probably the rate limiting step in the HCOO-mediated pathway for HCOOH decomposition.

*COOH** → $CO_2$* + H**

As the O-H bond in COOH points towards the surface in its lowest-energy configuration, COOH decomposition proceeds directly from the most stable configuration with the O-H bond-breaking taking place over the bridge site of all three Cu surfaces. This reaction is exothermic, and activation energy barriers are slightly different on the three surfaces, with values of 0.98 eV, 1.12 eV and 1.08 eV on Cu(111), Cu(100) and Cu(211), respectively. The similar activation energies of this

reaction on the three Cu surfaces are probably due to the similar transition states seen on these surfaces, as shown in **Figure 7-2**. COOH decomposition has comparable barriers as HCOO decomposition on Cu(111) and Cu(100) surfaces while it is much easier than HCOO decomposition on Cu(211), 1.08 eV versus 1.47 eV, respectively.

$H^* + H^* \rightarrow H_2(g) + 2^*$

$H_2$ recombinative desorption starts with two H atoms adsorbed on adjacent fcc and hcp sites on the Cu(111) surface with H-H bond formation taking place over the bridge site, while the reaction starts with two H atoms adsorbed on two adjacent bridge sites on Cu(100) and Cu(211) with H-H bond formation over the off-top and top sites, respectively. Cu(111) and Cu(100) have similar activation energies, 0.74 eV and 0.72 eV, and reaction energies (0.23 eV and 0.25 eV on Cu(111) and Cu(100), respectively) for $H_2$ recombination, while both energy values are higher on the Cu(211) surface (Ea=0.97 eV; $\Delta$E=0.47 eV). This difference is entirely due to the difference in the binding strength of H, the reactant, on different surfaces, as the activation energy of the reverse reaction ($H_2$ dissociation) is practically the same on all three surfaces at ca. 0.5 eV.

### 7.3.3 Potential energy surfaces (PES)

The thermochemistry and activation energy barriers of the elementary steps described in the previous sections were used to plot the potential energy surfaces (PESs) for the three Cu facets, see **Figure 7-3**. The PESs shown in **Figure 7-3 (a)-(c)** compare the HCOO- and COOH-mediated pathways on the three Cu facets respectively. It is clear from the PESs that the HCOO-mediated pathway is more favorable than the COOH-mediated pathway for HCOOH decomposition on Cu(111), Cu(100) and Cu(211), due to the substantially lower TS energies in the HCOO-mediated path. **Figure 7-3(d)** compares the most favorable HCOO-mediated pathway on the three Cu facets.

On all three Cu facets, HCOO decomposition has a higher TS energy and also a higher activation energy than HCOO formation from HCOOH in the HCOO-mediated pathway. Though HCOO decomposition has a similar TS energy to that for hydrogen recombination, its activation energy is much higher than hydrogen recombination (by ca. 0.2-0.5 eV). Thus, HCOO decomposition is likely to be the rate limiting step for HCOOH decomposition.

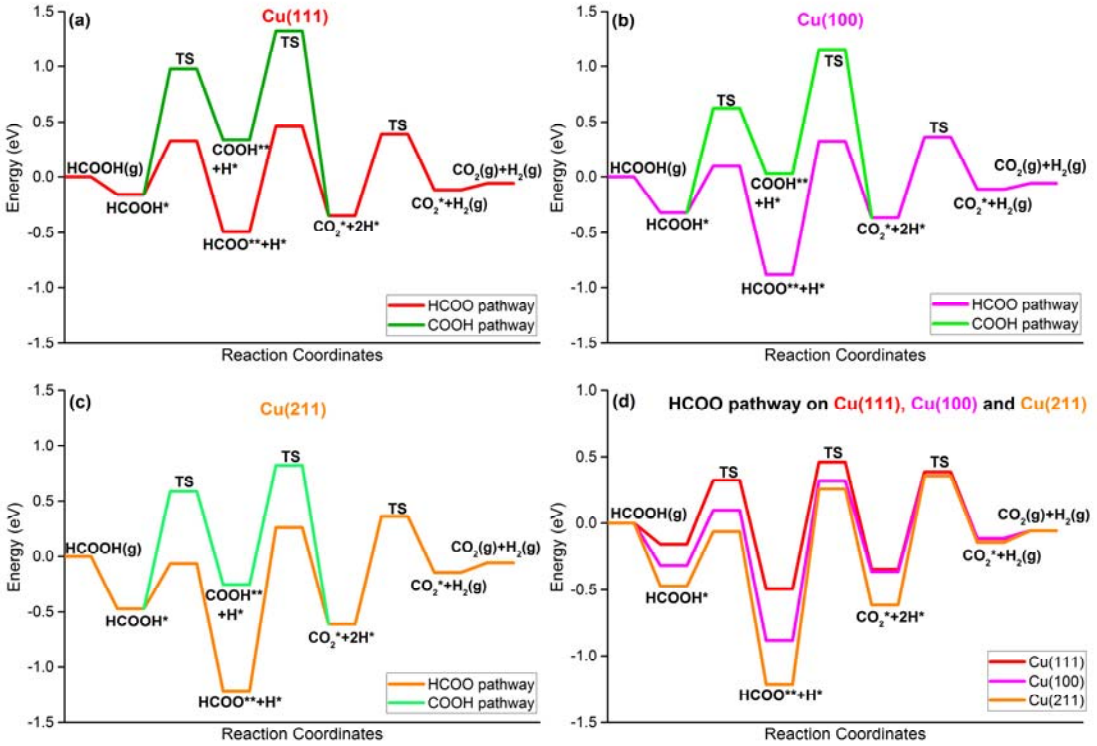


**Figure 7-3** PESs of HCOOH decomposition reaction via the HCOO- and COOH-mediated pathways on Cu(111) (a), Cu(100) (b), and Cu(211) (c), and a comparison of the most favorable HCOO-mediated pathway on all three facets (d).

The PES of the HCOO-mediated pathway decreases in energy in the order Cu(111) > Cu(100) > Cu(211). For the HCOO-mediated pathway, Cu(100) and Cu(211) show similar TS energies (within ca. 0.2 eV) which are lower than that on Cu(111). Cu(211) binds intermediates more strongly than the Cu(100) surface, and accordingly shows lower energies for the adsorbed states

and subsequently higher activation energy barriers than those on Cu(100). Since HCOO decomposition is likely the rate limiting step among the three catalytic steps, and Cu(211) has a similar TS energy for HCOO decomposition as on Cu(100) but much higher activation energy, it is likely that Cu(211) surface is less active than Cu(100) for HCOOH decomposition. On the PES, coadsorbed HCOO and H represents the most stable state, and the subsequent decomposition reaction of HCOO has the highest activation energy among the three catalytic steps. Therefore, these surfaces are likely to be partially covered by HCOO, especially on the Cu(100) and Cu(211) surfaces, which bind HCOO more strongly than Cu(111) by 0.38 eV and 0.60 eV, respectively. As a result, HCOOH decomposition may take place more readily on the terraces of the Cu catalysts, while the under-coordinated step sites and defect sites may be blocked by strongly adsorbed HCOO. The Cu catalysts used in Iglesia and Boudart's study [200] contain relatively big nanoparticles with sizes 5-40 nm, within which range small fraction of under-coordinated sites is predicted and is potentially occupied by the HCOO intermediate; hence, the activity of Cu catalysts might come from the unoccupied terrace sites entirely. Accordingly, similar activation energies were observed for different particle-size catalysts. Their findings cannot differentiate the contributions from different types of sites (such as terrace, step, corner, defect sites) on Cu. To evaluate the contribution of under-coordinated sites to this chemistry, experiments should be conducted on Cu single crystals or smaller copper nanoparticles, where perimeter/corner/defect sites are present at a substantial percentage. It would also be necessary to substantiate these predictions from the DFT calculations using an experimentally validated microkinetic model, which is an ongoing endeavor and will be presented in a future report.

## 7.4 Conclusions

HCOOH decomposition was investigated using self-consistent, periodic DFT calculations on three Cu model surfaces ─ Cu(111), Cu(100) and Cu(211) ─ by exploring both HCOO-mediated and COOH-mediated routes. It is found that the HCOO-mediated route is energetically more favorable than the COOH-mediated route on all three Cu surfaces. For the HCOO-mediated route, HCOO decomposition is likely to be the rate determining step due to the fact that it has the highest TS energy as well as the highest activation energy barrier among the three catalytic steps. Cu(100) and Cu(211) show similar TS energies in the HCOO pathway, which are lower than those on Cu(111). While Cu(211) has similar TS energies as Cu(100), it binds the intermediates more strongly and has a higher activation energy for the likely rate limiting step (HCOO decomposition); hence, Cu(211) might be less active than the Cu(100) facet for HCOOH decomposition. Coadsorbed HCOO and H represents the most stable state on the PES, implying a surface partially covered with HCOO intermediate, especially at the under-coordinated step and defect sites. As a result, under realistic reaction conditions, HCOOH decomposition may be most facile on the terraces of the Cu catalysts and may show an invariance in turn-over-frequency as a function of nanoparticle size, as always under-coordinated step/defect sites might be poisoned by HCOO. Yet, we showed here that HCOOH decomposition reaction on Cu surfaces is highly structure sensitive at the atomic scale level. We are currently exploring this reaction using a combined DFT, experiments and microkinetic modeling approach to corroborate our tentative conclusions regarding the decreased, due to poisoning, importance of under-coordinated step or defect sites in HCOOH decomposition on Cu catalysts.

## 7.5 Supplementary material

**Table 7S-1** Binding energies (BEs) on clean Cu(111), Cu(100) and Cu(211) facets with (W) and without (W/O) ZPE corrections.

| Species | Cu(111) | | | Cu(100) | | | Cu(211) | | |
|---|---|---|---|---|---|---|---|---|---|
| | Adsorption Site | BE / eV | | Adsorption Site | BE / eV | | Adsorption Site | BE / eV | |
| | | W ZPE | W/O ZPE[a] | | W ZPE | W/O ZPE | | W ZPE | W/O ZPE |
| H | Fcc | -2.26 | -2.43 | Hollow | -2.27 | -2.37 | Fcc, terrace | -2.38 | -2.55 |
| $CO_2$ | Physisorbed | -0.06 | -0.08 | Physisorbed | -0.05 | -0.07 | Physisorbed | -0.09 | -0.11 |
| HCOO | Top-Top | -2.57 | -2.68 | Top-Top | -2.95 | -3.07 | Top-Top, edge | -3.17 | -3.29 |
| COOH | Top-Top | -1.44 | -1.52 | Bridge-Bridge | -1.74 | -1.82 | Top-Top, edge | -1.90 | -2.00 |
| HCOOH | Top | -0.16 | -0.22 | Top | -0.32 | -0.37 | Top, edge | -0.47 | -0.53 |

a: Non-ZPE corrected BEs on Cu(111) are taken from ref. [102].

**Table 7S-2** Reaction energies ($\Delta E$) and activation energies ($E_a$) on clean Cu(111), Cu(100) and Cu(211) facets with (W) and without (W/O) ZPE corrections.

| # | Reaction | Cu(111) | | | | Cu(100) | | | | Cu(211) | | | |
|---|---|---|---|---|---|---|---|---|---|---|---|---|---|
| | | $\Delta E$ / eV | | $E_a$ / eV | | $\Delta E$ / eV | | $E_a$ / eV | | $\Delta E$ / eV | | $E_a$ / eV | |
| | | W ZPE | W/O ZPE[a] | W ZPE | W/O ZPE[a] | W ZPE | W/O ZPE | W ZPE | W/O ZPE | W ZPE | W/O ZPE | W ZPE | W/O ZPE |
| 1 | HCOOH(g) + * ↔ HCOOH* | -0.16 | -0.22 | - | - | -0.32 | -0.37 | - | - | -0.47 | -0.53 | - | |
| 2 | HCOOH* + 2* ↔ HCOO** + H* | -0.33 | -0.23 | 0.48 | 0.68 | -0.57 | -0.39 | 0.42 | 0.62 | -0.74 | -0.63 | 0.41 | 0.60 |
| 3 | HCOOH* + 2* ↔ COOH** + H* | 0.49 | 0.59 | 1.13 | 1.32 | 0.35 | 0.52 | 0.94 | 1.10 | 0.22 | 0.33 | 1.06 | 1.23 |
| 4 | HCOO** ↔ $CO_2$* + H* | 0.15 | 0.25 | 0.95 | 1.12 | 0.52 | 0.71 | 1.21 | 1.40 | 0.60 | 0.73 | 1.47 | 1.58 |
| 5 | COOH** ↔ $CO_2$* + H* | -0.68 | -0.55 | 0.98 | 1.23 | -0.39 | -0.20 | 1.12 | 1.37 | -0.36 | -0.23 | 1.08 | 1.31 |
| 6 | 2H* ↔ $H_2$(g) + 2* | 0.23 | 0.29 | 0.74 | 0.82 | 0.25 | 0.17 | 0.72 | 0.66 | 0.47 | 0.53 | 0.97 | 1.02 |
| 7 | $CO_2$* ↔ $CO_2$(g) + * | 0.06 | 0.08 | - | - | 0.05 | 0.07 | - | - | 0.09 | 0.11 | - | - |

a: Non-ZPE corrected reaction energies and activation energies on Cu(111) are taken from ref. [102].

# Chapter 8 Formic Acid Decomposition on Cu catalysts: Self-consistent Solutions from DFT, Microkinetic Modeling, and Experiments

## 8.1 Introduction

Formic Acid (FA) decomposition on transition metal catalysts is a very well-studied system, both in heterogeneous catalysis and fundamental surface science. It is of applied interest because of FA's potential as a liquid hydrogen carrier[214] with a high hydrogen-to-carbon ratio and a closed carbon cycle.[41, 214-218] FA is used as a fuel in fuel cells that operate at low temperatures and have been shown to exhibit better efficiency than alcohol fuel cells.[219, 220] It is also an equimolar byproduct in the production of levulinic acid from biomass,[15, 17] and can be utilized in situ to provide molecular hydrogen for the subsequent hydrogenation of levulinic acid to gamma-valerolactone.[42, 221] Moreover, being the simplest carboxylic acid, FA has been widely used to probe the catalytic properties of metals[49, 56, 86, 115, 222-224], metal oxides[57-59, 61], metal carbides[53-55], and alloys.

Early work for FA decomposition on Cu catalysts examined infrared spectroscopy, the kinetic isotope effect, and decomposition rate measurements, and served to shed some light on the mechanistic aspect of this reaction.[200, 222, 225-228] Subsequently, Madix and coworkers, in their pioneering work on Cu single crystals[55, 229-231], demonstrated the key role of a very stable formate (HCOO) species in this reaction; this work resulted in a series of studies on Cu single crystals that continue to date.[201, 208, 209, 231-235] Despite the abundance of experimental studies for FA decomposition on Cu catalysts, there is a general lack of consensus regarding the reaction

† S. Singh contributed to the microkinetic analysis in this study; calculations on clean Cu(100) surface were performed by J. Scaranto; kinetic experiments were conducted by BJ. O'Neill.

mechanism and the nature of the active site. Iglesia and Boudart[200, 222, 225, 228] observed that the turnover rates for this reaction were insensitive to the particle size and to the nature of the support. Their results, together with other studies that reported similar activation energy barriers for this reaction on different preferentially oriented and polycrystalline Cu catalysts,[203-205, 236-240] suggested that this reaction was structure insensitive. Additionally, they proposed that the catalytic FA decomposition was a bimolecular process, in which the HCOO decomposition was assisted by adsorbed FA molecules.[200]

In contrast to these findings, Bowker and coworkers[201, 208, 209, 231, 233-235, 241] reported that FA did not undergo dissociation on clean Cu(111), and that the presence of pre-dosed oxygen was required for this surface to exhibit any appreciable reaction rates; under similar conditions, clean Cu(100) and Cu(110) were shown to be active for this reaction. More recently, Nakamura and coworkers[206, 242] claimed that FA decomposition on Cu catalysts was in fact a structure sensitive reaction, with notably different activation energy barriers for H abstraction from HCOO species on Cu(111) as compared to Cu(100); they also demonstrated a strong promotional effect of $H_2$ co-feed on the rate of this reaction on Cu(111), and showed that HCOO decomposition was enhanced 17 times in the presence of $H_2$ on Cu(111), but not on Cu(100) facet.

This study aims to provide a comprehensive description of the supported Cu catalyst surface under operating conditions by elucidating the nature of active sites for FA decomposition using reaction kinetics measurements, DFT calculations, and an iterative and rigorous microkinetic modeling based approach.

The importance and contemporary relevance of microkinetic modeling as a tool for performing comparisons between experimental observations and DFT-derived predictions has been highlighted in several recent reports.[7, 64, 102, 103] Since parameter optimization using microkinetic

modeling is often a non-convex optimization problem,[243] the final solutions, and the ensuing conclusions that are drawn from these solutions, depend on the initial guesses for the thermodynamics and kinetics parameters that are obtained from DFT calculations on representative model surfaces. Hence, the importance of ensuring the accuracy of these DFT derived parameters to obtain reliable conclusions and inferences from the microkinetic model cannot be overstated. The two primary sources of errors in these parameters are (a) the inherent errors associated with DFT calculations, and (b) the errors that arise when the model surfaces used in DFT calculations do not accurately represent the active site and/or the surface environment under reaction conditions. While the recent advances in computational techniques have contributed towards quantifying and minimizing the former, it is the inconsistency between the surface environment (surface coverages of most abundant surface species) predicted by the model and that employed in the DFT calculations that is overlooked and can cause misleading conclusions. This study employs an iterative approach for microkinetic modeling that ensures self-consistency between the surface environment employed in the DFT calculations and that predicted by the model, and discusses the possible ramifications that this might have on the final conclusions regarding the active sites on a catalyst.

Hence, the objective of this work is two-fold, to (1) demonstrate a generally applicable, yet rigorous and iterative microkinetic modeling-based methodology that yields holistically self-consistent solutions, and (2) employ this method to settle the unsatisfying status quo that exists regarding the reaction mechanism, nature of active sites, and structure sensitivity for FA decomposition reaction on Cu catalysts.

## 8.2 Methods

### 8.2.1 DFT calculations

Several key elementary steps in the FA decomposition reaction network on Cu(111) were studied and reported in our earlier work, as part of the methanol synthesis reaction network.[102] For consistency, the same setup that was employed in that study is utilized for the calculations reported in this study. All calculations were performed using the DACAPO total energy code.[88, 89] The Cu(111) surface was modeled by a three-layer slab with a p(3×3) unit cell with all surface atoms being fixed in their bulk truncated positions, while the Cu(100) facet was modeled by a p(3x3) unit cell with four layers of metal atoms, the top two of which were allowed to relax. The surface Brillouin zone of (111) slabs was sampled at 54 special Chadi-Cohen[92] k points, while that for the (100) slabs was sampled by using a 4×4×1 Monkhorst-Pack[93] k-point mesh. The exchange-correlation energy and potential were described self-consistently using the generalized gradient approximation (GGA-PW91).[95, 96] The binding energies (BEs) were calculated with respect to the total energy of the clean slabs ($E_{slab}$) and the corresponding adsorbates in the gas phase ($E_{adsorbate, gas\text{-}phase}$), i.e., $BE_{adsorbate} = E_{total} - E_{slab} - E_{adsorbate, gas\text{-}phase}$. In the discussion of the DFT results, we refer to electronic energy values including the zero point energy (ZPE) corrections, unless otherwise noted. Throughout the text, (g) stands for ‘gas phase species’ and each '*' represents a single surface site occupied by the corresponding adsorbate. Our calculations do not take into account the long-range interactions, such as van der Waals forces,[104, 105] which may contribute an additional stabilization of ~ 0.1 eV – 0.2 eV per carbon atom.The minimum energy pathways and activation energy barriers for all elementary steps were determined using the climbing image nudged elastic band (CI-NEB) method.[99, 244, 245]. More detailed computational methods,

experimental synthesis protocols (of the Cu/γ-$Al_2O_3$ catalysts) and kinetic measurement could be found in SI.

### 8.2.2 Microkinetic modeling

Mean-field microkinetic modeling was employed to describe the experimentally measured FA conversions, apparent activation energy barrier, and reaction orders apropos of all gaseous components. The different aspects of the model development are reported below:

**Reaction Network**

All the steps included in **Table 8-2** were explicitly considered in the microkinetic model for the clean Cu(111) and Cu(100) surfaces, while an abridged version of this reaction network showing in **Table 8-4** was implemented for the 'high-coverage' models.

**Model Inputs**

(1) DFT derived parameters: The microkinetic model was parameterized in terms of the Shomate parameters of the gas phase reactants and products, most stable adsorption states of all surface species, and the transition states of all activated elementary steps. The temperature and ZPE corrected reaction enthalpies and entropies of all these states were used to calculate the equilibrium constants, pre-exponential factors, and forward/reverse reaction rate constants for all elementary steps, as reported in our earlier studies.[102, 246] (2) Experimental data: The experimental data that was used in this study comprised of the inlet flow rates of all gaseous components, reaction temperatures, total pressures, number of active sites in the catalyst, and the experimentally determined FA conversions and selectivity to $CO_2$.

**Adjustable parameters and objective function**

The objective function that was used to quantitatively compare and assess the different solutions and the corresponding fits was the normalized sum of squared residuals (nSSR), which is a measure

of the absolute difference between the experimental and model predicted flow rates of the gaseous components.

$$nSSR = min\left(\sum_{i\in n}\sum_{j\in G}\left(\frac{M_{ji}^{out}}{E_{ji}^{out}} - 1\right)^2\right) \quad (1)$$

where $M_{ji}^{out}$ and $E_{ji}^{out}$ are the model predicted and experimental outlet flow rates for species *j* and experimental condition *i.* The summation is performed over the flow rates of all outlet species (G) for all experimental conditions (n). An additional metric that was used in this study to compare the quality of different solutions was the mean absolute error (MAE), defined as MAE $= {\sum_i abs\ (TOF_{model} - TOF_{experiment})}/{n}$, where TOF stands for turnover frequency. The DFT derived enthalpies of thermodynamic and transition states were chosen as the adjustable parameters for fitting purposes, while the surface entropies and pre-exponential factors were fixed to their DFT derived values.

**Model Formulation**

The model was formulated as a plug flow reactor (PFR), which was comprised of 5 differential equations (one for each gaseous flow rate) and 7 algebraic equations (one each for all reaction intermediates, and an additional one for the vacant site), in a manner described by Madon et al.[247] The inbuilt MATLAB solvers and optimization routines were employed to solve these equations and perform subsequent parameter optimization. In addition to starting with the exact DFT derived values as the initial guesses, the parameter space was also sampled in the vicinity of these values (± 0.4 eV (~40 kJ/mol) from the DFT derived initial guesses for each adjustable parameter). In this study, a manual approach for sampling the parameter space has been adopted; an automated multi-

start approach using latin hypercube sampling has recently been reported by Nason et al., [243] but it is outside the scope of this work.

Rate Controlling Steps

Campbell's degree of rate control ($X_{RC}$) was employed to analyze the reaction mechanisms and quantitatively determine the rate determining steps for a set of experimental conditions. This approach quantifies the kinetic importance of an elementary step in a reaction scheme by computing the relative change in the overall reaction rate upon changing the forward and reverse rate constants for that step, while holding the equilibrium constant for that step as well as the rate constants for all other steps constant. In this formalism, the degree of rate control ($X_{RC}$) of each elementary step can be evaluated using the following relation:

$$X_{RC,i} = \frac{k_i}{r}\left(\frac{\delta r}{\delta k_i}\right)_{K_{i,eq},k_j} \quad (2)$$

where $k_i$ is the rate constant for step $i$, $K_{i,eq}$ is the equilibrium constant for this step and $r$ is the overall reaction rate.

## 8.3 Results and discussion

### 8.3.1 DFT calculations

A reaction network consists of various pathways for FA decomposition, including the direct and 'adsorbate-assisted' HCOO, COOH and HCO pathways was proposed with the list of elementary steps showing in **Table 8-2**. Cu(111) was chosen first as the representative model surface for DFT calculations to obtain the thermodynamic and kinetic parameters for all the elementary steps included in the reaction network. Cu(111) is the thermodynamically most stable Cu facet, it has been shown to be the preferentially exposed facet for supported Cu catalysts via TEM studies,[248]

and has been proposed to be active for several reactions involving small oxygenates. HCOO species has for long been considered a key surface intermediate for several reactions on Cu(111); however, despite an overwhelming spectroscopic evidence of its existence under reaction conditions on Cu catalysts, its exact surface coverage under these conditions has never been well quantified. In the absence of any definitive knowledge regarding the surface environment under reaction conditions, a 'clean' Cu(111) facet (all surface sites being vacant) was employed as the initial model facet for DFT calculations. Subsequently, these DFT calculations were repeated on a clean Cu(100) surface, together with Cu(111) and Cu(100) surfaces with pre-adsorbed 'spectator' HCOO and H species to conclusively determine the true nature of active site. The 'high-coverage' models with spectators comprised of an abridged version of this reaction network, as shown in **Table 8-4**. The key findings from all the DFT calculations on the surfaces listed above are reported below.

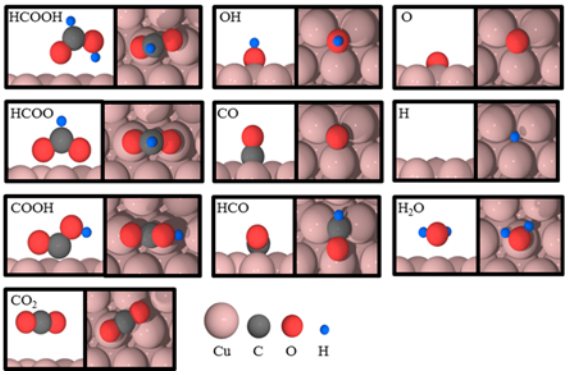


**Figure 8-1** Most stable adsorption configurations for all surface adsorbates on a clean Cu(111) facet. The pink, grey, red and blue spheres represent Cu, C, O, and H atoms respectively.

**Clean Cu(111) and Cu(100)**

The adsorption geometries for the most stable binding configurations of all surface species on Cu(111) and Cu(100) are illustrated in **Figure 8-1** and **Figure 8-2** respectively, and a summary of the binding energies (BEs) and preferred adsorption sites is included in **Table 8-1. Table 8-2**

reports the reaction energies (ΔE) and activation energy barriers ($E_A$) for all elementary steps involved in this reaction network.

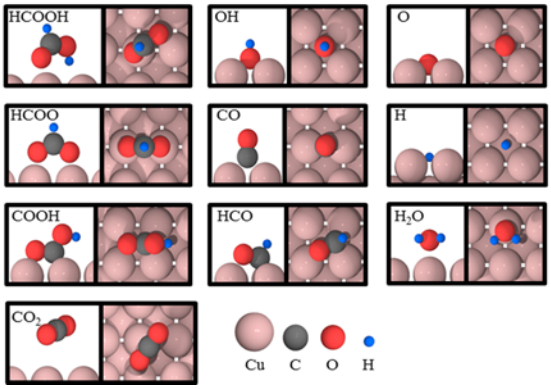


**Figure 8-2** Most stable adsorption configurations for all surface adsorbates on a clean Cu(100) facet. The pink, grey, red and blue spheres represent Cu, C, O, and H atoms respectively.

**Table 8-1** BEs on Clean Cu(111) and Cu(100) facets

| Species | Clean Cu(111) | | Clean Cu(100) | |
|---|---|---|---|---|
| | Adsorption Site | BE / eV | Adsorption Site | BE / eV |
| H* | Fcc | -2.26 | Hollow | -2.27 |
| O* | Fcc | -4.18 | Hollow | -4.65 |
| OH* | Fcc | -2.61 | Hollow | -2.92 |
| $H_2O$* | Top | -0.16 | Top | -0.23 |
| CO* | Fcc | -0.82 | Bridge | -0.86 |
| $CO_2$* | Physisorbed | -0.06 | Physisorbed | -0.05 |
| HCO* | Bridge | -1.07 | Bridge-Top | -1.39 |
| HCOO* | Top-Top | -2.57 | Top-Top | -2.95 |
| COOH* | Top | -1.44 | Bridge-Bridge | -1.74 |
| HCOOH* | Top | -0.16 | Top | -0.32 |

The BEs include zero point energy (ZPE) corrections.

Preliminary insights from microkinetic modeling suggested that several elementary steps that have high values of $E_A$ (> 1.5 eV) were highly unlikely to have any considerable reaction flux under the operating conditions employed in this study; although all these steps were explicitly included in the microkinetic model, in-text comments on only some key elementary steps that were found to

be part of the catalytic cycle, and the reaction intermediates that are formed during the course of the reaction, are provided here; all relevant information pertaining to the other elementary steps and reaction intermediates can be found in the tables.

**Table 8-2** Reaction Energies and Activation Energies on Clean Cu(111) and Cu(100) facets

| # | Reaction | Clean Cu(111) | | Clean Cu(100) | |
|---|---|---|---|---|---|
| | | ΔE / eV | $E_A$ / eV | ΔE / eV | $E_A$ / eV |
| 1[a] | HCOOH + * ↔ HCOOH* | -0.16 | - | -0.32 | - |
| 2[a] | HCOOH* + 2* ↔ HCOO** + H* | -0.33 | 0.48 | -0.57 | 0.42 |
| 3[a] | HCOOH* + * ↔ COOH* + H* | 0.49 | 1.13 | 0.35 | 0.94 |
| 4[a] | HCOOH* + * ↔ HCO* + OH* | 1.10 | 1.52 | 0.64 | 1.05 |
| 5[a] | HCOO** ↔ $CO_2$* + H* | 0.15 | 0.95 | 0.52 | 1.21 |
| 6 | HCOO** + O* ↔ $CO_2$* + OH* + * | -0.48 | 1.43 | 0.07 | 1.47 |
| 7 | HCOO** + OH* ↔ $CO_2$* + $H_2O$* + * | 0.06 | 1.64 | 0.68 | 1.34 |
| 8 | HCOO** + H* ↔ $H_2$ + $CO_2$* + 2* | 0.37 | 1.91 | 0.77 | 1.84 |
| 9[a] | HCOO** ↔ HCO* + O* | 2.06 | 2.25 | -- | -- |
| 10[a] | COOH* + * ↔ $CO_2$* + H* | -0.68 | 0.98 | -0.39 | 1.12 |
| 11[a] | COOH* + * ↔ CO* + OH* | -0.26 | 0.33 | -0.30 | 0.21 |
| 12 | COOH* + O*↔ CO* + $H_2O$* | -1.31 | -0.32 | -0.84 | -0.09 |
| 13[a] | COOH* + OH*↔ $CO_2$* + $H_2O$* | -0.77 | -0.44 | -0.24 | -0.58 |
| 14 | COOH* + H*↔ CO* + $H_2O$* | -0.35 | 1.14 | -0.15 | 1.69 |
| 15 | HCOO* + COOH*↔ HCOOH* + $CO_2$* | -0.35 | 0.11 | 0.17 | 0.67 |
| 16[a] | HCO* + *↔ CO* + H* | -0.87 | 0.07 | -0.60 | 0.21 |
| 17[a] | CO* + O*↔ CO2* + * | -1.05 | 0.65 | -0.54 | 0.63 |
| 18[a] | O* + H*↔ OH* + * | -0.62 | 0.88 | -0.45 | 1.13 |
| 19[a] | 2OH*↔ $H_2O$* + O* | 0.53 | 0.53 | 0.60 | 0.66 |
| 20[a] | OH* + H*↔ $H_2O$* + * | -0.09 | 1.09 | 0.15 | 0.98 |
| 21 | 2H*↔ $H_2$ + 2* | 0.23 | 0.74 | 0.25 | 0.72 |
| 22[a] | CO*↔ CO + * | 0.82 | - | 0.86 | - |
| 23[a] | $CO_2$*↔ $CO_2$ + * | 0.06 | - | 0.05 | - |
| 24[a] | $H_2O$*↔ $H_2O$ + * | 0.16 | - | 0.23 | - |

[a] : These values have been taken from our earlier publication for the Cu(111) facet.[102] All the $E_A$s and ΔEs are ZPE corrected.

The most stable adsorption configuration for FA (HCOOH) on Cu(111) is one in which all its atoms lie in a plane perpendicular to the surface. It binds to the surface with BE of -0.16 eV [249, 250] via its carbonyl O atom on a top site, with the C-H bond pointing away from the surface, and O-H bond pointing towards the surface. On Cu(100), it binds via its O atoms in an off-top position, with a BE of -0.32 eV. The potential importance of the formate intermediate (HCOO) for this reaction has been highlighted in earlier sections; on both Cu(111) and Cu(100) surfaces, it binds in a bidentate configuration with both its O atoms on the adjacent top sites, [251, 252] with BEs of -2.57 eV[249, 253] and -2.95 eV on the two surfaces. Atomic hydrogen (H) binds preferentially on the three fold sites on Cu(111) with a BE of -2.26 eV[249, 253]; both the fcc and hcp sites are found to be energetically quasi-degenerate. In the absence of a threefold site on Cu(100), H preferentially binds on a fourfold hollow site, with BE = -2.27 eV. $CO_2$ binds extremely weakly on both surfaces (BE = -0.06 eV and -0.05 eV on Cu(111) and Cu(100), respectively) and does not exhibit a site preference for its most stable adsorption configuration, as evidenced by the energy degeneracy of its several adsorption states. As shown in **Table 8-1**, Cu(100) exhibits stronger binding for all reaction intermediates when compared to Cu(111), in-line with the conventional wisdom that surfaces with lower coordination of surface atoms exhibit stronger adsorption.

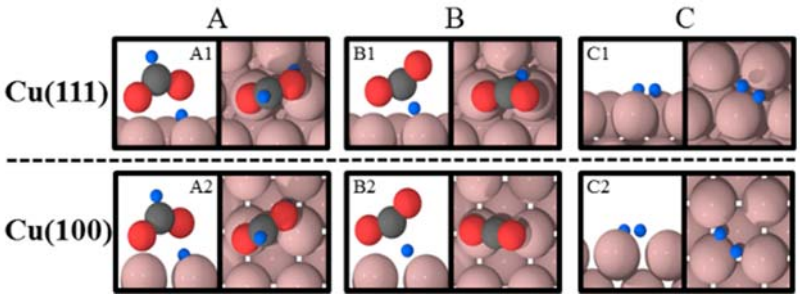


**Figure 8-3** Side and top views of the transition states for the three key elementary steps: (A) HCOOH → HCOO + H, (B) HCOO → $CO_2$ + H, (C) 2H → $H_2$ (g) on a clean Cu(111) surface (top pannel) and Cu(100) surface (bottom pannel).

For the reaction conditions employed in our experiments, FA decomposition is found to proceed via a direct dehydrogenation pathway that involves HCOO intermediate on both (111) and (100) facets. This step proceeds directly from the most stable perpendicular configuration of FA, and the HCOO-H bond cleavage takes place over a bridge site (**Figure 8-3A**), the $E_A(\Delta E)$ for this step being 0.48 eV (-0.33 eV)[62, 249]on Cu(111) and 0.42 eV (-0.57 eV) on Cu(100). The significantly higher $E_A$s for the two alternate initiation steps, FA dehydrogenation to COOH ($E_A$ = 1.13 eV on Cu(111) and 0.94 eV on Cu(100)) and FA dehydroxylation to HCO ($E_A$ = 1.52 eV on Cu(111) and 1.05 eV on Cu(100)), are the reasons why these steps do not contribute to the reaction rates. The second dehydrogenation step, HCOO conversion to $CO_2$ and H, involves rotation of the HCOO molecule such that the C-H bond is aligned towards the surface; one Cu-O bond is cleaved first, followed by a C-H bond scission over a bridge site (**Figure 8-3B**), with an $E_A(\Delta E)$ of 0.95 eV[254] (0.15 eV) and 1.21 eV (0.52 eV) on Cu(111) and Cu(100), respectively. On both facets, the C-H bond length in the transition state (TS) is 1.52 Å, compared to 1.11 Å in adsorbed HCOO. $H_2$ recombinative desorption starts from the two H atoms on adjacent three-fold sites on Cu(111), and diagonally-adjacent fourfold hollow sites on Cu(100), and the H-H bond formation takes place over a bridge site on both facets (**Figure 8-3C**). The transition state H-H bond length is 0.97 Å (Cu(111)) and 1.17 Å(Cu(100)), compared to $H_2$ gas phase bond length of 0.75 Å, and the $E_A$ is 0.74 eV[62, 253, 255, 256] (Cu(111)) and 0.72 eV (Cu(100))[255, 256].

A mean-field microkinetic model that used the DFT derived thermochemical and kinetic parameters reported above as initial guesses to fit the experimental rate data yielded two 'best-fit solutions' for both Cu(111) and Cu(100) surfaces, one that predicted high HCOO coverage and another, high H coverage, under reaction conditions. DFT calculations were repeated for key

elementary steps on these additional surfaces, the results of which are reported below; a detailed discussion on the different solutions is included in subsequent sections.

**Cu(111) and Cu(100) with 4/9 ML preadsorbed HCOO**

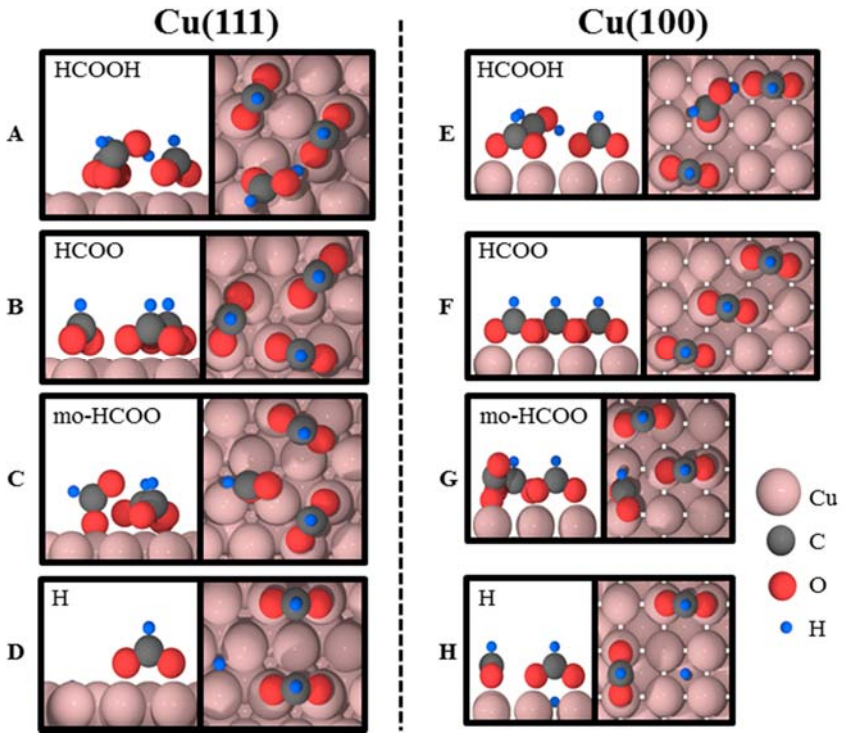


**Figure 8-4** Most stable adsorption configurations of the four key surface adsorbates on the Cu(111)-2HCOO and Cu(100)-2HCOO surface. The pink, grey, red and blue spheres represent Cu, C, O, and H atoms respectively.

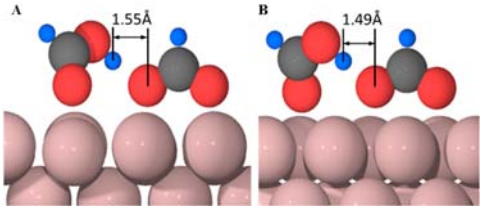


**Figure 8-5** Most stable adsorption configuration of HCOOH on (A) Cu(111)-2HCOO and (B) Cu(100)-2HCOO surfaces.

Using the DFT values from the clean surfaces, the microkinetic model predicted surface coverage of HCOO species was found to vary with the experimental conditions within a range of 0.32 ML and 0.70 ML on both facets. It should be noted here that since HCOO is a bidentate species, (a) the surface concentration of HCOO species is half that of the predicted surface coverage (in ML),

and (b) for DFT calculations on a 3x3 unit cell, its coverage can only be varied in increments of 2/9 ML (as opposed to 1/9 ML for monodentate species). The high-coverage DFT calculations were performed in presence of 4/9 ML of 'spectator' HCOO, which corresponds to two HCOO species in a (3x3) unit cell employed for both Cu(111) and Cu(100); these surfaces will be referred to as the 'Cu(111)-2HCOO' and 'Cu(100)-2HCOO' surfaces throughout the text, for brevity.

FA is found to exhibit strong binding in the presence of two spectator HCOO species, with BEs of -0.55 eV and -0.69 eV on Cu(111)-2HCOO and Cu(100)-2HCOO surfaces, as opposed to -0.16 eV and -0.32 eV on their clean counterparts, respectively. This is primarily because of H-bonding that exists between the hydroxyl H of HCOOH and the neighboring oxygen atom of the HCOO species, with the distance between the two atoms being 1.49 Å and 1.55 Å on the (111) and (100) facets respectively, as illustrated in **Figure 8-4**. Also, the most stable binding configuration of FA on Cu(111)-2HCOO is one where it binds to the surface via the O atom on the bridge site (**Figure 8-4A**), as opposed to the top site on clean Cu(111). HCOO binds preferentially in a bidentate configuration where the two O atoms are slightly displaced from the top sites (**Figure 8-4B**), and exhibits marginally weaker binding of -2.40 eV and -2.85 eV on Cu(111)-2HCOO and Cu(100)-2HCOO surfaces, as opposed to -2.57 eV and -2.95 eV on the clean surfaces. Also, in contrast with the clean surface, the presence of a stable monodentate adsorption state for HCOO intermediate that binds to the surface through one O atom on the hcp site of Cu(111)-2HCOO facet (BE = -2.16 eV, **Figure 8-4C**), and a bridge site of Cu(100)-2HCOO facet (BE = -2.39 eV, **Figure 8-4G**), was observed. The existence of a monodentate HCOO on Cu(111) was reported by Gokhale et al.[7], wherein they had employed a (2x2) unit cell for their calculations; this further highlights the role of surface coverage effects on the structural stability of adsorbed states. The BEs were found to be nearly identical to their clean-slab equivalents.

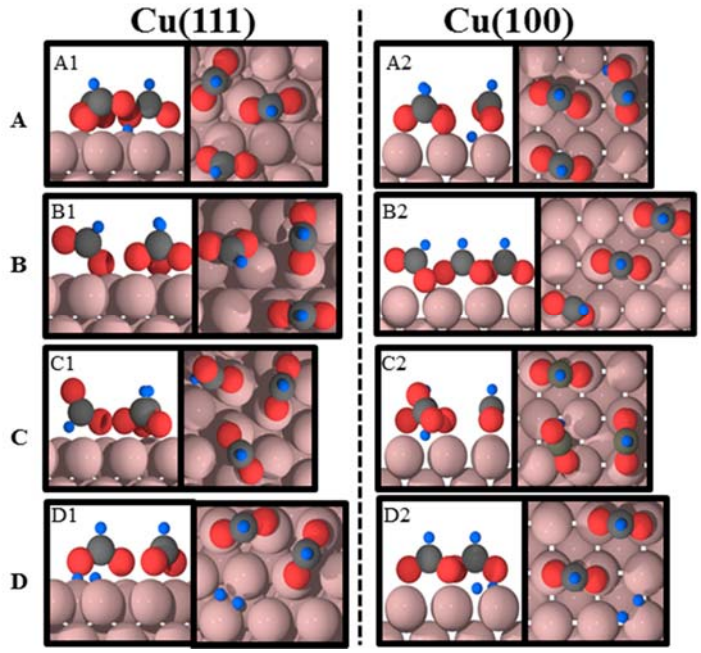


**Figure 8-6** Side and top views of the transition states for the four key elementary steps: (A) HCOOH → HCOO + H, (B) HCOO → mo-HCOO (C) mo-HCOO → $CO_2$ + H, (D) 2H → $H_2$(g) on the Cu(111)-2HCOO (left panel) and Cu(100)-2HCOO (right panel) facet.

The $E_A$ for FA dehydrogenation to HCOO on Cu(111)-2HCOO and Cu(100)-2HCOO are 1.01 eV ($\Delta E$ = 0.23 eV) and 1.09 eV (-0.06 eV) respectively, both of which are much higher than the corresponding value on the clean slab, primarily because of stabilization of the initial state via H-bonding (**Figure 8-5**). Also, the HCOO-H bond scission takes place on a 3-fold site on the (111) facet and an off-bridge site on the (100) facet, as opposed to a bridge site on the clean slabs of both facets. In contrast with the clean slabs, the HCOO decomposition to $CO_2$ is a two-step process on both facets in presence of HCOO spectator species. The first step is the rotation of bidentate HCOO that involves a Cu-O bond cleavage, and results in a metastable monodentate 'mo-HCOO' intermediate; this step has an $E_A$ ($\Delta E$) of 0.30 eV (0.24 eV) and 0.54 eV (0.46 eV) on Cu(111)-2HCOO and Cu(100)-2HCOO respectively. This intermediate undergoes dehydrogenation to form $CO_2$ and H, with an $E_A$($\Delta E$) of 0.49 eV (-0.20 eV) and 0.51 eV (0.03 eV), on the (111) and (100) slabs, respectively. The recombinative desorption of $H_2$ from adsorbed H atoms is the step that is least affected by the presence of spectator HCOO species with similar $E_A$s, $\Delta E$s, and reaction coordinates on the two HCOO-covered surfaces as their clean slab counterparts.

**Cu(111) with 6/9 ML preadsorbed H**

As was mentioned above and discussed in greater detail in subsequent sections, an additional 'best-fit' solution was obtained using the thermochemistry and kinetic parameters from clean Cu(111) as the initial guesses; for this solution, the microkinetic model predicted surface coverage of atomic H was found to be in the range of 0.51 ML – 0.76 ML, depending on the reaction temperature. For the majority of the experiments that were performed at 130°C, this coverage was predicted to be ~0.66 ML. Hence, the DFT calculations for key reaction intermediates and elementary steps were repeated on a unit cell with 0.66 ML of pre-adsorbed H as spectator species; this surface will be referred to as the Cu(111)–6H surface throughout the text, for brevity.

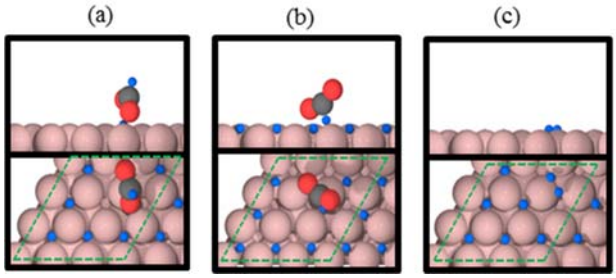


**Figure 8-7** Most stable adsorption configurations for the four key surface adsorbates on the Cu(111)-6H surface. The pink, grey, red and blue spheres represent Cu, C, O, and H atoms respectively.

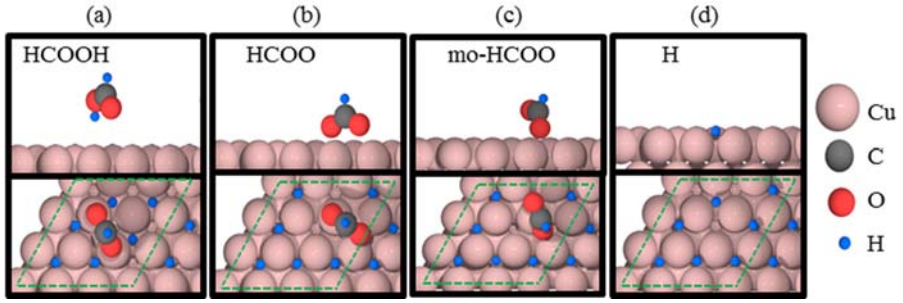


**Figure 8-8** Side and top views of the transition states for the three key elementary steps: (A) HCOOH → mo-HCOO + H, (B) mo-HCOO → $CO_2$ + H, (C) 2H → $H_2$ (g) on the Cu(111)-6H surface.

FA exhibits very weak binding (BE = -0.03 eV) on Cu(111)-6H surface, with several energetically degenerate adsorption configurations, one of which is shown in **Figure 8-7A**. HCOO binds

preferentially in a bidentate configuration; however, one of the two O atoms binds on the bridge site on the Cu(111)-6H surface, as opposed to both of them being on adjacent top sites on the clean slab (**Figure 8-7B**), which results in a significantly weaker binding (BE = -1.96 eV, as opposed to -2.57 eV on the clean slab). A monodentate adsorption configuration for HCOO, where it binds to the surface via one O atom on the bridge site, with the other O atom pointing away from the surface, with BE = -1.41 eV was also observed. **Figure 8-7C** shows the most stable adsorption configuration of 7 H atoms on the surface; all the H atoms are found to occupy the hollow sites and the differential BE of the seventh H atom is -2.09 eV, as opposed to the BE of -2.26 eV of H on clean Cu(111) .

**Table 8-3** ZPE corrected BEs on Cu(111)-2HCOO, Cu(100)-2HCOO, and Cu(111)-6H surfaces

| Species | Cu(111) -2HCOO | | Cu(100) -2HCOO | | Cu(111)-6H | |
|---|---|---|---|---|---|---|
| | Adsorption Site | BE / eV | Adsorption Site | BE / eV | Adsorption Site | BE / eV |
| H* | fcc | -2.26 | hollow | -2.25 | fcc/hcp | -2.09 |
| HCOO** | top-top | -2.40 | top-top | -2.85 | top-bridge | -1.96 |
| mo-HCOO* | hcp | -2.16 | bridge | -2.39 | bridge | -1.41 |
| HCOOH* | bridge | -0.55 | top | -0.69 | top | -0.03 |

**Table 8-4** ZPE-Corrected Reaction Energies and Activation Energy Barriers on Cu(111)-2HCOO, Cu(100)-2HCOO, and Cu(111)-6H surfaces

| # | Reaction | Cu(111)-2HCOO | | Cu(100)-2HCOO | | Cu(111)-6H | |
|---|---|---|---|---|---|---|---|
| | | ΔE / eV | $E_A$ / eV | ΔE / eV | $E_A$ / eV | ΔE / eV | $E_A$ / eV |
| 1 | HCOOH + *↔ HCOOH* | -0.55 | - | -0.69 | - | -0.03 | - |
| 2 | HCOOH* + 2*↔ HCOO** + H* | 0.23 | 1.01 | -0.06 | 1.09 | - | - |
| 3 | HCOO**↔ mo-HCOO* + * | 0.24 | 0.30 | 0.46 | 0.54 | - | - |
| 4 | mo-HCOO* + *↔ $CO_2$* + H* | -0.20 | 0.49 | 0.03 | 0.51 | -0.23 | 0.73 |
| 5 | 2H*↔ $H_2$ + 2* | 0.23 | 0.84 | 0.21 | 0.77 | -0.12 | 0.80 |
| 6 | HCOOH* + *↔ mo-HCOO* + * | - | - | - | - | 0.32 | 0.77 |

In contrast with the clean Cu(111) surface, the minimum energy pathway for FA dehydrogenation to $CO_2$ and $H_2$ on the Cu(111)-6H surface does not involve the most stable, bidentate configuration of HCOO intermediate, and proceeds directly via its monodentate equivalent; the first dehydrogenation step (HCOOH → mo-HCOO + H) has an $E_A$ = 0.77 eV ($\Delta E$ = 0.32 eV), with the O-H bond scission taking place over a threefold site, as opposed to a bridge site on clean Cu(111) (**Figure 8-8**). The transition state geometries of mo-HCOO dehydrogenation and $H_2$ recombination are both very similar to their clean-slab counterparts, and this is reflected in the comparable $E_A$s of these elementary steps. Despite the similar $E_A$s as on clean slabs, the corresponding transition states on Cu(111)-6H surface have substantially higher total energies, due to the significant destabilizations in the initial states of these steps; this is illustrated in the enthalpy surface shown in **Figure 8-13**.

### 8.3.2 Microkinetic modeling

Cu(111) As reported in earlier sections, clean Cu(111) was chosen first as the most-probable active site for FA decomposition on supported Cu catalysts. A microkinetic model that was parameterized using the DFT derived thermodynamics and kinetics parameters obtained on this facet was employed to analyze the reaction mechanism and perform comparisons with the experimental kinetic dataset. Prior to making any adjustments in the DFT derived initial guesses, the model predicted 100% conversion for all reaction conditions; the surface was predicted to be completely clean, and the reaction was found to proceed via the following sequence of elementary steps: HCOOH → HCOO + H → CO2 +2H → CO2 + H2, with the first step being the rate controlling step. Since the DFT derived parameters for Cu(111) were inadequate to describe the experimental observations on supported Cu catalysts, parameter optimization was performed to obtain improved fits with the experimental data. With a complex model comprising of 30 adjustable parameters

being used to fit an experimental kinetic dataset that had 18 unique conditions, one could expect multiple solutions that yield reasonably good fits with the experimental observations. Hence, in addition to employing the DFT derived parameters as the initial guesses, a greater region of the parameter space was sampled in the vicinity of the DFT derived initial guesses to ensure that a feasible solution was not missed. As a result of this exercise, two unique solutions that provided excellent fits with the experimental dataset were identified, both of which were able to successfully emulate the experimentally observed apparent activation energy barrier and the reaction orders for the reactants and products. Henceforth, these two solutions will be referred to as the 'Clean Cu(111)-HCOO solution' and the 'Clean Cu(111)-H solution', for reasons described in the following sections. A discussion on these two solutions is presented below:

**Clean Cu(111) surface – HCOO solution**

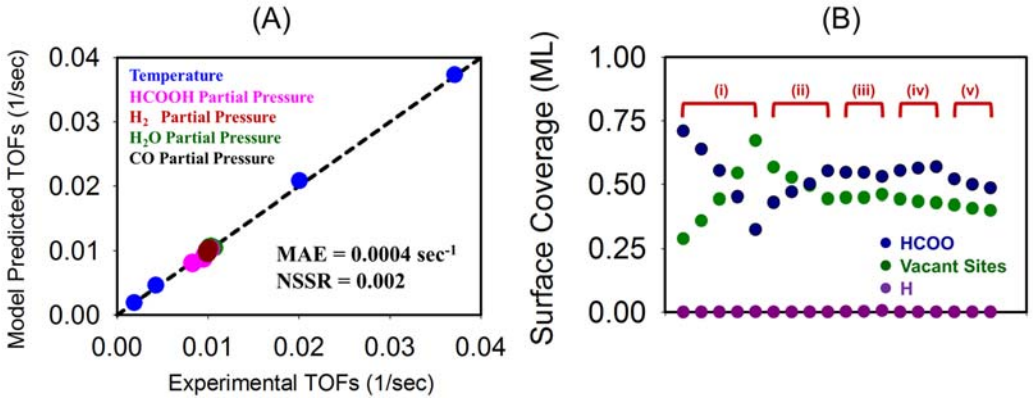


**Figure 8-9** (A) Parity plot of experimental and model predicted TOFs. The different colored circles represent the different set of experiments. The $H_2O$ and CO partial pressure variation points are hidden behind the $H_2$ Partial Pressure (dark red). (B) Surface coverage (ML) of the most abundant surface species for the different experimental conditions (i) Temperature (ii) HCOOH PP (iii) $H_2$ PP) (iv) $H_2O$ PP (v) CO PP variation.

Starting from the DFT derived parameters as the initial guesses, the reaction rate was found to be most sensitive to the binding energies of HCOO and the transition state energies of the direct HCOO formation and decomposition steps (Steps 2 and 5 in **Table 8-2**). Small (< 0.1 eV),

successive adjustments were made in the most sensitive parameters until a good match was obtained between the model predictions and experimental reaction rates. Full optimization of the model was then performed (by nonlinear least-squares data fitting, using the nlinfit function in Matlab that makes use of the Gauss-Newton algorithm), to refine the fit and obtain the final, optimized set of parameters. The parity plot of the experimental and model predicted TOFs corresponding to the best fit solution is shown in **Figure 8-9A**; it has an MAE of 0.0004 sec-1 and an nSSR value of 0.98.

The adjustments made to the DFT derived initial guesses in order to obtain this solution are reported in **Table 8-5** and **Table 8-6**. While the transition state energies for both HCOO formation and decomposition steps required modest stabilizations of -0.04 eV and -0.09 eV respectively, both of which are within the DFT uncertainty (±0.2 eV, ~20 kJ $mol^{-1}$) , the HCOO intermediate had to be stabilized by 0.32 eV. The surface was predicted to have 0.33 ML – 0.71 ML of adsorbed HCOO with the remaining sites being vacant. The HCOO surface coverage decreased with increasing temperature and increased with increasing FA partial pressure, accompanied by a commensurate change in the number of vacant sites. For the majority of experiments that were performed at 130°C (the temperature used to obtain $H_2$/$H_2O$/CO reaction orders), the HCOO surface coverage was nearly constant (~ 0.55 ML). Campbell's degree of rate control was calculated for all the elementary steps, and HCOO decomposition was found to be the rate controlling step under all reaction conditions, as reported in **Table 8-6**.

**Table 8-5** Adjustments needed in the DFT derived BEs on clean Cu(111) corresponding to the best fit

| Species | HCOO Solution ΔBE / eV | H Solution ΔBE / eV |
|---|---|---|
| H* | 0.00 | -0.01 |
| HCOO** | -0.32 | 0.00 |

**Clean Cu(111) surface – H solution**

The 'multi-start' approach led to an alternate solution that exhibited near-identical fits with the experimental data as the preceding HCOO solution. The quality of the fit between the model predicted and experimental TOFs is shown in **Figure 8-10**, and the adjustments that were required in the DFT derived parameters to obtain this fit are reported in **Table 8-5** and **Table 8-6**. To obtain these fits, the transition state for the $H_2$ recombination step was destabilized by 0.42 eV, while those for HCOO formation and decomposition steps were stabilized by -0.18 eV and -0.22 eV respectively. The surface was predicted to have H coverage of 0.51 ML -0.76 ML, with the remaining sites being vacant. $H_2$ recombination was found to be the rate controlling step under all reaction conditions, as reported in **Table 8-6**.

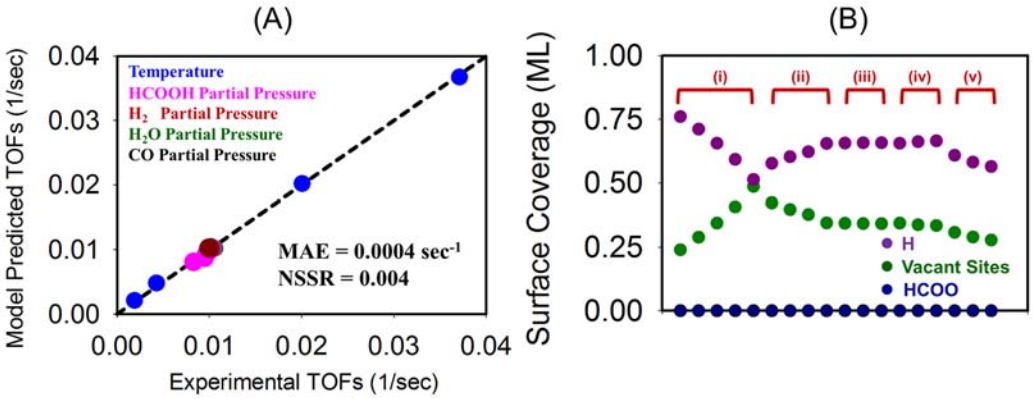


**Figure 8-10** (A) Parity plot of experimental and model predicted TOFs. The different colored circles represent the different set of experiments. The $H_2O$ and CO partial pressure variation points are hidden behind the $H_2$ Partial Pressure (dark red). (B) Surface coverage (ML) of the most abundant surface species for the different experimental conditions (i) Temperature (ii) HCOOH PP (iii) $H_2$ PP (iv) $H_2O$ PP (v) CO PP variation.

After careful sampling of the parameter space, it was established that the two solutions presented here were the only ones on the Cu(111) surface that were able to accurately describe all the experimental measurements, including the reaction orders, apparent activation energy barrier, and

turnover frequencies. An enthalpy surface that compares the DFT derived energetics with those corresponding to 'HCOO solution' and 'H solution', at 130°C, is shown in **Figure 8-11**.

**Table 8-6** Adjustments needed in the DFT derived TS energies corresponding to the best fit, and the Cambell's degree of rate control (XRC) for the kinetically relevant elementary steps on clean Cu(111)

| Reaction | HCOO Solution | | H Solution | |
|---|---|---|---|---|
| | ΔETS / eV | XRC | ΔETS / eV | XRC |
| HCOOH* + 2*↔ HCOO** + H* | -0.04 | 0.11-0.30 | -0.18 | 0.01-0.02 |
| HCOO* + *↔ $CO_2$* + H* | -0.09 | 0.57-0.88 | -0.22 | 0.15-0.27 |
| 2H*↔ $H_2$ + 2* | 0.00 | 0.00-0.01 | 0.42 | 0.62-0.83 |

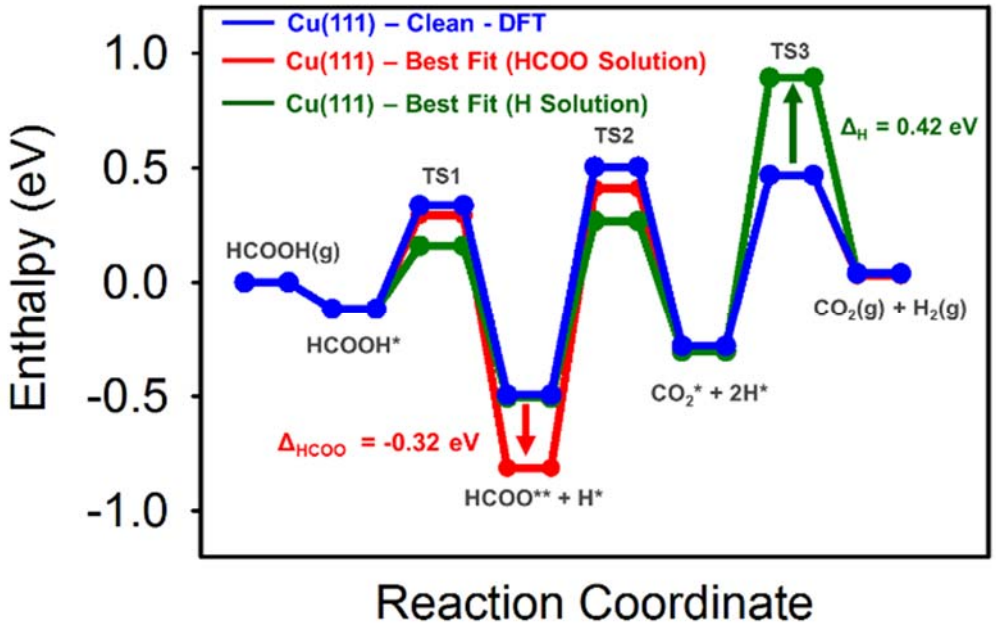


**Figure 8-11** 2-dimensional PESs of FA decomposition reaction via the HCOO pathway on clean Cu(111). Zero-energy corresponds to the gasphase enthalpy of FA molecule. The blue line corresponds to the DFT derived PES, and the red and green lines reflect the enthalpies of the thermodynamic and transition states for the HCOO solution and H solution, respectlively. The maximum adjustments made for both these solutions is also reported.

Although the thermodynamics and kinetic parameters used in the model were all collected on a clean Cu(111) surface, both solutions predicted substantial coverages of either HCOO or H species on the surface. Hence, there existed a disparity between the model predicted surface environment

and that employed in the DFT calculations, and a direct comparison of the optimized thermodynamic and kinetic parameters obtained from microkinetic modeling with their DFT derived counterparts on clean Cu(111) was deemed as logically fallacious. An attempt to close this gap was made by performing additional DFT calculations with more appropriately chosen unit cells, i.e., a Cu(111) surface with 4/9 ML of pre-adsorbed HCOO and another with 6/9 ML of pre-adsorbed atomic H. A discussion on the DFT calculations on these slabs has been included in earlier sections.

**Table 8-7** Adjustments needed in the DFT derived BEs on high HCOO/H covered Cu(111) corresponding to the best fit

| Species | HCOO Solution ΔBE / eV | H Solution ΔBE / eV |
|---|---|---|
| H* | 0.00 | -0.30 |
| HCOO** | -0.51 | -0.09 |
| HCOOH* | 0.00 | -0.10 |

**Table 8-8** Adjustments needed in the DFT derived TS energies on high HCOO/H covered Cu(111) corresponding to the best fit, and the Cambell's degree of rate control (XRC) for the kinetically relevant elementary steps

| Reaction | HCOO Solution | | H Solution | |
|---|---|---|---|---|
| | ΔETS / eV | XRC | ΔETS / eV | XRC |
| HCOOH* + 2* ↔ HCOO** + H* | -0.19 | 0.10-0.26 | -- | -- |
| HCOO** ↔ mo-HCOO* + * | 0.00 | 0.00 | -- | -- |
| mo-HCOO* + * ↔ $CO_2$* + H* | -0.06 | 0.60-0.89 | -- | -- |
| 2H* ↔ $H_2$ + 2* | 0.00 | 0.01-0.00 | -0.23 | -0.73-0.88 |
| HCOOH* + * ↔ mo-HCOO* + H* | -- | -- | -0.56 | 0.11-0.26 |
| mo-HCOO* + * ↔ $CO_2$* + H* | -- | -- | -0.72 | 0.00-0.01 |

**Cu(111)-2HCOO surface**

With no adjustments to the DFT derived parameters on high HCOO-covered surface, the model under-predicted the rates by 2 orders of magnitude. Starting from this curtailed model with a revised set of initial guesses for the DFT parameters, parameter optimization was performed to obtain good fits with the experimental data, much the same way as described in the previous

section. **Table 8-7** and **Table 8-8** report the adjustments that were required in the DFT parameters in order to obtain these fits. The model predicted a HCOO surface coverage of 0.34 ML – 0.72 ML; hence, from the surface coverage standpoint alone, this was a self-consistent solution in that the model predicted surface coverages were consistent with those employed in DFT calculations. However, while the adjustments made in most parameters are within the DFT error bar (0.2 eV), the HCOO binding energy required stabilization by -0.51 eV. This adjustment was too large to be attributed solely to the errors in our DFT calculations, and hence, the Cu(111)-2HCOO surface couldn't be unambiguously claimed to be the active site for this reaction.

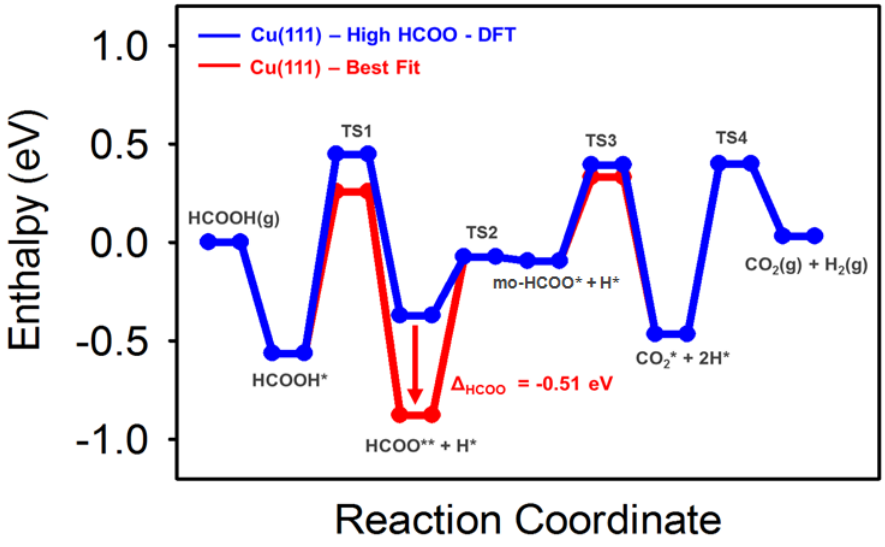


**Figure 8-12** 2-dimensional PESs of FA decomposition reaction via the HCOO pathway on the Cu(111)-2HCOO facet. Zero-energy corresponds to the gasphase enthalpy of FA molecule. The blue line corresponds to the DFT derived PES, and the red line corresponds to the best-fit solution. The adjustment required in the binding energy of HCOO is also reported.

**Cu(111)–6H surface**

A microkinetic model that used the DFT derived values for all the parameters on Cu(111)-6H surface as the initial guesses under-predicted the FA decomposition rate by > 6 orders of magnitude. In order to obtain good fits with the experimental data starting from these initial

guesses, significant adjustments were required for several parameter values. The adsorbed HCOOH, HCOO and H had to be stabilized by -0.10 eV, -0.09 eV, and -0.30 eV respectively, whereas the transition state energies of HCOO formation, HCOO decomposition, and $H_2$ recombination steps were adjusted by -0.56 eV, -0.72 eV and -0.23 eV respectively. As before, several of these adjustments are too large to be attributed simply to the inaccuracies in the DFT calculations.

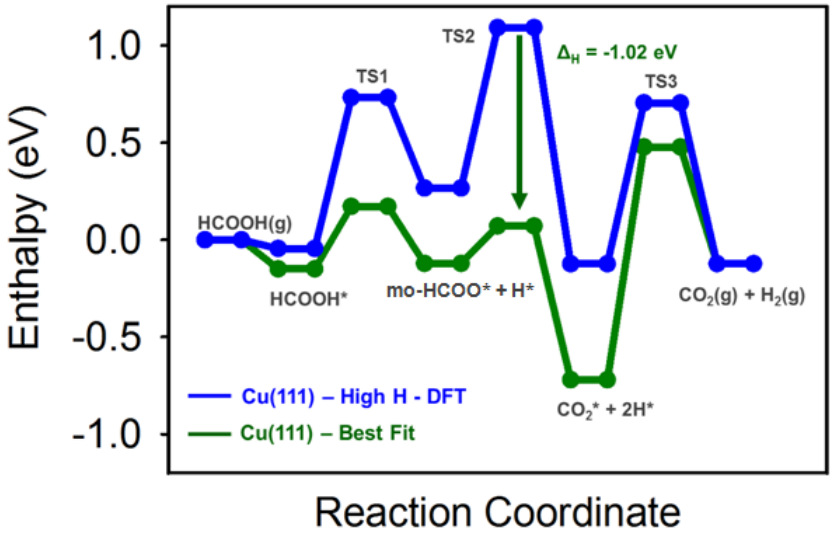


**Figure 8-13** 2-dimensional PESs of FA decomposition reaction via the HCOO pathway on the Cu(111)-6H facet. Zero-energy corresponds to the gasphase enthalpy of FA molecule. The blue line corresponds to the DFT derived PES, and the green line corresponds to the best-fit solution. The adjustment required in the transition state energy for HCOO decomposition is also reported.

**Table 8-9** Adjustments needed in the DFT derived binding energies on clean Cu(100) corresponding to the best fit.

| Species | HCOO Solution ΔBE / eV | H Solution ΔBE / eV |
|---|---|---|
| H* | 0.00 | -0.02 |
| HCOO** | -0.09 | 0.00 |

Hence, the DFT derived parameters on all three Cu(111) surfaces (clean and high HCOO/H covered Cu(111)) proved inadequate in describing the experimental observations without requiring large deviations from the initial guesses. For these reasons, Cu(100) was chosen for subsequent

studies, as it is the next most stable facet and is the only facet other than Cu(111) that is visible in the TEM images under reaction conditions.[248]

**Cu(100) surface**

A similar approach to the one described in the preceding sections was adopted to perform parameter optimization starting with the thermochemistry and kinetics parameters obtained on Cu(100) as the initial guess. With no adjustments to these parameters, the model predicted reaction rates were one order of magnitude smaller than the experimentally measured rates. Starting with these parameters as the initial guesses, a solution that offers excellent fits with the experimental dataset with minimal adjustments in the DFT parameters was obtained. The alterations made in the DFT parameters are reported in **Table 8-9** and **Table 8-10**; the maximum adjustment required in the DFT parameters was -0.14 eV, in the transition state energy for HCOO decomposition step, which is well within the uncertainty of our DFT calculations. The sequence of elementary steps that describe the reaction mechanism was the same as the one observed for the Cu(111) surface, i.e. : $HCOOH \rightarrow HCOO + H \rightarrow CO_2 + 2H \rightarrow CO_2 + H_2$. For this solution, the surface was predicted to have a high coverage (0.32 ML – 0.78 ML) of surface HCOO, with ~ 0.55 ML being the predicted coverage for most experimental conditions that were collected at the 130 °C. Hence, as before, there existed an inconsistency between the surface coverages predicted by the model and those employed in the DFT calculations. Also, the parameter space was sampled within ± 0.4 eV of the DFT derived initial guesses to capture any other feasible solutions that might have been missed by starting only from the DFT derived initial guesses and performing gradient based search. A 'Cu(100)-H-solution' was identified; this solution also exhibited excellent fits with the experimental data, but predicted adsorbed H to be the most abundant surface intermediate (MASI) instead, with a coverage of 0.53 ML – 0.67 ML. The adjustments required in the DFT derived

parameters to obtain this solution were significantly higher than the ones in the 'HCOO solution', with the transition state energy for $H_2$ recombination step requiring destabilization by ~ 0.42 eV. This solution both required adjusting parameters outside of the uncertainty of DFT, and was not self-consistent with respect to the surface coverages of the model and those employed in the DFT calculations.

**Table 8-10** Adjustments needed in the DFT derived TS energiees corresponding to the best fit, and the Cambell's degree of rate control (XRC) for the kinetically relevant elementary steps on clean Cu(100).

| Reaction | HCOO Solution | | H Solution | |
|---|---|---|---|---|
| | ΔETS / eV | XRC | ΔETS / eV | XRC |
| HCOOH* + 2*↔ HCOO** + H* | 0.08 | 0.08-0.26 | 0.00 | 0.02-0.07 |
| HCOO* + *↔ $CO_2$* + H* | -0.14 | 0.75-0.91 | -0.11 | 0.33-0.36 |
| 2H*↔ $H_2$ + 2* | 0.00 | 0.00 | 0.42 | 0.58-0.62 |

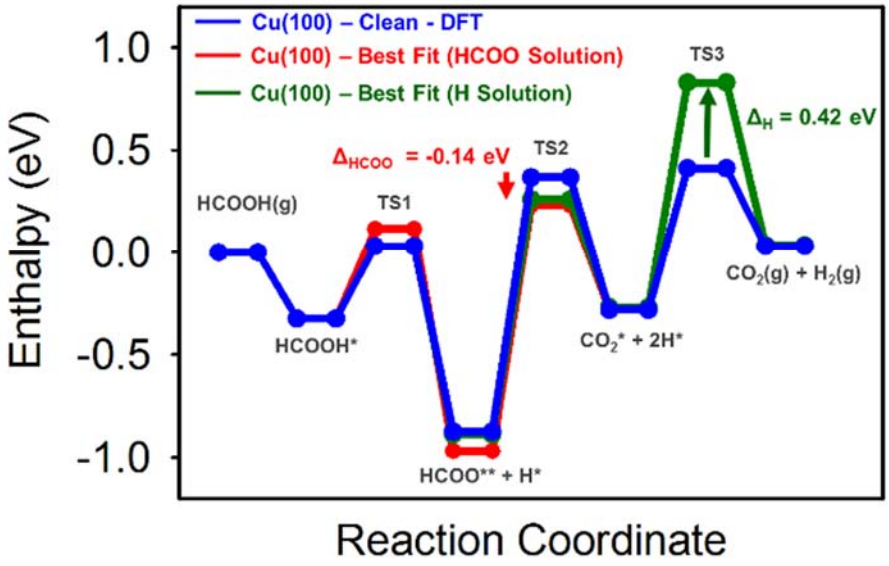


**Figure 8-14** 2-dimensional PESs of FA decomposition reaction via the HCOO pathway on clean Cu(100). Zero-energy corresponds to the gasphase enthalpy of FA molecule. The blue line corresponds to the DFT derived PES, and the red and green lines reflect the enthalpies of the thermodynamic and transition states for the HCOO solution and H solution, respectlively. The maximum adjustments made for both these solutions is also reported.

**Cu(100)–2HCOO surface**

A microkinetic model that uses the DFT numbers obtained on high HCOO-covered Cu(100) as the initial guesses under-predicted the TOFs by one order of magnitude; however, adjusting parameters within the uncertainty of DFT parameters provided convergence to a solution that demonstrated an excellent fit with the experimental TOFs, and accurately described the experimentally observed reaction rates and apparent activation energy barrier. The model predicted a HCOO surface coverage of 0.34 ML – 0.72 ML, with HCOO → $CO_2$ + H being the rate controlling step. Hence, for this solution, the surface coverages of all species, as predicted by the model, were consistent with those employed in the unit cell that was used in the DFT calculations to obtain the initial guesses for the energetics (thermochemistry and kinetics) for FA decomposition.

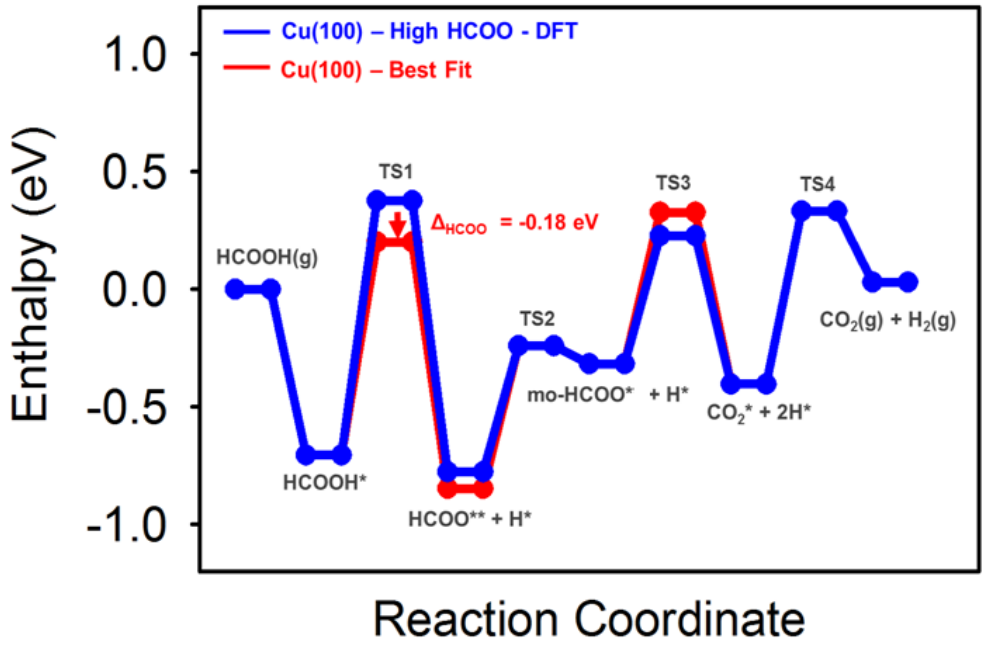


**Figure 8-15** 2-dimensional PESs of FA decomposition reaction via the HCOO pathway on a HCOO-covered Cu(111) surface. Zero-energy corresponds to the gasphase enthalpy of FA molecule. The blue line corresponds to the DFT derived PES, and the red line corresponds to the best-fit solution. The adjustment required in the transition state energy for the HCOO formation step is also reported.

**Table 8-11** Adjustments needed in the DFT derived BEs on high HCOO covered Cu(100) corresponding to the best fit

| Species | HCOO Solution ΔBE / eV |
|---|---|
| H* | 0.00 |
| HCOO** | -0.07 |

**Table 8-12** Adjustments needed in the DFT derived TS energies on high HCOO covered Cu(111) corresponding to the best fit, and the Cambell's degree of rate control (XRC) for the kinetically relevant elementary steps

| Reaction | HCOO Solution | |
|---|---|---|
| | ΔETS / eV | XRC |
| HCOOH* + 2*↔ HCOO** + H* | -0.18 | 0.10-0.23 |
| HCOO**↔ mo-HCOO* + * | 0.00 | 0.00 |
| mo-HCOO* + *↔ $CO_2$* + H* | 0.10 | 0.60-0.89 |
| 2H*↔ $H_2$ + 2* | 0.00 | 0.01-0.00 |

## 8.4 Conclusions

Using an iterative approach that involves first principles DFT calculations, reaction kinetics measurements, and mean-field microkinetic modeling, a systematic investigation of the formic acid decomposition reaction on supported Cu catalysts was performed. Cu(111) and Cu(100) surfaces were chosen first as the single crystal facets representative of the supported Cu catalysts employed in the reaction kinetics experiments. An extensive set of periodic, self-consistent DFT calculations was performed on these surfaces to obtain the initial guesses for the thermodynamics and kinetics parameters to be used in the mean-field microkinetic model. While it was possible to obtain excellent fits with the experimental dataset starting from these initial guesses, the models predicted high coverages (0.30 ML – 0.80 ML) of either HCOO or H species on the two surfaces, for all reaction conditions. Hence, there existed an inconsistency in the surface environments predicted by the models and those used to obtain the initial guesses for the thermochemistry and kinetics parameters. Ignoring this discrepancy, as is often done, would have led to an incorrect description of the active catalytic surface. To address this disparity, additional DFT calculations

were performed for key elementary steps, using unit cells that had pre-adsorbed HCOO and H as 'spectator' species. In order to be adjudged the active site for this reaction, a solution must satisfy the following criteria: (1) it must exhibit good agreement with the experimental observations, (2) the maximum deviations from the DFT derived initial guesses should be within the uncertainty (0.2 eV), and (3) the surface environment predicted by the model should be consistent with the one used in the DFT calculations to obtain the initial guesses for all thermochemistry and kinetics parameters. Among all the surfaces that were explored, only one surface, a Cu(100) surface with 4/9 ML of pre-adsorbed spectator HCOO species, satisfied all the three criteria.

Hence, it is proposed that contrary to several earlier reports, Cu(111), in all likelihood, does not contribute significantly to the overall rates for this reaction under realistic reactions conditions. Instead a Cu(100) surface with 4/9 ML of pre-adsorbed spectator HCOO species is the most probable active site for this reaction, and the overall energetics (thermochemistry and kinetics ) of this reaction vary, to a great extent, with the surface coverages of reaction intermediates employed in the DFT calculations. This formic acid dehydrogenation reaction was found to proceed via the following sequence of elementary steps: $HCOOH \rightarrow HCOO + H \rightarrow CO_2 + 2H \rightarrow CO_2\,(g) + H_2\,(g)$; HCOO decomposition to $CO_2$ and H was found to be the rate controlling step for all the experimental conditions that were studied, and the Cu(100) surface was shown to have a HCOO coverage of 0.36 ML – 0.73 ML under the reaction conditions. In addition to elucidating the true nature of active sites for formic acid decomposition on supported catalysts, this study demonstrates, in detail, the steps involved in an iterative process that ensures holistic self-consistency of the solutions with respect to the surface coverages, which is crucial in developing an accurate fundamental understanding of the chemistries of heterogeneously catalyzed reactions.

# Chapter 9 Conclusions and Suggestions for Future Work

## 9.1 Conclusions

The studies reported in this thesis showed how DFT calculations can be used to obtain a fundamental mechanistic understanding of catalytic reactions, including the reaction pathways, active surface intermediates, rate limiting steps, and how the tentative conclusions based on the DFT analysis about the reaction mechanism and active sites can be confirmed when the DFT derived parameters are input into a microkinetic model to explain the experimentally observed reaction rates.

Specifically speaking, formic acid decomposition, being a promising reaction that can utilize the byproduct generated in biomass reforming and selectively produce $H_2$ *in situ*, was studied on several transition metal catalysts ─ gold, palladium, platinum and copper.

For the gold catalysts, DFT calculations were performed for formic acid decomposition on three facets of Au ─ Au(111), Au(100) and Au(211), which serve as our initial guesses of the active site of Au ─ to obtain the thermodynamic and kinetic parameters that were later input into a microkinetic model to compare the reaction kinetics data collected on SiC supported gold catalysts. By adjusting the DFT derived parameters, a good fit to the experimental results can be obtained, which suggests the reaction proceeds through a simple closed catalytic cycle: two dehydrogenation steps of HCOOH through the HCOO intermediate followed by a hydrogen recombination reaction. The large adjustments required to get a solution on all three surfaces of gold indicates that they are not the active site for this reaction. Further reaction rate measurements on gold catalysts at various different dispersions together with measurement of Au particle-size distribution from TEM images claim that the highly under-coordinated corner sites are the active site on gold for formic acid

reaction. To corroborate this hypothesis, this reaction was further investigated on small Au clusters in the sub-nanometer range using the AIMD-DFT method. Through a rigorous screening process based on the activation energy of the first dehydrogenation step, several Au clusters ($Au_4$, $Au_5$, $Au_7$ and $Au_{17}$-$Au_{19}$) were selected for a complete reaction pathway study including both the HCOO mediated route and also the COOH mediated route. It is found that all Au clusters being investigated are more active than the Au(211) surface, and similar as on the extended surfaces, the reaction also proceed through the HCOO pathway on Au clusters. By inputting the DFT derived parameters on the candidate clusters into the microkinetic model and comparing with the experimental data, $Au_{18}$ was identified as a model for the active site, as it is the only cluster on which the DFT derived parameters are only finely tuned to fit the experimental data, while the adjustments required for the other clusters to obtain a good fit are too large to be justified. Hence, an integrated approach combining DFT calculations, experiments, and microkinetic modeling and implementing an iterative process on the active site models used in DFT calculations was presented to unravel the reaction mechanism and identify the true active site.

This approach was extended to the studies on copper catalysts that were presented in Chapter 7 and 8. The difference from the studies on gold catalysts is that the microkinetic model predicted a high surface coverage of either H or HCOO using the DFT obtained parameters on clean copper surfaces ─ Cu(100) and Cu(111), thus to resolve the inconsistency between model input and predictions about the surface coverage, DFT calculations were repeated on H- or HCOO-covered Cu(111) and Cu(100) surfaces and the newly derived DFT parameters were again inputted into the model to fit the experimental data. The iterative DFT calculations and fitting processes lead to the identification of Cu(100) as the active site for HCOOH decomposition, with the surface being covered by about 0.4 ML of HCOO under reaction conditions. The two studies on Au and Cu

catalysts highlighted the importance of obtaining a 'self-consistent' solution from the model that not only fits the experimental data but also has a consistent description about surface environments between the model input and predictions. A 'self-consistent' solution from the microkinetic model is critical in understanding the catalytic behavior under reaction conditions and determining the true active site of the reaction.

On Pt and Pd catalysts, studies were conducted at high surface coverage of CO since the two catalysts are prone to be poisoned by CO, which is a possible product from HCOOH decomposition. It was shown that the presence of adsorbed CO species can significantly affect the reaction energetics as well as reaction pathways. Thus, an explicit information about the surface coverage of poison species obtained from surface science experiments and advanced characterization techniques are important to understand the reaction mechanism under realistic conditions. The integrated method presented in the studies on Cu catalysts can also be employed to obtain an accurate description about the catalytic process on Pt and Pd catalysts.

In addition to the work presented in this thesis, the AIMD-DFT based approach was also adopted to study another industrially important route for hydrogen production ─ water gas shift (WGS) reaction ─ on Au catalysts. The primary aim of this study was to explain the high activity of supported gold catalysts and identify the active sites for the reaction. By calculating the BE of key intermediates and reaction energy of key elementary steps of WGS reaction on a series of Au cluster models, the active sites are determined to be atomically isolated and oxidized Au species Au-Ox-(OH)y, which was corroborated by experimental observations. This work has been published in Science.

## 9.2 Suggestions for future work

Though the free Au cluster $Au_{18}$ has been nicely shown to be the active site for HCOOH decomposition, its stability or intactness of the structure when supported on SiC (the support used in experiments) under reaction conditions and the effect of support on the reactivity remain unknown. This can be tackled by first investigating the structure of this cluster on SiC support with the DFT approach and further preforming rigorous DFT-based reaction pathway studies on SiC supported Au clusters; calculated results on such a surface should be directly comparable to the experimental rates and information regarding the support effect on the morphology of Au clusters, reactivity, and reaction mechanism would be obtained.

For studies on Au clusters, albeit the mean–field microkinetic modelling is an appealing approach to compute reaction rates due to the mathematical simplicity and low computational cost, it might give inaccurate results with the assumption of an average distribution of molecular events on the catalyst surface, which is not the case for small sized Au clusters, where a strong adsorbate–adsorbate interaction is observed. Kinetic Monte Carlo (KMC) method might be a good choice to compare the DFT derived results on Au clusters with the experimental rates by fully resolving all molecular events occurring on a catalytic surface and explicitly taking into account spatial inhomogeneity associated with different site types and spatial correlations arising from adsorbate–adsorbate interactions.

Catalyst design for the HCOOH decomposition reaction can be achieved by identifying the reactivity descriptors, developing scaling relations and Brønsted-Evans-Polanyi (BEP) relationships based on our results on surfaces of the transition metals and constructing a volcano type of plot by implementing the relations developed in the microkinetic model. The volcano plot based catalyst design practices fail to account for the coverage effects, which have been shown to

be dramatic on the reaction energetics and reaction pathways in our studies on Cu, Pd and Pt for HCOOH decomposition, hence the current catalyst design methods can be further improved by incorporating the coverage effects. Since the most abundant surface intermediates and coverages are usually different on different catalysts, great endeavor will be needed to make this happen.

# References


1. Cronshaw, I. (2015) World Energy Outlook 2014 projections to 2040: natural gas and coal trade, and the role of China, *Australian Journal of Agricultural and Resource Economics 59*, 571-585.
2. Bartholomew, C. H., and Farrauto, R. J. (2006) Fundamentals of Industrial Catalytic Processes, 2nd Edition, *Fundamentals of Industrial Catalytic Processes, 2nd Edition*, 1-970.
3. Sholl, D. S. (2006) Applications of Density Functional Theory to Heterogeneous Catalysis, In *Chemical Modelling: Applications and Theory, Vol 4* (Hinchliffe, A., Ed.), pp 108-160, Royal Soc Chemistry, Cambridge.
4. Sholl, D. S., and Steckel, J. A. (2009) *Density Functional Theory: A Practical Introduction*, John Wiley $ Sons, Inc.
5. Campbell, C. T. (1994) Micro- and macro-kinetics: their relationship in heterogeneous catalysis, *Topics in Catalysis 1*, 353-366.
6. Dumesic, J. A., Rudd, D. F., Aparicio, L. M., Rekoske, J. E., and Treviño, A. A. (1993) *The Microkinetics of Heterogeneous Catalysis*, 1 edition ed., American Chemical Society.
7. Gokhale, A. A., Kandoi, S., Greeley, J. P., Mavrikakis, M., and Dumesic, J. A. (2004) Molecular-level descriptions of surface chemistry in kinetic models using density functional theory, *Chemical Engineering Science 59*, 4679-4691.
8. Kandoi, S., Greeley, J., Sanchez-Castillo, M. A., Evans, S. T., Gokhale, A. A., Dumesic, J. A., and Mavrikakis, M. (2006) Prediction of experimental methanol decomposition rates on platinum from first principles, *Topics in Catalysis 37*, 17-28.
9. Alonso, D. M., Bond, J. Q., and Dumesic, J. A. (2010) Catalytic conversion of biomass to biofuels, *Green Chemistry 12*, 1493-1513.
10. Tilman, D., Socolow, R., Foley, J. A., Hill, J., Larson, E., Lynd, L., Pacala, S., Reilly, J., Searchinger, T., Somerville, C., and Williams, R. (2009) Beneficial Biofuels-The Food, Energy, and Environment Trilemma, *Science 325*, 270-271.
11. Berndes, G., and Hansson, J. (2007) Bioenergy expansion in the EU: Cost-effective climate change mitigation, employment creation and reduced dependency on imported fuels, *Energy Policy 35*, 5965-5979.
12. Lange, J. P., Price, R., Ayoub, P. M., Louis, J., Petrus, L., Clarke, L., and Gosselink, H. (2010) Valeric Biofuels: A Platform of Cellulosic Transportation Fuels, *Angewandte Chemie-International Edition 49*, 4479-4483.
13. Braden, D. J., Henao, C. A., Heltzel, J., Maravelias, C. T., and Dumesic, J. A. (2011) Production of liquid hydrocarbon fuels by catalytic conversion of biomass-derived levulinic acid, *Green Chemistry 13*, 1755-1765.
14. Bozell, J. J., and Petersen, G. R. (2010) Technology development for the production of biobased products from biorefinery carbohydrates-the US Department of Energy's "Top 10" revisited, *Green Chemistry 12*, 539-554.
15. Rackemann, D. W., and Doherty, W. O. S. (2012) A review on the production of levulinic acid and furanics from sugars, *Proceedings of the 34th Conference of the Australian Society of Sugar Cane Technologists held at Cairns, Queensland, Australia, 1-4 May 2012*, 20-M 20.
16. Zhang, T., and Wyman, C. E. (2011) Integrated production of levulinic acid and furfural from cellulosic biomass, *Abstracts of Papers of the American Chemical Society 241*.
17. Girisuta, B., Janssen, L. P. B. M., and Heeres, H. J. (2007) Kinetic study on the acid-catalyzed hydrolysis of cellulose to levulinic acid, *Industrial & Engineering Chemistry Research 46*, 1696-1708.
18. Serrano-Ruiz, J. C., Braden, D. J., West, R. M., and Dumesic, J. A. (2010) Conversion of cellulose to hydrocarbon fuels by progressive removal of oxygen, *Applied Catalysis B-Environmental 100*, 184-189.

19. Xingwen, Y., and Pickup, P. G. (2008) Recent advances in direct formic acid fuel cells (DFAFC), *Journal of Power Sources 182*, 124-132.
20. Xingwen, Y., and Pickup, P. G. (2011) Codeposited PtSb/C catalysts for direct formic acid fuel cells, *Journal of Power Sources 196*, 7951-7956.
21. Xingwen, V., and Pickup, P. G. (2011) Screening of PdM and PtM catalysts in a multi-anode direct formic acid fuel cell, *Journal of Applied Electrochemistry 41*, 589-597.
22. Vansanten, R. A., and Neurock, M. (1995) Concepts in theoretical heterogeneous catalytic reactivity, *Catalysis Reviews-Science and Engineering 37*, 557-698.
23. McWeeny, R., and Sutcliffe, B. T. (1976) Methods of molecular quantum mechanics, *Methods of molecular quantum mechanics*, xii+307 pp-xii+307 pp.
24. McWeeny, R. (1992) *Methods of molecular quantum mechanics*, 2nd edition ed., Academic Press.
25. Bartlett, R. J., and Stanton, J. F. (1994) Applications of Post-Hartree-Fock methods - a tutorial, *Reviews in Computational Chemistry V 5*, 65-169.
26. Ceperley, D. M. (1996) Quantum Monte Carlo methods in chemistry, *Advances in Chemical Physics, Vol Xciii 93*, 1-38.
27. Foulkes, W. M. C., Mitas, L., Needs, R. J., and Rajagopal, G. (2001) Quantum Monte Carlo simulations of solids, *Reviews of Modern Physics 73*, 33-83.
28. Hammond, B. L., Lester, W. A., Jr., and Reynolds, P. J. (1994) *Monte Carlo methods in ab initio quantum chemistry*.
29. Mitas, L. (1997) Electronic structure calculations by quantum Monte Carlo methods, *Physica B 237*, 318-320.
30. Hohenberg, P., and Kohn, W. (1964) Inhomogeneous electron gas, *Physical Review 136*, B864-B871.
31. Kohn, W., and Sham, L. J. (1965) Self-consistent equations including exchange and correlation effects, *Physical Review 140*, A1133-A1138.
32. Perdew, J. P., and Zunger, A. (1981) Self-interaction correction to density-functional approximations for many-electron systems, *Physical Review B 23*, 5048-5079.
33. Vosko, S. H., Wilk, L., and Nusair, M. (1980) Accurate spin-dependent electron liquid correlation energies for local spin-density calculations - a critical analysis, *Canadian Journal of Physics 58*, 1200-1211.
34. Perdew, J. P., Chevary, J. A., Vosko, S. H., Jackson, K. A., Pederson, M. R., Singh, D. J., and Fiolhais, C. (1992) Atoms, molecules, solids, and surfaces - application of the generalized gradient approximation for exchange and correlation, *Physical Review B 46*, 6671-6687.
35. Boddien, A., Loges, B., Junge, H., Gaertner, F., Noyes, J. R., and Beller, M. (2009) Continuous Hydrogen Generation from Formic Acid: Highly Active and Stable Ruthenium Catalysts, *Advanced Synthesis & Catalysis 351*, 2517-2520.
36. Fellay, C., Yan, N., Dyson, P. J., and Laurenczy, G. (2009) Selective Formic Acid Decomposition for High-Pressure Hydrogen Generation: A Mechanistic Study, *Chemistry-a European Journal 15*, 3752-3760.
37. Fellay, C., Dyson, P. J., and Laurenczy, G. (2008) A viable hydrogen-storage system based on selective formic acid decomposition with a ruthenium catalyst, *Angewandte Chemie-International Edition 47*, 3966-3968.
38. Gan, W., Dyson, P. J., and Laurenczy, G. (2009) Hydrogen storage and delivery: immobilization of a highly active homogeneous catalyst for the decomposition of formic acid to hydrogen and carbon dioxide, *Reaction Kinetics and Catalysis Letters 98*, 205-213.
39. Fukuzumi, S. (2008) Bioinspired energy conversion systems for hydrogen production and storage, *European Journal of Inorganic Chemistry*, 1351-1362.
40. Boddien, A., Gaertner, F., Jackstell, R., Junge, H., Spannenberg, A., Baumann, W., Ludwig, R., and Beller, M. (2010) ortho-Metalation of Iron(0) Tribenzylphosphine Complexes: Homogeneous Catalysts for the Generation of Hydrogen from Formic Acid, *Angewandte Chemie-International Edition 49*, 8993-8996.

41. Johnson, T. C., Morris, D. J., and Wills, M. (2010) Hydrogen generation from formic acid and alcohols using homogeneous catalysts, *Chemical Society Reviews 39*, 81-88.
42. Bond, J. Q., Alonso, D. M., Wang, D., West, R. M., and Dumesic, J. A. (2010) Integrated Catalytic Conversion of gamma-Valerolactone to Liquid Alkenes for Transportation Fuels, *Science 327*, 1110-1114.
43. Columbia, M. R., and Thiel, P. A. (1994) The Interaction of Formic-Acid with Transition-Metal Surfaces, Studied in Ultrahigh-Vacuum, *Journal of Electroanalytical Chemistry 369*, 1-14.
44. Madix, R. J. (1980) Surface reaction modifiers - General overview, *Abstracts of Papers of the American Chemical Society 180*, 26-PHYS.
45. Larson, L. A., and Dickinson, J. T. (1979) Decomposition of formic acid on Ru(1010), *Surface Science 84*, 17-30.
46. Sun, Y. K., and Weinberg, W. H. (1991) Catalytic Decomposition of Formic Acid on Ru(001) - Transient Measurements, *Journal of Chemical Physics 94*, 4587-4599.
47. Solymosi, F., Kiss, J., and Kovacs, I. (1987) Adsorption of HCOOH on Rh(111) and its Reaction with Preadsorbed Oxygen, *Surface Science 192*, 47-65.
48. Jorgensen, S. W., and Madix, R. J. (1988) Active Oxygen on Group VIII Metals - Activation of Formic Acid and Formaldehyde on Pd(100) *Journal of the American Chemical Society 110*, 397-400.
49. Bulushev, D. A., Beloshapkin, S., and Ross, J. R. H. (2010) Hydrogen from formic acid decomposition over Pd and Au catalysts, *Catalysis Today 154*, 7-12.
50. Solymosi, F., Koos, A., Liliom, N., and Ugrai, I. (2011) Production of CO-free H-2 from formic acid. A comparative study of the catalytic behavior of Pt metals on a carbon support, *Journal of Catalysis 279*, 213-219.
51. Ying, D. H. S., and Madix, R. J. (1980) Thermal Desorption Study of Formic Acid Decomposition on a Clean Cu(110) Surface, *Journal of Catalysis 61*, 48-56.
52. Boddien, A., Mellmann, D., Gaertner, F., Jackstell, R., Junge, H., Dyson, P. J., Laurenczy, G., Ludwig, R., and Beller, M. (2011) Efficient Dehydrogenation of Formic Acid Using an Iron Catalyst, *Science 333*, 1733-1736.
53. Koos, A., and Solymosi, F. (2010) Production of CO-Free H-2 by Formic Acid Decomposition over Mo2C/Carbon Catalysts, *Catalysis Letters 138*, 23-27.
54. Flaherty, D. W., Berglund, S. P., and Mullins, C. B. (2010) Selective decomposition of formic acid on molybdenum carbide: A new reaction pathway, *Journal of Catalysis 269*, 33-43.
55. McCarty, J., and Madix, R. J. (1975) Study of kinetics and mechanism of decomposition of formic-acid on carburized and graphitized Ni(110) using AES, LEED and flash desorption, *Journal of Catalysis 38*, 402-417.
56. Kubota, J., Bandara, A., Wada, A., Domen, K., and Hirose, C. (1996) IRAS study of formic acid decomposition on NiO(111)/Ni(111) surface: Comparison of vacuum and catalytic conditions, *Surface Science 368*, 361-365.
57. Dilara, P. A., and Vohs, J. M. (1993) TPD and HREELS investigation of the reaction of formic-acid on $ZrO_2$(100), *Journal of Physical Chemistry 97*, 12919-12923.
58. Larsson, R., Jamroz, M. H., and Borowiak, M. A. (1998) On the catalytic decomposition of formic acid. I. The activation energies for oxide catalysis, *Journal of Molecular Catalysis a-Chemical 129*, 41-51.
59. Senanayake, S. D., and Mullins, D. R. (2008) Redox pathways for HCOOH decomposition over CeO2 surfaces, *Journal of Physical Chemistry C 112*, 9744-9752.
60. Peng, X. D., and Barteau, M. A. (1991) Acid-base Properties of Model MgO surfaces, *Langmuir 7*, 1426-1431.
61. Outka, D. A., and Madix, R. J. (1987) Acid-base and nucleophilic chemistry of atomic oxygen on the Au(110) surface - reactions with formic-acid and formaldehyde, *Surface Science 179*, 361-376.
62. Lin, C.-H., Chen, C.-L., and Wang, J.-H. (2011) Mechanistic Studies of Water-Gas-Shift Reaction on Transition Metals, *Journal of Physical Chemistry C 115*, 18582-18588.

63. Davis, B. H. B. H., Jacobs, G., Patterson, P. M. P. M., Graham, U. M. U. M., and Crawford, A. C. A. C. (2005) Low temperature water gas shift: the link between the catalysis of WGS and formic acid decomposition over Pt/ceria, *International Journal of Hydrogen Energy 30*, 1265-1276.
64. Gokhale, A. A., Dumesic, J. A., and Mavrikakis, M. (2008) On the mechanism of low-temperature water gas shift reaction on copper, *Journal of the American Chemical Society 130*, 1402-1414.
65. Liu, C., Chen, M., Du, C., Zhang, J., Yin, G., Shi, P., and Sun, Y. (2012) Durability of Ordered Mesoporous Carbon Supported Pt Particles as Catalysts for Direct Formic Acid Fuel Cells, *International Journal of Electrochemical Science 7*, 10592-10606.
66. Rice, C., Ha, S., Masel, R. I., and Wieckowski, A. (2003) Catalysts for direct formic acid fuel cells, *Journal of Power Sources 115*, 229-235.
67. Yu, X. W., and Pickup, P. G. (2011) Codeposited PtSb/C catalysts for direct formic acid fuel cells, *Journal of Power Sources 196*, 7951-7956.
68. Yinghui, P., Ruiming, Z., and Blair, S. L. (2009) Anode poisoning study in direct formic acid fuel cells, *Electrochemical and Solid-State Letters 12*, B23-26.
69. Markovic, N. M., and Ross, P. N. (2002) Surface science studies of model fuel cell electrocatalysts, *Surface Science Reports 45*, 121-229.
70. Choi, J.-H., Jeong, K.-J., Dong, Y., Han, J., Lim, T.-H., Lee, J.-S., and Sung, Y.-E. (2006) Electro-oxidation of methanol and formic acid on PtRu and PtAu for direct liquid fuel cells, *Journal of Power Sources 163*, 71-75.
71. Brandon, N. P., Skinner, S., and Steele, B. C. H. (2003) Recent advances in materials for fuel cells, *Annual Review of Materials Research 33*, 183-213.
72. Xu, J. B., Zhao, T. S., and Liang, Z. X. (2008) Carbon supported platinum-gold alloy catalyst for direct formic acid fuel cells, *Journal of Power Sources 185*, 857-861.
73. Sheng, Z., Yuyan, S., Geping, Y., and Yuehe, L. (2010) Facile synthesis of PtAu alloy nanoparticles with high activity for formic acid oxidation, *Journal of Power Sources 195*, 1103-1106.
74. Haruta, M., Kobayashi, T., Sano, H., and Yamada, N. (1987) Novel Gold Catalysts for the Oxidation of Carbon Monoxide at a Temperature Far Below 0-degree-C, *Chemistry Letters*, 405-408.
75. Hutchings, G. J. (1985) Vapor-Phase Hydrochlorination of Acetylene - Correlation of Catalytic Activity of Supported Metal Chloride Catalysts, *Journal of Catalysis 96*, 292-295.
76. Sa, J., Goguet, A., Taylor, S. F. R., Tiruvalam, R., Kiely, C. J., Nachtegaal, M., Hutchings, G. J., and Hardacre, C. (2011) Influence of Methyl Halide Treatment on Gold Nanoparticles Supported on Activated Carbon, *Angewandte Chemie-International Edition 50*, 8912-8916.
77. Guzman, J., and Gates, B. C. (2001) Gold nanoclusters supported on MgO: Synthesis, characterization, and evidence of Au(6), *Nano Letters 1*, 689-692.
78. Janssens, T. V. W., Clausen, B. S., Hvolbaek, B., Falsig, H., Christensen, C. H., Bligaard, T., and Norskov, J. K. (2007) Insights into the reactivity of supported Au nanoparticles: combining theory and experiments, *Topics in Catalysis 44*, 15-26.
79. Gong, J. (2012) Structure and Surface Chemistry of Gold-Based Model Catalysts, *Chemical Reviews 112*, 2987-3054.
80. Coquet, R., Howard, K. L., and Willock, D. J. (2008) Theory and simulation in heterogeneous gold catalysis, *Chemical Society Reviews 37*, 2046-2076.
81. Davis, R. J. (2003) All that glitters is not Au-0, *Science 301*, 926-927.
82. Bond, G. C., and Thompson, D. T. (1999) Catalysis by gold, *Catalysis Reviews-Science and Engineering 41*, 319-388.
83. Hashmi, A. S. K., and Hutchings, G. J. (2006) Gold catalysis, *Angewandte Chemie-International Edition 45*, 7896-7936.
84. Guzman, J., Anderson, B. G., Vinod, C. P., Ramesh, K., Niemantsverdriet, J. W., and Gates, B. C. (2005) Synthesis and reactivity of dimethyl gold complexes supported on MgO: Characterization by infrared and x-ray absorption spectroscopies, *Langmuir 21*, 3675-3683.

85. Yi, N., Saltsburg, H., and Flytzani-Stephanopoulos, M. (2013) Hydrogen Production by Dehydrogenation of Formic Acid on Atomically Dispersed Gold on Ceria, *Chemsuschem 6*, 816-819.
86. Ojeda, M., and Iglesia, E. (2009) Formic Acid Dehydrogenation on Au-Based Catalysts at Near-Ambient Temperatures, *Angewandte Chemie-International Edition 48*, 4800-4803.
87. Gazsi, A., Bansagi, T., and Solymosi, F. (2011) Decomposition and Reforming of Formic Acid on Supported Au Catalysts: Production of CO-Free H-2, *Journal of Physical Chemistry C 115*, 15459-15466.
88. Hammer, B., Hansen, L. B., and Norskov, J. K. (1999) Improved adsorption energetics within density-functional theory using revised Perdew-Burke-Ernzerhof functionals, *Physical Review B 59*, 7413-7421.
89. Greeley, J., Norskov, J. K., and Mavrikakis, M. (2002) Electronic structure and catalysis on metal surfaces, *Annual Review of Physical Chemistry 53*, 319-348.
90. Neugebauer, J., and Scheffler, M. (1992) Adsorbate-substrate and adsorbate-adsorbate interactions of Na and K adlayers on Al(111), *Physical Review B 46*, 16067-16080.
91. Bengtsson, L. (1999) Dipole correction for surface supercell calculations, *Physical Review B 59*, 12301-12304.
92. Chadi, D. J., and Cohen, M. L. (1973) Special points in Brillouin zone, *Physical Review B 8*, 5747-5753.
93. Monkhorst, H. J., and Pack, J. D. (1976) Special Points for Brillouin-Zone Integrations, *Physical Review B 13*, 5188-5192.
94. Vanderbilt, D. (1990) Soft Self-Consistent Pseudopotentials in a Generalized Eigenvalue Formalism, *Physical Review B 41*, 7892-7895.
95. Perdew, J. P., Chevary, J. A., Vosko, S. H., Jackson, K. A., Pederson, M. R., Singh, D. J., and Fiolhais, C. (1992) Atoms, Molecules, Solids, and Surfaces - Applications of the Generalized Gradient Approximation for Exchange and Correlation, *Physical Review B 46*, 6671-6687.
96. White, J. A., and Bird, D. M. (1994) Implementation of Gradient-Corrected Exchange-Correlation Potentials in Car-Parrinello Total-Energy Calculations, *Physical Review B 50*, 4954-4957.
97. Kresse, G., and Furthmuller, J. (1996) Efficiency of ab-initio total energy calculations for metals and semiconductors using a plane-wave basis set, *Computational Materials Science 6*, 15-50.
98. Donohue, J. I. (1974) The Structures of the Elements, *Wiley: New York*, 222.
99. Henkelman, G., Uberuaga, B. P., and Jonsson, H. (2000) A climbing image nudged elastic band method for finding saddle points and minimum energy paths, *Journal of Chemical Physics 113*, 9901-9904.
100. Henkelman, G., and Jonsson, H. (2000) Improved tangent estimate in the nudged elastic band method for finding minimum energy paths and saddle points, *Journal of Chemical Physics 113*, 9978-9985.
101. Greeley, J., and Mavrikakis, M. (2003) A first-principles study of surface and subsurface H on and in Ni(111): diffusional properties and coverage-dependent behavior, *Surface Science 540*, 215-229.
102. Grabow, L. C., and Mavrikakis, M. (2011) Mechanism of Methanol Synthesis on Cu through CO2 and CO Hydrogenation, *Acs Catalysis 1*, 365-384.
103. Grabow, L. C., Gokhale, A. A., Evans, S. T., Dumesic, J. A., and Mavrikakis, M. (2008) Mechanism of the water gas shift reaction on Pt: First principles, experiments, and microkinetic modeling, *Journal of Physical Chemistry C 112*, 4608-4617.
104. Chakarova-Kack, S. D., Schroder, E., Lundqvist, B. I., and Langreth, D. C. (2006) Application of van der Waals density functional to an extended system: Adsorption of benzene and naphthalene on graphite, *Physical Review Letters 96*.
105. Sauer, J., Ugliengo, P., Garrone, E., and Saunders, V. R. (1994) Theoretical Study of van der Waals Complexes at Surface Sites in Comparison with the Experiment, *Chemical Reviews 94*, 2095-2160.
106. Lopez, N., Janssens, T. V. W., Clausen, B. S., Xu, Y., Mavrikakis, M., Bligaard, T., and Norskov, J. K. (2004) On the origin of the catalytic activity of gold nanoparticles for low-temperature CO oxidation, *Journal of Catalysis 223*, 232-235.

107. Hu, C. Q., Ting, S. W., Chan, K. Y., and Huang, W. (2012) Reaction pathways derived from DFT for understanding catalytic decomposition of formic acid into hydrogen on noble metals, *International Journal of Hydrogen Energy 37*, 15956-15965.
108. Yu, Y. L., Wang, X., and Lim, K. H. (2011) A DFT Study on the Adsorption of Formic Acid and Its Oxidized Intermediates on (100) Facets of Pt, Au, Monolayer and Decorated Pt@Au Surfaces, *Catalysis Letters 141*, 1872-1882.
109. Campbell, C. T., and Daube, K. A. (1987) A Surface Science Investigation of the Water-Gas Shift Reaction on Cu(111), *Journal of Catalysis 104*, 109-119.
110. Vanherwijnen, T., and Dejong, W. A. (1980) Kinetics and Mechanism of the Co Shift on Cu-Zno .1. Kinetics of the Forward and Reverse Co Shift Reactions, *Journal of Catalysis 63*, 83-93.
111. Edwards, J. F., and Schrader, G. L. (1984) Infrared-Spectroscopy of Cu/Zno Catalysts for the Water-Gas Shift Reaction and Methanol Synthesis, *Journal of Physical Chemistry 88*, 5620-5624.
112. Bowker, M., Hadden, R. A., Houghton, H., Hyland, J. N. K., and Waugh, K. C. (1988) The Mechanism of Methanol Synthesis on Copper-Zinc Oxide Alumina Catalysts, *Journal of Catalysis 109*, 263-273.
113. Neophytides, S. G., Marchi, A. J., and Froment, G. F. (1992) Methanol Synthesis by Means of Diffuse Reflectance Infrared Fourier-Transform and Temperature-Programmed Reaction Spectroscopy, *Applied Catalysis a-General 86*, 45-64.
114. Sakakini, B., Tabatabaei, J., Watson, M. J., Waugh, K. C., and Zemicael, F. W. (1996) Identification of the intermediate involved in methanol synthesis by gaseous titration, *Faraday Discussions 105*, 369-376.
115. Senanayake, S. D., Stacchiola, D., Liu, P., Mullins, C. B., Hrbek, J., and Rodriguez, J. A. (2009) Interaction of CO with OH on Au(111): HCOO, CO3, and HOCO as Key Intermediates in the Water-Gas Shift Reaction, *Journal of Physical Chemistry C 113*, 19536-19544.
116. Meunier, F. C., Reid, D., Goguet, A., Shekhtman, S., Hardacre, C., Burch, R., Deng, W., and Flytzani-Stephanopoulos, M. (2007) Quantitative analysis of the reactivity of formate species seen by DRIFTS over a Au/Ce(La)O-2 water-gas shift catalyst: First unambiguous evidence of the minority role of formates as reaction intermediates, *Journal of Catalysis 247*, 277-287.
117. Nishimura, K., Kunimatsu, K., Machida, K., and Enyo, M. (1989) Electrocatalysis of Pd + Au Alloy Electrodes .4. Ir Spectroscopic Studies on the Surface Species Derived from Formaldehyde and Formate in Alkaline-Solutions, *Journal of Electroanalytical Chemistry 260*, 181-192.
118. Chen, Y., Cheng, J., Hu, P., and Wang, H. F. (2008) Examining the redox and formate mechanisms for water-gas shift reaction on Au/CeO2 using density functional theory, *Surface Science 602*, 2828-2834.
119. Duan, S., Ji, Y. F., Fang, P. P., Chen, Y. X., Xu, X., Luo, Y., and Tian, Z. Q. (2013) Density functional theory study on the adsorption and decomposition of the formic acid catalyzed by highly active mushroom-like Au@Pd@Pt tri-metallic nanoparticles, *Physical Chemistry Chemical Physics 15*, 4625-4633.
120. Zhong, W. H., Liu, Y. X., and Zhang, D. J. (2012) Theoretical Study of Methanol Oxidation on the PtAu(111) Bimetallic Surface: CO Pathway vs Non-CO Pathway, *Journal of Physical Chemistry C 116*, 2994-3000.
121. Greeley, J., and Mavrikakis, M. (2005) Surface and subsurface hydrogen: Adsorption properties on transition metals and near-surface alloys, *Journal of Physical Chemistry B 109*, 3460-3471.
122. Huang, S.-C., Lin, C.-H., and Wang, J. H. (2010) Trends of Water Gas Shift Reaction on Close-Packed Transition Metal Surfaces, *Journal of Physical Chemistry C 114*, 9826-9834.
123. Barton, D. G., and Podkolzin, S. G. (2005) Kinetic study of a direct water synthesis over silica-supported gold nanoparticles, *Journal of Physical Chemistry B 109*, 2262-2274.
124. Ford, D. C., Nilekar, A. U., Xu, Y., and Mavrikakis, M. (2010) Partial and complete reduction of O-2 by hydrogen on transition metal surfaces, *Surface Science 604*, 1565-1575.

125. Jalili, S., Isfahani, A. Z., and Habibpour, R. (2012) Atomic oxygen adsorption on Au (100) and bimetallic Au/M (M = Pt and Cu) surfaces, *Computational and Theoretical Chemistry 989*, 18-26.
126. Xu, Y., and Mavrikakis, M. (2003) Adsorption and dissociation of O-2 on gold surfaces: Effect of steps and strain, *Journal of Physical Chemistry B 107*, 9298-9307.
127. Mehmood, F., Kara, A., Rahman, T. S., and Henry, C. R. (2009) Comparative study of CO adsorption on flat, stepped, and kinked Au surfaces using density functional theory, *Physical Review B 79*.
128. Ojifinni, R. A., Froemming, N. S., Gong, J., Pan, M., Kim, T. S., White, J. M., Henkelman, G., and Mullins, C. B. (2008) Water-enhanced low-temperature CO oxidation and isotope effects on atomic oxygen-covered Au(111), *Journal of the American Chemical Society 130*, 6801-6812.
129. Liu, S. P., Jin, P., Zhang, D. H., Hao, C., and Yang, X. M. (2013) Reaction mechanism for methanol oxidation on Au(1 1 1): A density functional theory study, *Applied Surface Science 265*, 443-451.
130. Bi, Q.-Y., Du, X.-L., Liu, Y.-M., Cao, Y., He, H.-Y., and Fan, K.-N. (2012) Efficient Subnanometric Gold-Catalyzed Hydrogen Generation via Formic Acid Decomposition under Ambient Conditions, *Journal of the American Chemical Society 134*, 8926-8933.
131. Grabow, L. C., Hvolbaek, B., and Norskov, J. K. (2010) Understanding Trends in Catalytic Activity: The Effect of Adsorbate-Adsorbate Interactions for CO Oxidation Over Transition Metals, *Topics in Catalysis 53*, 298-310.
132. Flytzani-Stephanopoulos, M., and Gates, B. C. (2012) Atomically Dispersed Supported Metal Catalysts, *Annual Review of Chemical and Biomolecular Engineering, Vol 3 3*, 545-574.
133. Fu, Q., Weber, A., and Flytzani-Stephanopoulos, M. (2001) Nanostructured Au-CeO2 catalysts for low-temperature water-gas shift, *Catalysis Letters 77*, 87-95.
134. Deng, W. L., De Jesus, J., Saltsburg, H., and Flytzani-Stephanopoulos, M. (2005) Low-content gold-ceria catalysts for the water-gas shift and preferential CO oxidation reactions, *Applied Catalysis a-General 291*, 126-135.
135. Gates, B. C. (2013) Supported gold catalysts: new properties offered by nanometer and sub-nanometer structures, *Chemical Communications 49*, 7876-7877.
136. Campbell, C. T. (2001) Finding the rate-determining step in a mechanism - Comparing DeDonder relations with the "degree of rate control", *Journal of Catalysis 204*, 520-524.
137. Dumesic, J. A. (1999) Analyses of reaction schemes using De Donder relations, *Journal of Catalysis 185*, 496-505.
138. Shekhar, M., Wang, J., Lee, W.-S., Williams, W. D., Kim, S. M., Stach, E. A., Miller, J. T., Delgass, W. N., and Ribeiro, F. H. (2012) Size and Support Effects for the Water-Gas Shift Catalysis over Gold Nanoparticles Supported on Model Al2O3 and TiO2, *Journal of the American Chemical Society 134*, 4700-4708.
139. Shekhar, M., Wang, J., Lee, W.-S., Akatay, M. C., Stach, E. A., Delgass, W. N., and Ribeiro, F. H. (2012) Counting Au catalytic sites for the water-gas shift reaction, *Journal of Catalysis 293*, 94-102.
140. Williams, W. D., Shekhar, M., Lee, W.-S., Kispersky, V., Delgass, W. N., Ribeiro, F. H., Kim, S. M., Stach, E. A., Miller, J. T., and Allard, L. F. (2010) Metallic Corner Atoms in Gold Clusters Supported on Rutile Are the Dominant Active Site during Water-Gas Shift Catalysis, *Journal of the American Chemical Society 132*, 14018-14020.
141. Sanchez, A., Abbet, S., Heiz, U., Schneider, W. D., Hakkinen, H., Barnett, R. N., and Landman, U. (1999) When gold is not noble: Nanoscale gold catalysts, *Journal of Physical Chemistry A 103*, 9573-9578.
142. Wang, J. L., Wang, G. H., and Zhao, J. J. (2002) Density-functional study of Au-n(n=2-20) clusters: Lowest-energy structures and electronic properties, *Physical Review B 66*.
143. Idrobo, J. C., Walkosz, W., Yip, S. F., Oeguet, S., Wang, J., and Jellinek, J. (2007) Static polarizabilities and optical absorption spectra of gold clusters (Au-n, n=2-14 and 20) from first principles, *Physical Review B 76*.

144. Ferrando, R., Fortunelli, A., and Johnston, R. L. (2008) Searching for the optimum structures of alloy nanoclusters, *Physical Chemistry Chemical Physics 10*, 640-649.
145. Marx, D., and Hutter, J. (2000) Ab initio molecular dynamics: Theory and Implementation, *Modern Methods and Algorithms of Quantum Chemistry*, 301-449.
146. Zhai, Y. P., Pierre, D., Si, R., Deng, W. L., Ferrin, P., Nilekar, A. U., Peng, G. W., Herron, J. A., Bell, D. C., Saltsburg, H., Mavrikakis, M., and Flytzani-Stephanopoulos, M. (2010) Alkali-Stabilized Pt-OHx Species Catalyze Low-Temperature Water-Gas Shift Reactions, *Science 329*, 1633-1636.
147. Mager-Maury, C., Chizallet, C., Sautet, P., and Raybaud, P. (2012) Platinum Nanoclusters Stabilized on gamma-Alumina by Chlorine Used As a Capping Surface Ligand: A Density Functional Theory Study, *Acs Catalysis 2*, 1346-1357.
148. Kresse, G., and Furthmuller, J. (1996) Efficient iterative schemes for ab initio total-energy calculations using a plane-wave basis set, *Physical Review B 54*, 11169-11186.
149. Kresse, G., and Joubert, D. (1999) From ultrasoft pseudopotentials to the projector augmented-wave method, *Physical Review B 59*, 1758-1775.
150. Blochl, P. E., Jepsen, O., and Andersen, O. K. (1994) Improved Tetrahedron Method for Brillouin-Zone Integrations, *Physical Review B 49*, 16223-16233.
151. Perdew, J. P., and Wang, Y. (1992) Accurate and simple analytic representation of the electron-gas correlation-energy, *Physical Review B 45*, 13244-13249.
152. Nose, S. (1984) A Unified Formulation of the Constant Temperature Molecular Dynamics Methods, *Journal of Chemical Physics 81*, 511-519.
153. Haruta, M., Yamada, N., Kobayashi, T., and Iijima, S. (1989) Gold Catalysts Prepared by Coprecipitation for Low-Temperature Oxidation of Hydrogen and of Carbon Monoxide, *Journal of Catalysis 115*, 301-309.
154. Gruene, P., Butschke, B., Lyon, J. T., Rayner, D. M., and Fielicke, A. (2014) Far-IR Spectra of Small Neutral Gold Clusters in the Gas Phase, *Zeitschrift Fur Physikalische Chemie-International Journal of Research in Physical Chemistry & Chemical Physics 228*, 337-350.
155. Li, Y. D., and Gao, Y. (2014) Theoretical advances of the structures and catalytic activities of small-sized gold nanoclusters, *Chinese Science Bulletin 59*, 239-246.
156. Schooss, D., Weis, P., Hampe, O., and Kappes, M. M. (2010) Determining the size-dependent structure of ligand-free gold-cluster ions, *Philosophical Transactions of the Royal Society a-Mathematical Physical and Engineering Sciences 368*, 1211-1243.
157. Woodham, A. P., and Fielicke, A. (2014) Gold Clusters in the Gas Phase, In *Gold Clusters, Colloids and Nanoparticles I* (Mingos, D. M. P., Ed.), pp 243-278, Springer Int Publishing Ag, Cham.
158. Gao, Y., Shao, N., Pei, Y., Chen, Z., and Zeng, X. C. (2011) Catalytic Activities of Subnanometer Gold Clusters (Au-16-Au-18, Au-20, and Au-27-Au-35) for CO Oxidation, *Acs Nano 5*, 7818-7829.
159. Furche, F., Ahlrichs, R., Weis, P., Jacob, C., Gilb, S., Bierweiler, T., and Kappes, M. M. (2002) The structures of small gold cluster anions as determined by a combination of ion mobility measurements and density functional calculations, *Journal of Chemical Physics 117*, 6982-6990.
160. Johansson, M. P., Lechtken, A., Schooss, D., Kappes, M. M., and Furche, F. (2008) 2D-3D transition of gold cluster anions resolved, *Physical Review A 77*.
161. Xiaopeng, X., Bokwon, Y., Landman, U., and Parks, J. H. (2006) Structural evolution of Au nanoclusters: from planar to cage to tubular motifs, *Physical Review B (Condensed Matter and Materials Physics) 74*, 165423-165421-165426.
162. Lechtken, A., Neiss, C., Kappes, M. M., and Schooss, D. (2009) Structure determination of gold clusters by trapped ion electron diffraction: Au-14(-)-Au-19(-), *Physical Chemistry Chemical Physics 11*, 4344-4350.
163. Gruene, P., Rayner, D. M., Redlich, B., van der Meer, A. F. G., Lyon, J. T., Meijer, G., and Fielicke, A. (2008) Structures of neutral Au-7, Au-19, and Au-20 clusters in the gas phase, *Science 321*, 674-676.

164. Hakkinen, H., Yoon, B., Landman, U., Li, X., Zhai, H. J., and Wang, L. S. (2003) On the electronic and atomic structures of small Au-N(-) (N=4-14) clusters: A photoelectron spectroscopy and density-functional study, *Journal of Physical Chemistry A 107*, 6168-6175.
165. Yoon, B., Koskinen, P., Huber, B., Kostko, O., von Issendorff, B., Hakkinen, H., Moseler, M., and Landman, U. (2007) Size-dependent structural evolution and chemical reactivity of gold clusters, *Chemphyschem 8*, 157-161.
166. Li, J., Li, X., Zhai, H. J., and Wang, L. S. (2003) Au-20: A tetrahedral cluster, *Science 299*, 864-867.
167. Huang, W., Bulusu, S., Pal, R., Zeng, X. C., and Wang, L.-S. (2009) Structural Transition of Gold Nanoclusters: From the Golden Cage to the Golden Pyramid, *Acs Nano 3*, 1225-1230.
168. Bulusu, S., Li, X., Wang, L.-S., and Zeng, X. C. (2007) Structural transitions from pyramidal to fused planar to tubular to core/shell compact in gold clusters: Au-n(-) (n=21-25), *Journal of Physical Chemistry C 111*, 4190-4198.
169. Wang, L.-M., and Wang, L.-S. (2012) Probing the electronic properties and structural evolution of anionic gold clusters in the gas phase, *Nanoscale 4*, 4038-4053.
170. Jinlan, W., Guanghou, W., and Jijun, Z. (2002) Density-functional study of Au n(n=2-20) clusters: Lowest-energy structures and electronic properties, *Physical Review B (Condensed Matter and Materials Physics) 66*, 035418/035411-035416.
171. Cai, W., Liang, L., Zhang, Y., Xing, W., and Liu, C. (2013) Real contribution of formic acid in direct formic acid fuel cell: Investigation of origin and guiding for micro structure design, *International Journal of Hydrogen Energy 38*, 212-218.
172. Rice, C., Ha, R. I., Masel, R. I., Waszczuk, P., Wieckowski, A., and Barnard, T. (2002) Direct formic acid fuel cells, *Journal of Power Sources 111*, 83-89.
173. Mikolajczuk, A., Borodzinski, A., Kedzierzawski, P., Stobinski, L., Mierzwa, B., and Dziura, R. (2011) Deactivation of carbon supported palladium catalyst in direct formic acid fuel cell, *Applied Surface Science 257*, 8211-8214.
174. Masel, R. I., Larsen, R., and Ha, S. Y. Formic acid fuel cell used for power plant, has anode catalyst made of palladium, formed on surface of solid polymer proton conducting electrolyte, Univ Illinois Found.
175. Kuan-Lun, C., Shannon, M. A., and Masel, R. I. (2006) An improved miniature direct formic acid fuel cell based on nanoporous silicon for portable power generation, *Journal of the Electrochemical Society 153*, A1562-1567.
176. Hu, C., Pulleri, J. K., Ting, S.-W., and Chan, K.-Y. (2014) Activity of Pd/C for hydrogen generation in aqueous formic acid solution, *International Journal of Hydrogen Energy 39*, 381-390.
177. Mori, K., Dojo, M., and Yamashita, H. (2013) Pd and Pd-Ag Nanoparticles within a Macroreticular Basic Resin: An Efficient Catalyst for Hydrogen Production from Formic Acid Decomposition, *Acs Catalysis 3*, 1114-1119.
178. Jeroro, E., and Vohs, J. M. (2009) Reaction of Formic Acid on Zn-Modified Pd(111), *Catalysis Letters 130*, 271-277.
179. Bulushev, D. A., Bulusheva, L. G., Beloshapkin, S., O'Connor, T., Okotrub, A. V., and Ryan, K. M. (2015) Pd Clusters Supported on Amorphous, Low-Porosity Carbon Spheres for Hydrogen Production from Formic Acid, *Acs Applied Materials & Interfaces 7*, 8719-8726.
180. Bowker, M., Stone, P., Bennett, R., and Perkins, N. (2002) Formic acid adsorption and decomposition on TiO2(110) and on Pd/TiO2(110) model catalysts, *Surface Science 511*, 435-448.
181. Navlani-Garcia, M., Mori, K., Wen, M. C., Kuwahara, Y., and Yamashita, H. (2015) Size Effect of Carbon-Supported Pd Nanoparticles in the Hydrogen Production from Formic Acid, *Bulletin of the Chemical Society of Japan 88*, 1500-1502.
182. Luo, Q. Q., Wang, T., Beller, M., and Jiao, H. J. (2013) Hydrogen generation from formic acid decomposition on Ni(211), Pd(211) and Pt(211), *Journal of Molecular Catalysis a-Chemical 379*, 169-177.

183. Yoo, J. S., Abild-Pedersen, F., Norskov, J. K., and Studt, F. (2014) Theoretical Analysis of Transition-Metal Catalysts for Formic Acid Decomposition, *Acs Catalysis 4*, 1226-1233.
184. Luo, Q., Beller, M., and Jiao, H. (2013) Formic Acid Dehydrogenation on Surfaces - A Review of Computational Aspect, *Journal of Theoretical & Computational Chemistry 12*.
185. Luo, Q., Feng, G., Beller, M., and Jiao, H. (2012) Formic Acid Dehydrogenation on Ni(111) and Comparison with Pd(111) and Pt(111), *Journal of Physical Chemistry C 116*, 4149-4156.
186. Yue, C. M. Y., and Lim, K. H. (2009) Adsorption of Formic Acid and its Decomposed Intermediates on (100) Surfaces of Pt and Pd: A Density Functional Study, *Catalysis Letters 128*, 221-226.
187. Davis, J. L., and Barteau, M. A. (1991) Reactions of Carboxylic-Acids on the Pd(111)-(2 X 2)O Surface - Multiple Roles of Surface Oxygen-Atoms, *Surface Science 256*, 50-66.
188. Zhao, Y., Deng, L., Tang, S.-Y., Lai, D.-M., Liao, B., Fu, Y., and Guo, Q.-X. (2011) Selective Decomposition of Formic Acid over Immobilized Catalysts, *Energy & Fuels 25*, 3693-3697.
189. Bako, I., and Palinkas, G. (2006) Vibration of small molecules on Pt(111) surface, *Surface Science 600*, 3809-3814.
190. Columbia, M. R., and Thiel, P. A. (1990) The Reaction of Formic-Acid with Clean and Water-Covered Pt(111), *Surface Science 235*, 53-59.
191. Columbia, M. R., Crabtree, A. M., and Thiel, P. A. (1993) Chemical reactions between atomic oxygen and formic acid on Pt(111), *Journal of Electroanalytical Chemistry 351*, 207-226.
192. Abbas, N., and Madix, R. J. (1983) Surface reaction modification - The effect of structured overlayers of sulfur on the kinetics and mechanism of the decomposition of formic acid on Pt(111), *Applications of Surface Science 16*, 424-440.
193. Qi, Y. Y., Zhu, R. X., and Zhang, D. J. (2014) Adsorption behaviors of monomer and dimer of formic acid on Pt (111) in the absence and presence of water, *Journal of Molecular Modeling 20*, 9.
194. Qi, Y. Y., Gao, J., Zhang, D. J., and Liu, C. B. (2015) Comparative theoretical study of formic acid decomposition on PtAg(111) and Pt(111) surfaces, *Rsc Advances 5*, 21170-21177.
195. Qi, Y. Y., Li, J. J., Zhang, D. J., and Liu, C. B. (2015) Reexamination of formic acid decomposition on the Pt(111) surface both in the absence and in the presence of water, from periodic DFT calculations, *Catalysis Science & Technology 5*, 3322-3332.
196. Chen, Y. X., Heinen, M., Jusys, Z., and Behm, R. J. (2006) Kinetics and mechanism of the electrooxidation of formic acid - Spectroelectrochemical studies in a flow cell, *Angewandte Chemie-International Edition 45*, 981-985.
197. Jensen, M. B., Myler, U., and Thiel, P. A. (1993) Local and Collective Structure of Formate on Pt(111), *Surface Science 290*, L655-L661.
198. Avery, N. R. (1982) Adsorption of Formic Acid on Clean and Oxygen Covered Pt(111), *Applications of Surface Science 11-2*, 774-783.
199. Scaranto, J., and Mavrikakis, M. (2015) HCOOH decomposition on Pt(111): A DFT study, *Surface Science in press*.
200. Iglesia, E., and Boudart, M. (1983) Decomposition of Formic Acid on Copper, Nickel, and Copper-Nickel Alloys. 2. Catalytic and Temperature-Programmed Decomposition of Formic Acid on Cu/SiO2, Cu/Al2O3, and Cu Powder, *Journal of Catalysis 81*, 214-223.
201. Bowker, M., Haq, S., Holroyd, R., Parlett, P. M., Poulston, S., and Richardson, N. (1996) Spectroscopic and kinetic studies of formic acid adsorption on Cu(110), *Journal of the Chemical Society-Faraday Transactions 92*, 4683-4686.
202. Yang, Y., Evans, J., Rodriguez, J. A., White, M. G., and Liu, P. (2010) Fundamental studies of methanol synthesis from CO2 hydrogenation on Cu(111), Cu clusters, and Cu/ZnO(000(1)over-bar), *Physical Chemistry Chemical Physics 12*, 9909-9917.
203. Quinn, D. F., and Taylor, D. (1965) Decomposition of Formic Acid and Methanol on Copper-Nickel Alloys, *Journal of the Chemical Society*, 5248-5251.
204. Rundell, D. N., Saltsburg, H. M., and Smith, W. D. (1980) The Role of Multiple Gas-Solid Collisions in the Catalytic Decomposition of Formic Acid, *Chemical Engineering Science 35*, 1113-1119.

205. Inglis, H. S., and Taylor, D. (1969) Decomposition of Formic Acid on Titanium, Vanadium, Chromium, Manganese, Iron, Cobalt, Nickel and Copper, *Journal of the Chemical Society a - Inorganic Physical Theoretical*, 2985-2987.
206. Nakano, H., Nakamura, I., Fujitani, T., and Nakamura, J. (2001) Structure-dependent kinetics for synthesis and decomposition of formate species over Cu(111) and Cu(110) model catalysts, *Journal of Physical Chemistry B 105*, 1355-1365.
207. Hu, Z. M., and Boyd, R. J. (2000) Structure sensitivity and cluster size convergence for formate adsorption on copper surfaces: A DFT cluster model study, *Journal of Chemical Physics 112*, 9562-9568.
208. Bowker, M., Rowbotham, E., Leibsle, F. M., and Haq, S. (1996) The adsorption and decomposition of formic acid on Cu{110}, *Surface Science 349*, 97-110.
209. Youngs, T. G. A., Haq, S., and Bowker, M. (2008) Formic acid adsorption and oxidation on Cu(110), *Surface Science 602*, 1775-1782.
210. Greeley, J., and Mavrikakis, M. (2002) Methanol decomposition on Cu(111): A DFT study, *Journal of Catalysis 208*, 291-300.
211. Herron, J. A., Scaranto, J., Ferrin, P., Li, S., and Mavrikakis, M. (2014) Trends in Formic Acid Decomposition on Model Transition Metal Surfaces: A Density Functional Theory study, *Acs Catalysis 4*, 4434-4445.
212. Straumanis, M. E., and Yu, L. S. (1969) Lattice parameters, densities, expansion coefficients and perfection of structure of Cu and of Cu-In alpha phase, *Acta Crystallographica, Section A (Crystal Physics, Diffraction, Theoretical and General Crystallography) A25*, 676-682.
213. Singh, S., Li, S., Carrasquillo-Flores, R., Alba-Rubio, A. C., Dumesic, J. A., and Mavrikakis, M. (2014) Formic acid decomposition on Au catalysts: DFT, microkinetic modeling, and reaction kinetics experiments, *Aiche Journal 60*, 1303-1319.
214. Loges, B., Boddien, A., Gaertner, F., Junge, H., and Beller, M. (2010) Catalytic Generation of Hydrogen from Formic acid and its Derivatives: Useful Hydrogen Storage Materials, *Topics in Catalysis 53*, 902-914.
215. Grasemann, M., and Laurenczy, G. (2012) Formic acid as a hydrogen source - recent developments and future trends, *Energy & Environmental Science 5*, 8171-8181.
216. Enthaler, S., von Langermann, J., and Schmidt, T. (2010) Carbon dioxide and formic acid-the couple for environmental-friendly hydrogen storage?, *Energy & Environmental Science 3*, 1207-1217.
217. Hull, J. F., Himeda, Y., Wang, W.-H., Hashiguchi, B., Periana, R., Szalda, D. J., Muckerman, J. T., and Fujita, E. (2012) Reversible hydrogen storage using CO2 and a proton-switchable iridium catalyst in aqueous media under mild temperatures and pressures, *Nature Chemistry 4*, 383-388.
218. Jiang, H.-L., Singh, S. K., Yan, J.-M., Zhang, X.-B., and Xu, Q. (2010) Liquid-Phase Chemical Hydrogen Storage: Catalytic Hydrogen Generation under Ambient Conditions, *Chemsuschem 3*, 541-549.
219. Rees, N. V., and Compton, R. G. (2011) Sustainable energy: a review of formic acid electrochemical fuel cells, *Journal of Solid State Electrochemistry 15*, 2095-2100.
220. Uhm, S., Lee, H. J., and Lee, J. (2009) Understanding underlying processes in formic acid fuel cells, *Physical Chemistry Chemical Physics 11*, 9326-9336.
221. Wettstein, S. G., Bond, J. Q., Alonso, D. M., Pham, H. N., Datye, A. K., and Dumesic, J. A. (2012) RuSn bimetallic catalysts for selective hydrogenation of levulinic acid to gamma-valerolactone, *Applied Catalysis B-Environmental 117*, 321-329.
222. Iglesia, E., and Boudart, M. (1986) Unimolecular and Bimolecular Formic Acid Decomposition on Copper, *Journal of Physical Chemistry 90*, 5272-5274.
223. Sun, Y. K., and Weinberg, W. H. (1991) Catalytic decomposition of formic-acid on Ru(001) - transient measurements, *Journal of Chemical Physics 94*, 4587-4599.

224. Columbia, M. R., Crabtree, A. M., and Thiel, P. A. (1992) The temperature and coverage dependence of adsorbed formic acid and its conversion to formate on Pt(111), *Journal of the American Chemical Society 114*, 1231-1237.
225. Iglesia, E., and Boudart, M. (1983) Decomposition of Formic Acid on Copper, Nickel, and Copper-Nickel Alloys. 1. Preparation and Characterization of Catalysts, *Journal of Catalysis 81*, 204-213.
226. Iglesia, E., and Boudart, M. (1983) Decomposition of Formic Acid on Copper, Nickel and Copper-Nickel Alloys. 3. Catalytic Decomposition on Nickel and Copper-Nickel Alloys, *Journal of Catalysis 81*, 224-238.
227. Iglesia, E., and Boudart, M. (1984) Decomposition of Formic Acid on Copper, Nickel and Copper-Nickel Alloys. 4. Temperature-Programmed Decomposition of Bulk Nickel Formate and of Formic Acid Preadsorbed on Nickel Powder, *Journal of Catalysis 88*, 325-332.
228. Iglesia, E., and Boudart, M. (1985) Catalytic and Temperature-Programmed Decomposition of Formic Acid on Copper Catalysts, *Abstracts of Papers of the American Chemical Society 189*, 92-COLL.
229. Wachs, I. E., and Madix, R. J. (1979) Oxidation of H2CO on a Copper(110) Surface, *Surface Science 84*, 375-386.
230. Ying, D. H. S., and Madix, R. J. (1980) Thermal-desorption study of formic-acid decomposition on a clean Cu(110) surface, *Journal of Catalysis 61*, 48-56.
231. Bowker, M., and Madix, R. J. (1981) XPS, UPS and Thermal Desorption Studies of the Reactions of Formaldehyde and Formic Acid with the Cu(110) Surface, *Surface Science 102*, 542-565.
232. Baber, A. E., Mudiyanselage, K., Senanayake, S. D., Beatriz-Vidal, A., Luck, K. A., Sykes, E. C. H., Liu, P., Rodriguez, J. A., and Stacchiola, D. J. (2013) Assisted deprotonation of formic acid on Cu(111) and self-assembly of 1D chains, *Physical Chemistry Chemical Physics 15*, 12291-12298.
233. Poulston, S., Bennett, R. A., Jones, A. H., and Bowker, M. (1997) STM study of formic acid adsorption on Cu(110), *Physical Review B 55*, 12888-12891.
234. Bowker, M., Poulston, S., Bennett, R. A., Stone, P., Jones, A. H., Haq, S., and Hollins, P. (1998) A combined STM molecular beam study of formic acid oxidation on Cu(110), *Journal of Molecular Catalysis a-Chemical 131*, 185-197.
235. Bowker, M., Bennett, R. A., Poulston, S., and Stone, P. (1998) Insights into surface reactivity: formic acid oxidation on Cu(110) studied using STM and a molecular beam reactor, *Catalysis Letters 56*, 77-83.
236. Volter, J., and Alsdorf, E. (1971) Surface Composition and Catalytic Activity of Nickel-Copper Alloys, *Zeitschrift Fur Anorganische Und Allgemeine Chemie 380*, 303-&.
237. Schwab, G. M., and Watson, A. M. (1964) Isotope effect in catalytic formic-acid dehydrogenation, pp 1833 - 1846, Royal Society of Chemistry, Trans. Faraday Soc.
238. Howe, R. F., and Metcalfe, A. (1969) Dehydrogenation of Formic Acid by Cu3Au, *Journal of Catalysis 14*, 55-&.
239. Schwab, G. M., and Schmidt, R. (1972) Influence of Plastic Deformation on Catalytic Properties on Metals, *Zeitschrift Fur Physikalische Chemie-Frankfurt 82*, 174-184.
240. Dowden, D. A., and Reynolds, P. W. (1950) Some reactions over alloy catalysts, *Discussions of the Faraday Society 8*, 184-190.
241. Bennett, R. A., Poulston, S., and Bowker, M. (1998) Elevated temperature scanning tunneling microscopy study of formic acid adsorption and reaction on oxygen (2x1) covered Cu(110), *Journal of Chemical Physics 108*, 6916-6922.
242. Nakamura, I., Nakano, H., Fujitani, T., Uchijima, T., and Nakamura, J. (1999) Synthesis and decomposition of formate on Cu(111) and Cu(110) surfaces: Structure sensitivity, *Journal of Vacuum Science & Technology a-Vacuum Surfaces and Films 17*, 1592-1595.
243. Rubert-Nason, P., Mavrikakis, M., Maravelias, C. T., Grabow, L. C., and Biegler, L. T. (2014) Advanced solution methods for microkinetic models of catalytic reactions: A methanol synthesis case study, *Aiche Journal 60*, 1336-1346.

244. Ulitsky, A., and Elber, R. (1990) A New Technique to Calculate Steepest Descent Paths in Flexible Polyatomic Systems, *Journal of Chemical Physics 92*, 1510-1511.
245. Mills, G., Jonsson, H., and Schenter, G. K. (1995) Reversible Work Transition-State Theory - Application to Dissociative Adsorption of Hydrogen, *Surface Science 324*, 305-337.
246. Singh, S., Li, S., Carrasquillo-Flores, R., Alba-Rubio, A. C., Dumesic, J. A., and Mavrikakis, M. (2014) Formic acid decomposition on Au catalysts: DFT, microkinetic modeling, and reaction kinetics experiments, pp 1303-1319, AIChE Journal.
247. Madon, R. J., Braden, D., Kandoi, S., Nagel, P., Mavrikakis, M., and Dumesic, J. A. (2011) Microkinetic analysis and mechanism of the water gas shift reaction over copper catalysts, *Journal of Catalysis 281*, 1-11.
248. Hansen, P. L., Wagner, J. B., Helveg, S., Rostrup-Nielsen, J. R., Clausen, B. S., and Topsoe, H. (2002) Atom-resolved imaging of dynamic shape changes in supported copper nanocrystals, *Science 295*, 2053-2055.
249. Lin, S., Johnson, R. S., Smith, G. K., Xie, D., and Guo, H. (2011) Pathways for methanol steam reforming involving adsorbed formaldehyde and hydroxyl intermediates on Cu(111): density functional theory studies, *Physical Chemistry Chemical Physics 13*, 9622-9631.
250. Zuo, Z.-J., Wang, L., Han, P.-D., and Huang, W. (2014) Insights into the reaction mechanisms of methanol decomposition, methanol oxidation and steam reforming of methanol on Cu(111): A density functional theory study, *International Journal of Hydrogen Energy 39*, 1664-1679.
251. Fujitani, T., Choi, Y., Sano, M., Kushida, Y., and Nakamura, J. (2000) Scanning tunneling microscopy study of formate species synthesized from CO2 hydrogenation and prepared by adsorption of formic acid over Cu(111), *Journal of Physical Chemistry B 104*, 1235-1240.
252. Sotiropoulos, A., Milligan, P. K., Cowie, B. C. C., and Kadodwala, M. (2000) A structural study of formate on Cu(111), *Surface Science 444*, 52-60.
253. Tang, Q.-L., Chen, Z.-X., and He, X. (2009) A theoretical study of the water gas shift reaction mechanism on Cu(111) model system, *Surface Science 603*, 2138-2144.
254. Lin, S., Xie, D., and Guo, H. (2011) Methyl Formate Pathway in Methanol Steam Reforming on Copper: Density Functional Calculations, *Acs Catalysis 1*, 1263-1271.
255. Wang, G.-C., and Nakamura, J. (2010) Structure Sensitivity for Forward and Reverse Water-Gas Shift Reactions on Copper Surfaces: A DFT Study, *Journal of Physical Chemistry Letters 1*, 3053-3057.
256. Wang, G. C., Jiang, L., Zhou, Y. H., Cai, Z. S., Pan, Y. M., Zhao, X. Z., Li, Y. W., Sun, Y. H., Zhong, B., Pang, X. Y., Huang, W., and Xie, K. C. (2003) Investigation of the kinetic properties for the forward and reverse WGS reaction by energetic analysis, *Journal of Molecular Structure-Theochem 634*, 23-30.